



HAL
open science

Physics of the thermal behavior of photovoltaic devices

Olivier Dupré

► **To cite this version:**

Olivier Dupré. Physics of the thermal behavior of photovoltaic devices. Thermics [physics.class-ph]. INSA de Lyon, 2015. English. NNT : 2015ISAL0089 . tel-01368592

HAL Id: tel-01368592

<https://theses.hal.science/tel-01368592>

Submitted on 19 Sep 2016

HAL is a multi-disciplinary open access archive for the deposit and dissemination of scientific research documents, whether they are published or not. The documents may come from teaching and research institutions in France or abroad, or from public or private research centers.

L'archive ouverte pluridisciplinaire **HAL**, est destinée au dépôt et à la diffusion de documents scientifiques de niveau recherche, publiés ou non, émanant des établissements d'enseignement et de recherche français ou étrangers, des laboratoires publics ou privés.

Ph.D. Thesis

**Physics of the thermal behavior of
photovoltaic devices**

Submitted to
Institut National des Sciences Appliquées de Lyon
Doctoral school: Mechanical, Energetics, Civil, and Acoustics Engineering

In fulfillment of the requirements for the
Ph.D. Degree

By
Olivier Dupré
(Engineer – INSA Lyon)

Defended on October 16th, 2015 before the examining committee composed of:

D. Lincot	CNRS Professor (Institut de Recherche et Développement sur l'Energie Photovoltaïque (IRDEP), Chatou, France)	Reviewer
A. Marti Vega	Professor (Instituto de Energía Solar, Universidad Politécnica de Madrid, Madrid, Espagne)	Reviewer
S. Dubois	Ph.D. (CEA - Institut National de l'Énergie Solaire (INES), Le Bourget-du-Lac, France)	
N. Wyrsh	Ph.D., Scientific collaborator (Laboratoire de photovoltaïque et couches minces électroniques (PV-LAB), Ecole Polytechnique Fédérale de Lausanne (EPFL), Neuchâtel, Suisse)	
M.A. Green	Professor (Australian Centre for Advanced Photovoltaics (ACAP), School of Photovoltaic and Renewable Energy Engineering, University of New South Wales (UNSW), Sydney, Australie)	Advisor
R. Vaillon	CNRS Professor (Centre for Energy and Thermal Sciences of Lyon (CETHIL), Villeurbanne, France)	Supervisor

Research Laboratory: Centre for Energy and Thermal Sciences of Lyon (CETHIL)

INSA Direction de la Recherche - Ecoles Doctorales – Quinquennal 2011-2015

SIGLE	ECOLE DOCTORALE	NOM ET COORDONNEES DU RESPONSABLE
CHIMIE	CHIMIE DE LYON http://www.edchimie-lyon.fr Sec : Renée EL MELHEM Bat Blaise Pascal 3 ^e étage 04 72 43 80 46 Insa : R. GOURDON secretariat@edchimie-lyon.fr	M. Jean Marc LANCELIN Université de Lyon – Collège Doctoral Bât ESCPE 43 bd du 11 novembre 1918 69622 VILLEURBANNE Cedex Tél : 04.72.43 13 95 directeur@edchimie-lyon.fr
E.E.A.	ELECTRONIQUE, ELECTROTECHNIQUE, AUTOMATIQUE http://edeea.ec-lyon.fr Sec : M.C. HAVGOUDOUKIAN Ecole-doctorale.eea@ec-lyon.fr	M. Gérard SCORLETTI Ecole Centrale de Lyon 36 avenue Guy de Collongue 69134 ECULLY Tél : 04.72.18 60.97 Fax : 04 78 43 37 17 Gerard.scorletti@ec-lyon.fr
E2M2	EVOLUTION, ECOSYSTEME, MICROBIOLOGIE, MODELISATION http://e2m2.universite-lyon.fr Sec : Safia AIT CHALAL Bat Atrium- UCB Lyon 1 04.72.44.83.62 Insa : S. REVERCHON Safia.ait-chalal@univ-lyon1.fr	M. Fabrice CORDEY Laboratoire de Géologie de Lyon Université Claude Bernard Lyon 1 Bât Géode – Bureau 225 43 bd du 11 novembre 1918 69622 VILLEURBANNE Cédex Tél : 04.72.44.83.74 Sylvie.reverchon-pescheux@insa-lyon.fr fabrice.cordey@univ-lyon1.fr
EDISS	INTERDISCIPLINAIRE SCIENCES- SANTÉ http://www.ediss-lyon.fr Sec : Safia AIT CHALAL Bat Atrium – UCB Lyon 1 04 72 44 83 62 Insa : Safia.ait-chalal@univ-lyon1.fr	Mme Emmanuelle CANET-SOULAS INSERM U1060, CarMeN lab, Univ. Lyon 1 Bâtiment IMBL 11 avenue Jean Capelle INSA de Lyon 696621 Villeurbanne Tél : 04.72.11.90.13 Emmanuelle.canet@univ-lyon1.fr
INFOMATHS	INFORMATIQUE ET MATHEMATIQUES http://infomaths.univ-lyon1.fr Sec : Renée EL MELHEM Bat Blaise Pascal 3 ^e étage infomaths@univ-lyon1.fr	Mme Sylvie CALABRETTO LIRIS – INSA de Lyon Bat Blaise Pascal 7 avenue Jean Capelle 69622 VILLEURBANNE Cedex Tél : 04.72. 43. 80. 46 Fax 04 72 43 16 87 Sylvie.calabretto@insa-lyon.fr
Matériaux	MATERIAUX DE LYON http://ed34.universite-lyon.fr Sec : M. LABOUNE PM : 71.70 –Fax : 87.12 Bat. Direction 1 ^{er} et. Ed.materiaux@insa-lyon.fr	M. Jean-Yves BUFFIERE INSA de Lyon MATEIS Bâtiment Saint Exupéry 7 avenue Jean Capelle 69621 VILLEURBANNE Cedex Tél : 04.72.43 71.70 Fax 04 72 43 85 28 Ed.materiaux@insa-lyon.fr
MEGA	MECANIQUE, ENERGETIQUE, GENIE CIVIL, ACOUSTIQUE http://mega.universite-lyon.fr Sec : M. LABOUNE PM : 71.70 –Fax : 87.12 Bat. Direction 1 ^{er} et. mega@insa-lyon.fr	M. Philippe BOISSE INSA de Lyon Laboratoire LAMCOS Bâtiment Jacquard 25 bis avenue Jean Capelle 69621 VILLEURBANNE Cedex Tél : 04.72 .43.71.70 Fax : 04 72 43 72 37 Philippe.boisse@insa-lyon.fr
ScSo	ScSo* http://recherche.univ-lyon2.fr/scso/ Sec : Viviane POLSINELLI Brigitte DUBOIS Insa : J.Y. TOUSSAINT viviane.polsinelli@univ-lyon2.fr	Mme Isabelle VON BUELTZINGLOEWEN Université Lyon 2 86 rue Pasteur 69365 LYON Cedex 07 Tél : 04.78.77.23.86 Fax : 04.37.28.04.48 isavonb@dbmail.com

*ScSo : Histoire, Géographie, Aménagement, Urbanisme, Archéologie, Science politique, Sociologie, Anthropologie

Physics of the thermal behavior of photovoltaic devices

Abstract (English)

This Ph.D. thesis manuscript reports on a study about the physics of the thermal behavior of photovoltaic (PV) devices. While it is long known that the conversion efficiency of PV devices deteriorates when their temperature increases, a detailed analysis of all the mechanisms involved was not available to date in the literature. Part I of this manuscript gathers and extends the existing works on the topic in order to offer a comprehensive view of the physics involved in the temperature sensitivities of PV systems. First, the fundamental reasons for the temperature dependence of the photovoltaic conversion process are described. Temperature coefficients, which quantify the temperature dependences, are analysed in the radiative limit (which is the fundamental limit for PV conversion). Then, the additional loss mechanisms of real PV devices are introduced and their impacts on the temperature coefficients are assessed. The existing theoretical expressions of the temperature coefficients of important solar cell parameters (namely open-circuit voltage, short-circuit current and fill factor) are reviewed. A new formulation of the temperature coefficient of the open-circuit voltage that incorporates the concept of External Radiative Efficiency (ERE) is proposed. The theoretical expressions are compared to experimental results on crystalline silicon cells from measurements made at the University of New South Wales (UNSW, Australia) and from the literature. Using the understanding of the relation between temperature coefficients and device physics, the specific cases of silicon heterojunction cells and cells made from compensated silicon are examined.

Because temperature has a critical impact on the performances of PV devices, several studies aimed on the one hand at predicting the temperature of PV modules from their operating conditions and on the other hand at designing inexpensive cooling solutions. The goal of Part II of this manuscript is to propose an original approach to minimize the temperature-induced losses in PV systems. The idea is to include the operating conditions in the optimization of the system parameters in order to maximize the power produced in these conditions rather than in the Standard Test Conditions (STC). These original optimizations are based on a comprehensive thermal model of PV cells that captures all of the physical mechanisms involved in the generation of heat within the cell. Following the presentation of this thermal model, several examples of original optimization (where a thermal criterion is added to the usual optical and electrical criteria) are presented. Some of these examples apply to standard solar cells while others demonstrate that this kind of optimization can be applied to other PV systems such as thermophotovoltaic (TPV) converters (solar or near-field TPV). The recent trend of the PV industry towards the design of products specifically adapted to a given use (climate, type of installation, etc) suggests that these original optimizations that take into account the system operating conditions could be implemented in the near future.

Synopsis (Français)

Cette thèse porte sur l'étude du comportement thermique des systèmes photovoltaïques (PV). Bien qu'il soit connu depuis longtemps que les rendements de conversion de ces systèmes se dégradent lorsque leur température augmente, une analyse détaillée de la physique de l'ensemble des mécanismes impliqués n'était pas jusqu'alors disponible. La première partie de ce manuscrit vise à proposer une vue unifiée sur la physique mise en jeu, qui rassemble et étend les travaux existants sur ce sujet. Dans un premier temps, les causes fondamentales de la dépendance des rendements de conversion photovoltaïque à la température du système sont exposées. Les coefficients de température (qui quantifient les dépendances en température des paramètres clés des performances des systèmes PV) sont analysés dans la limite radiative (qui correspond à une limite fondamentale pour la conversion photovoltaïque). Ensuite, les pertes additionnelles (par rapport à la limite

radiative) des systèmes PV réels sont introduites et leurs impacts sur les coefficients de température sont évalués. Les différentes expressions de ces coefficients sont passées en revue et une nouvelle expression qui incorpore le concept d'Efficacité Radiative Externe (ERE) est proposée pour le coefficient de température de la tension de circuit ouvert. Ces expressions sont ensuite examinées à l'aune de résultats expérimentaux comprenant une série de mesures réalisée à l'Université de Nouvelle-Galles du Sud (UNSW, Australie) sur des cellules en silicium cristallin ainsi que des données issues de la littérature. La compréhension des relations entre les coefficients de température et les phénomènes physiques mis en jeu permet par la suite d'analyser les cas particuliers des cellules en silicium compensé ainsi que le cas des cellules hétérojonctions en silicium.

Parce que la température a un impact critique sur les performances des systèmes PV, de nombreux travaux se sont attachés d'une part à prédire leur température en fonction de leurs conditions de fonctionnement (ensoleillement, température ambiante,...) et d'autre part à proposer des méthodes de refroidissement (à moindre coût). La deuxième partie de ce manuscrit a pour objectif de suggérer une nouvelle approche pour minimiser les pertes associées à la température de fonctionnement des systèmes photovoltaïques. L'idée défendue est qu'il est possible d'optimiser certains paramètres en fonction des conditions de fonctionnement du système afin de maximiser l'énergie produite dans ces conditions (au lieu de considérer des conditions standards de test qui ne sont pas forcément représentatives des conditions réelles de fonctionnement). Ces optimisations s'appuient sur l'établissement d'un modèle thermique complet d'une cellule PV qui rend compte de l'ensemble des mécanismes physiques responsables des différentes sources de chaleur. Après la présentation de ce modèle, plusieurs exemples d'optimisations qui prennent en compte les conditions réelles de fonctionnement (en incluant un critère thermique en plus des critères optiques et électriques usuels) sont présentés pour les systèmes PV classiques (solaires) mais aussi pour d'autres applications comme le thermophotovoltaïque (TPV), en champ lointain ou en champ proche. La récente tendance de l'industrie photovoltaïque qui consiste à proposer des produits spécifiquement adaptés à une utilisation donnée (climat, type d'installation, etc) laisse à penser que ce concept d'optimisations dédiées à des conditions de fonctionnement données devrait trouver des applications rapidement.

Acknowledgements

The three years that lasted my Ph.D. were extremely intense and rich. I had never worked so hard before but I took great pleasure in the work most of the time. Indeed, I think that this period really confirmed my vocation for research (and especially in a field such as photovoltaics which I believe is of critical importance for our society). I would like to use this page to thank all those who made this period so enjoyable and fruitful for me.

First of all, I would like to thank my supervisor, Prof. Rodolphe Vaillon, for his unreserved support, for all the hours he devoted to turn me into a researcher, for the freedom he gave me in my work and for all the great discussions we had on scientific and non-scientific topics during these years.

I would also like to express my deep gratitude towards my second supervisor, Prof. Martin A. Green, for inviting me at the University of New South Wales (while I did not come from a PV lab), for his kind supervision and for sharing his deep knowledge of photovoltaics with me.

I am thankful as well to all the members of my Ph.D. committee: Prof. Antonio Marti Vega and Prof. Daniel Lincot for their really thorough and insightful reviews of my Ph.D. manuscript, Dr. Sebastien Dubois and Dr. Nicolas Würsch for kindly accepting to participate to my Ph.D. jury and for their interesting questions and suggestions.

Also, I am very grateful to the persons that created a friendly and supportive environment where it felt good to go to everyday (members of CETHIL, the MINT group and UNSW). Special thanks to Damien and Rémi for providing some needed distractions from work.

I would like to thank Dr. Hamid Reza Mehrvarz for his help with the cells measured at the University of New South Wales, the Australian Centre for Advanced Photovoltaics (ACAP) and the School of Photovoltaic and Renewable Energy (SPREE) at the University of New South Wales (UNSW) for hosting me during 6 months and the doctoral school MEGA for financial support.

Last but not least, I thank my family and friends for their unconditional moral and physical support during my Ph.D.

Table of contents

Abstract (English)	1
Synopsis (Français)	2
Acknowledgements	5
Table of contents	7
List of Abbreviations	9
List of Symbols	11
1. General introduction	13
1.1. Why do we care about photovoltaics?	13
1.2. Why is it important to understand the thermal behavior of photovoltaic devices?	15
1.3. Original approach of the thermal behavior of PV devices	20
1.4. Brief plan of the thesis	21
Part 1. Physics of the temperature coefficients of solar cells	23
2. Introduction and state-of-the-art	25
3. Fundamental temperature coefficients of photovoltaic devices	37
3.1. The detailed balance principle and the thermodynamic argument	37
3.2. Bandgap temperature dependence and influence of the incident spectrum	49
3.3. Intrinsic temperature coefficient of silicon solar cells which includes Auger recombination	55
4. Temperature coefficients of real photovoltaic devices	61
4.1. Open-circuit voltage temperature sensitivity	65
4.2. Short-circuit current temperature sensitivity	72
4.3. Fill factor temperature sensitivity	75
5. Experimental assessment of temperature coefficient theories for crystalline silicon solar cells	79
5.1. Details on the experimental measurements	79
5.2. Short-circuit current temperature sensitivity	84
5.3. Open-circuit voltage temperature sensitivity	88
5.4. Fill factor temperature sensitivity	93
5.5. Temperature sensitivity of silicon heterojunction solar cells	96
5.6. Temperature sensitivity of compensated silicon solar cells	97
Part II: Thermal optimizations of photovoltaic devices	103
6. Introduction	105
6.1. The common approach to reduce the temperature-induced losses of PV systems: reducing the cell operating temperature via different cooling methods	107
6.2. Other approaches to reduce the temperature-induced losses of PV devices	112
6.3. Our approach to reduce the temperature-induced losses of PV devices: modeling the intertwined optical, electrical and thermal mechanisms to propose device optimizations that take into account actual operating conditions	113

7. A full thermal model of PV devices	119
7.1. A detailed review of the energy conversion loss processes	120
7.2. Temperature of the cell in a given environment	140
7.3. Revisiting the Normal Operating Conditions Temperature (NOCT)	141
8. Beyond STC: optimizations of PV devices that take into account actual operating conditions	143
8.1. Global optimizations of standard solar PV systems.....	144
8.2. Global optimizations of solar TPV systems	162
8.3. Global optimizations of near-field thermophotovoltaic systems	172
9. General conclusions	179
9.1. Conclusions and prospects for the research on the physics of the temperature coefficients of PV devices	179
9.2. Conclusions and prospects for the research on the thermal optimizations of PV devices	182
10. Appendices	187
10.1. Evaluating PV potential in the world taking into account thermal effects	187
10.2. On the temperature dependence of the diode saturation current	191
10.3. Analogy between a photovoltaic cell and a leaky bucket feeding a water wheel	197
10.4. Extrapolation of the integral rate of spontaneous emission from a c-Si cell from the experimental data of (Trupke et al. 2003)	199
10.5. Matlab code to extract the simple diode model parameters (R_s , R_{sh} , n , I_0 , I_{ph}) from light I-V curves	200
Bibliography	203
Curriculum Vitae (oct. 2015)	219

List of Abbreviations

ACAP	Australian Centre for Advanced Photovoltaics
AM	air mass
ARC	anti reflection coating
BGN	bandgap narrowing
BC	boundary condition
BSF	back surface field
c-Si	crystalline Silicon
CdS	Cadmium Sulfide
CdTe	Cadmium Telluride
CIGS	Copper Indium Gallium Selenide
CL	compensation level
CPV	concentrated photovoltaics
EG-Si	electronic grade silicon
EQE	external quantum efficiency
ERE	external radiative efficiency
EVA	ethylene-vinyl acetate
FF	fill factor
FZ	float zone
GaAs	Gallium Arsenide
Ge	Germanium
GHG	green house gas
HIT	heterojunction intrinsic thin layer
InP	Indium Phosphide
IR	infrared
LED	light-emitting diode
MPP	maximum power point
NF TPV	near-field thermophotovoltaic
NREL	National Renewable Energy Laboratory
NRR	non-radiative recombination

PERC	passivated emitter and rear cell
PERL	passivated emitter with rear locally diffused
PFD	photon flux density
PR	photon recycling
PV	photovoltaic
SHJ	silicon heterojunction
Si	Silicon
SiN	Silicon Nitride
SoGM-Si	solar-grade silicon purified by metallurgical route
SPREE	School of Photovoltaic and Renewable Energy Engineering
SQ	Shockley-Queisser
SRH	Shockley-Read-Hall
STC	standard test conditions
STPV	solar thermophotovoltaic
TC	temperature coefficient
TPV	thermophotovoltaic
UNSW	University of New South Wales
UV	ultraviolet
ZnS	Zinc Sulfide

List of Symbols

FUNDAMENTAL CONSTANTS

c	speed of light in vacuum, $c \approx 2.99792458 \cdot 10^8 \text{ m.s}^{-1}$
h	Planck constant, $h \approx 6.62606957 \cdot 10^{-34} \text{ J.s}$
k	Boltzmann constant, $k \approx 1.3806505 \cdot 10^{-23} \text{ J.K}^{-1}$
q	elementary charge, $q \approx 1.60217653 \cdot 10^{-19} \text{ C}$
σ	Stefan-Boltzmann constant $\sigma \approx 5.67037321 \cdot 10^{-8} \text{ W m}^{-2} \text{ K}^{-4}$

SYMBOLS

a	empirical parameter depending on the quality of the cell material and junction
b	empirical parameter depending on the quality of the cell material and junction
C	empirical parameter related to the cell's material
D	diffusion coefficient
E_g	bandgap energy
G	generation rate
I	current
J	current density
L	carrier diffusion length
n	diode ideality factor
n	spectral photon flux density
N	photon flux density or density of states
p	spectral power density
P	power density
Q	heat flux
R	electrical resistance or recombination rate
T	temperature
v	normalized voltage
V	voltage
W	useful work or thickness

Greek symbols

γ	parameter that includes the temperature dependences of several parameters determining J_0
β	temperature coefficient
μ	chemical potential
τ	carrier lifetime
ξ	parameter closely related to the product of carriers np ; introduced in (Green 2003)
ς	order dependence for the ratio between carrier diffusivity and lifetime (D/τ)

Subscripts and superscripts

a	ambient or absorber
b	background
c	cell
C	conduction band
d	depletion region
e	electrons or environment or emitter
F	Fermi
h	holes
MPP	maximum power point
n	n side
oc	open-circuit
p	p side
s	Sun or series
sc	short-circuit
sh	shunt
V	valence band
0	in the dark or at 0 K

1. General introduction

1.1. Why do we care about photovoltaics?

Since the middle of the 19th century, humankind has used fossil fuels to produce an ever increasing amount of work in order to make everyday life easier. According to the International Energy Agency, in 1973 the World production of fossil fuels (coal, oil and natural gas) was about 5 300 Million Tonnes of Oil Equivalent (Mtoe) and reached 11 000 Mtoe in 2012 (International Energy Agency 2014). Thus, in 2012, every human being on Earth consumed in average 4 litres of oil equivalent per day in fossil fuels. Using the concept of Energy Slave (Jancovici 2015) which corresponds to the quantity of energy that replaces a unit of human labor, these 4 oil equivalent litres of fossil fuels are equivalent to about 32 Energy Slaves per human on the planet¹ with huge variances highly correlated with the wealth of the individuals. Furthermore, the World energy consumption keep increasing...

Though the peak-oil production could happen in the years to come, there is still around 1 000 000 Mtoe of proven reserves of fossil fuels according to (British Petroleum 2015). At the current production rate, it corresponds to about 50 years of extraction for oil and gas and 100 years for coal. However, what remains is increasingly difficult and thus increasingly expensive to extract. Besides, even if there still was an abundance of fossil fuels extractable at low cost thanks to improving technologies, because of the accumulation of greenhouse gases (GHG) in the atmosphere, the Earth climate is going to become gradually more difficult to live for humans as we burn these fuels.

It is crucial that humankind realizes rapidly² that the emission of GHG associated with

¹ According to Jean-Marc Jancovici's website "How much of a slave master am I?" (Jancovici 2015): as a rough approximation, a body working hard can produce 0,5 kWh of energy per day. 1 litre of oil in an internal combustion engine provides about 4 kWh of mechanical energy. Thus, 4 litres of oil is equivalent to 32 Energy Slaves for one day.

² Unfortunately, the climate change is a complex problem to handle for our societies because: 1. it is driven by changes in the atmosphere composition and is thus a global phenomenon at the scale of the planet. Therefore it can only be solved by collective action worldwide. 2. It needs to be anticipated because

fossil fuel consumption³ leads to degradations of the environment that will ultimately have an impact on humans (among them: food production, health problems, water availability caused by desertification, extinctions of species, acidification of oceans, increasing number of storms, etc). These impacts will have a cost for the future generations, not only in terms of economy but also in terms of reduction of capabilities of human societies. In other words, there is some sort of “debt for humankind” associated with every emission of GHG. Furthermore, the climate change beyond 2100 could bring abrupt and irreversible changes. The Intergovernmental Panel on Climate Change (IPCC) states that: “Without additional mitigation efforts beyond those in place today, and even with adaptation, warming by the end of the 21st century will lead to high to very high risk of severe, widespread and irreversible impacts globally (high confidence)” (IPCC 2014).

The political target of the United Nations Framework Convention on Climate Change (UNFCCC) adopted in 2010 (in the “Cancun Agreements”) several targets in order to maintain global warming below 2 °C over the 21st century relative to pre-industrial levels (UNFCCC 2010). In that case, scientists think societies could probably adapt to face changes. To meet this goal, major actions are required. One of the challenges is to keep from using available fossil fuel resources. Indeed, the carbon contained in the fossil-fuel reserves (11 000 Gt CO₂-eq) is much more than the amount that can be emitted as CO₂ into the atmosphere (about 1 000 Gt CO₂-eq) if global warming is to be limited to 2°C; only about 10% of these reserves should be extracted and used without carbon capture (Jakob & Hilaire 2015). Considering this observation, it is urgent to develop alternative and sustainable solutions to produce energy such as hydroelectric installations, wind turbines, solar panels...

Photovoltaics (PV) is a method of conversion of radiative energy into electrical energy. Since the radiative energy from the Sun reaching the surface of Earth is about 5000 times larger than the World energy consumption in 2014 (Hermann 2006), solar cells have the potential to play a major role in the energetic transition from fossil fuels to renewables and be part of a global solution against climate change. Indeed, several scenarios proposing achievable road maps aiming at limiting climate change to an acceptable level

there is an inertia between today’s emission of Green House Gas (GHG) and the visible impact it will have on the climate.

³ The scientific community of the Intergovernmental Panel on Climate Change (IPCC) confirms that the fossil fuel consumption is one the main driver of the world climate change estimating that 65 % of the total annual anthropogenic GHG emissions in 2010 was due to fossil fuels and industrial processes (IPCC 2014)

rely significantly on the development of photovoltaic energy production (WBGU 2003; Pacala & Socolow 2004; Brown 2009). In a recent lecture at the University of New South Wales (UNSW), Martin Green pointed out several positive figures of the development of photovoltaics (Green 2015a). In 2015, photovoltaic installations will produce over 1% of the World's electricity. Even more important is the observation that if its current growth rate is maintained, PV production could contribute to over 25 % of the World's primary energy by 2050. This would go a long way towards reaching the goal of maintaining global warming below 2°C. However, to maintain the current rate of PV deployment, innovative technological solutions will have to be developed and important challenges such as the grid integration of this intermittent energy resource will have to be addressed.

1.2. Why is it important to understand the thermal behavior of photovoltaic devices?

Modeling the thermal behavior of PV devices is especially important because the power outputs of PV systems decrease when their temperatures rise. For example, Fig. 1a shows the power output (normalized to its value at 25°C) as a function of the cell temperature for solar cells made of different semiconductors⁴ and of different cells made of crystalline silicon (c-Si). All the output powers decrease with increasing temperature but at different rates. This means that two different cells or modules with the same rated power in the Standard Test Conditions (STC⁵), i.e. 1000 W m⁻² of AM1.5⁶ illumination on a cell at 25°C, may produce different powers under real outdoor conditions which are usually quite different from the STC (see Fig. 1b and Fig. 4a). In operation, temperature of PV modules is often quite larger than the STC value of 25°C (as illustrated in Fig. 2a) because they heat up above ambient temperature. Furthermore, the energy production of a PV system is function of the incoming irradiation which is unfortunately an important driver of the PV device's temperature (see Fig. 4a). This is due to two different effects: 1. the ambient

⁴ a-Si: amorphous Silicon. CdTe: Cadmium Telluride. c-Si: crystalline Silicon. CIGS: Copper Indium Gallium Selenide.

⁵ PV module performances are usually evaluated under Standard Test Conditions (STC) as defined in IEC 60904-3. In particular, powers that are advertised by module manufacturers or that of record cell efficiencies are always measured under STC.

⁶ AM1.5 stands for Air Mass 1.5 and corresponds to the spectrum of solar radiation after it has gone through a path in the Earth's atmosphere of 1.5 times the thickness of the vertical length of the atmosphere. It is the reference spectrum for PV applications (IEC 2008).

temperature tends to be larger when the solar irradiance is more important and 2. a large fraction of the incoming irradiation is dissipated as heat within the cell. Obviously, the most meaningful average temperature is that over energy production and is larger than a temperature averaged over time (see Fig. 2).

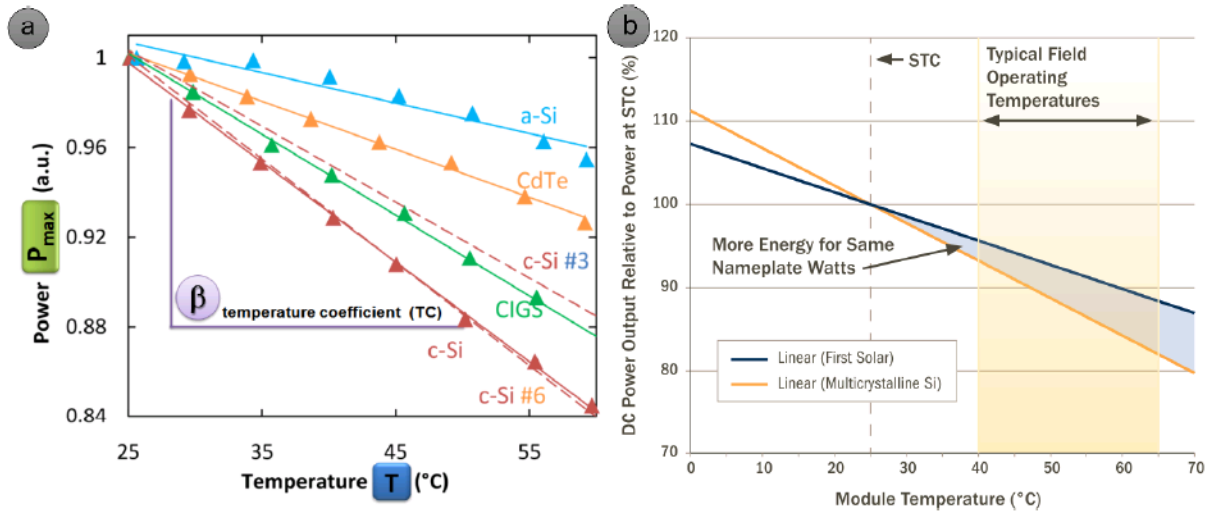


Fig. 1 a. Relative output power as a function of temperature for different PV cell technologies a. data from (Virtuani, Pavanello & Friesen 2010) and (Dupré, Vaillon & Green 2015a); b. extracted from a First Solar⁷ brochure (First Solar 2014).

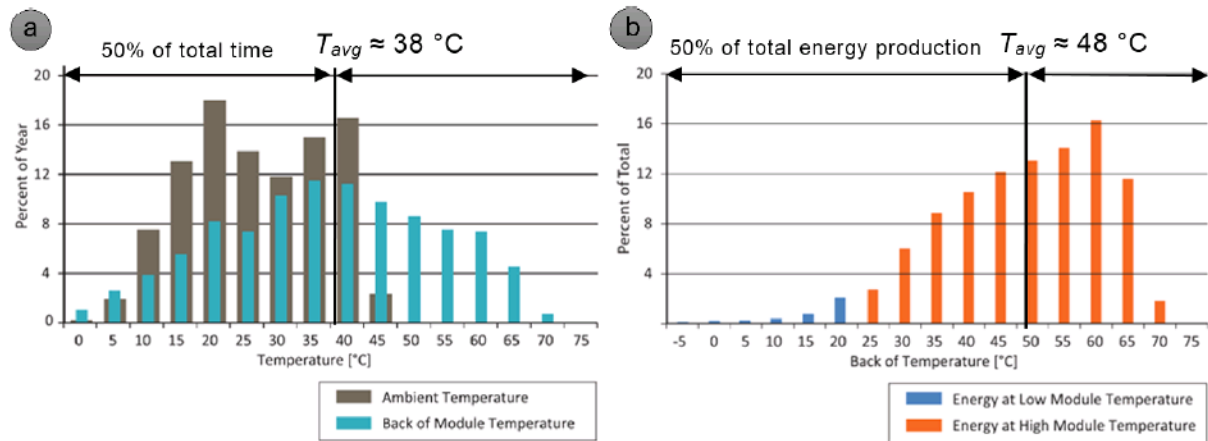


Fig. 2 Distribution in percent of: a. time in a year; b. produced energy; on PV module temperature under real operating conditions. Figure adapted from (Strevel et al. 2012).

Fig. 2 shows the mean temperature distribution of the back surface of CdTe modules located in a power plant in the US desert southwest. Obviously, the temperature reached

⁷ First Solar is one of the largest PV companies in the world and has the almost unique specificity to sell Cadmium Telluride (CdTe) based PV modules.

by a module depends on where it is located since it is a function of parameters such as solar radiation, outdoor temperature and wind speed. Fig. 3 indicates the modeled temperature distribution in hours per year of modules in different sites illustrating the impact of the climate on module temperature variations (Kurtz et al. 2011). The module temperature also depends on how it is mounted (open-rack, roof mounted, insulated back, tracker) because this impacts the heat transfer coefficient between the module and the ambient. Fig. 3 depicts the modeled temperature distribution of modules mounted on open-racks on the left (Fig. 3a) and that of modules with insulated backs on the right (Fig. 3b). As expected, the modules with insulated backs reach higher temperatures than those mounted on open-racks. Note that the temperature distributions depicted in Fig. 3 consider every hours including those with no sunshine: as discussed above, the temperature distribution in terms of energy production would be quite different.

There are other factors that influence the temperature of modules (such as surface reflectivity) and a large number of correlations using different parameters were derived to model the operating temperature of PV modules (Skoplaki & Palyvos 2009b).

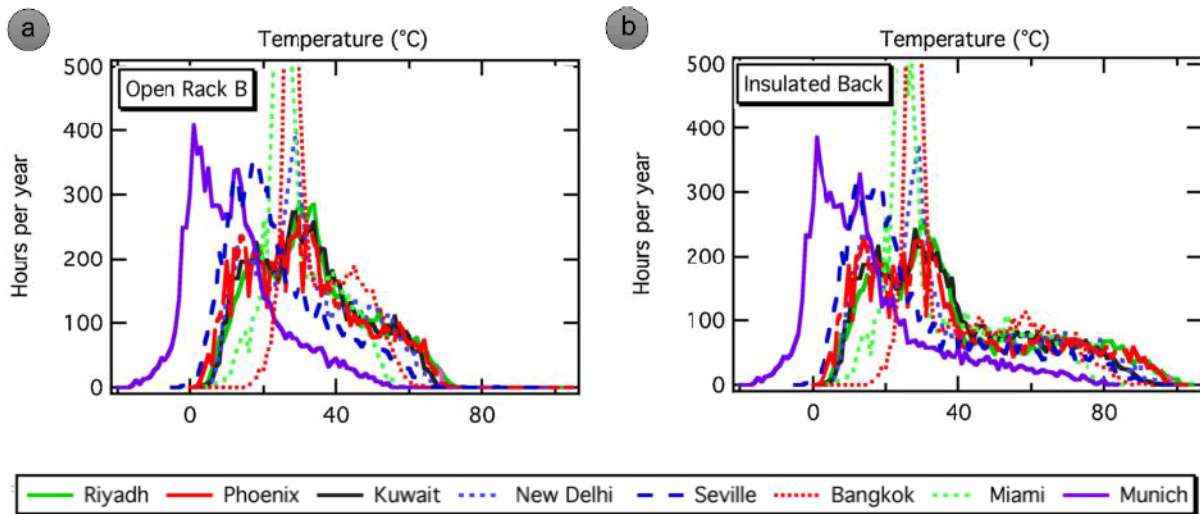


Fig. 3 Temperature distributions of PV modules for two different mounting configurations in several locations (Kurtz et al. 2011).

It is widely acknowledged that PV modules often operate at temperatures and irradiance conditions respectively above and below those defined by the STC. This is illustrated in Fig. 4a which shows field data of the power versus module temperature and irradiance of

a pc-Si⁸ module installed in Italy (Moser, Pichler & Nikolaeva-Dimitrova 2013). In order to quantify the thermal design of a given module, the concept of Nominal Operating Cell Temperature (NOCT) was introduced. The NOCT is the temperature reached by the open-circuited cells in a module mounted on an open-rack with a wind velocity of 1 m.s⁻¹, an ambient air temperature of 20°C and under a 800 W m⁻² illumination (Ross & Gonzalez 1980). Fig. 4a illustrates several facts: 1. PV devices operate in a large range of temperatures and irradiances; 2. these conditions are rarely (or even never in this example) the STC; 3. there is a correlation between the device power output in operation and its temperature; 4. the NOCT is more representative of the device temperature in operation than the 25°C of the STC. However, while the NOCT gives an idea of the quality of the thermal design of the module, it does not take account of its mounting configuration. In the predictive model PVFORM (Skoplaki & Palyvos 2009b), the major input parameter is the "installed" nominal operating cell temperature (INOCT) which adds to the standardized NOCT the impact of mounting configuration. Its impact on cell temperature is illustrated in Fig. 4b.

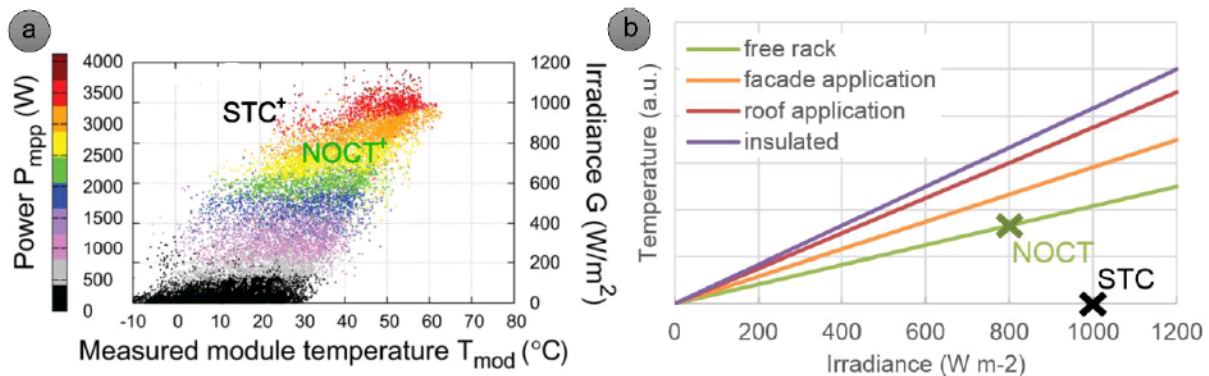


Fig. 4 a. Field data of the power versus module temperature and irradiance of a pc-Si module installed in Italy. Figure adapted from (Moser, Pichler & Nikolaeva-Dimitrova 2013); b. temperature difference between cell and ambient as a function of irradiance for different mounting configurations. Figure adapted from (Bloem 2008).

The fact that temperature negatively affects the efficiency of PV devices is widely known. Some researchers even tried to assess the effect of temperature on the potential of PV generation in the whole world (Appendix A). Buyers in the PV market are now considering the energy yield of the installations rather than simply their rated power and PV companies

⁸ pc-Si stands for polycrystalline silicon. It is often used as a synonym of multi-crystalline silicon (mc-Si) but these denominations refer to materials with different grain sizes according to the terminology defined by Basore (Basore 1994); >10 cm: c-Si ; 1mm-10cm: mc-Si; 1µm-1mm: pc-Si; <1µm : µc-Si (microcrystalline silicon).

that produce panels with superior energy yield are effectively advertising it (e.g. First Solar with its CdTe cells (Strevel et al. 2012), AltaDevices with its Gallium Arsenide (GaAs) cells (Silverman et al. 2013) or Sanyo with its high efficiency HIT cells (see section 5.5 or (Mishima et al. 2011)). However, while the importance of the thermal behavior of PV devices seems to be seriously acknowledged in the industry, academic research mainly focused on improving the device efficiencies in the STC (as can be inferred by the recurrent apparitions in every lectures on PV of the famous graph from NREL that shows the evolution of record cell efficiencies in the STC, see Fig. 5).

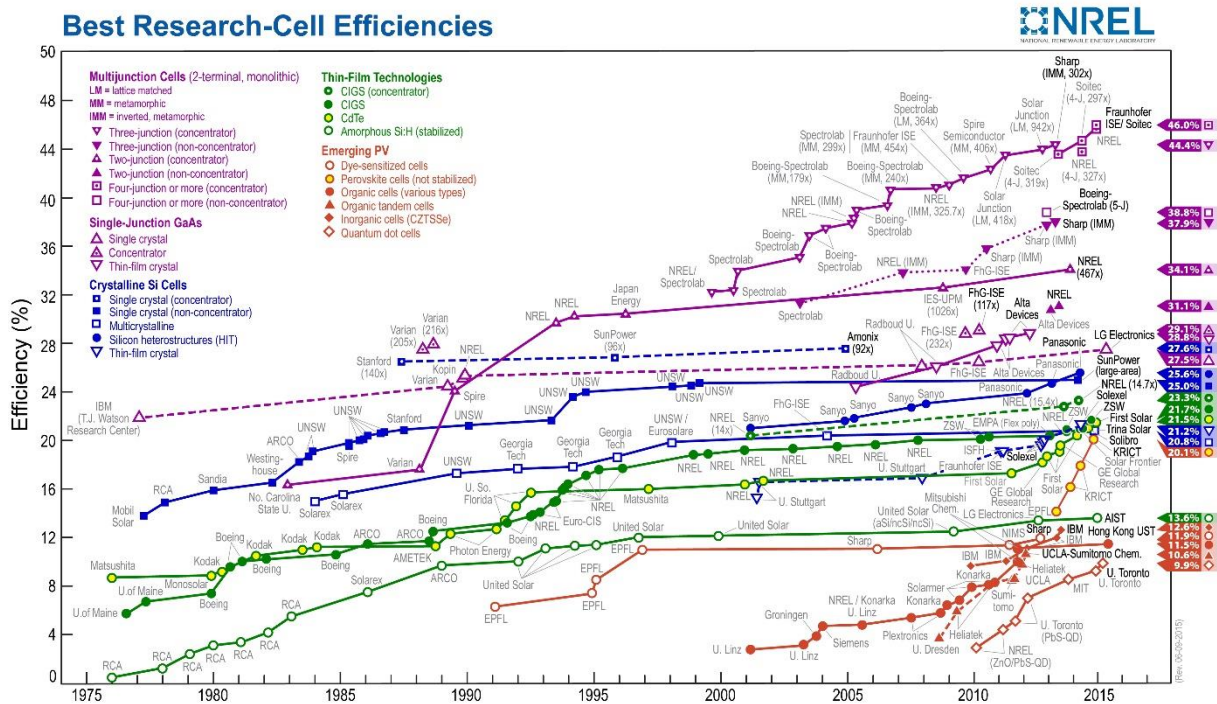


Fig. 5 Evolution of the record cell efficiencies (in the standard test conditions) of the different PV technologies since 1975. Figure from (NREL 2015).

On the one hand, while there were several research works (both theoretical and experimental) on the temperature coefficients of PV cells (they will be presented in the introduction of Part I), the findings were scattered in the literature and a global understanding has not been reached yet. Indeed, recent publications are still reporting new phenomena related to temperature coefficients (Helmers, Schachtner & Bett 2013; Deceglie et al. 2014).

On the other hand, a large number of ideas were proposed in order to reduce the operating temperature of PV modules (they will be presented in the introduction of Part II) mostly through the use of active or passive cooling devices. However, these methods for minimizing the temperature-induced loss are often but “add-ons” to the photovoltaic (PV)

system that add to its complexity and its price. In this work, a global understanding of the thermal behavior of PV systems will be developed and original strategies where thermal losses are minimized by design of the PV device itself will be proposed.

1.3. Original approach of the thermal behavior of PV devices

In this manuscript, an original and general approach to the thermal behavior of PV devices will be introduced. Additionally, evidences that this global understanding can lead to original optimizations of photovoltaic devices such as solar PV but also thermophotovoltaic (TPV) (Bauer 2013), solar TPV (Swanson 1979) or near-field TPV (Whale & Cravalho 2002) will be presented.

Fig. 6 shows a global schematic of the thermal behavior of a PV device. The common way of dealing with the problem of temperature in PV devices is to cool them down by increasing the heat transfer out of the device. A lot of different ideas of “cooling techniques” were proposed and will be reviewed in Part II. Fig. 6 illustrates that the whole thermal problem is more than just the thermal boundary conditions and that thermal, optical and electrical behaviors are deeply intertwined. The device temperature is driven by the internal heat source Q which is the sum of different heat generation mechanisms within the device. Almost all the energy absorbed by the device and not converted into electrical energy is eventually dissipated as heat in the device⁹ (the different heat generation mechanisms will be described in detail in Part II). Thus, the heat source Q obviously depends on the level of incoming radiation (or concentration) which is part of the radiative boundary conditions (BCs). As we mentioned, the heat source is a function of the irradiation that is absorbed by the cell. Therefore it depends on some parameters of the PV device such as the thickness and the absorption coefficient of the active material or the light trapping scheme of the device. Some of the parameters that drive the heat source (such as the absorption coefficient or the non-radiative recombination rates) depend on the temperature causing a feedback effect of the device temperature on itself. Furthermore, it will be shown in Part II that the heat source also depends on the irradiation spectrum so that there are spectral optimizations to be envisaged. Additionally, Fig. 6

⁹ This energy corresponds to about 80% of the incoming solar energy for typical commercial cells.

shows that the device temperature depends on the heat source but also on the thermal environment (thermal BCs) which can include several parameters (such as ambient temperature and wind speed) that depend on the installation site of the PV system. For example, identical modules operate at different temperatures depending on whether they are installed in Germany or in Arizona. Finally, the maximum output power P_{max} of the device is a function of its temperature T_c via the so-called temperature coefficient β . This coefficient depends on many physical parameters such as doping levels and bulk material quality. Also, certain radiative boundary conditions such as the incident light intensity and spectrum have an important impact on the cell temperature coefficient. The physics that lies behind the temperature sensitivities of solar cells will be described in Part I.

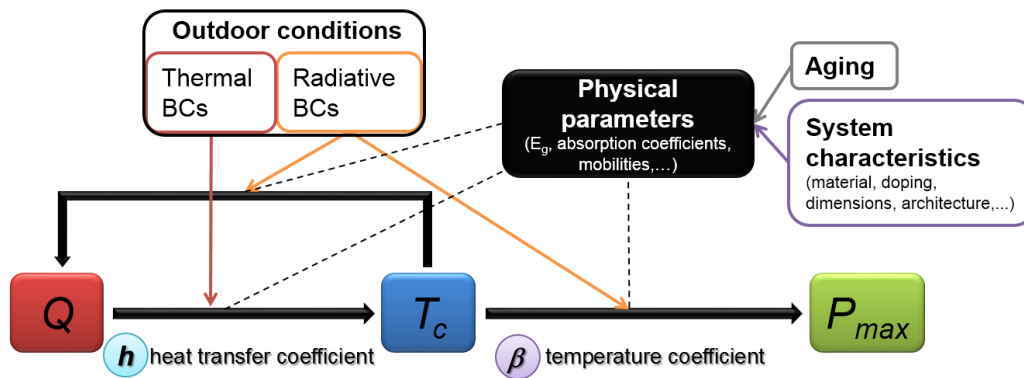


Fig. 6 Schematic of the thermal behavior of a photovoltaic device. Figure adapted from (Dupré & Vaillon 2014).

To our knowledge, the idea of this work is original since it does not target an increase of the heat transfer coefficient. Instead, by developing a global analysis of the thermal problem, this work aims ultimately at developing new optimizations of the PV devices parameters that would include thermal criteria in addition to the electrical and optical ones.

1.4. Brief plan of the thesis

As illustrated in Fig. 1a, temperature coefficients of PV cells vary with the semiconductor used and they can even vary between cells made of the same semiconductor. In Part I, a thorough investigation of the physics that drives the temperature sensitivities of solar cells will be presented. First, the fundamental causes of the negative impact of temperature on

PV conversion performances will be analysed. Then, the temperature sensitivities of open circuit voltage, short circuit current and fill factor will be discussed separately. The theoretical formulations will be assessed against experimental results for different technologies of PV cells. In Part II, a complete model of the heat generation mechanisms in PV devices will be introduced. Then, the factors that drive the PV device temperature in real operating conditions will be discussed and some original optimizations of the design of PV devices (solar PV, solar TPV and near-field TPV) that include thermal criteria will be presented.

Part 1. Physics of the temperature coefficients of solar cells

Table of contents of Part I

<i>Part 1. Physics of the temperature coefficients of solar cells</i>	23
2. Introduction and state-of-the-art	25
3. Fundamental temperature coefficients of photovoltaic devices	37
3.1. The detailed balance principle and the thermodynamic argument	37
3.2. Bandgap temperature dependence and influence of the incident spectrum	49
3.3. Intrinsic temperature coefficient of silicon solar cells which includes Auger recombination	55
4. Temperature coefficients of real photovoltaic devices	61
4.1. Open-circuit voltage temperature sensitivity	65
4.2. Short-circuit current temperature sensitivity	72
4.3. Fill factor temperature sensitivity	75
5. Experimental assessment of temperature coefficient theories for crystalline silicon solar cells	79
5.1. Details on the experimental measurements	79
5.2. Short-circuit current temperature sensitivity	84
5.3. Open-circuit voltage temperature sensitivity	88
5.4. Fill factor temperature sensitivity	93
5.5. Temperature sensitivity of silicon heterojunction solar cells	96
5.6. Temperature sensitivity of compensated silicon solar cells	97

2. Introduction and state-of-the-art

The concept of Temperature Coefficient (TC) was introduced for quantifying the temperature sensitivities of the performances of solar cells. In order to compare different technologies, TCs are defined normalized at 25°C / 298.15K (Emery et al. 1996), and are often expressed in ppm K⁻¹:

$$\beta_G(T_c) = \frac{10^6}{G(298.15\text{K})} \frac{G(T_c) - G(298.15\text{K})}{T_c - 298.15} \quad (1)$$

where G is the parameter of interest and T_c is the cell temperature. If the variation is linear with temperature, β_G is well described by a single value. This is the case for most types of PV cells as shown by the linear variations of output powers in Fig. 7.

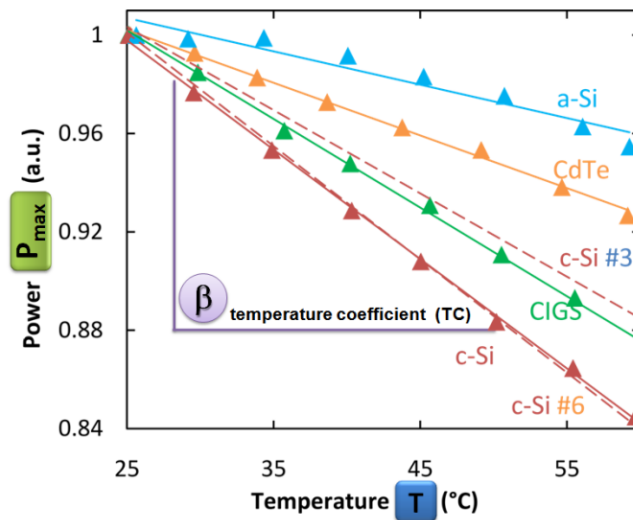


Fig. 7 Relative output power as a function of temperature for different PV cell technologies (data from (Virtuani, Pavanello & Friesen 2010) and (Dupré, Vaillon & Green 2015a)).

It can be noticed in Fig. 7 that the linear fit is not convenient for the cell made of amorphous silicon (a-Si). This is because the temperature behavior of amorphous silicon is impacted by specific mechanisms such as light soaking and thermal annealing (Carlson, Lin & Ganguly 2000). These mechanisms drive metastable changes in a-Si cells (this is known as the Staebler-Wronsky effect) and cause the cell performances to vary non-linearly with temperature. This annealing-promoted regeneration effect is the main cause of seasonal variation of performance ratio of a-Si PV modules (Makrides, Zinsser,

Phinikarides, et al. 2012). This phenomenon also explains the positive temperature coefficients of amorphous silicon modules that are sometimes observed in the field (Moser, Pichler & Nikolaeva-Dimitrova 2013; Fischer et al. 2009; Silverman et al. 2014). This regeneration is so important that Fischer et al. actually tested a backside isolated module against a classic freestanding module and showed that the former had a better energy yield over a year. They showed that the performance ratio improved together with peak module temperature at a rate of $0.87 \% K^{-1}$. This is linked to the very strong and positive temperature dependence of the annealing rate. This is quite interesting and we wonder if it could be worth short-circuiting (briefly) these a-Si modules when the irradiation is maximum in order to reach even higher maximum temperatures and increase the regeneration rates (trade-off between an increase of the regeneration rate and a power loss during the short-circuit). Anyhow, the annealing effect is specific to amorphous silicon cells which are not discussed in the present manuscript. The reader can refer to (Carlson, Lin & Ganguly 2000) for a particularly interesting analysis of the thermal behavior of amorphous silicon cells. Cells made of organic materials also often exhibit non-linear temperature behaviors and sometimes positive temperature dependence of their efficiencies (Ali et al. 2012; Riedel et al. 2004; Katz et al. 2001). This is attributed to important losses at room temperature that decrease with increasing temperature (Katz et al. 2001). In this manuscript, we will focus on the more common and maybe simpler case of cells made of inorganic crystalline semiconductors (c-Si, CdTe, CIGS, ...). Several works investigated the temperature dependences of the output parameters of such cells both experimentally and theoretically. In the next paragraphs, we will present chronologically the main findings of a selection of works on the temperature coefficients of solar cells.

As early as 1960, Wysocki and Rappaport were working on a model for the temperature behavior of PV devices (Wysocki & Rappaport 1960). They identified some of the parameters that cause the conversion efficiency to be temperature dependent but neglected some important mechanisms (such as the temperature dependence of the short-circuit current). Also their analysis could not be generalized because they used semi-empirical parameters based on best estimates of that time. Some of their arguments have been proven erroneous (e.g. “the conversion performance of any given semiconductor improves as the doping level is increased”) but they reached the interesting conclusion that temperature

coefficients are a function of the bandgap: thus the semiconductor bandgap leading to optimum conversion efficiency is a function of temperature. This temperature dependence of the optimum can be obtained from the Shockley-Queisser limit (cf Fig. 14 in chapter 3) and illustrates why one could think of using different PV devices for different temperature conditions. A very specific example is the “Bepi Colombo” mission to Mercury where the operating temperature of the PV devices is expected to reach between 200–230 °C (Zimmermann et al. 2011). Also, even on Earth, the operating temperatures of PV modules can be quite different depending on their locations as illustrated in Fig. 3 (page 17).

In 1982, Green discussed in his first textbook (Green 1982) the effect of temperature on PV conversion. He used the single-diode model (eq. (2)) with a general expression of the diode saturation current density (eq. (3)), and neglected the temperature dependence of the short-circuit current to express the temperature coefficient of open-circuit voltage mainly as a function of the bandgap and the open-circuit voltage (eq. (4)), through the following equations:

$$J \approx J_{sc} - J_0 \exp\left(\frac{qV}{kT_c}\right) \quad (2)$$

$$J_0 = AT_c^\gamma \exp\left(-\frac{E_{g0}}{kT_c}\right) \quad (3)$$

$$\frac{dV_{oc}}{dT_c} = -\frac{\frac{E_{g0}}{q} - V_{oc} + \gamma \frac{kT_c}{q}}{T_c} \quad (4)$$

$$E_{g0} = E_g - T_c \frac{dE_g}{dT_c} \quad (5)$$

where A is a factor independent of temperature, E_{g0} is the bandgap of the semiconductor linearly extrapolated to 0 K, and γ includes the temperature dependences of several parameters which determine the diode saturation current density J_0 .

To understand the origin of this expression of the diode saturation current (eq. (3)), which was used with different semi-empirical parameters in many works dealing with temperature coefficients (Fan 1986; Landis 1994; Friedman 1996; Yoon & Garboushian 1994), the reader can refer to appendix 10.2. The reader can also find a really interesting discussion on the physical meaning of the parameter J_0 in (Cuevas 2014). In short, the

term γ includes the temperature dependences of many parameters such as carrier mobilities and carrier lifetimes (which depend on the recombination mechanisms), the number of effectively available states in the conduction and valence bands.

Eq. (4) shows the important relation between open-circuit voltage and its temperature sensitivity. Green et al. stated that “as the open-circuit voltage of silicon solar cells continues to improve, one resulting advantage, not widely appreciated, is reduced temperature sensitivity of device performance” (Green, Emery & Blakers 1982). This was an important understanding. However the parameter γ in eq. (4) was not directly related to device physics.

In 1986, Fan (Fan 1986) introduced an expression of the diode saturation current with additional empirical parameters:

$$J_0 = CT_c^{3/a} \exp\left(-\frac{E_g}{bkT_c}\right) \quad (6)$$

where C is an empirical parameter related to the cell material and a, b are “empirical parameters depending on the quality of the cell material and junction” (Fan 1986). They used this expression to derive a general expression of the temperature coefficient of the open-circuit voltage:

$$\frac{\partial V_{oc}}{\partial T_c} = \frac{1}{T_c} \left[V_{oc} - \frac{nE_g}{bq} - \frac{3nkT_c}{aq} \right] + \frac{n}{bq} \frac{\partial E_g}{\partial T_c} + \frac{nkT_c}{qJ_{sc}} \frac{\partial J_{sc}}{\partial T_c} \quad (7)$$

where n is the diode ideality factor¹⁰ which relates the current going through the diode to

the ideal diode law as $J = J_0 \left(\exp\left(\frac{qV}{nkT_c}\right) - 1 \right)$.

While this equation (6) enables to model more situations (different kinds of recombinations¹¹ ...), there is still no direct link with the underlying physics. Fan

¹⁰ The value of the ideality factor depends upon the recombination mechanisms. It equals one when SRH recombinations limited by one type of carrier dominate. It equals two when both carrier concentrations are important (in the depletion region or in the bulk in high injection). It can also be larger than two when the defect concentration is so high (at the edges, or at defects such as scratches, ...) that recombinations take place through several defect levels (Breitenstein et al. 2006). For Auger recombination, the ideality factor goes from one in low injection to 2/3 in high injection.

¹¹ For example, it was shown later (Siefer et al. 2005) that when the saturation current is dominated by recombination in the depletion zone, the saturation current density reads $J_0 = B_2 T_c^{2.5} \exp(-E_g(T_c)/(2kT_c))$. This situation can be fitted with Fan’s equation with $a=1.2$ and $b=2$.

determined the empirical parameters of his equation via a fit of the best achieved open-circuit voltages at that time.

The analysis of Fan was followed by a number of works which highlighted different interesting features of the thermal behavior of PV cells. In 1987, Nell and Barnett (Nell & Barnett 1987) documented the physical parameters hidden in the empirical parameters in eq. (3) (see appendix 10.2) and specified that their values were typically determined by matching experimental results. They also reviewed the different models proposed for the diode saturation current (Loferski 1956; Green 1982; Fan 1986).

In 1994, Geoffrey A. Landis proposed an interesting review of solar cell temperature coefficients especially dedicated to space applications. He used the theory previously derived by Fan but made a number of interesting observations. For example, he explained the discrepancies observed in the short-circuit current temperature coefficients (TCs) by exhibiting the impacts of the incident spectra on these TCs (this is discussed in details in section 4.2). Also he suggested that the temperature coefficient of PV cells could be considered as a design parameter: “Temperature coefficient is rarely considered as a design parameter for solar cells. From the standpoint of temperature coefficient, increasing open-circuit voltage, even at the expense of decreases in other cell parameters (for example, by increasing base doping of the cell) may result in higher power under actual space operating conditions”. This is the kind of idea that we promote as “thermal optimizations” in Part II.

The same year, Zhao et al. reported the lowest value of temperature coefficient achieved at that time for silicon PV cells (Zhao et al. 1994). A normalized efficiency temperature variation (β_η) of -2632ppm K^{-1} was measured on the latest high efficiency PERL¹² cell from UNSW. Also, they observed that cells with a different design (the PERC¹² cells) had larger temperature sensitivities while their open-circuit voltages were similar. They explained this observation by adding the effect of series resistance (R_s) into the temperature coefficient of the fill factor previously derived in (Green, Emery & Blakers 1982):

¹² PERC (Passivated Emitter and Rear Cell) and PERL (Passivated Emitter and Rear Locally-diffused) are high efficiency silicon solar cells developed at the University of New South Wales (Green 1995).

$$\frac{1}{FF} \frac{dFF}{dT_c} = (1 - 1.02 FF_0) \left(\frac{1}{V_{oc}} \frac{dV_{oc}}{dT_c} - \frac{1}{T_c} \right) - \frac{R_s}{V_{oc} / I_{sc} - R_s} \left(\frac{1}{R_s} \frac{dR_s}{dT_c} \right) \quad (8)$$

where FF_0 is the ideal fill factor defined by:

$$FF_0 = \frac{v_{oc} - \ln(v_{oc} + 0.72)}{v_{oc} + 1} \quad (9)$$

where v_{oc} is a normalized voltage equal to:

$$v_{oc} = \frac{nkT_c}{q} V_{oc} \quad (10)$$

This set of equations will be discussed in more detail in section 4.3.

Still in 1994, Yoon and Garboushian proved experimentally that cells operating under concentration have reduced temperature sensitivities (Yoon & Garboushian 1994). Also, in their theoretical model, they used an expression for the diode saturation current of a form similar to that proposed by Fan (Fan 1986) but that have the advantage that the parameters are explicitly related to physical quantities:

$$J_0 = CT_c^{(3+\frac{\zeta}{2})} \exp\left(-\frac{E_g(T_c)}{kT_c}\right) \quad (11)$$

where “the temperature dependence exponent $(3+\zeta/2)$ is from the third order dependence of intrinsic carrier concentration (n_i^2) and ζ order dependence for the ratio between carrier diffusivity and lifetime (D/τ)” (Yoon & Garboushian 1994). This is clear in Appendix 10.2 where it can be observed that the product of the effective density of states in the conduction and valence bands $N_c N_v$ varies as T_c^3 if the temperature dependence of the effective masses of the carriers is neglected. If we assume that (D/τ) varies as T_c^ζ and neglect the temperature dependences of other parameters, we get back to eq. (11).

In 1996, Friedman detailed all the assumptions necessary to obtain Fan’s equation (7) and assessed the thermal behavior of GaInP/GaAs tandem cells¹³ (Friedman 1996). In the case of standard multi-junction cells, the temperature coefficient of the open-circuit voltage is simply the sum of that of all the sub-cells since they are serially connected. However, the short-circuit current (J_{sc}) is limited by the sub-cell that produces the least current. Since the bandgaps are temperature dependent, the limiting sub-cell can change with

¹³ GaInP: Gallium Indium Phosphide.

temperature leading to changes in the temperature coefficients of the multi-junction cell. In the case investigated by Friedman, “the bottom-cell J_{sc} of the GaInP/GaAs series-connected tandem has a much smaller temperature variation than does an unfiltered GaAs cell. For this reason, the rate of increase of the full tandem J_{sc} with temperature becomes smaller as the temperature is raised through the crossover temperature at which the top and bottom cells are current-match”. Friedman also observed that there was also a change in the TC of the fill factor (FF) during the transition from top-cell to bottom-cell limited current. Surprisingly, for the cells he measured, the changes in the TCs of J_{sc} and FF happened to cancel out so that the efficiency remained a relatively smooth function of temperature.

The same year, at the 25th IEEE Photovoltaic Specialists Conference, Emery et al. presented a review of the reported temperature coefficients of the different existing PV cells and modules (Emery et al. 1996). They mainly discussed the measurement methods and the possible error sources.

In 1997, King et al. added to the work of Emery et al. and identified other sources of systematic errors in the measurements of the temperature coefficients of PV modules and arrays (King 1997). They investigated in particular the influence of non-uniform temperature distributions which complicate the estimation of the TCs of modules from the TCs of the cells. Also, they emphasized the fact that irradiance has an impact on temperature coefficients and this impact is different between crystalline and amorphous silicon cells.

The analyses presented above provided important information on the general trends of the temperature behavior of solar cells explaining for example the small temperature sensitivity of cells with large bandgaps. However, the use of one or several semi-empirical parameters to calculate the diode current restricted the generality of the conclusions and in some cases led to systematic errors in the modeling as demonstrated in (Green 2003). In this article from 2003, Green made a general analysis of the temperature behavior of a PV cell based on internal device physics. He expressed that the temperature dependence of open-circuit voltage is mainly driven by the recombination mechanisms which depend themselves on the excess carrier concentrations. Shockley-Read-Hall (SRH), Auger and radiative recombination rates can be written as a function of the product of the electron and hole carrier concentrations np . This np product depends on the intrinsic carrier

concentration, n_i , and of the splitting of the quasi-Fermi levels, ϕ_p - ϕ_n , which is related to the potential in the cell:

$$np = n_i^2 \exp\left[\frac{q(\phi_p - \phi_n)}{kT_c}\right] \quad (12)$$

For convenience, Green introduced the term ξ , which is closely related to the np product:

$$\xi = np \exp\left(-\frac{E_g}{kT_c}\right) / n_i^2 \quad (13)$$

Regardless of the recombination mechanisms, the output current of a cell (I) can be described by:

$$I = I_L(V, T_c) - \sum_{i=1}^N A_i(V) T_c^{\gamma_i} f_i(\xi_i) \quad (14)$$

where I_L is the current photogenerated by the solar irradiation and the subscript i stands for any recombination mechanism. Differentiating and neglecting some second-order terms, the temperature coefficient of the open-circuit voltage can then be written as:

$$\frac{dV_{oc}}{dT_c} = -\frac{\left(\frac{\langle E_{g0} \rangle}{q} - V_{oc} + \frac{kT_c}{q} \left\langle \gamma \frac{f}{\xi} \frac{d\xi}{df} \right\rangle\right)}{T_c} \quad (15)$$

where $\langle x \rangle$ is the weighted value of the parameter of interest defined as:

$$\langle x \rangle = \frac{\sum_{i=1}^N x_i A_i T_c^{\gamma_i} \xi_i (df_i / d\xi_i)}{\sum_{i=1}^N A_i T_c^{\gamma_i} \xi_i (df_i / d\xi_i)} \quad (16)$$

Eq. (15) can be applied to any kind of PV cell as it was derived from really general arguments. However, it requires the detailed knowledge of the recombination mechanisms

to evaluate the term $\left\langle \gamma \frac{f}{\xi} \frac{d\xi}{df} \right\rangle$. In the same article, Green also discussed the parameters

that usually determine the temperature coefficients of the short-circuit current and of the fill factor. The short-circuit current density (J_{sc}) is expressed as the product of an ideal short-circuit current density ($J_{sc, Isun}$), which is determined only by the bandgap and the incident Photon Flux Density (PF), and a collection fraction (f_c):

$$J_{sc} = J_{sc,lsun} f_c \quad (17)$$

$$J_{sc,lsun} = q \int_{E_g(T_c)}^{\infty} PFD(E) dE \quad (18)$$

The collection fraction is the fraction of potentially useful photons ($E \geq E_g$) that excites a carrier that eventually gets collected (in short circuit configuration).

The temperature coefficient of the short-circuit current can then be written as:

$$\beta_{J_{sc}} = \frac{1}{J_{sc}} \frac{dJ_{sc}}{dT_c} = \frac{1}{J_{sc,lsun}} \frac{dJ_{sc,lsun}}{dE_g} \frac{dE_g}{dT_c} + \frac{1}{f_c} \frac{df_c}{dT_c} \quad (19)$$

This expression is interesting because it separates the influence of intrinsic material properties from that of device parameters. The first term is a function of the solar cell material (its bandgap and its bandgap temperature sensitivity) and the intensity and spectrum of the irradiation. The second term is related to the cell light trapping ability and collection efficiency. It can be derived from External Quantum Efficiency (EQE) measurements on a range of temperatures. Experimental results highlighting the impact of collection fraction on $\beta_{J_{sc}}$ will be presented in section 4.2.

In (Green 2003), Green explains that it is complicated to derive generic expressions for the temperature coefficient of the fill factor. This is because fill factors depend on a large number of cell parameters and in particular on current and voltage operating levels. In the case where series and shunt resistances and diode ideality factor do not vary strongly with temperature, the following approximate formula is reasonably accurate:

$$\frac{1}{FF} \frac{dFF}{dT_c} = (1 - 1.02 FF_0) \left(\frac{1}{V_{oc}} \frac{dV_{oc}}{dT_c} - \frac{1}{T_c} \right) \quad (20)$$

Green also emphasized that the fill factor temperature sensitivity plays an important role in the overall temperature behavior of “less-developed technologies” (amorphous silicon or nanocrystalline dye cells) and is often the reason of the temperature-insensitive PV cells reported in the literature.

In 2011, Tanay et al. (Tanay et al. 2011) investigated the differences between the thermal behavior of PV cells made of solar-grade silicon purified by metallurgical route (SoG_M-Si) and that of more common cells made of electronic grade silicon (EG-Si). They found that SoG_M-Si cells have advantageous temperature sensitivities and explained it by the

different mechanisms limiting the mobilities. This could be an advantage for the commercialization of SoG_M-Si cells. However, the cells compared had different efficiencies in the STC (and especially different short-circuit currents) so it could be that the comparison of cells of similar rated power would not show such differences in temperature coefficients (see section 5.6).

In 2012, Braun et al. investigated the temperature coefficients of concentrator solar cell performance parameters (Braun, Katz & Gordon 2012). In particular, they had the very interesting idea of assessing temperature coefficients in the radiative limit as a function of bandgap energy. They derived the following expression for the temperature coefficient of the open-circuit voltage:

$$\begin{aligned} \frac{dV_{oc}(T_c, X)}{dT} = & - \frac{V_{oc,1sun}(T_c) + \frac{kT_c}{q} \ln(X) - \frac{E_g(T_c)}{q}}{T_c} - \frac{k}{q} \left(1 + 2 \frac{d \ln E_g(T_c)}{d \ln(T_c)} \right) \\ & + \frac{1}{q} \frac{dE_g(T_c)}{dT_c} + \frac{k}{q} \frac{d \ln J_{sc,1sun}(T_c)}{d \ln(T_c)} \end{aligned} \quad (21)$$

In section 4.2, the details of the derivation of this equation will be presented as well as a demonstration that it can be written in a form similar to eq. (4). It should be noted that Braun et al. neglected the influence of the temperature dependence of the bandgap. It will be demonstrated in section 4.2 that this parameter actually has an important impact on temperature coefficients.

Also in 2012, Siefer and Bett (Siefer & Bett 2012) made theoretical calculations illustrating that temperature coefficients depend upon the dominant recombination processes. They used two different expressions for the saturation current density in the case where bulk recombinations are dominant and in the case where recombinations are mainly in the depletion zone. They showed that the thermal behavior was expected to be significantly different in these two cases. They used their models to analyse the temperature coefficients of some III-V multi-junction concentrator cells. They concluded that variations in the incident spectrum should not change significantly the temperature coefficients of the PV system they considered and measured that concentration reduced the temperature-related losses by a factor between 2 and 3.

In 2014, a group from NREL observed experimentally that metastable changes due to light exposure modify the temperature dependence of thin film CIGS cell performances

(Deceglie et al. 2014). Their experimental results illustrate the depth of the correlation between device physics and temperature coefficients. Their results will be discussed in more detail in section 4.3.

In this introduction section, we have presented a selection of the previous works that investigated the temperature coefficients of solar cells. Several important ideas have been introduced. It also appears that the generality of a number of analyses is restricted because of the use of empirical parameters. In the following chapter, we will investigate the physics that governs the temperature behavior of solar cells starting from the temperature dependences of the “fundamental” losses to evaluate the temperature sensitivities expected in the radiative limit for the different technologies of solar cells. Then, in order to understand the temperature coefficients of realistic cells, we will extend the analysis to additional losses such as non-radiative recombinations. The different physical mechanisms driving the temperature sensitivity of open-circuit voltage (V_{oc}), short-circuit current (J_{sc}) and fill factor (FF) will be analysed. We will also present some comparisons between existing and newly derived theories and experimental measurements.

3. Fundamental temperature coefficients of photovoltaic devices

3.1. The detailed balance principle and the thermodynamic argument

Fundamentally, solar cells are energy converters that take thermal energy from the Sun and turn it into electrical energy. This means that a solar cell, like any heat engine, is ultimately limited by the Carnot efficiency (Landsberg & Badescu 2000; Green 2001). However, even ideal PV devices differ from Carnot engines because the energy exchanged is radiative and because the energy emitted by the devices is considered a loss in PV conversion since the hot reservoir is the Sun (Fig. 8a). Moreover, typical PV cells absorb solar photons from a small solid angle while they emit in a much broader solid angle (Fig. 8b). Additionally, for typical single junction cells, there is an important loss due to the spectral mismatch between the incident radiation and the absorption in the cell that generates electrical carriers. In the following, we will show how these different losses impact the conversion efficiency of PV systems.

The first assessment of the physical limit of photovoltaic conversion was established by Shockley and Queisser in 1961 using the so-called detailed balance principle (Shockley & Queisser 1961). This limit was later derived from a thermodynamic argument (Ross 1967; Markvart 2008) and extended by several authors (Henry 1980; Tiedje et al. 1984; Araújo & Martí 1994). Shockley and Queisser considered that all the recombinations are radiative (i.e. each recombination event creates a photon) and assumed that each photon excites only one electron so that the population of photons and excited electrons are directly related (Fig. 8b). In this case, the electrical current density (J) that can be extracted from a solar cell is proportional to the difference between the rates of photon absorption (n_{abs}) and emission (n_{emit}):

$$J = q(n_{abs} - n_{emit}) \quad (22)$$

We consider now that the source of incident photons, the Sun in this case, can be modeled by a blackbody at temperature $T_s=5800$ K seen by the cell from a solid angle Ω_{abs} ¹⁴. Also, we assume that the cell absorbs (and thus emits) every photon that has at least its bandgap energy (E_g) and none that has less energy. Thus the rate of photon absorption is given by:

$$n_{abs}(E_g, T_s, \Omega_{abs}) = \frac{2\Omega_{abs}}{c^2 h^3} \int_{E_g}^{\infty} \frac{E^2}{\exp\left(\frac{E}{kT_s}\right) - 1} dE \quad (23)$$

where c is the speed of light in vacuum, and h and k are the Planck's and Boltzmann's constants, respectively.

Assuming that charge transport is perfect, the free enthalpy of the photogenerated electron-hole pairs, namely the chemical potential μ of the electron-hole system (Ruppel & Würfel 1980), is equal to qV where V is the voltage across the PV cell terminals. The chemical potential of the electron-hole system indicates a deviation from equilibrium. Because the system strives to come back in equilibrium, its recombination rate (which is directly linked to its emission rate in this case) increases together with μ . Considering a cell temperature T_c and an emission solid angle Ω_{emit} ¹⁵, the photon emission rate from the cell is given by the generalized Planck's equation (Würfel 1982):

$$n_{emit}(E_g, V, T_c, \Omega_{emit}) = \frac{2\Omega_{emit}}{c^2 h^3} \int_{E_g}^{\infty} \frac{E^2}{\exp\left(\frac{E - qV}{kT_c}\right) - 1} dE \quad (24)$$

¹⁴ More precisely, here and in the rest of the manuscript, as in (Harder & Würfel 2003), it should be mentioned that Ω corresponds to $\int \cos\theta d\Omega = \int_0^{2\pi} \int_0^\alpha \cos\theta \sin\theta d\theta d\varphi$ (where θ and φ are the polar and azimuthal angles, respectively, and α is the angle of the cone of light) because an isotropic intensity is assumed. Note that, in normal incidence, this value is approximately equal to the solid angle if it is really small (such as the solid angle of the Sun seen from Earth $= 6.87 \cdot 10^{-5} \approx \Omega_{abs} = \int \cos\theta d\Omega$)

¹⁵ Again, it must be clarified that here and in the rest of this manuscript, as in (Harder & Würfel 2003), Ω corresponds to $\int \cos\theta d\Omega = \int_0^{2\pi} \int_0^\alpha \cos\theta \sin\theta d\theta d\varphi$ (where α is the angle of the cone of light) because an isotropic intensity is assumed. Note that this value is equal to $1/2$ of the solid angle in the case of an hemispherical solid angle (this is why usually $\Omega_{emit} = \int \cos\theta d\Omega = 1/2(2\pi) = \pi$)

Eqs. (22) and (24) show that emission increases with the voltage V that builds in the cell and thus reduces the current that can be collected. As a consequence, there exists an optimum for the photovoltaic conversion of the radiative power incident on the cell (P_{inc}):

$$\eta_{\max}(E_g, V, T_s, T_c, \Omega_{abs}, \Omega_{emit}) = \max(JV) / P_{inc} \quad (25)$$

The maximum efficiency corresponds to a trade-off between current and voltage and depends on the difference between the rates of generation and recombination (or simply emission in the radiative limit). In a given configuration ($T_s, T_c, \Omega_{abs}, \Omega_{emit}$ are fixed), the cell efficiency is only a function of E_g and V . Thus, its maximum (η_{\max}) can be found by solving the following equations:

$$\left(\frac{\partial \eta}{\partial E_g} \right)_V = 0 \quad (26)$$

$$\left(\frac{\partial \eta}{\partial V} \right)_{E_g} = 0 \quad (27)$$

An interesting analytical solution of eq. (26) can be derived by using Boltzmann's approximation¹⁶ in eqs. (23) and (24) and calculating the integrals by parts (Hirst & Ekins-Daukes 2011):

$$qV_{opt} = E_g \left(1 - \frac{T_c}{T_s} \right) - kT_c \ln \left(\frac{\Omega_{emit}}{\Omega_{abs}} \right) \approx qV_{MPP} \quad (28)$$

This analytical solution (V_{opt}) gives exactly the maximum efficiency for the optimal E_g only (i.e. when eq. (27) is satisfied too) but it provides an excellent approximation of the voltage at maximum power point (V_{MPP}) in the range of bandgaps of materials used in solar cells (Hirst & Ekins-Daukes 2011). In this equation, derived from the detailed balance principle, classical thermodynamic terms appear. The first term on the right hand side, $E_g \left(1 - \frac{T_c}{T_s} \right)$, contains the Carnot efficiency that expresses the necessity of evacuating the incoming entropy (associated to the incoming energy flow). The second term on the

¹⁶ Photons enter the class of particles (called bosons) that follows Bose-Einstein statistics. The Boltzmann approximation consists in considering the simpler Boltzmann statistics (i.e. neglecting the -1 term in the denominator of the integrand in eq. (23) for example). This approximation is really accurate in the range of bandgaps that we consider here (better than one part in 10^8 for $E_g > 0.5$ eV, (Braun, Katz & Gordon 2012)).

right hand side, $kT_c \ln\left(\frac{\Omega_{emit}}{\Omega_{abs}}\right)$, corresponds to the voltage loss related to the entropy generated due to the solid angle mismatch between absorption and emission¹⁷. This would be included in the entropy generation term, S_{gen} , in Fig. 8a and is theoretically avoidable by eliminating this solid angle mismatch (interestingly, it can be achieved either by concentrating the incident light or by restricting the angle of emission from the device, (Martí & Araújo 1996)). It is worth noting that these losses are function of the cell's bandgap, temperature and solid angles of emission and absorption.

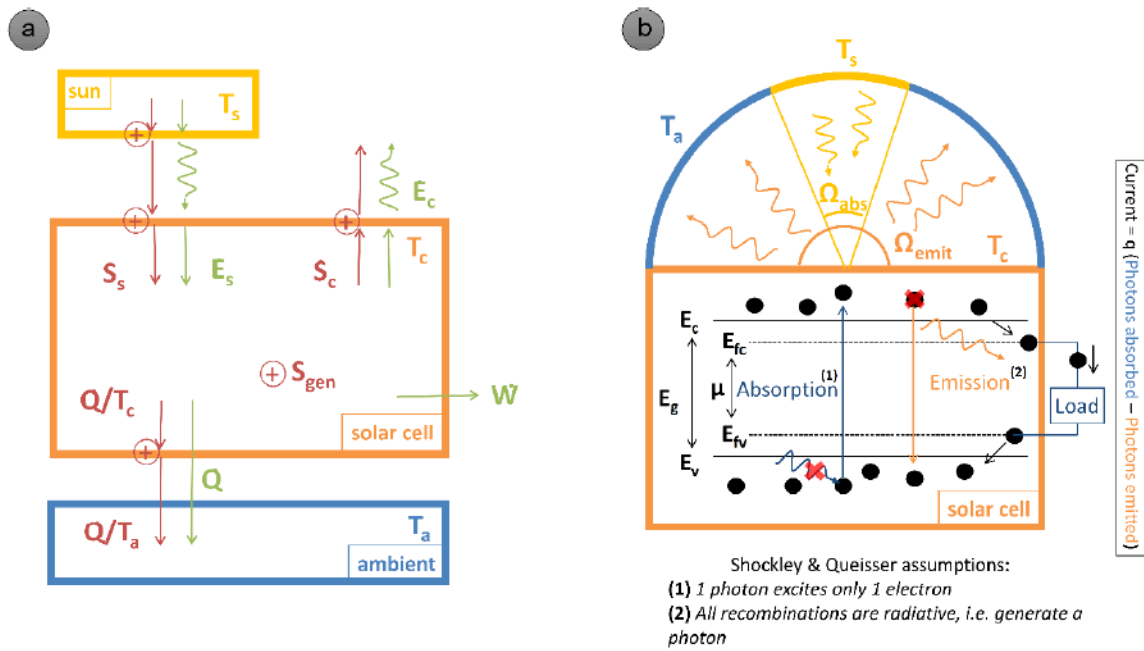


Fig. 8 a. Energy (in green) and entropy (in red) flows in and out of a PV system. The solar cell (in orange) absorbs radiative energy from the Sun (in yellow) with the associated entropy (the reader can refer to (Green 2001) for the corresponding expressions), it also emits some radiative energy with the associated entropy and evacuates some heat with the associated entropy towards the ambient. The symbol + symbolizes the creation of entropy. The temperature of the cell increases until the flow of entropy out of the cell equals that entering the cell. The "extra" energy flow is converted into an electrical power source (W) with no associated entropy flow; b. detailed balance principle illustrated with the photons fluxes in and out of a schematic PV system. This schematic shows the direct relation that exists in the radiative limit between the populations of excited carriers and photons. It also specifies the assumptions made by Shockley and Queisser to derive their famous efficiency limit (Shockley & Queisser 1961).

¹⁷ In non-concentrated PV cells, there is obviously an increase of entropy since electrical charges are excited in a little number of directions and they end up recombining in every direction, emitting photons in the entire hemisphere above the cell's surface.

The current density at maximum power point (J_{MPP}) is given by:

$$J_{MPP} = q(n_{abs} - n_{emit}(V_{MPP})) \quad (29)$$

Table 1 shows the analytical expressions of the energy losses related to the effects mentioned previously. The first two losses are related to the spectral mismatch between the broadband incident radiation and the limited cell absorption: 1/ some photons have more energy than the bandgap (E_g) and this “extra” energy is quickly lost by the excited electrons to the lattice atoms in a process called thermalization; 2/ some photons have less energy than the bandgap (E_g) and are not able to excite any electron (“Below E_g ” loss). The last three losses impact the balance between absorption and emission rates; we will call them in the following “balance losses”.

Table 1. “Fundamental” losses in a single junction solar cell.

Spectral mismatch	Thermalization	$\frac{2\Omega_{abs}}{c^2 h^3} \int_{E_g}^{\infty} \frac{E^2}{\exp\left(\frac{E}{kT_s}\right) - 1} (E - E_g) dE$	(30)
	Below E_g	$\frac{2\Omega_{abs}}{c^2 h^3} \int_0^{E_g} \frac{E^2}{\exp\left(\frac{E}{kT_s}\right) - 1} E dE$	(31)
Absorption-emission balance	Emission	$E_g \frac{2\Omega_{emit}}{c^2 h^3} \int_{E_g}^{\infty} \frac{E^2}{\exp\left(\frac{E - qV_{MPP}}{kT_c}\right) - 1} dE$	(32)
	Angle mismatch	$kT_c \ln\left(\frac{\Omega_{emit}}{\Omega_{abs}}\right) J_{MPP}$	(33)
	Carnot	$E_g \left(\frac{T_c}{T_s}\right) J_{MPP}$	(34)

Fig. 9a shows the fundamental losses (for single junction PV cells under one Sun illumination) calculated from this analytical solution as a function of the bandgap energy together with the numerical solution of the Shockley-Queisser (SQ) limit. This representation, first introduced in (Hirst & Ekins-Daukes 2011), makes it straightforward to visualize the potential improvements that can derive from the different “advanced” PV concepts. It is evident from Fig. 9a why many concepts aim at reducing the spectral

mismatch losses (Hot carriers (Green 2001), Down conversion/ Multiple Exciton Generation (Nozik 2008; Beard 2011), Intermediate band (Luque & Martí 1997; Brown & Green 2002; Luque, Martí & Stanley 2012), Up conversion, Multi-junctions (Henry 1980), Spectral splitting (Martin A. Green et al. 2015)...). Other strategies, such as concentrating sunlight (Press 1976) or limiting the cell's emission angle (Kosten et al. 2013), improve the absorption-emission balance and thus reduce the “Angle mismatch” and “Emission” losses. Fig. 9a also shows that the bandgap of silicon is close to the optimal bandgap for PV conversion in the radiative limit (≈ 1.3 eV). Additionally, one can easily observe the trade-off between increasing the current by absorbing more photons (thus minimizing the Below E_g loss) and maximizing the voltage in the cell (reducing the thermalization and angle mismatch losses).

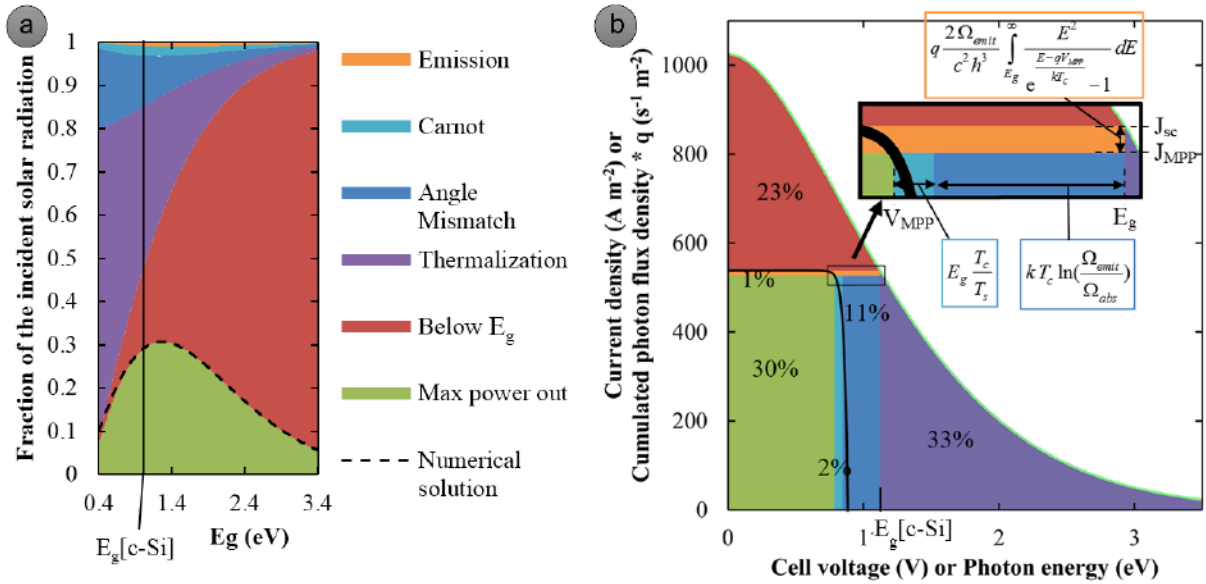


Fig. 9 a. Distribution of the incident solar radiation at the optimal working point for PV conversion at 300 K under one sun illumination as a function of bandgap energy (as in (Hirst & Ekins-Daukes 2011)); the dashed line corresponds to the numerical solution of the Shockley-Queisser limit; b. fundamental losses in PV conversion in a c-Si PV cell at 300 K under one Sun illumination depicted together with its J-V characteristic (as in (Hirst & Ekins-Daukes 2011)).

Fig. 9b represents these fundamental loss mechanisms at the maximum power point together with the ideal current density-voltage (J-V) characteristic of a crystalline silicon (c-Si) solar cell at 300 K ($E_g \approx 1.12$ eV). The pale green line corresponds to the cumulated photon flux density plotted as a function of photon energy. Thus, the area below this line corresponds to the total power density of the incident photons. In the following, in order to simplify the text, we will often use “energy” instead of “power density” (the energy

simply corresponds to the spatial and temporal integral of the power density). Using energies makes it easier to apprehend the global energy balance. The different colored areas in Fig. 9b correspond to the different energy conversion losses in an ideal c-Si cell (except for the pale green rectangle that corresponds to the electrical output energy). The thermalized power (depicted in purple) corresponds to the energy in excess of the bandgap of every photon that is absorbed (in this ideal case, all the photons with at least the bandgap energy). This representation makes it straightforward to understand that increasing the cell bandgap reduces the thermalization loss. However, it is also easy to apprehend that an increase of the cell bandgap will increase the loss depicted by the red area and termed Below Eg. This Below Eg loss simply corresponds to the cumulated energy of the photons with less energy than the bandgap (thus that cannot participate to the generation of excited carriers).

The dual title on the y-axis of Fig. 9b illustrates the relation between current and photon flux density. Indeed, each absorbed photon generates one carrier that can participate to the current that goes through the load (if it does not recombine on its way). In short-circuit, the current density (J_{sc}) is equal (neglecting the radiative emission that is really small in short-circuit) to the cumulated photon flux density at the bandgap. When the voltage of the cell increases, so does the radiative emission rate and the current drops. The energy lost through radiative emission at the cell maximum power point is depicted in orange and corresponds to the number of emitted photons times their energy (approximately equal to the bandgap energy).

As for the dual title on the x-axis of Fig. 9b, it illustrates that the voltage of the cell is limited by the bandgap energy for standard single junction devices¹⁸. Indeed, the potential energy of the excited carrier cannot exceed the energy it carries after the thermalization process. Fig. 9b shows that the voltage at the maximum power point is lower than the bandgap because of the so-called Carnot and Angle mismatch losses (in pale and dark blue respectively). These terms correspond to the optimum voltage reduction associated to radiative recombination. Indeed, any recombination process has a dual impact: 1/ a current loss because some excited charges don't make it to the external circuit; 2/ a voltage loss because the generation-recombination balance is diminished thus reducing the voltage that

¹⁸ This limit can be overcome through advanced concepts such as hot-carrier solar cells as discussed above.

can build in the cell. For an easier understanding, an analogy between a PV cell and a leaky bucket feeding a water wheel is proposed in appendix 10.3. The Carnot loss corresponds to the voltage loss associated to the minimum radiative recombination rate: in the radiative limit when there is no angle mismatch between radiative absorption and emission. If there is an angle mismatch, there is more emission¹⁹ so there has to be more radiative recombination and thus a larger voltage loss (hence the Angle mismatch loss term). It is important to remember that the expressions given in Table 1 describe only the maximum power point of the cell operation. However, it can be deduced from Fig. 9b how the incident energy is distributed in other (J, V) configurations.

The p-n junction diagram depicted in Fig. 10 can help understanding the relation between the J-V curve and the different losses indicated in Fig. 9. In the open-circuit configuration, the voltage across the cell is such that the recombination rate equal that of generation: all the absorbed power that is not thermalized ($\approx J_{sc} \times E_g/q$) is dissipated via radiative recombinations (ultimately resulting in the emission of photons). In the short-circuit configuration, there is no voltage across the cell so almost none of the photogenerated carriers recombine. All the power absorbed by the carriers (that is not thermalized) is dissipated by the carrier flow through the the potential drop at the junction (which is approximately equal to E_g/q in short-circuit). At the Maximum Power Point (MPP), there are some recombinations (current loss = emission loss term) and the voltage loss at the junction depends on the recombination rate (driven by the cell temperature and the angle mismatch).

¹⁹ Kirchhoff's law of radiation dictates that $\Omega_{emit} \geq \Omega_{abs}$.

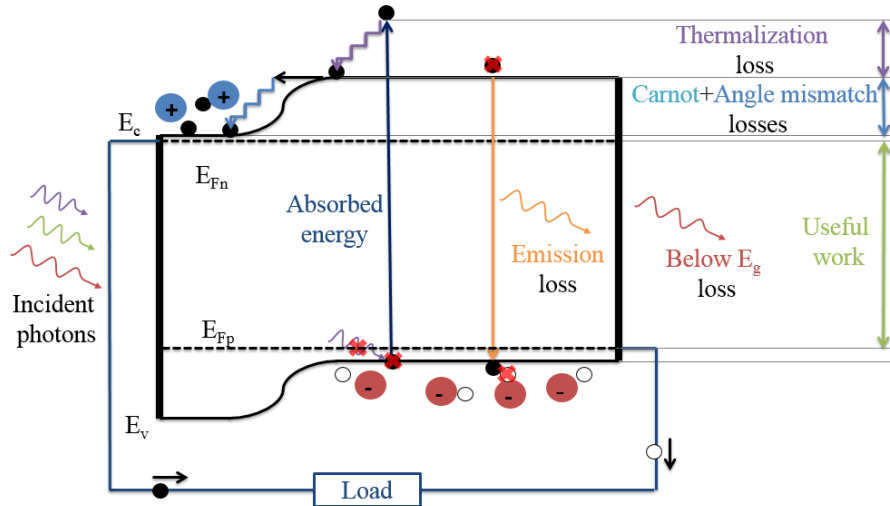


Fig. 10 Fundamental loss mechanisms illustrated on a p-n junction diagram (from (Dupré, Vaillon & Green 2015b)). E_c and E_v are the energies of the bottom edge of the conduction band and the top edge of the valence band, respectively. E_{Fn} and E_{Fp} are the quasi-Fermi levels of electrons and holes, respectively.

Fig. 10 depicts how the energy of the incident photons is converted within an ideal p-n junction solar cell. The voltage losses can be observed on the vertical axis while the current losses are depicted by photon losses along the horizontal axis. The Below E_g loss represents the low energy photons that leave the cell unabsorbed. The dashed lines show the quasi-Fermi levels of the electrons and holes. The distances between the quasi-Fermi levels and the conduction/valence bands give an indication on the concentrations of carriers in these bands (Würfel 2009). From this representation, we understand that the Carnot and Angle mismatch losses occur at the p-n junction or more generally where the charges are separated (it will be explained afterward that this voltage loss can be split into different regions). This voltage drop is necessary to efficiently collect the photogenerated charges before too many of them recombine. Physically, a fraction of their potential energy is converted into kinetic energy during the acceleration they undergo in the junction electric field. Then, they quickly relax to the potential energy of the conduction band of the other side through collisions with the lattice atoms. This heat generation process can be identified as Peltier heating (Baldasaro et al. 2001). This mechanism, seldom if ever reported in the PV literature, will be discussed in more details in chapter 7. This phenomenon means that a large part of the heat generation in PV cells is located where the charges are separated. In most PV cells, the p-n junction (where the separation takes place) is located near the front of the cell. Additionally, high energy photons that

contribute to most of the heat generation by thermalization also happen to be absorbed mostly near the front of the cell.

Eq. (24) shows that radiative emission increases with cell temperature. This is the consequence of increased recombination rate at larger temperature due to the augmentation of the equilibrium carrier concentration. This leads to a negative temperature sensitivity of the absorption-emission rate balance that is the origin of the temperature behavior of PV cells and explains why all²⁰ PV devices become less efficient as they heat up.

This conclusion can also be derived from a thermodynamical argument. The photogenerated carriers need to somehow dissipate the absorbed (and eventually generated) entropy. They do so by giving away some energy (that carries entropy) to the lattice atoms. Because at larger temperature it requires more energy to evacuate entropy in an environment ($\delta S = \delta Q / T$), the maximum PV conversion efficiency decreases as the temperature of the system increases.

Fig. 11 shows the temperature dependence of the previously discussed “fundamental losses” (Fig. 11a applies to the case of one Sun illumination and Fig. 11b to the case of a concentration factor of 10000). In this simplistic case, only the “balance losses” are sensitive to temperature. On the temperature range of PV device operation, their variations with temperature are approximatively linear. This explains the generally observed linear behavior of the output power. This is also why the temperature sensitivities of solar cells can often be described by a single value of the temperature coefficient (TC). By comparing Fig. 11a and Fig. 11b, one can also understand directly the benefit of concentrating sunlight in terms of temperature coefficient.

²⁰ We have mentioned previously that positive temperature coefficients were sometimes reported for amorphous silicon and organic solar cells. However, the argument developed above hold for any kind of PV conversion thus the temperature coefficients of these cells are expected to decrease and become negative as these technologies improve towards the radiative limit (i.e. towards negligible non radiative loss mechanisms).

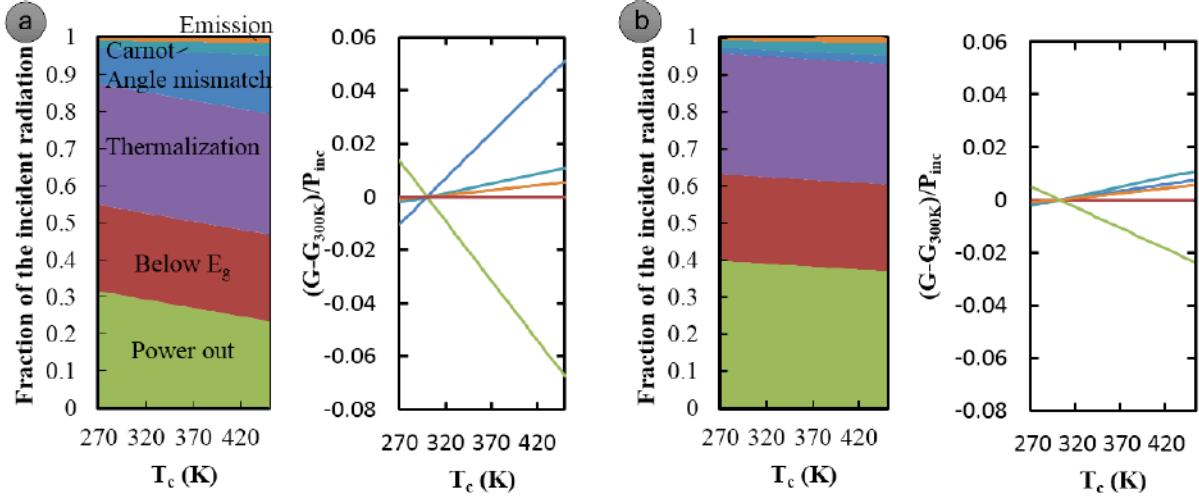


Fig. 11 Temperature dependences of the fundamental losses for a bandgap of 1.12eV ($\approx E_g$ of c-Si at 300 K) a. under one Sun illumination. Figure from (Dupré, Vaillon & Green 2015b). b. under 10000 suns.

We are going to derive below an approximate expression of the fundamental temperature coefficient of solar cells that will highlight the importance of the “balance losses”. Using Boltzmann’s approximation in eq. (30) and neglecting $2E_g kT + 2k^2 T^2$ in front of E_g^2 in the integration by parts produces a linear approximation of the “Emission” loss term (at the maximum power point):

$$Emission \approx T_c \times \left(k E_g^3 \frac{2\Omega_{abs}}{c^2 h^3} \exp\left(-\frac{E_g}{kT_s}\right) \right) \quad (35)$$

Neglecting the temperature variation of J_{MPP} , eqs. (33) and (34) indicate that the “Angle mismatch” and “Carnot” losses also vary linearly with temperature. These approximations enable to find an estimate of the temperature coefficient of the maximum efficiency as a function of the balance losses (Emission, Carnot and Angle mismatch) at a reference temperature:

$$\beta_{\eta_{max}} \approx \frac{10^6}{P_{max}(298.15K)} \frac{-\text{balance losses}(298.15K)}{298.15} \quad (36)$$

Because temperature coefficients are normalized, any mechanism impacting the efficiency of the cell modifies its temperature coefficient. The approximate expression in eq. (36) emphasizes that fundamental temperature sensitivities are mainly a function of the generation-recombination balance of the cell. It was observed long ago that temperature sensitivity of device performance improves together with open-circuit voltage (Green, Emery & Blakers 1982). This is due to the fact that the open-circuit voltage of the cell is

a good indicator of the generation-recombination balance. One way of improving this balance is by concentrating more light upon the cell. Indeed, concentration is known to increase V_{oc} and reduce temperature sensitivity (Yoon & Garboushian 1994; Braun, Katz & Gordon 2012). This is illustrated in Fig. 11 which shows side by side the variations of the different losses with temperature for a non-concentrated cell (Fig. 11a) and for cell receiving 10000 suns (Fig. 11b). Another way of changing the generation-recombination balance is by modifying Non-Radiative Recombination (NRR) rates. In section 4, we will consider NRRs and analyse how they impact temperature coefficients.

Fig. 12 shows temperature coefficients in the radiative limit calculated as a function of the PV cell bandgap with different approximations. The analytical solution (from eqs. (28) and (29)) and its approximation, eq. (36), provide a good estimate of temperature coefficients as long as E_g is not too small. One can observe that the absolute value of the temperature coefficient is larger for smaller bandgaps. This is because temperature coefficients are normalized values that are mainly driven by the open-circuit voltage (see section 4.1 or (Green 2003)).

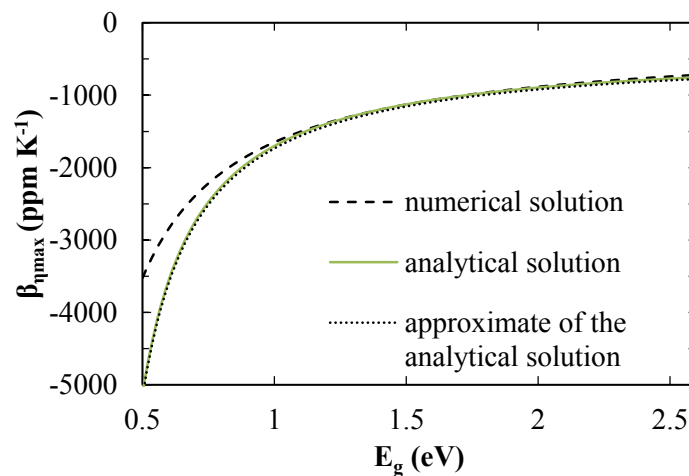


Fig. 12 Fundamental temperature coefficient at 350K of the maximum efficiency of photovoltaic cells as a function of their bandgap.

3.2. Bandgap temperature dependence and influence of the incident spectrum

All the fundamental losses in PV conversion are function of the bandgap (Table 1). Fig. 12 shows the temperature coefficient of maximum efficiency at different bandgaps with a simplistic assumption. In practice, the bandgaps of semiconductors change substantially with temperature. These variations are due to modifications of the band energies caused by electron-phonon interactions and by thermal expansion of the lattice (Dey et al. 2013). Most semiconductor bandgaps decrease almost linearly in the temperature range of operation of PV cells (Yu et al. 2011). However, there is no general relation between bandgap and temperature dependence of bandgap as shown in Fig. 13. There are some exceptions where bandgap actually increases with temperature. Of particular interest for photovoltaics are the perovskite²¹ semiconductor compounds $\text{CH}_3\text{NH}_3\text{PbI}_{3-x}\text{Cl}_x$ (Wu et al. 2014), CsSnI_3 (Yu et al. 2011)²²... A notable feature of the perovskite cells is a reverse ordering of their band-edges states. Their conduction band is constituted of p-like states (Even et al. 2012) and their valence band of s-like states (while it is the opposite for most semiconductors). “Interestingly, reverse band-edge ordering also gives a bandgap that increases with increasing temperature for any given phase (Ishihara 1994; D’Innocenzo et al. 2014), which is the opposite trend to that of tetrahedrally coordinated semiconductors”²³ (Green, Ho-Baillie & Snaith 2014).

²¹ Perovskites are materials described by the formula ABX_3 where A and B are cations of different sizes (A larger than B) and X is an anion. It can be observed in Fig. 5 (on page 6) that a new class of solar cells based on mixed organic-inorganic halide perovskites (such as $\text{CH}_3\text{NH}_3\text{PbI}_{3-x}\text{Cl}_x$) has recently emerged and shows an extraordinary quick development (Green, Ho-Baillie & Snaith 2014). The inorganic counterpart CsSnI_3 has only achieved very low efficiency so far for reasons that are not understood yet but also has a suitable bandgap for PV applications (Xu et al. 2014) and does not contain any lead.

²² There are also non-perovskite materials whose bandgaps increase with temperature such as lead chalcogenides semiconductors (PbS, PbSe, PbTe), CuCl, CuBr, CuI and some ternary chalcopyrites containing Ag and Cu (Dey et al. 2013). We do not discuss them here as they are not used in PV applications.

²³ Note that the lead chalcogenide semiconducting compounds crystallize with the NaCl structure where the atoms are not tetrahedrally coordinated (Holt & Yacobi 2007), p.27.

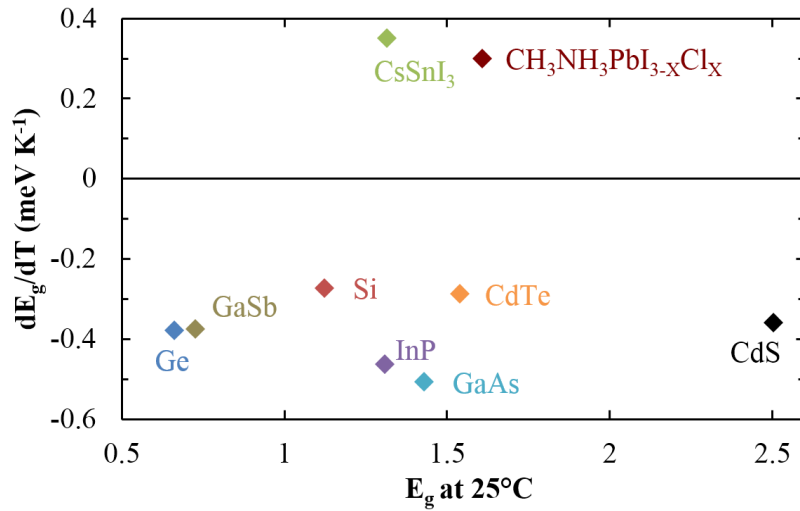


Fig. 13 Slope of the linear approximation of bandgap temperature dependence around 300K. $E_g=f(T)$ from (Singh & Ravindra 2012), from (Green 1990) for Si, from (Yu et al. 2011) for CsSnI₃, from (Wu et al. 2014) for CH₃NH₃PbI_{3-x}Cl_x and from (Vurgaftman, Meyer & Ram-Mohan 2001) for GaSb.

These bandgap temperature dependences impact directly the temperature coefficients and also create an influence of the incident spectrum on TCs as can be observed in Fig. 14 and Fig. 15. Fig. 14 shows the “Shockley-Queisser efficiency limit” calculated with the latest AM1.5 spectrum (IEC 2008) at different temperatures. The maximum efficiencies of different semiconductors are plotted using their bandgap temperature dependences (references are listed in the legend of Fig. 13). One can observe that different behaviors are expected of the perovskites compounds whose bandgaps increase with temperature (cf. Fig. 13). Fig. 15 shows the TCs of these materials together with extrapolations of $TC=f(E_g)$ assuming different values of dE_g/dT . Two extremes values of dE_g/dT are chosen for illustration so the TCs of the materials considered are sandwiched between the dashed lines. In practice, TCs are not necessarily located between these dashed lines as there exists probably materials with larger and smaller dE_g/dT values. The “waves” in the extrapolations (dashed lines in Fig. 15) correspond to the “waves” in the plots of maximum efficiency as a function of bandgap (Fig. 14) which come from the irregularities in the incident AM1.5 spectrum caused by the absorption of some components of the atmosphere (Fig. 16). Because of these irregularities, the impact of dE_g/dT on the maximum power temperature coefficient varies importantly with the value of the bandgap at 25 °C. We observe that, while their bandgaps at room temperature are similar, CsSnI₃ will ultimately (i.e. in the radiative limit) be less temperature sensitive than InP because of the unusual behavior of its bandgap. On the other hand, it can be observed that PV cells made of

$\text{CH}_3\text{NH}_3\text{PbI}_{3-x}\text{Cl}_x$ will, in the radiative limit, suffer more severely from heating than cells made of other semiconductors with similar bandgaps. However we will see in section 4.1 that the temperature coefficients of real cells depend on their External Radiative Efficiencies (ERE) and the best perovskite cells to date already show relatively high EREs (Green, Ho-Baillie & Snaith 2014). This suggests that these perovskite solar cells should quickly have good temperature coefficients²⁴. Fig. 14 and Fig. 15 show that the impact of dE_g/dT on TC is function of $d\eta/dE_g$ and thus depends on E_g and the incident spectrum (because it dictates the shape of the Shockley-Queisser limit). This explains why dE_g/dT is of particular importance for semiconductors whose bandgaps are away from the optimum (such as top and bottom cells of multi-junction PV cells). Some works state that the bandgap temperature dependence (dE_g/dT) of some quantum dots change with their size (Olkhovets et al. 1998; Dey et al. 2013). This indicates a potential way of tuning dE_g/dT to optimize the TC of future PV cells. For example, looking at Fig. 14, we observe that it should be possible to create PV cells with temperature-insensitive performances²⁵. As we have mentioned above, one of the reasons why the bandgap of semiconductors varies with temperature is the thermal expansion of the lattice. Menard et al. (Menard, Meitl & Burroughs 2012) noticed that in the case of ultra-thin micro-transfer printed cells, the thermal expansion of the substrate has an impact on the thermal expansion of the cell active layer and thus on the bandgap temperature coefficient dE_g/dT . This indicates another possible way (mechanical stress) of adjusting dE_g/dT in order to optimize the thermal performances of really thin film cells.

²⁴ Temperature coefficients of perovskites cells have not yet been reported in the literature probably because of the significant instability of these devices (Green, Ho-Baillie & Snaith 2014; Ono et al. 2015).

²⁵ Cells with temperature-insensitive performances have been claimed by a research team from the Netherlands (Schropp 2008). However, they did not use the idea of tuning dE_g/dT . The temperature-insensitivity of their device efficiency is probably due to important losses at room temperature that have positive temperature dependences. Their cells had really low efficiencies ($\approx 5\%$).

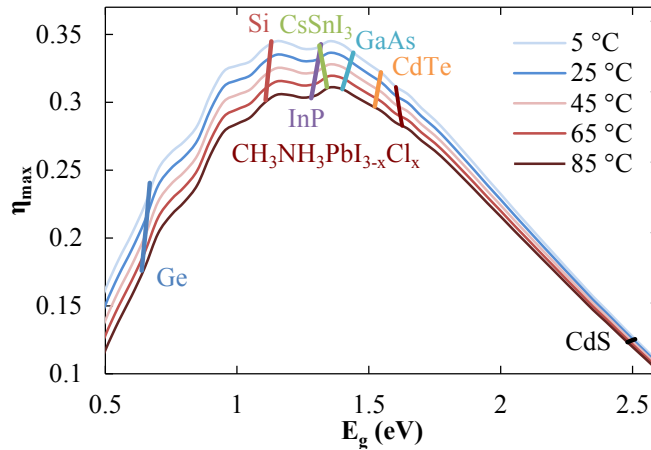


Fig. 14 Shockley-Queisser limit at different temperatures. The thicker segments (more or less vertical) correspond to the maximum theoretical efficiencies of different semiconductors at their respective bandgap between 5 and 85 °C. Figure from (Dupré, Vaillon & Green 2015b).

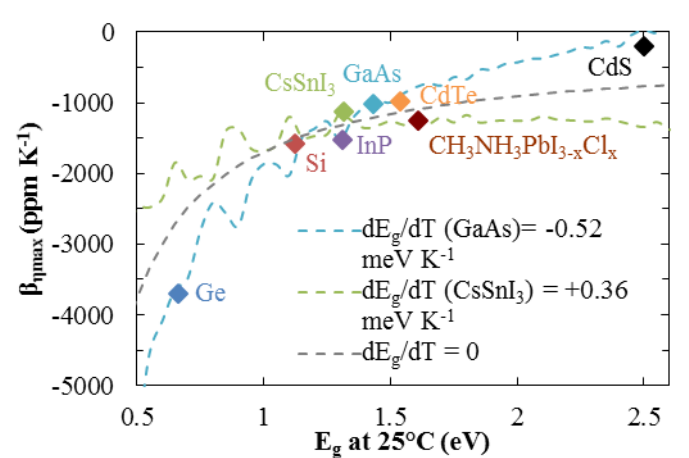


Fig. 15 Temperature coefficients of several semiconductors and extrapolations using different values of dE_g/dT . Figure from (Dupré, Vaillon & Green 2015b).

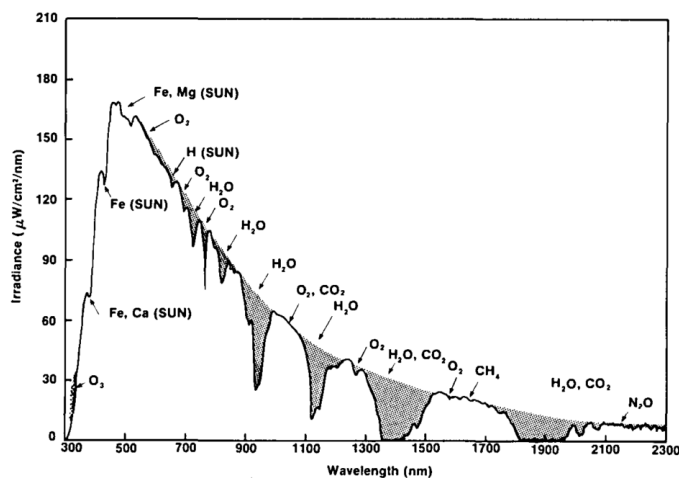


Fig. 16 Global spectral irradiance from Bedford, Massachusetts, 18 July 1980 at 12:36 LST with spectral absorption features designated. Figure from (Bird et al. 1982).

Variations of the incident spectrum do not necessarily cause important changes in the temperature coefficient of the PV conversion efficiency as can be observed in Fig. 17. However, we will show in section 3.2 that spectra have an important influence on the temperature coefficients of short-circuit currents. In Fig. 18, we show that TCs are expected to change a little through the day as the Air Mass (AM) changes (variations of AM through the day in an arbitrary location is illustrated in Fig. 19). This effect is not spectral but is due to the variations of the global intensity of irradiation which impacts the temperature coefficient of open-circuit voltage. This is similar to changing the concentration factor as will be discussed in detail in section 4.1.

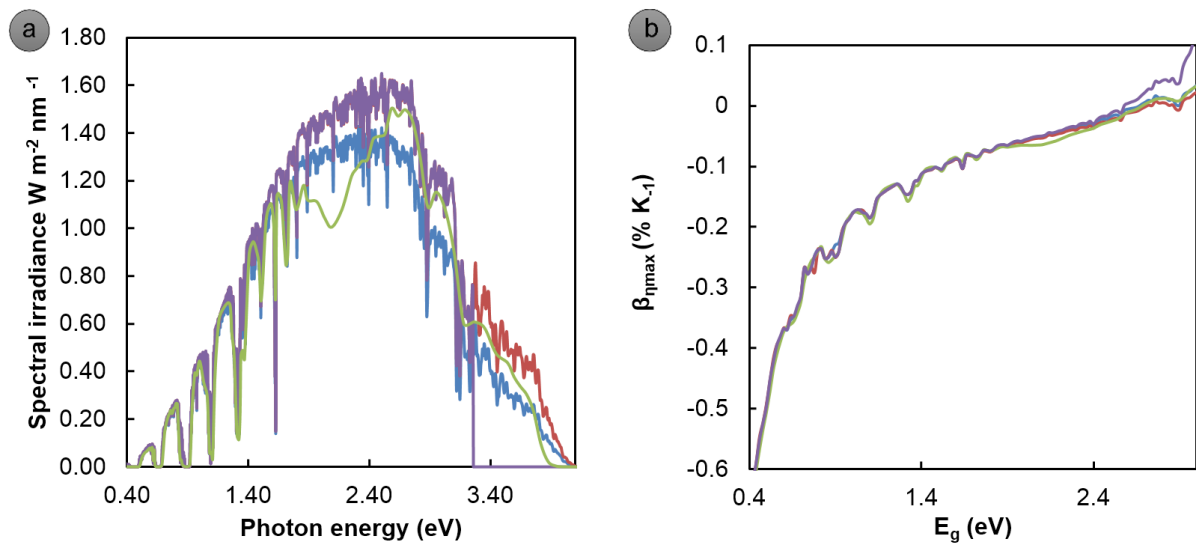


Fig. 17 Influence of the spectrum on fundamental temperature coefficients. a. AM1.5 global (in red) and direct (in blue) spectrum (defined in IEC 60904-3 edition 2), AM1.5 global spectrum truncated at 380 μm to simulate the absorption of an EVA (Ethylene-Vinyl Acetate) encapsulation layer (in purple) and spectrum calculated with the "spectral2" software available as shareware from NREL's website (Bird & Riordan n.d.) using the following parameters setting: $O_3=2$ and H_2O precipitation=6 (in green); b. fundamental efficiency temperature coefficients calculated using the spectra of Fig. 17a and $dE_g/dT=-0.36 \text{ meV.K}^{-1}$ (arbitrary choice).

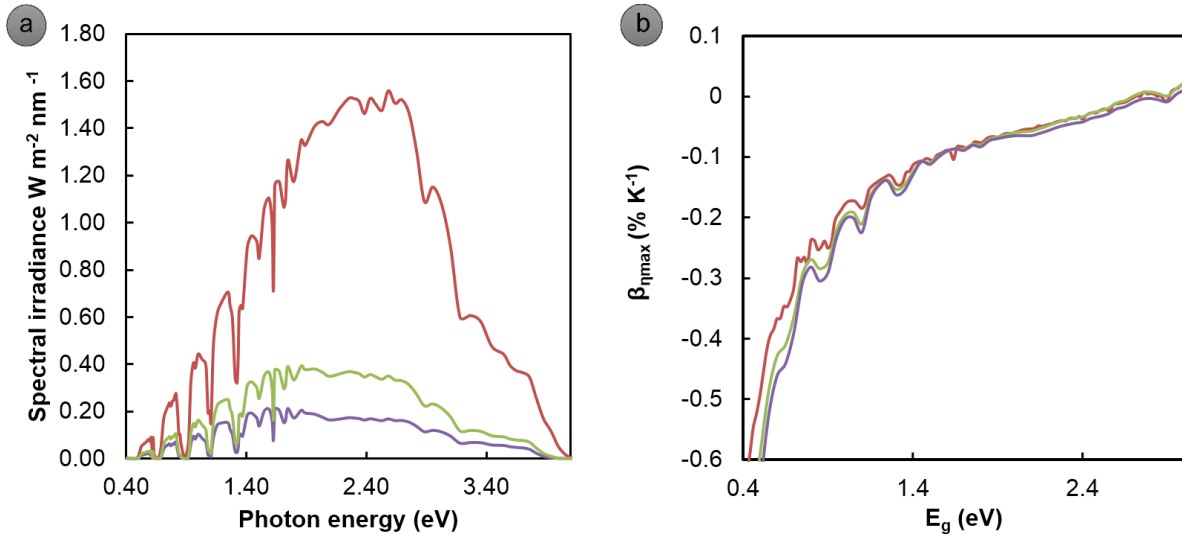


Fig. 18 Influence of the Air Mass (AM) on fundamental temperature coefficients. a. AM1.5 global (in red), AM4 (in green) and AM6 (in purple) global spectra calculated with the "spectral2" software available as shareware from NREL's website (Bird & Riordan n.d.); b. fundamental efficiency temperature coefficients calculated using the spectra of Fig. 18a and $dE_g/dT = -0.36 meV.K^{-1}$ (arbitrary choice).

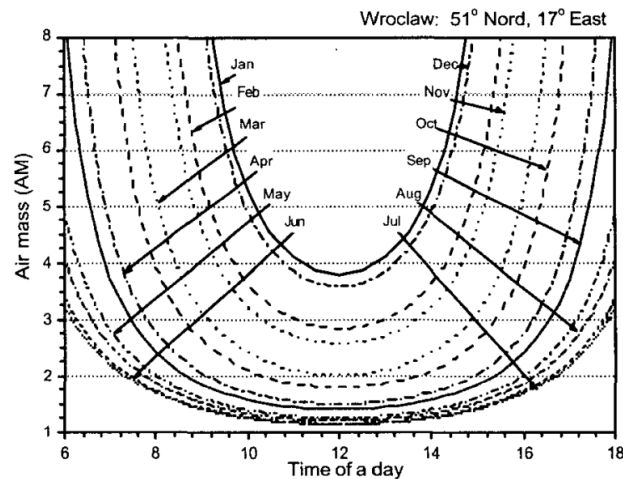


Fig. 19 Values of AM factor as a function of time for different months in Wroclaw (Zdanowicz 2003).

In this section, the analysis has been derived in the radiative limit (where radiative recombination dominates non-radiative recombination processes such as Auger or Shockley-Read-Hall). While this situation corresponds to the ultimate efficiency of solar cells, it does not give the theoretical minima of temperature coefficients. Among the additional losses, some may decrease with temperature (series resistance in c-Si cells for

example (Singh et al. 2008)). This can lead to unusually large or even positive²⁶ temperature coefficients as sometimes observed for newly-developed technologies (Green 2003). However, temperature coefficients are expected to converge towards these “fundamental” values as technologies improve towards the radiative limit (this will be illustrated for silicon cells in Fig. 22).

3.3. Intrinsic temperature coefficient of silicon solar cells which includes Auger recombination

In order to determine the temperature coefficient corresponding to the intrinsic limiting conversion efficiency of a given material, one should take into account Auger recombination which is also (together with radiative recombination) an intrinsic limiting mechanism.

An Auger recombination corresponds to the crossing of an electron from the conduction band to the valence band via the transfer of some energy (at least E_g) to another electron of the conduction band. The electron of the conduction band that receives the energy quickly thermalizes back to the lower energy level of the conduction band (E_c). This process is illustrated on a p-n junction diagram in Fig. 20 (page 62). It does not depend on defects but mainly on the local concentration of carriers (electrons and holes) in the conduction and valence bands.

Using the state-of-the-art parameters (Richter, Hermle & Glunz 2013) and considering carefully their temperature dependences, we derive in the following the temperature coefficient of the limiting efficiency of crystalline silicon solar cells. This derivation is strongly based on (Richter, Hermle & Glunz 2013). We consider an ideal cell, i.e. with no surface and defect recombinations and with a perfect anti-reflection coating (ARC) (i.e. no reflection loss) and a perfect reflecting rear mirror. The current density extracted from the cell (J) is equal to the photogenerated current density (J_L) minus the recombination

²⁶ There are several references in the literature that report on positive temperature coefficients of the maximum output power of organic solar cells (Riedel et al. 2004; Ali et al. 2012; Katz et al. 2001). This is due to important losses at room temperature that are reduced by a temperature increase. According to Katz et al., the origin of the large TCs of cells made of conjugated polymer-fullerene composites originates from the temperature dependence of their mobilities (Katz et al. 2001). Therefore we expect TCs of organic solar cells to decrease as the technologies improve (which is the opposite of the trend for inorganic cells).

current which depends on the cell thickness (W) and the intrinsic (radiative and Auger) recombination rate (R_{intr}):

$$J = J_L - qW R_{intr} \quad (37)$$

The intrinsic excess recombination rate is a function of the excess carrier concentration (Δn) and the intrinsic lifetime (τ_{intr}):

$$R_{intr} = \Delta n / \tau_{intr} \quad (38)$$

We assume that there are no transport losses (no series resistances) so the quasi-Fermi level separation is constant in the cell and equal to the cell output voltage (V). The use of a constant recombination rate within the entire cell in eq. (37) is also based on this assumption. In this case, Δn is related to V by:

$$np = (n_0 + \Delta n)(p_0 + \Delta n) = n_{i0}^2 \exp\left(\frac{qV}{kT_c}\right) \quad (39)$$

where n and p are the electrons and holes concentrations, n_0 and p_0 are the respective equilibrium concentrations and n_{i0} is the intrinsic equilibrium carrier concentration. Solving eq. (39), we get²⁷:

$$\Delta n = 0.5 \left(\sqrt{(p_0 - n_0)^2 + 4n_{i0}^2 \exp\left(\frac{qV}{kT_c}\right)} - (n_0 + p_0) \right) \quad (40)$$

Following (Richter, Hermle & Glunz 2013), we consider here undoped silicon (because it gives the maximum possible conversion efficiency) so we have $p_0 = n_0 = n_{i0}$. We use the parameterization of Sproul and Green (Sproul & Green 1993), scaled to correct for the influence of bandgap narrowing²⁸ as suggested in (Wolf et al. 2010)²⁹, in order to calculate the intrinsic equilibrium carrier concentration n_{i0} as a function of the cell temperature:

²⁷ There is a sign error in Eq. 5 of (Kerr, Cuevas & Campbell 2003): one should read $(p_0 - n_0)^2$ instead of $(n_0 + p_0)^2$.

²⁸ Bandgap narrowing (BGN) is a term used to describe the variation of effective bandgap observed when impurity concentrations are particularly high (such that the defect states start to form a so-called impurity band).

²⁹ There is an error in the value of C given in Appendix B of (Wolf et al. 2010): one should read $C=1.589 \cdot 10^{15} \text{ cm}^{-3}$ instead of $C=1.589 \cdot 10^9 \text{ cm}^{-3}$.

$$n_{i0}(T_c) = 0.9688 \times 1.64 \cdot 10^{15} T_c^{1.706} \exp\left(-\frac{E_g(T_c)}{2kT_c}\right) \quad (41)$$

The bandgap of silicon is given in eV as a function of temperature by (Green 1990)³⁰:

$$E_g(T_c) = 1.206 - 2.73 \cdot 10^{-4} T_c \quad (42)$$

The intrinsic excess recombination rate is the sum of the excess radiative and Auger recombination rates. The excess radiative recombination rate of silicon R_{rad} is given by (Altermatt 2011):

$$R_{rad} = B_{low} g_{eh} (np - n_i^2) \quad (43)$$

where B_{low} is the hypothetical radiative recombination coefficient at low carrier density and g_{eh} (sometimes noted B_{rel}) is a factor that accounts for Coulomb attraction. Coulomb attraction causes excited electrons to stay physically close to the holes they left in the valence band (these localized pairs of electron-hole are called excitons). This phenomenon increases band-to-band recombination rate compared to the free-carrier model. This Coulomb enhancement is reduced when the carrier concentration increases because the excitons are separated faster by interactions with other free-carriers (screening effect). We used the empirical parameterization given in (Altermatt et al. 2005)³¹ to calculate g_{eh} and we fitted³² the experimental values from (Trupke et al. 2003) to obtain B_{low} as a function of temperature. To include the fact that each photon emitted by radiative recombination has a certain chance to be reabsorbed in the cell and excite another carrier (phenomenon called photon recycling), R_{rad} has to be multiplied by $(1-PR)$ where PR is the photon recycling probability. Eq. (37) becomes:

$$J = J_L - qW(R_{Auger} + R_{rad}(1-PR)) \quad (44)$$

³⁰ We did not add the temperature-dependent BGN model of (Schenk 1998) as in (Wolf et al. 2010) because we only considered intrinsic (i.e. undoped) silicon.

³¹ There are missing brackets around $n+p$ in Eq. 4 of (Altermatt et al. 2005) and Altermatt reported in (Altermatt 2011) that b_1 should be replaced by $2b_1$ and b_2 by $2b_2$. The corrected expression reads:

$$g_{eh} = b_{min}(T_c) + \frac{b_{max} - b_{min}(T_c)}{1 + \left(\frac{n+p}{2b_1(T_c)}\right)^{2b_2} + \left(\frac{n+p}{b_3(T_c)}\right)^{b_4}}, \quad \text{where the values of the parameters can be found in (Altermatt$$

et al. 2005).

³² We fitted the experimental data using Origin and adding some weights to have the exact value at 300 K and a reasonable extrapolation on the 300-400 K range (see appendix 10.4).

In the range of excess carrier density of interest and for a cell thickness of 100 μm (value chosen to enable comparisons with a previous study (Kerr, Cuevas & Campbell 2003)), the photon recycling probability is about 0.56.

To evaluate the excess Auger recombination rate of silicon (R_{Auger}), we used the expression proposed in Table 2 in (Richter et al. 2012). We integrated the temperature dependences detailed in (Altermatt et al. 1997) that take into account phonon-assisted Auger recombination and the temperature dependence of the enhancement factors due to phonon-screening of the excitons. Similarly to the case of radiative recombination, excitons (electron and hole “linked” by the Coulomb force) enhance the Auger recombination rate. Because of screening, excitonic effects decrease with increasing temperature or free-carrier concentration. The resulting expression of R_{Auger} writes:

$$R_{Auger} = 2.5 \cdot 10^{-31} g_{eh}(T_c) n_0(T_c) + C_p(T_c) g_{ehh}(T_c) p_0(T_c) + 3 \cdot 10^{-29} \Delta n(T_c, V)^{0.92} \quad (45)$$

with

$$g_{eh}(T_c) = 1 + 13(T_c / 300)^{-1.5013} \left[1 - \tanh \left[\left(\frac{n_0(T_c)}{3.3 \cdot 10^{17}} \right)^{0.66} \right] \right] \quad (46)$$

$$g_{ehh}(T_c) = 1 + 7.5(T_c / 300)^{-1.6546} \left[1 - \tanh \left[\left(\frac{p_0(T_c)}{7 \cdot 10^{17}} \right)^{0.63} \right] \right] \quad (47)$$

$$C_p(T_c) = 7.91 \cdot 10^{-32} - 4.13 \cdot 10^{-35} T_c + 3.59 \cdot 10^{-37} T_c^2 \quad (48)$$

The photogenerated current density is calculated considering the photon flux density (PFD) of the AM1.5 reference spectrum (IEC 2008) and that an absorption generates only one excited carrier (multiple excitons generation is neglected as it contributes to less than 0.1 $\text{mA}\cdot\text{cm}^{-2}$ in silicon (Green 1999)). Also, a Lambertian randomizing light trapping scheme together with an isotropic response of the cell is assumed. In this case, the light rays travel a mean path length of $4n_r^2 W$ inside the cell (Tiedje et al. 1984) where n_r is the refractive index of silicon. The parasitic absorption by free-carriers is also taken into account via the free-carriers’ absorption coefficient α_{FCA} as follows:

$$J_L = q \int_0^{\infty} A_{bb}(E) PFD(E) dE \quad (49)$$

where the interband absorptance of the cell A_{bb} is given by:

$$A_{bb}(E) = \frac{\alpha_{bb}(E)}{\alpha_{bb}(E) + \alpha_{FCA}(E) + \frac{1}{4n_r^2 W}} \quad (50)$$

where α_{bb} is the interband absorption coefficient. The term $\frac{1}{4n_r^2 W}$ corresponds to the escape rate of unabsorbed photons in the optical configuration described above (Tiedje et al. 1984). α_{bb} and n_r are calculated at any temperature from tabulated data at 300 K and temperature coefficients available in (Green 2008). α_{FCA} is calculated from the recent expression proposed in (Rüdiger et al. 2013).

The maximum power can be found by calculating the maximum of the current-voltage product numerically (using the software Mathematica for example). In our case, we are particularly interested in the temperature dependence of the intrinsic limiting efficiency of silicon solar cells ($\beta_{\eta,int}[\text{Si}]$). Applying the aforementioned methodology, we calculated $\beta_{\eta,int}[\text{Si}]^{33}$ to be -2380 ppm K^{-1} which is significantly larger than the value in the radiative limit (-1582 ppm K^{-1}). As discussed previously, this does not correspond to a minimum. However, as they improve, temperature sensitivities of crystalline silicon solar cells are expected to converge towards this value.

³³ In this intrinsic limit configuration, we also calculated the temperature coefficient of the open-circuit voltage (-2290 ppm K^{-1}), of the short-circuit current (454 ppm K^{-1}) and of the fill factor (-544 ppm K^{-1}).

4. Temperature coefficients of real photovoltaic devices

Present commercial photovoltaic cells have efficiencies considerably lower than the Shockley-Queisser (SQ) limit defined by the fundamental losses described previously. For example, average silicon solar modules on the market today (in 2015) have rated efficiencies of about 15% (good modules reach 20% and above) while the SQ limit for silicon is 33.4% (and the intrinsic limit efficiency calculated in (Richter, Hermle & Glunz 2013) is 29.43 %) ³⁴. In this section, the additional losses limiting real device performances are introduced and their impacts on temperature coefficients are analysed.

Fig. 20 shows the band diagram of a realistic solar cell operating at its maximum power point. The most important losses stem from the non-radiative recombinations (NRR). The different NRR processes (Shockley-Read-Hall³⁵, Auger, surface³⁶) are illustrated. Other losses include reflection at the front of the cell, electrical shunts, imperfect contacts and finite mobilities of the carriers. Transmission losses (i.e. photons with sufficient energy that are not absorbed) are not depicted here but can also reduce the efficiency of thin PV cells with insufficient light trapping (see section 5.2). The representation of Fig. 20 is interesting in that it shows where and how the different energy losses happen. For example, the “Resistance loss” corresponds to the kinetic energy lost by the charges to the semiconductor atoms during collisions along their paths.

Similarly to Fig. 10, Fig. 20 shows that mechanisms reducing the generation-recombination rate balance result in a voltage loss which occurs at the interfaces with the selective membranes that drive the photogenerated charges in opposite directions. In this

³⁴ With the years, the best crystalline silicon cell is getting closer to this intrinsic limit. The official record to date (June 2015) is claimed by Panasonic with a 25.6 % efficient silicon cell.

³⁵ Shockley Read Hall (SRH) recombination is an extrinsic two steps process by which an excited carrier recombine through a defect state in the forbidden region (bandgap). Defects in the crystal lattice can have several origins such as the presence of impurities (unintentional or intentional, case of dopants). SRH recombination depends strongly on the defect type and can have various dependences on temperature (Schenk 1992).

³⁶ Surfaces are regions where the lattice structure is bound to be filled with defects. Additionally, impurities tend to gather in these regions. This means that the bandgap is filled with defect states and recombinations happen extremely fast. A parameter called “surface recombination velocity” is used to quantify the recombination rate at a surface.

example, it occurs at the p-n junction and also slightly in the region of the Back Surface Field (BSF) which can be seen as a p-p+ junction. For other configurations it could be different (e.g. pin structure consists in two separate junctions so this loss is split more equally in two separate regions). Reflection, transmission and shunts, like any current losses, also add to this voltage drop but their contribution is usually negligible so it is not depicted in Fig. 20 (and subsequently in Fig. 21). The product of the current and this potential drop corresponds to a “collection cost”: the energy required to efficiently extract from the cell the photogenerated electrical carriers. From a thermodynamic point of view, a stable system needs to have a zero net entropy balance. This “collection cost” also corresponds to the heat flow from the excited carrier population necessary to equilibrate the entropy balance (see Fig. 8a).

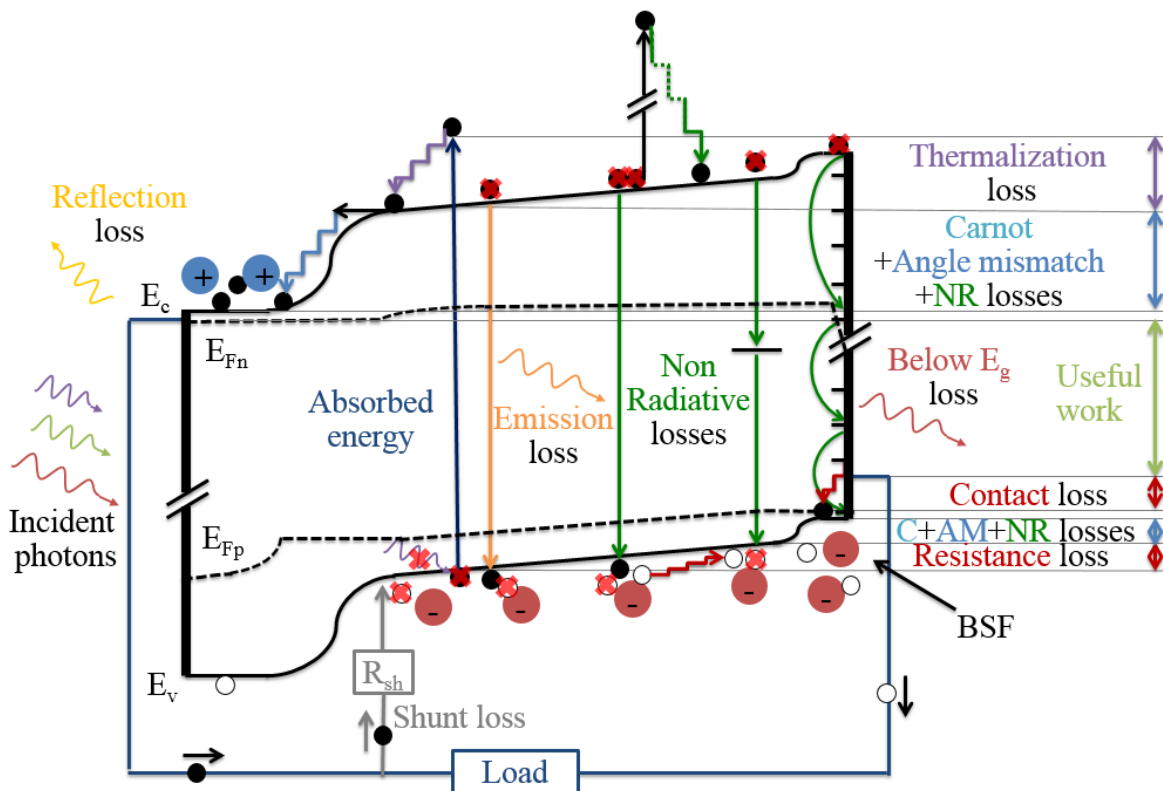


Fig. 20 Conversion loss mechanisms of a PV cell illustrated on a p-n junction diagram. From (Dupré, Vaillon & Green 2015b).

In Fig. 21, the light J-V curve of a c-Si cell is depicted together with the different losses at the Maximum Power Point (MPP). Fig. 21 shows both the cumulated photon flux density as a function of photon energy and the current density as a function of the cell voltage (see description of Fig. 9b). While Fig. 9b shows the cumulated photon flux density of a blackbody emission spectrum at 5800 K, Fig. 21 shows the cumulated photon

flux density of the AM1.5 spectrum (dashed line). The full line corresponds to the cumulated photon flux density absorbed by a planar crystalline silicon cell (calculated from reflectivity data obtained with OPALv1.3 (Baker-Finch & McIntosh 2010)). The area between these two cumulated photon flux densities corresponds to the total energy³⁷ of the reflected photons. The rectangle in pale yellow illustrates the energy lost for the conversion process: the bandgap energy times the number of reflected photons that have more energy than the bandgap energy. Note that the reflection loss in real c-Si cells is much lower because they have anti-reflection coatings and their front surface is usually texturized (often with random pyramids). A planar silicon surface was considered here only for the sake of illustration. Fig. 21 illustrates the different “fundamental” losses (presented before in the description of Fig. 9b) together with the additional losses that occur in real PV devices (that were described above and depicted in Fig. 20).

As in Fig. 9b, by identifying the losses that limit current (density) and voltage, it is possible to understand the shape of the J-V characteristic (non-ideal in this case). In short-circuit configuration, there is an important current flow and no voltage across the cell: all the absorbed power is dissipated because the charges lose their potential energy to the phonons in voltage drops across the cell. In open-circuit configuration, the voltage across the cell is such that the recombination rate equal that of generation: all the power is dissipated via recombinations (non-radiative ones resulting in heat sources and radiative ones resulting in photon emission). The differences in heat generation in these configurations will be discussed further in Part II. At the maximum power point, the transport loss mechanisms are visible because there is a current flow and a voltage across the cell.

³⁷ In this paragraph, we will once again simplify the text by using “energies” instead of “power densities”.

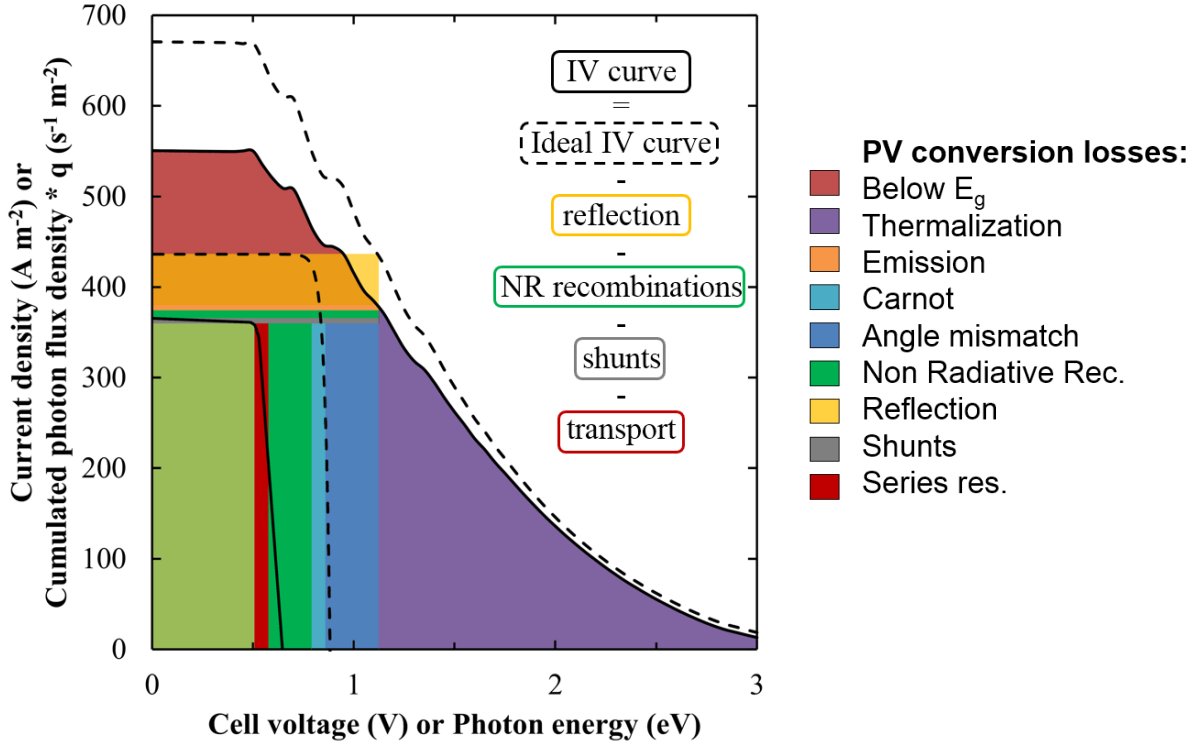


Fig. 21 Conversion loss mechanisms of a c-Si cell at MPP. Cumulated photon flux density of the AM1.5 spectrum (dashed line), of the transmitted fraction of this incident radiation perpendicularly through a planar c-Si surface (solid line). Ideal J-V characteristic (dashed line) and J-V characteristic of a c-Si PV cell with a planar surface (solid line). Adapted from (Dupré, Vaillon & Green 2015b).

Since the PV cell parameters (V_{oc} , J_{sc} , FF) usually vary approximately linearly with temperature, it is possible to separate the temperature sensitivity of the device performance into the sum of their temperature coefficients:

$$P_{\max}(T_c) = V_{oc}(T_c) J_{sc}(T_c) FF(T_c) \quad (51)$$

$$\beta_{P_{\max}} = \beta_{V_{oc}} + \beta_{J_{sc}} + \beta_{FF} \quad (52)$$

where P_{\max} is the maximum power by unit area. This is particularly interesting because these different TCs depend on different loss mechanisms.

4.1. Open-circuit voltage temperature sensitivity

The temperature sensitivity of open-circuit voltage is of particular importance since it accounts for 80-90% of the overall temperature sensitivity for reasonably good solar cells (Green 2003).

The open-circuit voltage of a solar cell corresponds to the state where the total rate of photogeneration equals that of recombination so that no current circulates through the circuit. Its relative change with temperature, $\beta_{V_{oc}}$, is thus an indication of the temperature dependence of the generation-recombination balance. The photogeneration rate is a function of incident spectrum, concentration, reflection, transmission and parasitic absorption³⁸. The recombination rate depends on the different recombination processes (radiative, SRH, Auger, surface, shunts).

Recognizing that every recombination mechanism is a function of the product of the local hole and electron concentrations np , Green derived a general expression for the temperature sensitivity of V_{oc} (Eq. 13 in (Green 2003)). This formula, derived from the basis of internal device physics, is always valid but requires the detailed knowledge of the recombination mechanisms in the cell of interest. On the other hand, Braun et al. proposed an approximate formulation for dV_{oc}/dT in the radiative limit for concentrator solar cells (Eq. 7 in (Braun, Katz & Gordon 2012)). We show in the following that dV_{oc}/dT can be written more simply in a form similar to the general expression derived by Green and propose an extension, eq. (57) with eq. (54) and eq. (58), that goes beyond the radiative limit by using the concept of External Radiative Efficiency (ERE). The ERE of a PV cell is similar to the External Quantum Efficiency (EQE) of a Light-Emitting Diode (LED). It is defined in (Green 2012) as “the fraction of the total dark current recombination in the device that results in radiative emission from the device”³⁹. We propose in the following

³⁸ Parasitic absorption corresponds to the absorption of potentially useful photons ($E \geq E_g$) by the lattice or by free carriers. These absorption mechanisms result in the generation of heat and no electron-hole pair.

³⁹ Note that ERE is different from the ratio of radiative recombination rate on total recombination rate (this is the internal radiative efficiency IRE) because of photon recycling (all the photons emitted through radiative recombinations do not directly exit the cell).

to express the open-circuit voltage temperature coefficient as a function of the external radiative efficiency.

From the definition of the ERE, the output current and the open-circuit voltage of the cell can be written as:

$$J = X J_{sc,1sun} - \frac{1}{ERE} J_{0,rad} \left(\exp\left(\frac{qV}{kT_c}\right) - 1 \right) \approx X J_{sc,1sun} - \frac{1}{ERE} J_{0,rad} \exp\left(\frac{qV}{kT_c}\right) \quad (53)$$

$$V_{oc} = \frac{kT_c}{q} \ln\left(\frac{X J_{sc,1sun}}{(1/ERE_{oc}) J_{0,rad}}\right) = V_{oc,1sun} + \frac{kT_c}{q} (\ln(ERE_{oc}) + \ln(X)) \quad (54)$$

Transport resistances are neglected, ERE_{oc} is the ERE at open-circuit, X is the concentration factor and $J_{0,rad}$ is the dark current density in the radiative limit. Writing $X J_{sc,1sun}$ instead of J_{sc} means that we assume a linear behavior between J_{sc} and the concentration factor X . This assumption can fail if an important loss mechanism in short-circuit has a significant intensity dependence. Using the same approximations as for eq. (35), we get:

$$J_{0,rad} \approx q \frac{2\Omega_{emit}}{c^2 h^3} k T_c E_g^2 \exp\left(-\frac{E_g}{k T_c}\right) \quad (55)$$

Assuming a linear variation of E_g on the temperature range of interest, i.e. $dE_g/dT = \text{cste}$, we use:

$$E_g = E_{g0} + T \frac{dE_g}{dT} \quad (56)$$

By differentiating eq. (54), the temperature dependence of V_{oc} becomes:

$$\frac{dV_{oc}}{dT_c} = -\frac{\frac{E_{g0}}{q} - V_{oc} + \gamma \frac{kT_c}{q}}{T_c} \quad (57)$$

with:

$$\gamma = 1 - \frac{d \ln ERE_{oc}}{d \ln T_c} + \left(2 \frac{d \ln E_g}{d \ln T_c} - \frac{d \ln J_{sc,1sun}}{d \ln T_c} \right) \quad (58)$$

Eq. (57) predicts a temperature coefficient of the open-circuit voltage approximately constant over the range of temperature typical of solar cell operation (Green 2003). Eq. (57) is the same as eq. 5.8 in (Green 1982), but the coefficient γ is explicitly quantified

in eq. (58). As previously mentioned in (Green, Blakers & Osterwald 1985), γ corresponds now explicitly to the temperature sensitivity of the mechanisms determining V_{oc} . The absolute value of the terms in parentheses in eq. (58) (considering bandgap temperature dependence and the ideal short-circuit current, cf section 4.2) is less than 0.5 for all the semiconductors considered here. Thus, it is $1 - \frac{d \ln ERE_{oc}}{d \ln T_c}$ (quite similar to the term $\gamma \frac{f}{\xi} \frac{d\xi}{df}$ in (Green 2003)) that plays a major role in the value of γ . The temperature dependence of the ERE depends on the recombination mechanisms within the cell so the parameter γ contains information on the dominant recombination processes. To illustrate this idea, let us analyse two situations where the saturation current is dominated by different recombination mechanisms (inspired by (Siefer & Bett 2012)). The starting point is the single-diode model as in eq. (53), but using the diode ideality factor, n , and the dark saturation current density J_0 (instead of ERE and $J_{0,rad}$). This gives:

$$J = J_{sc} - J_0 \left(\exp\left(\frac{qV}{nkT_c}\right) - 1 \right) \approx J_{sc} - J_0 \exp\left(\frac{qV}{nkT_c}\right) \quad (59)$$

The open-circuit voltage then reads:

$$V_{oc} \approx \frac{nkT}{q} \ln\left(\frac{J_{sc}}{J_0}\right) \quad (60)$$

The dark saturation current density (J_0) depends on a variety of parameters that depend on the cell temperature (see appendix 10.2 or (Friedman 1996)).

- Scenario 1: the dominant recombination mechanism is recombination through defects (Shockley-Read-Hall) in the bulk regions and at the surfaces. In this case, recombination rates are only limited by minority carrier concentration and the ideality factor is equal to one. The dark saturation current density can be written as (Green 1982):

$$J_{01} = q \left(\frac{D_e}{L_e} \frac{1}{N_A} F_P + \frac{D_h}{L_h} \frac{1}{N_D} F_N \right) n_i^2 \quad (61)$$

where F_P and F_N are factors that account for the finite dimensions of the P and N regions respectively (and are thus function of the surface recombination velocities). $D_{e,h}$ and $L_{e,h}$ are the diffusion coefficients and the diffusion lengths of the electrons and holes. $N_{A,D}$ are the doping concentration of acceptors and donors and n_i is the

intrinsic carrier concentration. If we neglect the temperature dependence of $\frac{D_e}{L_e} F_p$

and $\frac{D_h}{L_h} F_N$, the temperature dependence of J_0 comes only from n_i^2 . The square of

the intrinsic carrier concentration reads (Sze & Ng 1981):

$$n_i^2 = N_c N_v \exp(-E_g / kT_c) = 4(2\pi k T_c / h^2)^3 (m_e m_h^*)^{3/2} \exp(-E_g / kT_c) \quad (62)$$

Neglecting the temperature dependence of the electron and hole effective masses $m_e^* m_h^*$, it follows that:

$$n_i^2 \propto T_c^3 \exp(-E_g(T_c) / kT_c) \quad (63)$$

Thus:

$$J_{01} \propto C_1 T_c^3 \exp\left(-\frac{E_g(T_c)}{kT_c}\right) \quad (64)$$

where C_1 is a parameter that does not depend on temperature.

Using eq. (64) in the derivation of eq. (60), we get:

$$\frac{dV_{oc}}{dT_c} = -\frac{\frac{E_{g0}}{q} - V_{oc} + \frac{kT_c}{q} \left(3 - \frac{d \ln J_{sc}}{d \ln T_c}\right)}{T_c} \quad (65)$$

Eq. (65) corresponds to eq. (57) with $\gamma = 3 - \frac{d \ln J_{sc}}{d \ln T_c} \approx 3$

- Scenario 2: the dominant recombination mechanism is recombination through defects (Shockley-Read-Hall) in the depletion zone. In this case, the recombination rate is limited by both minority and majority carrier concentrations and the ideality factor is equal to two. The dark saturation current density can be written as (Siefer & Bett 2012):

$$J_{02} = \frac{n_i W_d k T_c}{2(V_d - V) \tau_{n0}} \quad (66)$$

where W_d is the width of the depletion zone, V_d is the diffusion voltage also known as built-in voltage and τ_{n0} is the minimum electron lifetime. Neglecting the temperature dependence of these parameters and using eq. (63), we get:

$$J_{02} \propto C_2 T_c^{2.5} \exp\left(-\frac{E_g(T_c)}{2kT_c}\right) \quad (67)$$

where C_2 is a parameter not depending on temperature.

Using eq. (67) in the derivation of eq. (60), we obtain:

$$\frac{dV_{oc}}{dT_c} = -\frac{\frac{E_{g0}}{q} - V_{oc} + \frac{kT_c}{q} \left(5 - 2 \frac{d \ln J_{sc}}{d \ln T_c}\right)}{T_c} \quad (68)$$

Eq. (68) corresponds to eq. (57) with $\gamma = 5 - 2 \frac{d \ln J_{sc}}{d \ln T_c} \approx 5$

Of course, there exist other recombination mechanisms that have different temperature dependences such as Auger or radiative recombination (see section 3.3). For crystalline silicon in the radiative limit ($ERE=1$), eq. (58) gives $\gamma \approx 1.2$ (see section 5.3). Also, it is possible that in some cases, the assumptions that have been made in the two scenarios presented above (neglecting the temperature dependence of the carrier lifetime or the surface recombination velocity for example) do not hold, leading to different values for γ . Besides, several mechanisms with different temperature and voltage dependences can participate to the global recombination rate. In this case, the J-V characteristic has to be modeled with a double (or more) diode model and it becomes complicated to obtain an analytical expression of dV_{oc}/dT_c as we have done above. However, Grover et al. showed that is possible to use a formulation different from the diode model in order to separate between different recombination pathways (by looking at the intensity and the temperature dependence of the open-circuit voltage) (Grover et al. 2013). Quite similarly to Green in (Green 2003), Grover et al. expressed the recombination rates and the open-circuit voltage as a function of a parameter closely related to the np product. Then, using the fact that the total generation rate in the cell is equal to the recombination rate at open-circuit, they expressed the open-circuit voltage as a function of parameters proportional to the different recombination mechanisms:

$$V_{oc} = 2 \frac{kT_c}{q} \ln \left[k_1 (\sqrt{1 + k_2 G_{avg}} - 1) \right] \quad (69)$$

where:

$$k_1 = \frac{R_0^d}{2(R_0^l + R_0^b)}; \quad k_2 = 4W \frac{(R_0^l + R_0^b)}{(R_0^d)^2} \quad (70)$$

where R_0^b , R_0^d and R_0^l are parameters that give the strength of the recombination mechanisms (respectively in the bulk, the depletion region and at the interfaces) independent of bias conditions. These parameters R_0 carry the same physical meaning as the parameters usually denoted J_0 in the diode models. G_{avg} corresponds to the average generation rate in the cell and W to the cell thickness.

Grover and Li derived a new expression of $\frac{dV_{oc}}{dT_c}$ based on their reformulation of the open-circuit voltage and were able to extract valuable informations on device physics from experimental measurements of open-circuit voltage temperature coefficient of Cu(InGa)Se₂ solar cells (Grover & Li 2015). It might be interesting, in a future work, to use this alternative approach to give a quantitative evaluation of the recombinations in different regions of “standard” homo-junction crystalline silicon cells.

Let us now come back to the analysis of the proposed expression of β_{Voc} as a function of the external radiative efficiency (eq. (57) with eqs. (54) and (58)). In eq. (57), the most important term in dV_{oc}/dT_c and thus in β_{Voc} is $E_{g0}/q - V_{oc}$. However the term $\gamma kT_c/q$ is non-negligible in the determination of β_{Voc} . For example, it accounts for between 0 and 10% of β_{Voc} for the cells described in (Green, Emery & Blakers 1982; Green, Blakers & Osterwald 1985; Zhao et al. 1994).

Making the rough approximations of neglecting the ERE and the bandgap temperature dependences (i.e. setting $\gamma=0$), we show in Fig. 22 approximated temperature coefficients as a function of cell bandgap for different EREs. This gives an idea of the evolution of TCs as cells improve towards the radiative limit. For illustration, crosses show experimental values of β_{Voc} for record-efficiency crystalline silicon cells over the years. Diamonds show values measured on cells made of GaAs, GaSb and Ge (Siefer et al. 2005). One should not deduce ERE values directly from this graph because the approximations used can have an important impact on β_{Voc} . This is illustrated in Fig. 23 where β_{Voc} is calculated with different temperature dependences of the ERE and the bandgap. One can observe that different values of γ , i.e. different values of $dERE/dT$ due to differences in dominant recombination mechanisms, lead to significant variations of β_{Voc} . Thus the

knowledge of the ERE at 25°C alone is not sufficient to accurately predict β_{Voc} . In section 5, we will compare the different terms of this theoretical formulation to the results of experimental measurements on crystalline silicon cells.

In Fig. 23 we also find that, in opposition to a conclusion derived elsewhere (Braun, Katz & Gordon 2012), dE_g/dT has an important impact on β_{Voc} . To illustrate this, if we assume that $\gamma=1$, the open-circuit voltage temperature coefficients of CsSnI₃ and InP are respectively -583 and -1320 ppm K⁻¹ while their bandgaps at 25°C are similar (1.316 and 1.309 eV respectively). However, their overall TCs are not so far apart (Fig. 15) because the short-circuit current TC of InP is positive while that of CsSnI₃ is negative owing to the unusual behavior of its bandgap.

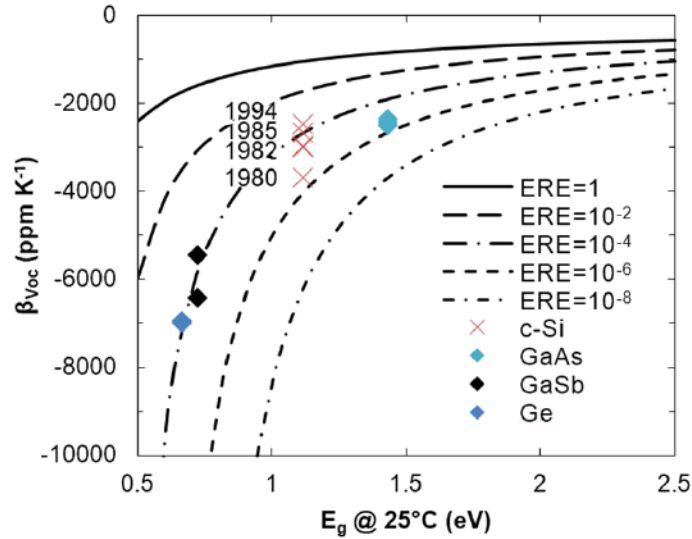


Fig. 22 Temperature coefficient of open-circuit voltage as a function of bandgap for different values of external radiative efficiency. dE_g/dT and $dERE/dT$ were neglected in the calculation (their importance can be observed in Fig. (23)). The crosses are experimental values of β_{Voc} for some record-efficiency c-Si cells over the years (Green, Emery & Blakers 1982; Green, Blakers & Osterwald 1985; Zhao et al. 1994). The diamonds are experimental values of β_{Voc} for GaAs, GaSb and Ge cells (Siefer et al. 2005). Figure adapted from (Dupré, Vaillon & Green 2015b).

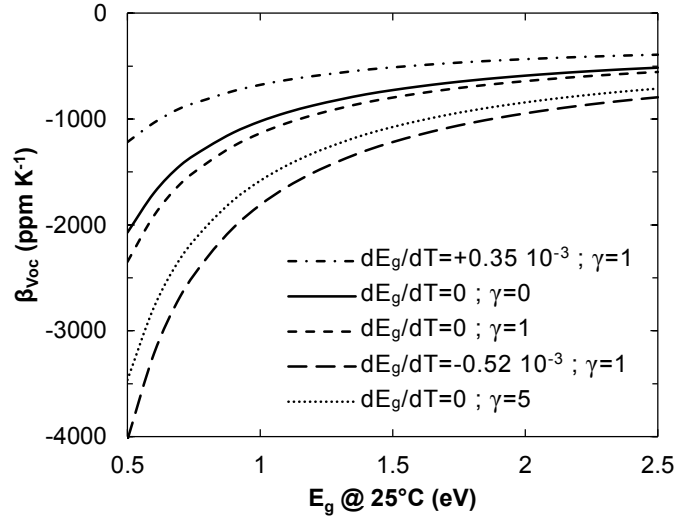


Fig. 23 Temperature coefficient of open-circuit voltage as a function of bandgap for $ERE=1$ and different values of dE_g/dT and γ . Figure from (Dupré, Vaillon & Green 2015b).

In this section, we have proposed and analysed an expression of the temperature coefficient of the open-circuit voltage as a function of the external radiative efficiency. The relation between β_{Voc} and the internal device physics has been illustrated through different scenarios. In the following section, we will investigate in detail an existing theoretical expression of short-circuit current density temperature coefficient.

4.2. Short-circuit current temperature sensitivity

Since most semiconductor bandgaps decrease with temperature (Fig. 13), the short-circuit current density J_{sc} generally increases with temperature. J_{sc} can be expressed as the product of an ideal short-circuit current density $J_{sc,1sun}$ and a collection fraction f_c (Green 2003) and potentially a concentration factor X :

$$J_{sc} = J_{sc,1sun} X f_c \quad (71)$$

The ideal short-circuit current density is determined by the photon flux density (PFD) of the incident radiation and the cell bandgap and its temperature dependence:

$$J_{sc,1sun} = q \int_{E_g(T_c)}^{\infty} PFD(E) dE \quad (72)$$

As in (Green 2003), the temperature coefficient of the short-circuit current can be written as:

$$\beta_{J_{sc}} = \frac{1}{J_{sc}} \frac{dJ_{sc}}{dT_c} = \frac{1}{J_{sc,1sun}} \frac{dJ_{sc,1sun}}{dE_g} \frac{dE_g}{dT_c} + \frac{1}{f_c} \frac{df_c}{dT_c} \quad (73)$$

The collection fraction is the fraction of potentially useful photons ($E \geq E_g$) that excites a carrier that gets collected in short-circuit. It accounts for optical losses such as reflection, insufficient or parasitic absorption as well as electrical losses such as bulk or surface recombination. It can be expressed as:

$$f_c(T) = \frac{J_{sc}(T)}{J_{sc,1sun}(T)} = \frac{q \int_0^{\infty} EQE(E) PFD(E) dE}{q \int_{E_g(T_c)}^{\infty} PFD(E) dE} \quad (74)$$

where PFD is the incoming photon flux density.

It is worth noticing that the variation with temperature of the collection fraction is expected to differ between direct and indirect bandgap materials because phonons play a notable role in the interband absorption of the latter. This point will be discussed in detail in section 5.2. Similarly to concentration, the effect of non-ideal absorption can easily be included in eqs. (54) and (57) through the collection fraction f_c . However, in practice, its impact on $\beta_{V_{oc}}$ is limited and thus has not been included in the previous section. For example, if a cell collection fraction increased from 60% to 80%, it would only cause a 2.6% change in the temperature coefficient of its open-circuit voltage.

Eqs. (72) and (73) indicate that $\beta_{J_{sc}}$ depends on the incident spectral intensity at wavelengths near the bandgap. Fig. 24 shows the photon flux density of the reference AM1.5 spectrum (IEC 2008) and that of a solar simulator (Emery 2008) together with the bandgaps of several semiconductors at 0 and 100°C. While the average intensity of the solar simulator is close to that of the reference spectrum, the photon flux density is quite different. As previously noted in (Landis 1994), this explains the scattering of $\beta_{J_{sc}}$ values found in the literature. Even for indoor measurements, the spectral intensity distributions vary because of differences between solar simulators (even of the same type). This stresses the complexity of accurately predicting $\beta_{J_{sc}}$ under real operating conditions, where the incident spectrum changes over time.

Fig. 24 shows that some semiconductor bandgaps lie near important fluctuations in the the AM1.5 photon flux density caused by the atmosphere absorption. This induces non-linearity in the temperature dependence of the ideal short-circuit current density ($J_{sc,1sun}$). This is illustrated for crystalline silicon cells in Fig. 25. One can observe that the temperature coefficient of the short-circuit current density (full black line) varies by 37% between 0 and 100°C. This variation can be related to the photon flux density fluctuations. To represent the local variations of $J_{sc,1sun}$, a local temperature coefficient ($\beta_{G,loc}$) is defined (in ppm K⁻¹) as:

$$\beta_{G,loc}(T_c) = \frac{10^6}{G(298.15K)} \frac{G(T_c + 1) - G(T_c - 1)}{2} \quad (75)$$

It is apparent in Fig. 25 that the local variations of the ideal short-circuit current density (dashed black line) are proportional to the local variations of the PFD (blue line). This figure demonstrates the impact of the photon flux density on the temperature coefficient of the short-circuit current density.

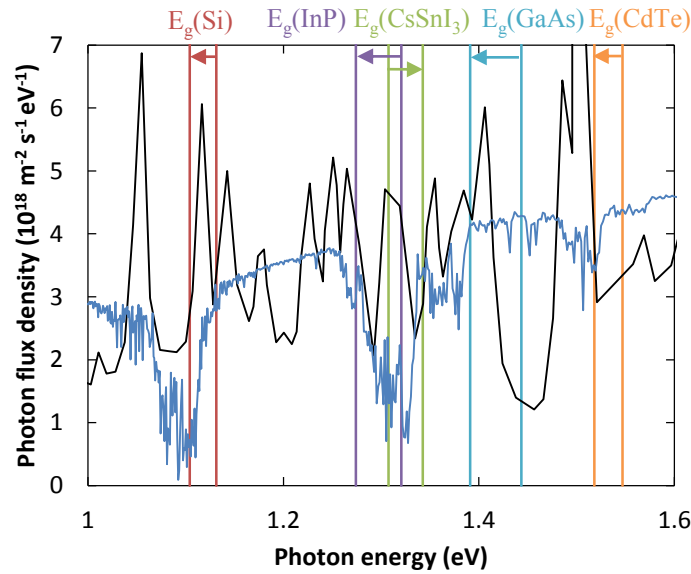


Fig. 24 Photon flux density of the AM1.5 reference spectrum (in blue), of a solar simulator (Emery 2008) (in black). Bandgaps of different semiconductors at 0 and 100 °C; arrows show the direction of increasing temperature. Figure from (Dupré et al. 2015).

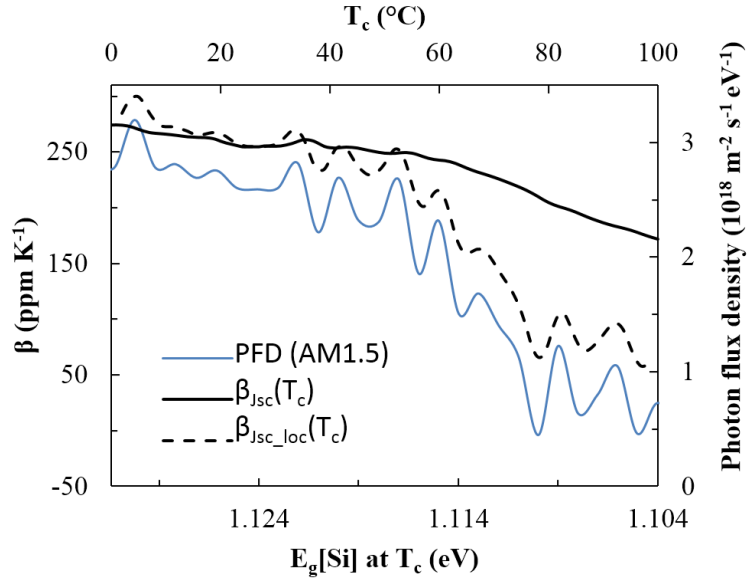


Fig. 25 Global (solid black line) and local (dotted black line) temperature coefficients of the short-circuit current density of a *c*-Si cell with ideal light collection ($f_c = 1$). Photon flux density of the AM1.5 reference spectrum (blue line). Figure from (Dupré et al. 2015).

In this section, it has been highlighted that the temperature coefficient of the short-circuit current density fundamentally depends upon the spectrum of the incident light and the temperature dependence of the bandgap of the absorbing material. Also, β_{Jsc} is function of the temperature dependence of the collection fraction of the device. In section 5.2 it will be shown that this effect dominates the temperature behavior of the short-circuit current of certain devices. The theoretical expression described above is interesting in that it enables to separate material related effects (the first summand in eq. (73)) from device related effects (second summand in eq. (73)). In the following section, we will discuss the loss mechanisms that can impact the temperature coefficient of the fill factor.

4.3. Fill factor temperature sensitivity

The fill factor (FF) relates the maximum power that can be extracted from a cell to the product of its open-circuit voltage (V_{oc}) and short-circuit current (I_{sc}). It indicates the minimal “cost” of extracting the photogenerated charges from the cell into the circuit and corresponds to the optimal current/voltage trade-off. This optimum depends on the generation-recombination balance (similarly to V_{oc}) but also on the transport losses associated to the current flow through the circuit at the maximum power point (MPP).

This somewhat appears in the terms of the expression derived for crystalline silicon cells in (Zhao et al. 1994)⁴⁰:

$$\frac{1}{FF} \frac{dFF}{dT_c} = (1 - 1.02 FF_0) \left(\frac{1}{V_{oc}} \frac{dV_{oc}}{dT_c} - \frac{1}{T_c} \right) - \frac{R_s}{V_{oc} / I_{sc} - R_s} \left(\frac{1}{R_s} \frac{dR_s}{dT_c} \right) \quad (76)$$

with:

$$FF_0 = \frac{v_{oc} - \ln(v_{oc} + 0.72)}{v_{oc} + 1} \quad (77)$$

and:

$$v_{oc} = \frac{nkT_c}{q} V_{oc} \quad (78)$$

FF_0 , R_s , and n , are respectively the ideal fill factor, the cell series resistance and the diode ideality factor. For good quality crystalline silicon cells (small R_s), β_{FF} is mainly function of $\beta_{V_{oc}}$ and can be described by a simpler expression (Green 2003):

$$\frac{1}{FF_0} \frac{dFF_0}{dT_c} = (1 - 1.02 FF_0) \left(\frac{1}{V_{oc}} \frac{dV_{oc}}{dT_c} - \frac{1}{T_c} \right) \quad (79)$$

This simpler expression was derived using the fill factor expression from (Green 1981), eq. (77), and assuming that the ideality factor and the series and shunt resistances do not vary significantly with temperature. It is important to emphasize that the fill factor expression given by eq. (77) is accurate only when both series and shunt resistances have a negligible impact on cell performance (Green 1981). Also, it should be noted that the expression proposed by Zhao et al., eq. (79), was derived using another fill factor expression from (Green 1981) that describes the case where the series resistance is important but the shunt resistance is so large as to have a negligible effect:

$$FF_s = FF_0 \left(1 - \frac{R_s}{V_{oc} / I_{sc}} \right) \quad (80)$$

In section 5.4, we will assess the range of validity of these different expressions with experimental data for c-Si cells.

⁴⁰ Eq. (76) is derived based upon eq. (2) in (Green, Emery & Blakers 1982) and eq. (5) in (Green 1981).

In technologies less-developed than crystalline silicon, the fill factor temperature sensitivity can be more complex. For example, in some amorphous silicon and nanocrystalline dye cells, the fill factor increases with temperature due to decreasing resistance effects or increasing "mobility-lifetime" products (Green 2003). It is worth noticing that resistance effects are expected to increase with irradiance as the current circulating through the cell increases (Helmers, Schachtner & Bett 2013).

A recent article (Deceglie et al. 2014) gave a concrete example of the complexity of fill factor temperature sensitivity. The temperature coefficient of the fill factor of some CIGS modules was found to be increased after light soaking. It was suggested that this is due to a light induced reduction in the conduction band offset between the buffer and the absorber. Since the charge transfer mechanism across this barrier (thermionic emission) is enhanced at high temperature (Sze & Ng 1981) p. 227, this metastable change could explain the observed variation of β_{FF} . The hypothesis can be stated in other terms: the decrease of interface resistance with temperature depends upon the barrier height the carriers have to go through. Light soaking modifies this barrier height and thus impact the temperature coefficient of the fill factor. This understanding is important because it is the final light soaked temperature coefficients that need to be known in order to model field performances.

This section has illustrated the complex temperature behavior of the fill factor. Its temperature coefficient depends on the generation-recombination balance at maximum power point (where there is current flowing in the device).

The following chapter compares experimental results of crystalline silicon cells to the theoretical expressions introduced previously.

5. Experimental assessment of temperature coefficient theories for crystalline silicon solar cells

This section reports on experimental measurements aimed at assessing the theoretical expressions of temperature coefficients described in the previous section in the case of crystalline silicon solar cells. The relevance of the relation presented previously between the temperature dependence of open-circuit voltage and the external radiative efficiency of photovoltaic devices will be demonstrated. We will show that cells made of indirect bandgap semiconductors with small collection fraction have unusual temperature sensitivities of short-circuit current and open-circuit voltage. Additionally, we will provide some explanations for the observed discrepancies between predicted and measured temperature coefficients of fill factor. Finally, two brief analyses of the specific temperature coefficients of cells made of compensated silicon and of silicon heterojunction cells will be presented.

5.1. Details on the experimental measurements

Six crystalline silicon cells fabricated at the Australian Centre for Advanced Photovoltaics (ACAP, UNSW, Sydney, Australia) were investigated⁴¹. These 4 cm² square cells were made from <100> oriented, 1Ω-cm, p-type, Float-Zone Silicon (FZ-Si) wafers with different thicknesses (200, 380 and 450 μm). A schematic of these cells is presented in Fig. 26. All these cells are textured with inverted pyramids. They are passivated with a thin SiO₂ layer (≈20 nm) and have a double layer anti-reflection coating (ZnS and MgF₂). The active areas and localized heavy doped areas under the front and rear contacts have a sheet resistivity of about 150-200 and about 20 ohm/square respectively. The heavy Phosphorous diffused area covers about 3 % of the active area and the front contacts are

⁴¹ The cells were provided by Dr. Hamid Mehrvarz, to whom we are thankful.

made of stacks of Ti/Pd/Ag. The heavy Boron diffused area covers around 1-2 % of the rear side and the rear contacts are made of stacks of Al/Ti/Pd/Ag. The cells were sintered at 400 °C for 30 minutes in forming gas ambient.

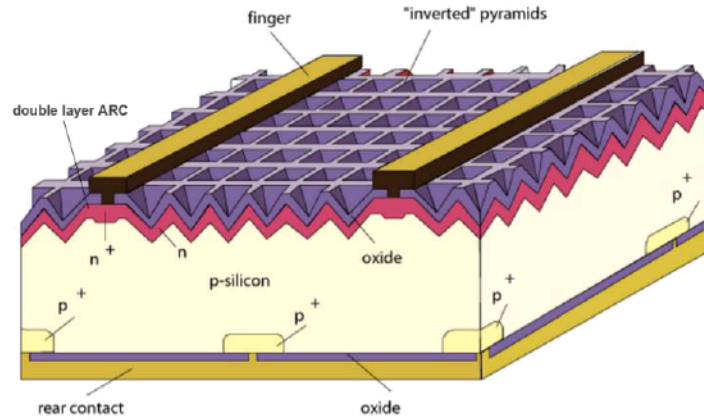


Fig. 26 Schematic of a passivated emitter with rear locally diffused (PERL) cell. Figure adapted from (Zhao et al. 1994).

The solar simulator used in this work consists of a set of ELH lamps. Its spectral photon flux density is plotted in Fig. 32. Its intensity was set to produce the same J_{sc} for a reference cell as the standard AM1.5 illumination (1000 W m^{-2}).

Illuminated J-V characteristics and EQE were measured at different temperatures between 15 and 70 °C. Fig. 27a shows the J-V characteristics of these cells at 25 °C and Fig. 27b shows their EQE at 25°C. The illuminated J-V characteristics of cell #6 at different temperatures are plotted in Fig. 28 for illustration.

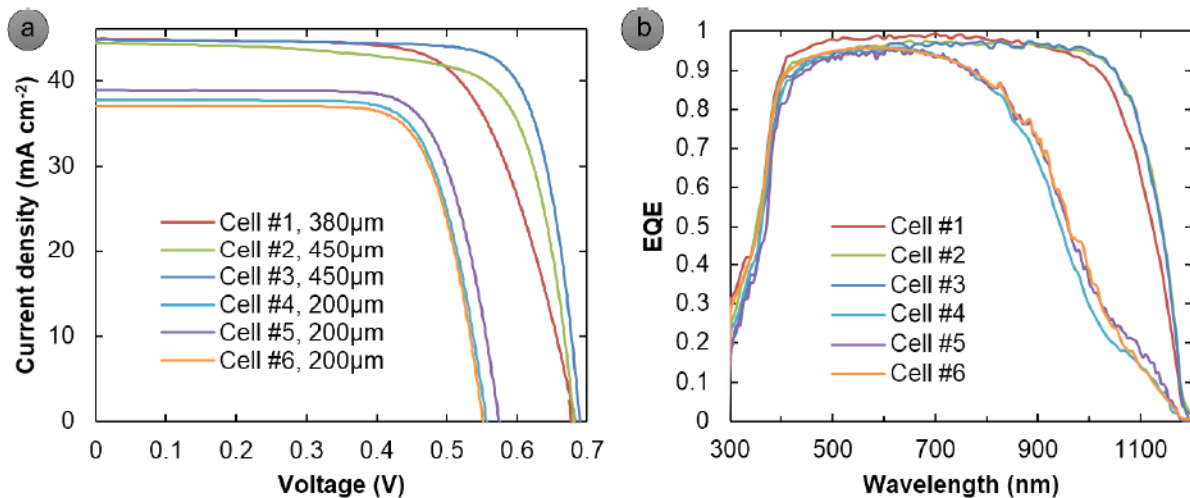


Fig. 27 Measurements results on the c-Si cells studied at UNSW at 25°C. a. Illuminated J-V characteristics; b. External Quantum Efficiencies.

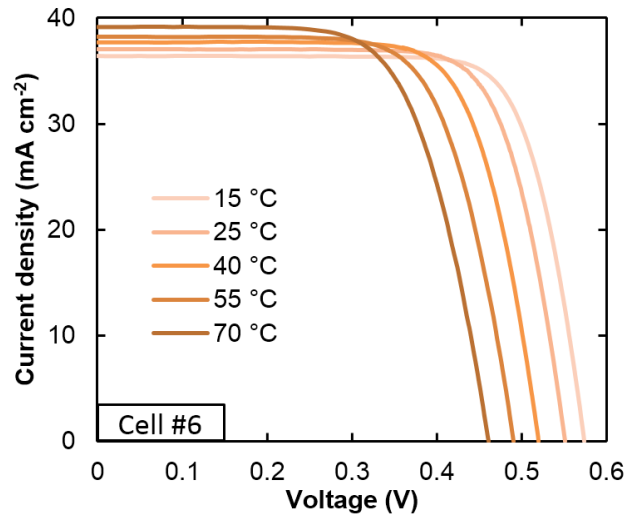


Fig. 28 Illuminated J-V characteristics of cell #6 at different temperatures between 15 and 70 °C.

Fig. 27 illustrates that the cells have notable differences. This could seem surprising as the cells have been fabricated using the same process. However, we did not pick the cells from the same batch and purposefully choose cells that had different rated efficiencies at 25°C (see Fig. 29a). The large shift visible in Fig. 27 between the cells #1, #2 and #3 and the cells #4, #5 and #6 is partly attributed to the differences in cell thickness (450 and 380 μm versus to 200 μm). The shapes of the EQE of cells #4, #5 and #6 also suggest that they suffer from high recombination velocities on their rear surfaces. This might have been caused by some error in the passivation process. The rest of the differences between the cells (relatively small shunt resistances of cell #2, large series resistances of cell #1, ...) are in the normal range of variations observed from batch to batch.

Fig. 29 shows some of the cells' important parameters (maximum power, open-circuit voltage, short-circuit current density and fill factor) as a function of temperature. A linear regression analysis shows that all these cell parameters vary linearly with temperature. The normalized temperature coefficients used in the following are extracted from these data.

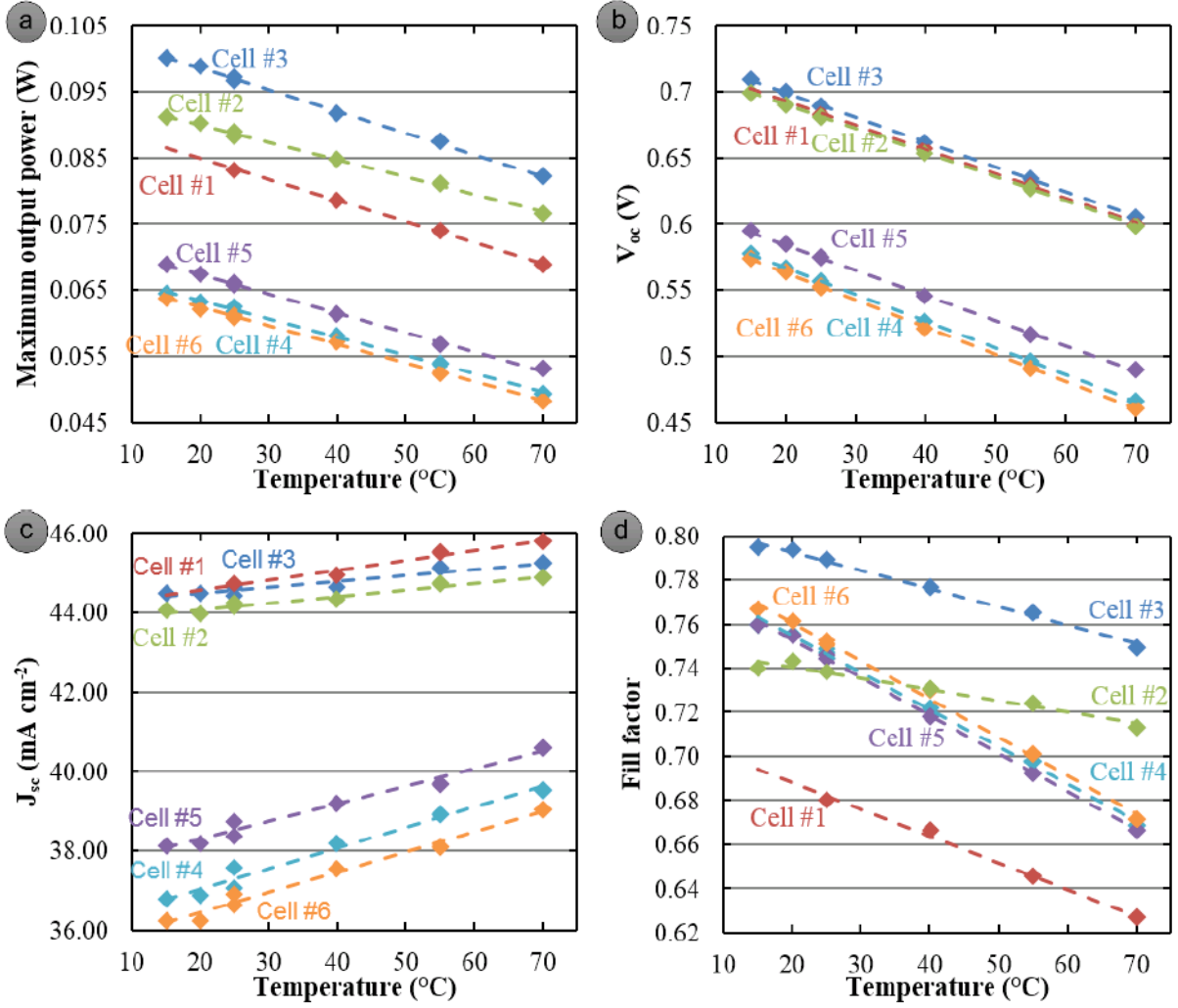


Fig. 29 a. Maximum output power; b. open-circuit voltage; c. short-circuit current density; d. fill factor of the c-Si cells studied at UNSW, plotted as a function of temperature.

The light J-V characteristics were also used to extract for each cell the best fitting parameters of a single-diode model (Chan & Phang 1987):

$$I = I_L - I_0 \left(\exp \left(\frac{q(V + IR_s)}{kT_c} \right) - 1 \right) - \frac{V + IR_s}{R_{sh}} \quad (81)$$

where I is the current, I_L is the current generated by the incident light, I_0 is the diode saturation current (see appendix 10.2), R_s is the series resistance and R_{sh} is the shunt resistance.

The method used to extract the parameters is described⁴² in (Zhang et al. 2011). However, we did not succeed in getting correct values with the information contained in their supplemental material (there is probably an error somewhere) so we wrote a slightly different Matlab program (detailed in appendix 10.5) which successfully extracts R_s , R_{sh} , n and I_0 from the light J-V data. The results of this method are quite dependent on the initial values of the parameters (Zhang et al. 2011) so we used the five points analytical method (Chan & Phang 1987) to initialize the parameters. The results obtained are close to the initial values given by the independent five points analytical method giving us confidence in the extracted parameters. The extracted parameters at 25°C are reported in Table 2 and their variations with temperature are plotted in Fig. 30. The shunt resistances of Cell #4, #5, #6 do not appear in Fig. 30c because their relative variations are negligible (their values remain around 10 kΩ).

Table 2 Parameters extracted from measured light J-V characteristics

	Cell #1	Cell #2	Cell #3	Cell #4	Cell #5	Cell #6
$R_s @25^\circ\text{C}$ (Ω)	0.40	0.08	0.09	0.25	0.24	0.23
β_{R_s} (ppm K ⁻¹)	920	3090	2160	2010	1490	4770
$n @25^\circ\text{C}$	1.72	1.49	1.26	1.12	1.21	1.12
$R_{sh} @25^\circ\text{C}$ (Ω)	420	60	240	10000	10000	10000
I_0 (A)	$3.4 \cdot 10^{-8}$	$3.1 \cdot 10^{-9}$	$9.6 \cdot 10^{-11}$	$6.0 \cdot 10^{-10}$	$1.4 \cdot 10^{-9}$	$6.8 \cdot 10^{-10}$

⁴² There are two missing parenthesis in Eq. 8 of (Zhang et al. 2011): one should read ...

$$\exp\left(\frac{q}{nkT_c}\left(R_s I_{sc} + \frac{R_{sh} V}{R_{sh} + R_s}\right)\right) \dots$$

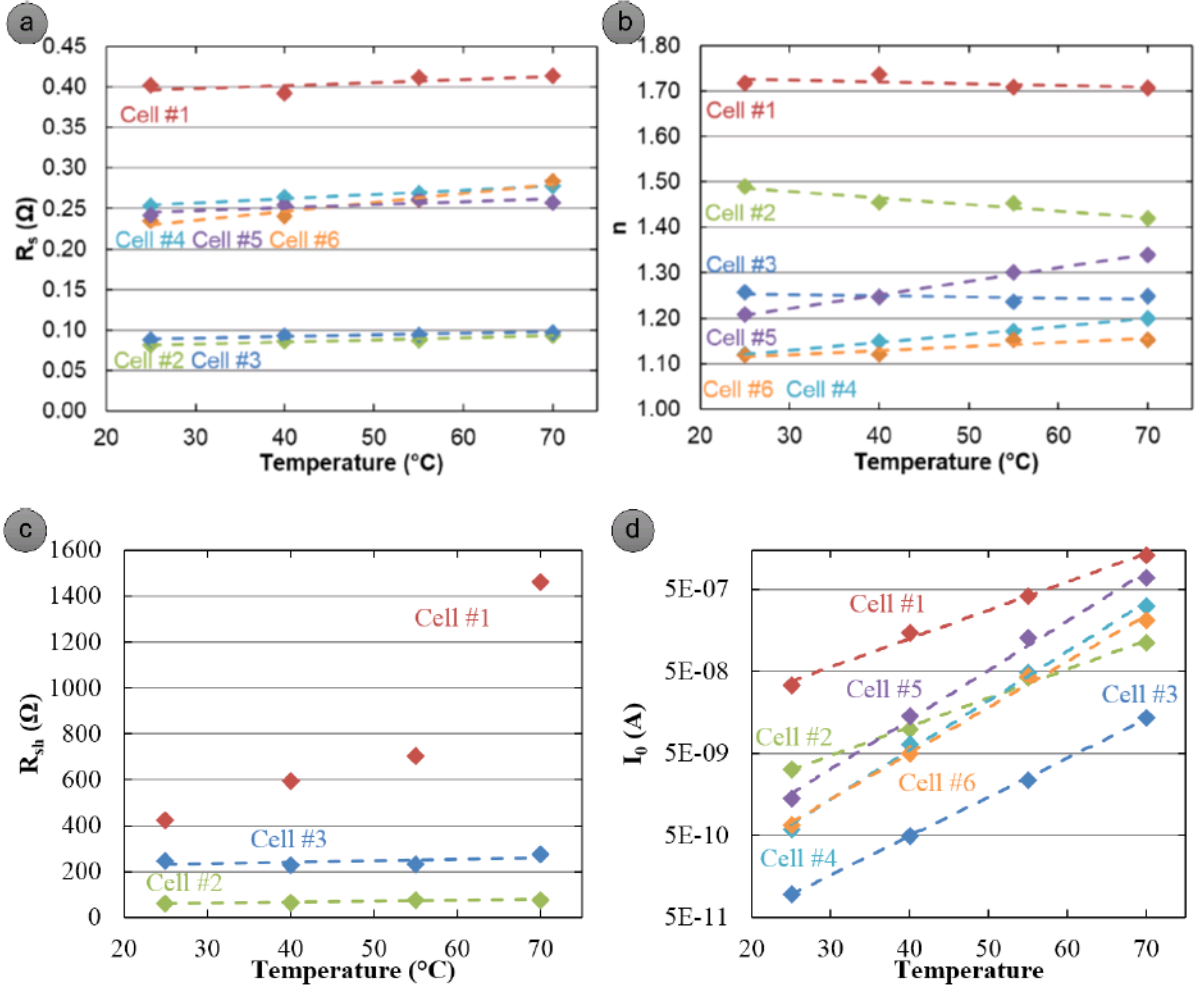


Fig. 30 Single-diode model parameters (extracted from the light J-V characteristics) of the measured UNSW cells as a function of temperature. a. Series resistances. The dashed lines are linear regressions used to calculate the β_{R_s} that are reported in Table 2; b. ideality factors. The dashed lines are linear regressions; c. shunt resistances, that of the cells #4, #5, #6 are not plotted for simplicity, they show negligible relative variations around 10k Ω . The dashed lines are linear regressions; d. diode saturation currents. The dashed lines are exponential regressions.

In the following sections, by using the experimental results, we will assess the importance of the different terms in the theoretical expressions introduced in chapter 4.

5.2. Short-circuit current temperature sensitivity

In this section, we evaluate the different terms in the theoretical expression of the temperature coefficient of the short-circuit current density presented in section 4.2. The associated equations are reminded below:

$$J_{sc} = J_{sc,1sun} X f_c \quad (82)$$

$$J_{sc,1sun} = q \int_{E_g(T_c)}^{\infty} PFD(E) dE \quad (83)$$

$$\beta_{J_{sc}} = \frac{1}{J_{sc}} \frac{dJ_{sc}}{dT_c} = \frac{1}{J_{sc,1sun}} \frac{dJ_{sc,1sun}}{dE_g} \frac{dE_g}{dT_c} + \frac{1}{f_c} \frac{df_c}{dT_c} \quad (84)$$

$$f_c(T) = \frac{J_{sc}(T)}{J_{sc,1sun}(T)} = \frac{q \int_0^{\infty} EQE(E) PFD(E) dE}{q \int_{E_g(T_c)}^{\infty} PFD(E) dE} \quad (85)$$

Fig. 31 shows the measured temperature coefficients of the short-circuit density as a function of the cell thickness together with other experimental results of record silicon solar cells. The green line corresponds to the first summand in eq. (84) (eq. (73)). This first summand is calculated using the bandgap temperature dependence of c-Si⁴³ (Green 1990):

$$E_g[Si] = 1.206 - 2.73 \cdot 10^{-4} T_c \quad (86)$$

and the spectrum of the lamp used for measurements (plotted in Fig. 32). Note that the comparison with literature data (x's in Fig. 31) may be biased because of possible differences in lamp spectra used in the different works. Indeed, we showed in Fig. 25 (page 75) that the temperature coefficient of the short-circuit current is function of the photon flux density around the bandgap energy. All the experimental data are significantly larger than the calculated value (green line). This demonstrates that the 2nd summand in eq. (84) is important for these cells. This means that the collection fractions increase with temperature, which is expected since silicon is an indirect bandgap semiconductor and thus its interband absorption coefficient increases significantly with temperature. This is confirmed by the EQE measurements (the collection fraction is related to the integral of the EQE, see eq. (85)). Indeed, Fig. 32 illustrates these increases in EQE when the temperature increases (from 25 to 40 °C). More interestingly, the difference between

⁴³ We use the up-to-date expression of the bandgap of silicon derived by Green (Green 1990). Some works (Braun, Katz & Gordon 2012; Singh & Ravindra 2012) still make use of that derived earlier by Varshni (Varshni 1967). However, Varshni's expression is outdated and differs significantly from that of Green. The impact on the calculated temperature coefficients is significant (causing for example a difference of about 200 ppm K⁻¹ in the TCs calculated in the radiative limit).

measured and calculated values in Fig. 31 seems to increase with decreasing cell thickness. This is because the relative increase with temperature of collection fraction is larger for cells that have small collection fraction (because they let a substantial portion of the useful photons escape at room temperature (insufficient light trapping) or because they suffer from bulk or back surface recombinations). Indeed, an increased absorption coefficient is especially benefic when it enhances photon absorption or when it reduces recombination. In Fig. 32, the increase of EQE between 25 and 40°C is colored in green for a thin (200 μm) and a thicker (380 μm) cell. In the thinner cell, less of the potentially useful photons are collected at room temperature so the increase of the absorption coefficient with temperature leads to a relatively larger increase of the short-circuit current. In other terms, cells that do not collect most of the useful photons at room temperature benefit relatively more from the increased absorption with temperature which is characteristic of indirect bandgap materials. As shown in Fig. 31, this phenomenon leads to unusually large short-circuit current density temperature coefficients for cells #4, #5 and #6 which are only 200 μm thick. It is worth keeping this fact in mind when dealing with thin cells (with insufficient light trapping) made of indirect bandgap semiconductors. More generally, any loss mechanism that decreases with increasing temperature will lead to favorable temperature coefficients. For example, it was noticed in (Seif et al. 2015) that when carrier transport is made easier with temperature, cells containing layers that impede carrier transport more at room temperature than at larger temperatures benefit from advantageous TCs of their fill factor. This will be detailed in section 5.4.

Also, from the shape of the EQE in Fig. 32, it seems that the thinner cells that we measured suffer from more rear surface recombination. As temperature increases, the absorption coefficient increases and overall the charges are generated further from the rear surface. This mean that rear surface recombination can have a similar effect to that of insufficient light trapping on the temperature coefficient of the short-circuit current. We will present in section 5.6 experimental measurements gathered from the literature that show a clear trend between the short-circuit current and its temperature coefficient: for silicon cells $\beta_{J_{sc}}$ is inversely proportional to J_{sc} . These results show that, for crystalline silicon whose absorption coefficient increases with temperature, the temperature sensitivity is better for cells with lower values of J_{sc} regardless of the limiting physical mechanism.

The cell thickness is not the best parameter to evaluate the importance of the 2nd summand in eq. (84) (even if one only considers optical losses). The mean optical path length

(related to the cell thickness by the light trapping efficiency) would be a more appropriate parameter. However, for cells with similar optical design (ARC, texturation, back reflector...), the cell thickness indicates the portion of usefull light that leaves a cell unabsorbed. Obviously, the impact of cell thickness on $\beta_{J_{sc}}$ will depend on the light trapping scheme of the cells (ARC, texturation, back reflector...). For example, the short-circuit current density temperature coefficient of cells with an excellent light trapping would converge towards the 1st summand in eq. (84) (green line) at lower thickness values than that of cells with poor light trapping.

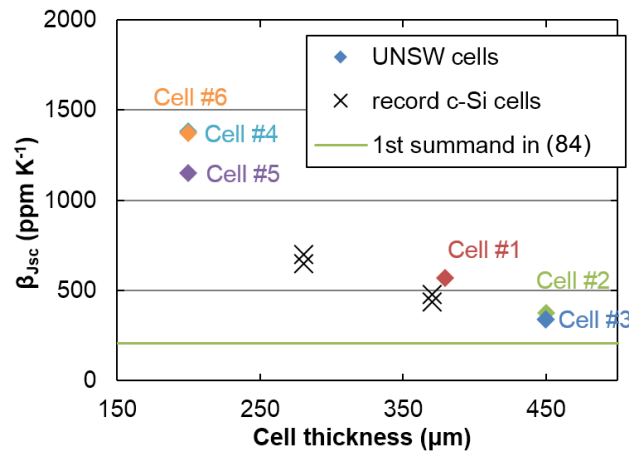


Fig. 31 Experimental temperature coefficients of the short-circuit current density (diamonds and x's) and 1st summand of eq. (84) (green line) plotted as a function of cell thickness. The experimental values of the record c-Si cells are from (Green, Emery & Blakers 1982; Green, Blakers & Osterwald 1985; Zhao et al. 1994). Figure from (Dupré, Vaillon & Green 2015a).

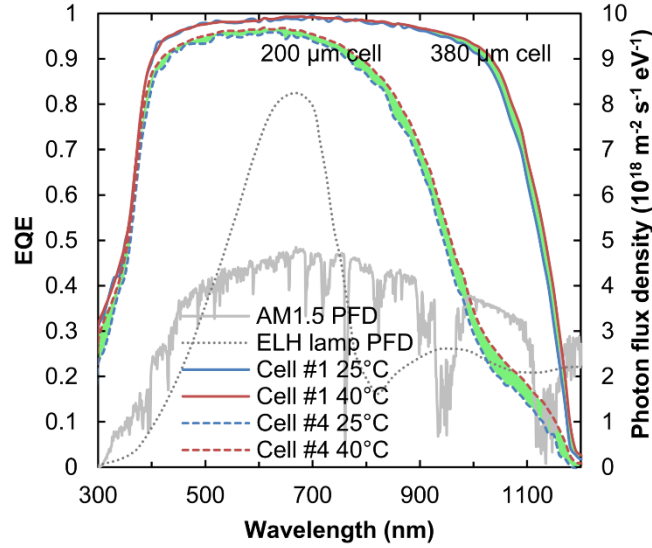


Fig. 32 EQEs at 25 and 40 °C (in blue and red respectively) of a thin cell (#4, dashed lines) a thicker cell (#1, solid lines). The variations of EQE between 25 and 40 °C are colored in green. The AM1.5 (solid line) and the ELH lamp (dotted line) photon flux densities are also plotted (in gray) to highlight the importance of the spectrum considered. Figure from (Dupré, Vaillon & Green 2015a).

In this section, we have argued that the term $\frac{1}{f_c} \frac{df_c}{dT_c}$ is related to optical considerations (absorptivity and its temperature dependence and mean optical path length) and also on the electrical losses in short-circuit (that reduce the collection fraction). All these parameters may impact the temperature coefficient of the short-circuit current.

In the next section, it is the temperature coefficient of the open-circuit voltage that will be investigated. Thus, we will analyse the temperature dependences of the main loss mechanisms in open-circuit configuration.

5.3. Open-circuit voltage temperature sensitivity

In this section, we assess experimentally the expression we have proposed for the temperature coefficient of the open-circuit voltage (eqs. (54), (57) and (58) in section 4.1). We recall the associated equations below:

$$\beta_{V_{oc}} = \frac{1}{V_{oc}} \frac{dV_{oc}}{dT_c} = -\frac{1}{V_{oc}} \frac{\frac{E_{g0} - V_{oc}}{q} + \gamma \frac{kT_c}{q}}{T_c} \quad (87)$$

with:

$$\gamma = 1 - \frac{d \ln ERE_{oc}}{d \ln T_c} + \left(2 \frac{d \ln E_g}{d \ln T_c} - \frac{d \ln J_{sc,1sun}}{d \ln T_c} \right) \quad (88)$$

$$V_{oc} = \frac{kT_c}{q} \ln \left(\frac{X J_{sc,1sun}}{(1/ERE_{oc}) J_{0,rad}} \right) = V_{oc,1sun} + \frac{kT_c}{q} (\ln(ERE_{oc}) + \ln(X)) \quad (89)$$

Practically, ERE_{oc} can be calculated from simple experimental measurements by using the reciprocity relation between External Quantum Efficiency (EQE) and electroluminescent emission of solar cells (Rau 2007)⁴⁴. This relation gives the following expression for the emission current density from a solar cell:

$$J_{em} = q \frac{2\Omega_{emit}}{c^2 h^3} \int_0^\infty \frac{\overline{EQE} E^2}{\exp\left(\frac{E - qV}{kT_c}\right) - 1} dE \quad (90)$$

where \overline{EQE} is the appropriately weighted value over all angles of incident light. For textured cells, it is close to the near perpendicular value of the commonly measured EQE (Green 2012). Using the definition of the ERE, we can write:

$$J = J_{sc} - \frac{1}{ERE} J_{em} \quad (91)$$

This gives in open-circuit condition:

$$ERE_{oc} = \frac{q \frac{2\Omega_{emit}}{c^2 h^3} \int_0^\infty \frac{\overline{EQE} E^2}{\exp\left(\frac{E - qV_{oc}}{kT_c}\right) - 1} dE}{J_{sc}} \quad (92)$$

⁴⁴ In 2007, Rau demonstrated a fundamental relation between the external quantum efficiency of a PV cell and its electroluminescent emission (Rau 2007). The EQE corresponds to the fraction of incident photons that creates a carrier that is collected in short-circuit. Rau showed that this collection fraction (defined under illumination at $V=0$) also corresponds to the fraction of photons that are emitted out of the cell (under a bias and in the dark) compared to the emission rate given by the generalized Planck's equation.

Fig. 33 shows measurements together with theoretical predictions (green lines) of open-circuit voltage temperature coefficients. The experimental data include the cells measured at UNSW, reported values for record silicon solar cells (between 1980 and 1994 (Green, Emery & Blakers 1982; Green, Blakers & Osterwald 1985; Zhao et al. 1994)) and reported values for commercial silicon cells fabricated with different processes and from different wafer types (Ponce-Alcántara et al. 2014). The theoretical value of 1.2 for γ (used to plot the solid green line) is calculated from eq. (88) with the bandgap temperature dependence of c-Si⁴⁵ (Green 1990), the spectrum of the lamp used for the measurements (note that a similar value of γ is found with the AM1.5 spectrum because the term $\frac{d \ln J_{sc, \text{sun}}}{d \ln T_c}$ is really small in both cases) and assuming that ERE_{oc} does not vary with temperature (i.e. neglecting the 2nd summand in eq. (88)). In Fig. 33, we observe that the measured $\beta_{V_{oc}}$ are in quite good agreement with the theory and especially for the cells with large V_{oc} (or, equivalently, large ERE_{oc}). However, there is a noticeable difference between the measured values for cells #4, #5 and #6 and the theoretical solid line. This difference is due to the 2nd summand in eq. (88) that we have neglected in the theoretical prediction (solid green line). Indeed, a substantial relative increase with temperature of ERE_{oc} of the cells #4, #5 and #6 can be observed. This leads to non-negligible values of $d \ln(ERE_{oc}) / d \ln(T_c)$ and to negative values of γ significantly far from the theoretical value of 1.2. The values of ERE_{oc} and γ calculated respectively from eq. (92) and eq. (88) with the experimental results are reported in Table 3. These temperature dependences of ERE_{oc} are attributed to the unusually large increases with temperature of the collection fractions of these cells that we have discussed in the previous section (notice the EQE term in eq. (92)). The term $d \ln(J_{sc}) / d \ln(T_c)$ in eq. (88) is also larger for these cells but accounts for a change in γ of only 0.25 on average. It is worth noticing that the deviation between the experimental results and the theoretical line in Fig. 33 is always proportional to the difference between γ and its reference value (1.2) divided by V_{oc} . The dotted green line in Fig. 33 shows that the temperature coefficient of the open-circuit voltage of the cells #4, #5 and #6 can be modeled with a different value of γ (-2).

⁴⁵ Using the bandgap temperature dependence of crystalline silicon from (Green 1990): the bandgap linearly extrapolated to 0 K, E_{g0} , is equal to 1.206 eV and dE_g/dT is equal to -0.273 meV.K⁻¹ in the temperature range of interest.

As we have demonstrated in the previous chapter, the value of γ is an indicator of the internal device physics and could be used to identify the mechanisms that limit the device performances. However the values of γ calculated from these experimental values of β_{Voc} of the crystalline silicon cells measured at UNSW range from -2.4 to 1.7 and thus match neither the scenario where SRH recombinations in the bulk and at the surfaces dominate ($\gamma \approx 3$) nor that where SRH recombinations in the depletion region dominate ($\gamma \approx 5$). Some values are around 1.2 which would correspond to the scenario where radiative recombination dominates which is obviously not the case⁴⁶. This gap between experimental results and the theoretical expectations could indicate that some assumptions that have been made do not hold for these cells (such as neglecting the temperature dependence of carrier lifetime (Johnston & Ahrenkiel 1999) or that of F_p and incidentally that of the rear surface recombination velocity). It would be interesting, in a future work, to calculate the parameter γ in different detailed scenarios that could include the temperature dependences of lifetimes related the known defects in silicon⁴⁷ (using Schenk's model for the temperature dependence of Shockley-Read-Hall lifetimes in silicon (Schenk 1992) and using Klaassen's model (Klaassen 1992a; Klaassen 1992b) for the temperature dependence of the carrier mobilities).

⁴⁶ Even the best crystalline silicon cell in 2012 had an ERE of only 0.57% (Green 2012).

⁴⁷ Data on energy levels and temperature dependences of the capture cross sections of typical defects in Boron doped Czochralski c-Si cells can be found in (Murphy, McGuire & Bothe 2014; Rein & Glunz 2003).

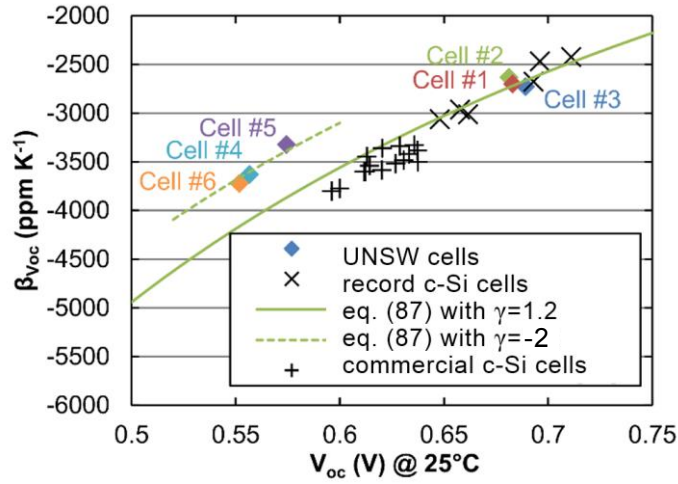


Fig. 33 Experimental temperature coefficients of the open-circuit voltage (diamonds, crosses and x's) and theoretical predictions (green lines) with different values of γ plotted as a function of V_{oc} at room temperature. The data for the record crystalline silicon cells are from (Green, Emery & Blakers 1982; Green, Blakers & Osterwald 1985; Zhao et al. 1994) and the data for the commercial c-Si cells are from (Ponce-Alcántara et al. 2014).

Table 3 ERE and γ values calculated from eq. (92) and eq. (88) with the experimental results.

	Cell #1	Cell #2	Cell #3	Cell #4	Cell #5	Cell #6
$ERE @25^{\circ}C$	$2.5 \cdot 10^{-3}$	$2.6 \cdot 10^{-3}$	$3.1 \cdot 10^{-3}$	$3.0 \cdot 10^{-6}$	$7.6 \cdot 10^{-6}$	$4.2 \cdot 10^{-6}$
$ERE @40^{\circ}C$	$2.6 \cdot 10^{-3}$	$3.0 \cdot 10^{-3}$	$3.3 \cdot 10^{-3}$	$6.9 \cdot 10^{-6}$	$1.1 \cdot 10^{-5}$	$8.3 \cdot 10^{-6}$
γ	1.0	0.4	1.7	-1.8	-2.4	-1.6

Even though there are some exceptions such as the case of cells #4, #5 and #6 we have discussed above, the relation between $\beta_{V_{oc}}$ and V_{oc} is obvious in Fig. 33. This trend confirms the long-observed fact that cells with high V_{oc} benefit from reduced temperature sensitivity (Green, Emery & Blakers 1982). In 1994, Geoffrey Landis formulated the idea that, in the case of space applications, it could be worth improving the open-circuit voltage (at the expense of performances at 25 °C) to reduce the temperature sensitivity of the devices thus reducing the temperature-related losses and obtaining ultimately better performances in real operating conditions (Landis 1994). We believe that this kind of optimization that considers the device real operating conditions could benefit regular terrestrial solar cells or concentrated PV cells or other kind of PV conversion device (such as thermophotovoltaic concepts). This idea will be discussed in details in section 8.1 in Part II.

In the following section, the temperature coefficient of the fill factor of c-Si cells will be experimentally investigated and the range of validity of the theoretical expression from (Zhao et al. 1994) will be discussed.

5.4. Fill factor temperature sensitivity

In section 4.3, two expressions for the temperature coefficients of fill factor of solar cells have been introduced. The present section aims at assessing the range of validity of these expressions against the experimental measurements on crystalline silicon cells made at UNSW. The theoretical formulations are reminded below:

$$FF_0 = \frac{v_{oc} - \ln(v_{oc} + 0.72)}{v_{oc} + 1} \quad \text{with} \quad v_{oc} = \frac{nkT_c}{q} V_{oc} \quad (93)$$

$$\frac{1}{FF_0} \frac{dFF_0}{dT_c} = (1 - 1.02 FF_0) \left(\frac{1}{V_{oc}} \frac{dV_{oc}}{dT_c} - \frac{1}{T_c} \right) \quad (94)$$

$$FF_s = FF_0 \left(1 - \frac{R_s}{V_{oc} / I_{sc}} \right) \quad (95)$$

$$\frac{1}{FF_s} \frac{dFF_s}{dT_c} = (1 - 1.02 FF_0) \left(\frac{1}{V_{oc}} \frac{dV_{oc}}{dT_c} - \frac{1}{T_c} \right) - \frac{R_s}{V_{oc} / I_{sc} - R_s} \left(\frac{1}{R_s} \frac{dR_s}{dT_c} \right) \quad (96)$$

Fig. 34 displays measured temperature coefficients of the fill factor together with a generic theoretical calculation (green line) and specific theoretical predictions based on experimental values for each cell (triangles). The experimental data are those of the studied cells (diamonds), that of record c-Si cells (x's) and that of commercial c-Si cells (+'s). The green line is calculated from eq. (94) and, in order to be generic, uses a single value of the ideality factor, 1, and assumes a single value of γ , 1.2, to calculate the open-circuit voltage (from eq. (87)). Using eq. (94) corresponds to neglecting the 2nd summand in eq. (96) which considers the effect of series resistances. It appears in Fig. 34 that most of the measured values lie below the generic theoretical calculation represented by the green line. This seems to indicate that the 2nd summand in eq. (96) is not negligible⁴⁸. As

⁴⁸ The difference could also come from values of the ideality factor different from 1 or values of γ significantly different from 1.2.

expected, the measured values of β_{FF} of cells with relatively large series resistances (cells #1, #4, #5 and #6; see Table 2) differ appreciably from the green line. As we have mentioned, the impact of the series resistance and its temperature dependence on β_{FF} was introduced in (Zhao et al. 1994) with the addition of the 2nd summand in eq. (96). In (Zhao et al. 1994), a temperature coefficient of the series resistances (β_{R_s}) of 6450 ppm.K-1 was used which is that of 0.5 Ω .cm silicon. In the present study, the temperature coefficients of the series resistances, β_{R_s} , calculated from linear regression of the calculated R_s (Fig. 30a) vary from 920 to 4770 ppm K-1 (Table 2). The temperature coefficient of the resistivity of p-type (Boron-doped) 1 Ω -cm silicon is 7200 ppm.K-1 (Bullis & Brewer 1968). This indicates that the series resistances of the studied cells probably do not come only from the bulk regions (but maybe also from contact resistances...). The triangles in Fig. 34 represent the results from the theoretical expression from (Zhao et al. 1994), eqs. (96) and (93), with the experimental values of $\beta_{V_{oc}}$, R_s , β_{R_s} and n . While these specific theoretical predictions are somewhat closer to the measured values of β_{FF} , there are still some large discrepancies between theory and measurements for several cells. Eq. (96) was derived from an expression of the FF , eq. (95), that is only accurate for cells with very large shunt resistances. Fig. 35 shows that this expression fails to predict accurately the FF of cell #2, which has a really small shunt resistance ($\approx 70 \Omega$, see Table 2). This explains why cell #2 has the only measured β_{FF} that is above the theoretical prediction. Fig. 35 also shows that eq. (95) is relatively accurate (better than 1%) for the FF of the rest of the cells. The discrepancies for these cells between the measured (diamonds) and the theoretical (triangles) values of β_{FF} may be due to the variations of the ideality factor, the series resistance and the shunt resistance with temperature (illustrated in Fig. 30) which are not neglected in the derivation of eqs. (94) and (96). It could be interesting, in a future work, to derive a more general expression for the temperature coefficient of the fill factor that would take into account these temperature dependences.

Green also derived an expression of the fill factor for the case where both series and shunt resistances matter (Green, Emery & Blakers 1982):

$$FF = FF_s \left(1 - \frac{v_{oc} + 0.7 FF_s}{v_{oc} r_{sh}} \right) \quad (97)$$

where r_{sh} is equal to the shunt resistance (R_{sh}) normalized by the cell characteristic resistance which is equal to V_{oc}/I_{sc} .

Fig. 35 shows that, as expected, this expression accurately predicts the fill factor of all the different cells. Thus, it could serve as a basis to derive a more general expression for the temperature coefficient of the fill factor.

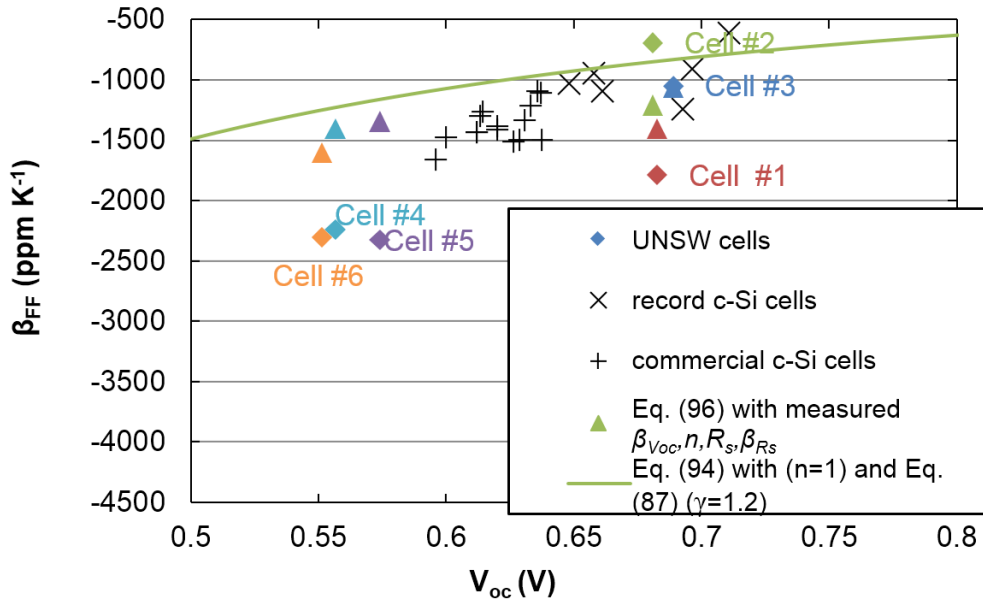


Fig. 34 Experimental temperature coefficients of the fill factor (diamonds and x's), generic theoretical calculation (green line) and specific theoretical predictions (triangles) plotted as a function of open-circuit voltage (V_{oc}) at 25 °C. The data for the record crystalline silicon cells are from (Green, Emery & Blakers 1982; Green, Blakers & Osterwald 1985; Zhao et al. 1994) and the data for the commercial c-Si cells are from (Ponce-Alcántara et al. 2014).

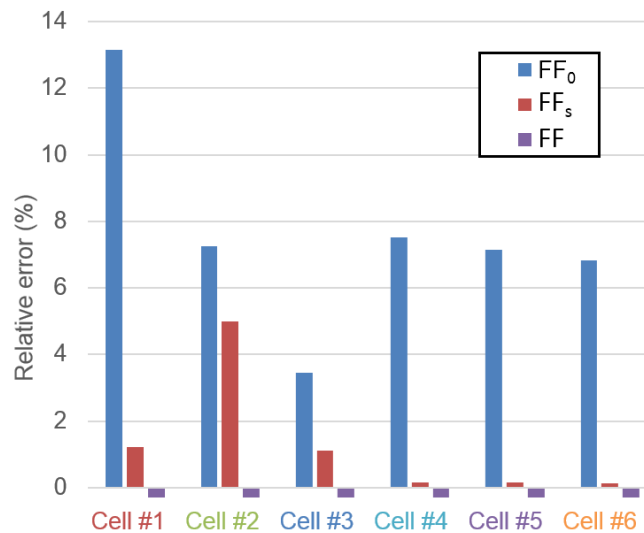


Fig. 35 Relative errors between approximate analytical expressions of the fill factor and measured values. FF_0 , FF_s and FF are calculated respectively from eqs. (93), (95) and (97).

We have mentioned in this section the importance of the ideality factor, the series resistance and the shunt resistance in the temperature sensitivity of the fill factor. These terms are driven by several physical mechanisms that can differ between different cell technologies or structures. For example, in silicon heterojunction cells, Seif et al. reported that the passivation effect of amorphous silicon stacks containing doped layers increases with temperature while it decreases with temperature for intrinsic-only amorphous silicon layers (Seif et al. 2015). This was shown to impact the temperature coefficient of the fill factor and that of the open-circuit voltage. In the next section, the distinctive features of the temperature dependence of silicon heterojunction cells will be discussed.

5.5. Temperature sensitivity of silicon heterojunction solar cells

Panasonic (previously Sanyo) is strongly advertising the fact that its modules made with HIT⁴⁹ cells produce more energy throughout the day than regular c-Si modules (Panasonic 2015). This “in operation” advantage is due to the relatively low temperature coefficient of the HIT cells. This low temperature coefficient is caused by the advantageous V_{oc} enabled by this cell structure as shown in Fig. 36a (Mishima et al. 2011). In Fig. 36b, we plotted temperature coefficients of conversion efficiency as a function of open-circuit voltage of HIT cells (yellow circles) together with that of “conventional” (p-n junction) c-Si cells (other symbols, refer to the legend). Fig. 36b shows that the HIT cells follow the same trend as regular crystalline silicon cells. This seems to indicate that the temperature dependences of the dominating loss mechanisms are similar in HIT and c-Si cells. Indeed, it was shown that the carrier transport in the HIT structure is dominated by the diffusion current⁵⁰ similarly as in “standard” diffused p-n homo-junctions (Taguchi,

⁴⁹ HIT stands for Heterojunction with Intrinsic Thin layers. This kind of silicon heterojunction (SHJ) solar cells consist of a layer of c-Si (which serves as absorber) sandwiched between two very thin layers (few nanometers) of amorphous silicon (a-Si) with different doping (which serves as selective membranes). These layers are separated by very thin layers of excellent quality amorphous silicon to passivate the interfaces (Wolf et al. 2012; Mishima et al. 2011).

⁵⁰ In the high forward bias region ($V > 0.4$ V) which includes the usual cell working conditions. In the low forward bias region ($0.1 < V < 0.4$ V), tunneling across the junction hetero-interfaces plays a dominant role in carrier transport (Taguchi, Maruyama & Tanaka 2008). However, this bias region does not impact the solar cell operating performances (Taguchi, Maruyama & Tanaka 2008). It is still interesting to note that this transport mechanism strongly depends on the density of localized states in the intrinsic amorphous layer and that it has a different voltage and temperature dependence than transport by diffusion (Sze & Ng 1981).

Maruyama & Tanaka 2008). While the temperature behavior of HIT cells (and SHJ cells in general) follows the same trend as that of conventional homo-junctions cells, several studies showed that the structure of a SHJ cell (such as the doping and thicknesses of the different layers) has an important impact on its temperature coefficients (Seif et al. 2015; Taguchi, Maruyama & Tanaka 2008).

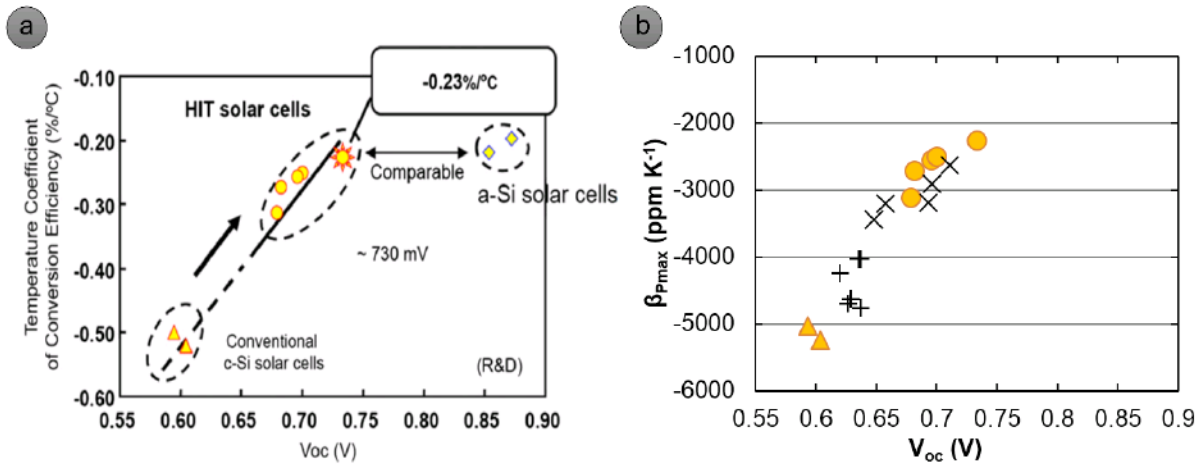


Fig. 36 Temperature coefficient of conversion efficiency as a function of open-circuit voltage. a. Figure from (Mishima et al. 2011): yellow circles represent HIT solar cells, yellow triangles represent conventional c-Si solar cells and the pale yellow diamonds represent a-Si solar cells; b. additional data are plotted: the black x's represent record "conventional" c-Si solar cells and the black +'s represent commercial c-Si solar cells (Ponce-Alcántara et al. 2014).

In the following section, the temperature sensitivity of another special kind of silicon cell is discussed: cells made from compensated silicon feedstock. Several experimental results from the literature are compiled in order to assess if the temperature coefficients of these cells are correctly described by the theoretical expressions described in chapter 4.

5.6. Temperature sensitivity of compensated silicon solar cells

Several recent works investigated the temperature sensitivities of cells made of compensated silicon also-called upgraded metallurgical silicon (UMG-Si) or solar-grade silicon directly purified by metallurgical route (SoGM-Si) (Tanay et al. 2011; Tayyib, Odden & Saetre 2013; Xiao et al. 2014; Ponce-Alcántara et al. 2014; Tayyib, Odden & Saetre 2014b; Tayyib, Odden & Saetre 2014a). This kind of silicon shows some promises

for the photovoltaic industry because it is cheaper to produce than the electronic-grade silicon (EG-Si) typically used in PV cells (Tanay et al. 2011). One particularity of this kind of silicon feedstock is that it contains high concentrations of Boron (B) and Phosphorous (P) that are respectively p-type and n-type dopants, which is the reason why it is named “compensated silicon”. The amount of compensation is quantified by a parameter called compensation level (CL) defined as $([B]+[P])/([B]-[P])$ where [B] and [P] are the Boron and Phosphorous concentrations, respectively (Tanay et al. 2011). Also, compensated silicon feedstock contains much larger amounts of metal impurities and light elements (oxygen, carbon) than standard EG-Si (Tanay et al. 2011).

All the works quoted above argue that solar cells made of compensated silicon benefit from advantageous temperature coefficients of their efficiencies. Their measurements show that these advantageous β_{η} are due to the larger $\beta_{J_{sc}}$. All the studies attribute (at least to some extent) the larger $\beta_{J_{sc}}$ to a smaller (compared to EG-Si) decrease of the minority carriers mobility with temperature. This happens because mobilities in UMG-Si are more impacted by impurity scattering which is temperature independent and thus less driven by phonon scattering which obviously increases with temperature. Xiao et al. illustrated this using Klaassen’s model for the carrier mobilities (Xiao et al. 2014). Tanay et al. also showed numerically that the temperature dependences of the carrier lifetimes associated with B-O defects participate to explain the larger $\beta_{J_{sc}}$ observed. Indeed, B-O defects are the main cause of recombinations in cells made from compensated silicon feedstocks and the lifetimes corresponding to these defects are known to increase significantly with cell temperature (Tanay et al. 2011).

Fig. 37 shows the data from three independent studies on the temperature sensitivities of compensated silicon cells (Tanay et al. 2011; Xiao et al. 2014; Ponce-Alcántara et al. 2014). The graphs suggest that the temperature advantage of cells made of compensated silicon may come at the price of reduced performances. Indeed, while impurity scattering reduces the relative decrease of mobility with temperature, it also causes a reduction of the mobilities (see Fig. 9a and b in (Xiao et al. 2014)). Similarly, recombination induced by B-O defects decreases with temperature but it also reduces the global minority carrier lifetime compared to a cell without these defects.

Fig. 37a shows the temperature coefficient of the efficiency plotted as a function of efficiency at room temperature. The cells from compensated silicon feedstock are depicted by filled triangles and these made of “standard” silicon are depicted by open circles. It

appears that most of the measured cells made of compensated silicon have smaller efficiencies than the cells made of standard silicon. Also, there seems to be a similar trend in the results from (Tanay et al. 2011) (in red) and from (Xiao et al. 2014) (in orange): the temperature coefficient of the efficiency becomes worse as the efficiency improves. This is somewhat surprising as we have seen before (in chapter 3) that $\beta_{V_{oc}}$ accounts for a large part of β_{η} and that it improves together with cell open-circuit voltage. Fig. 37c shows that the relation between $\beta_{V_{oc}}$ and V_{oc} is similar for cells made from compensated and “standard” silicon feedstocks. These experimental results agree with the theoretical prediction detailed in section 5.3 (with $\gamma=1.2$) and depicted by the green line in Fig. 37c. Fig. 37d shows that the trend of measured temperature coefficients of the fill factor of the cells from both compensated and “standard” silicon feedstocks is similar to that of the theoretical expression detailed in section 5.3 and depicted by the green line in Fig. 37d. An even better agreement is found with the theoretical expression that accounts for the effect of series resistance (depicted by the dashed green line and calculated with $\beta_{R_s}=6450 \text{ ppm K}^{-1}$ and $r_s=R_s/V_{oc}/I_{sc}=0.06$). Fig. 37c and Fig. 37d show that the temperature coefficients of the open-circuit voltage and that of the fill factor improve with open-circuit voltage⁵¹ both for cells made of “standard” and compensated silicon. Thus, what causes the temperature coefficient of the efficiency to decrease with increasing efficiency is the temperature coefficient of the short-circuit current density. Indeed, Fig. 37b shows a clear trend: $\beta_{J_{sc}}$ decreases significantly with increasing short-circuit current for both kinds of silicon cells. As concluded in (Ponce-Alcántara et al. 2014), we observe that the temperature coefficient of the short-circuit current has an important impact on the overall temperature sensitivity of these cells. This is also consistent with the analyses in (Tanay et al. 2011; Xiao et al. 2014) that state that the advantageous β_{η} of cells made from compensated silicon feedstocks originates from larger $\beta_{J_{sc}}$. The physics explaining why compensated silicon based solar cells have their short-circuit current improve with temperature⁵² has been detailed above (mobilities and lifetimes positive temperature dependences). For the temperature sensitivity of the short-circuit current density of “standard” c-Si cells, we have suggested in section 5.2 that the positive temperature

⁵¹ The temperature coefficients of the fill factor in (Tanay et al. 2011) seem to be decreasing with increasing open-circuit voltage. This could be due to differences in the series resistances between the different cells.

⁵² An increase larger than that expected from the temperature dependence of the bandgap of c-Si is implied here.

dependence of the absorption coefficient could play an important role. What is surprising in Fig. 37b is that both type of cells (EG-Si and UMG-Si) seem to follow the same trend while the physical limiting mechanisms are supposedly different. The temperature coefficients of open-circuit voltage (Fig. 37c) and fill factor (Fig. 37d) of the two different types of cells also follow similar trends. This seems to indicate that, when the efficiencies of compensated silicon solar cells will increase, their temperature coefficients will likely converge towards that of “standard” silicon cells. The only comparison we found in the literature (Tayyib, Odden & Saetre 2013) between cells of different silicon feedstocks (“standard” and compensated) that had similar efficiencies at 25 °C do not show any significant difference of temperature sensitivity (see Fig. 38). However, the differences between the different data sets (see Fig. 37) show that more experimental results are necessary to draw any definitive conclusions about the thermal behavior of compensated silicon solar cells.

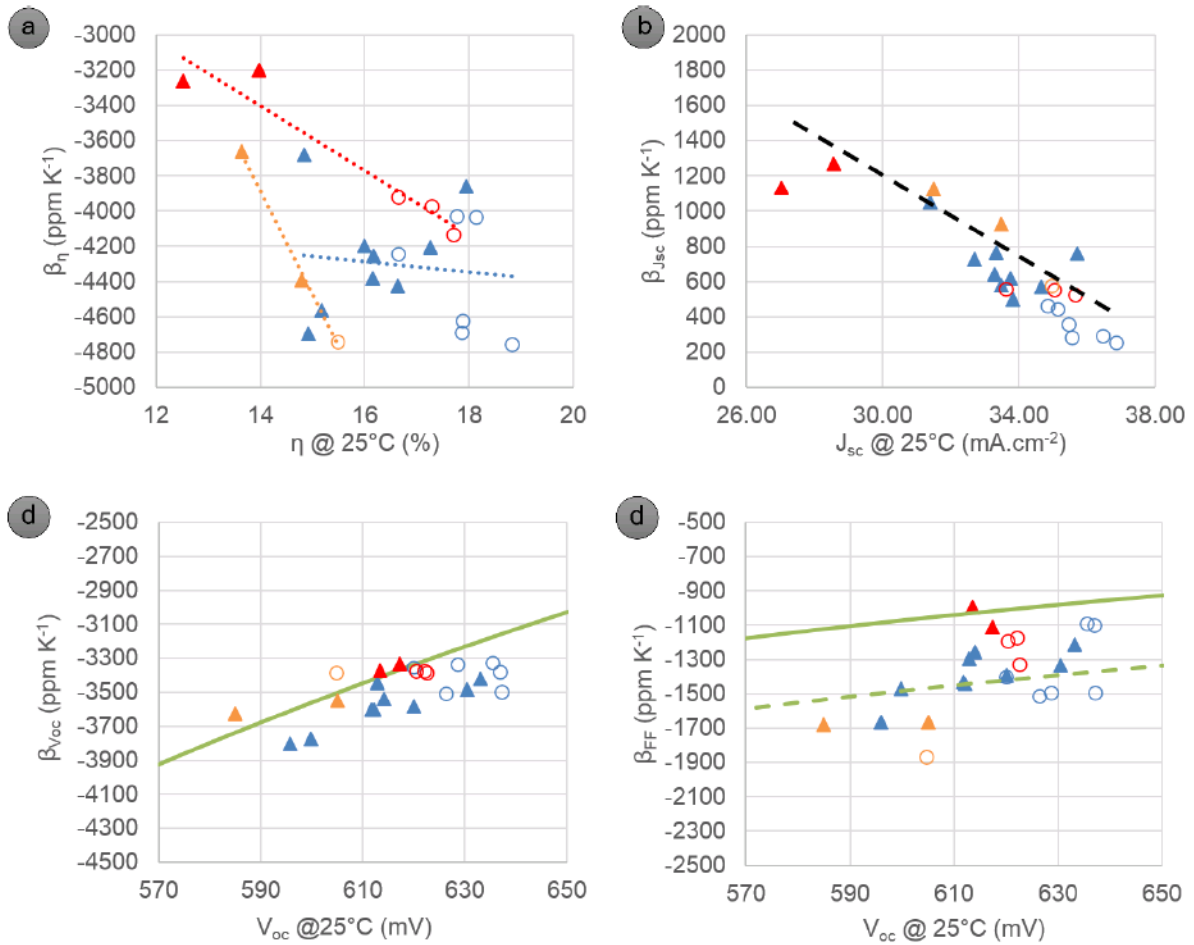


Fig. 37 Temperature coefficients of solar cells made from standard EG-Si (open circles) and compensated Si (filled triangles). The data in red, blue and orange are respectively from (Tanay et al. 2011), (Ponce-Alcántara et al. 2014) and (Xiao et al. 2014). Please note that the values plotted in red were estimated from the data in (Tanay et al. 2011). a. Temperature coefficient of the efficiency density plotted against efficiency at 25 °C. The dotted lines are linear fits that are not based on any physical model but are simply plotted here to show the trends in the data. The linear fit on the data from (Ponce-Alcántara et al. 2014) is really poor. This may be caused by the fact that different fabrication processes were used for the cells in this study; b. temperature coefficient of the short-circuit current density plotted against short-circuit current density at 25 °C; c. temperature coefficient of the open-circuit voltage plotted against open-circuit voltage at 25 °C. The green line corresponds to the theoretical calculation detailed in section 5.3; d. temperature coefficient of the fill factor plotted against open-circuit voltage at 25 °C. The green lines correspond to the theoretical calculation detailed in section 5.4 with $R_s=0$ (full line) and with $\beta_{R_s}=6450$ ppm K^{-1} and $r_s=R_s/V_{oc}/I_{sc}=0.06$ (dashed line).

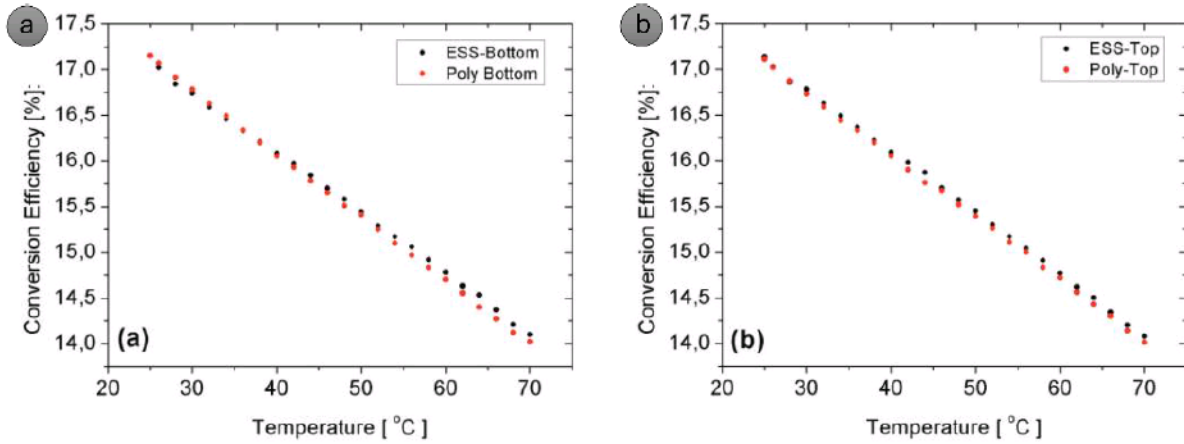


Fig. 38 Conversion efficiency as a function of temperature for cells made from silicon from two different feedstocks (in red: solar grade silicon produced by the Elkem Solar method ESSTM; in blue: standard polysilicon) from a. bottom batches; b. top batches (Tayyib, Odden & Saetre 2013).

In Part I of this thesis manuscript, we have investigated the relation between device temperature and conversion efficiency through a study of the so-called temperature coefficients. In Part II, we will study the parameters that drive the device temperature in order to develop a comprehensive thermal model of PV devices and eventually suggest original thermal optimizations.

Part II: Thermal optimizations of photovoltaic devices

Table of contents of Part II

Part II: Thermal optimizations of photovoltaic devices.....	103
6. Introduction	105
6.1. The common approach to reduce the temperature-induced losses of PV systems: reducing the cell operating temperature via different cooling methods	107
6.2. Other approaches to reduce the temperature-induced losses of PV devices	112
6.3. Our approach to reduce the temperature-induced losses of PV devices: modeling the intertwined optical, electrical and thermal mechanisms to propose device optimizations that take into account the real operating conditions	113
7. A full thermal model of PV devices	119
7.1. Description of the energy conversion loss processes	120
7.2. Temperature of the cell in a given environment.....	140
7.3. Revisiting the Normal Operating Conditions Temperature (NOCT)	141
8. Beyond STC: optimizations of PV devices that take into account actual operating conditions	143
8.1. Global optimizations of standard solar PV systems.....	144
8.2. Global optimizations of solar TPV systems	162
8.3. Global optimizations of near-field thermophotovoltaic systems	172

6. Introduction

In the general introduction of this manuscript, it has been emphasized that PV devices operate on a large range of temperatures. Also, the distributions of the operating temperatures of the PV devices change depending on the climate in which the system is installed (see Fig. 39).

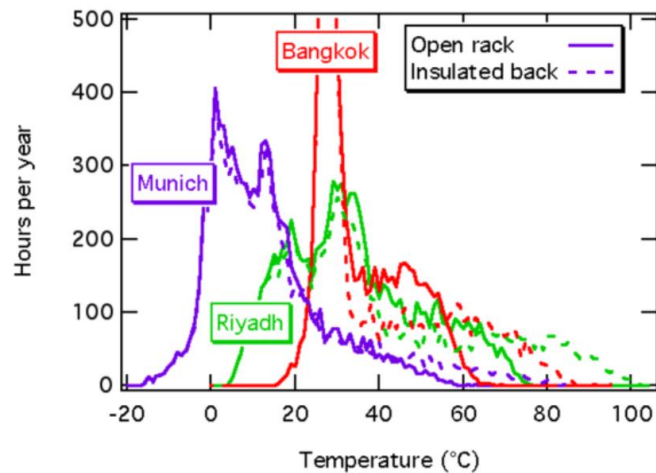


Fig. 39 Temperature distributions of PV modules for two different mounting configurations in several locations (Kurtz, Wohlgemuth, et al. 2011).

Furthermore, as discussed in the general introduction and illustrated once again in Fig. 40b, within the course of a year, the major part of the energy is produced when PV devices operate at high temperatures. This can be surprising because Part I demonstrated that any PV device temperature increase reduces its conversion efficiency⁵³. The reason why in the field more energy is produced at high device temperatures is that simultaneously to when

⁵³ It should be noted that there are some exceptions where temperature has a beneficial effect on device performances. It was mentioned in Part I that several references in the literature report on PV cells with positive temperature coefficients (Moser, Pichler & Nikolaeva-Dimitrova 2013; Riedel et al. 2004; Katz et al. 2001; Schropp, Schüttauf & van der Werf 2010; Fischer et al. 2009). The reasons for these positive temperature coefficients have been discussed in Part I. Another beneficial effect of module temperature that can be observed in the field is the evaporation of morning dew. Dew often collects at night and facilitates leakage currents which have been shown to be associated with Potential Induced Degradation (PID) (Hacke et al. 2011; Kurtz, Wohlgemuth, et al. 2011). Because module temperature rises as the incoming illumination increases in the morning, dew evaporates and PID diminishes. The evaporation of morning dew was also suspected to be the cause of positive temperature coefficients observed in the morning on certain modules (Whitaker et al. 1991).

the irradiation is large (lot of incoming energy), it happens that a large amount of energy is dissipated in the device (and also, the ambient temperature tends to be high).

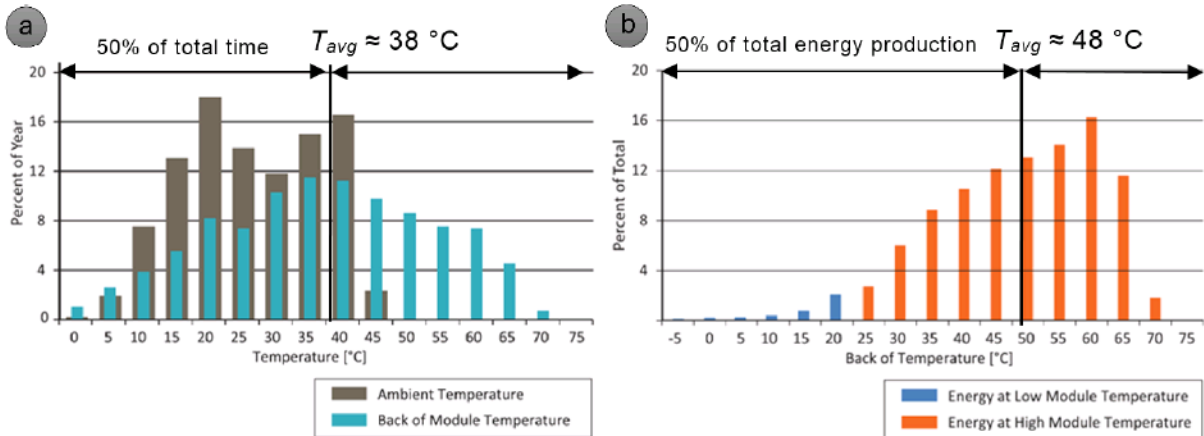


Fig. 40 Distribution in percent of: a. time in a year; b. produced energy on PV module temperature under real operating conditions. Figure adapted from (Strevel et al. 2012).

Fig. 40b shows that the range of operating temperature spans from -5°C to 70°C and that the mean operating temperature in terms of energy is about 50°C (in the case of an open-rack mounted module in the US desert southwest). Also, according to (Virtuani, Pavanello & Friesen 2010), building integrated photovoltaic systems can reach even higher temperatures (up to 92°C).

These simple observations and the fact that the efficiency of a PV system is negatively affected by its operating temperature tell us that: 1) in the field, the output power of PV panels varies greatly; 2) on average, they operate at lower efficiencies than those calculated in their design (at STC). As a consequence, a lot of research aimed at: 1) predicting the operating temperature of PV devices to anticipate their effective energy production; 2) reducing this operating temperature (at the lowest possible cost) to increase the effective energy production.

For item 1), a lot of empirical relations were established to determine the cell or the module temperature (Skoplaki & Palyvos 2009b) or directly the system output power (Skoplaki & Palyvos 2009a) from the outdoor conditions. The parameters usually considered are the illumination level, wind speed and ambient temperature. Unfortunately all these correlations remain valid only for a given module architecture with a given type of PV cell in a given configuration. For example, it is obvious that the effect of wind

speed on module temperature will be different if the module is in an open-rack configuration or if it is integrated in a building envelope.

For item 2), in order to reduce the operating temperature of PV devices, most of the literature reports on methods to evacuate the heat generated in the devices. Some works study the use of cooling systems (passive or active) while other discuss the design of components (e.g. frame, protective sheet, ...) with high thermal conductivities. The following section lists some of the different ideas that were proposed to cool down PV systems.

6.1. The common approach to reduce the temperature-induced losses of PV systems: reducing the cell operating temperature via different cooling methods

The most obvious way to reduce the operating temperature of a PV device is to cool it down. When the cooling system uses some energy, it is called active cooling. Otherwise the term passive cooling is used. In the case of active cooling, it is important to take into account the energy used by the cooling system in the efficiency calculations. For both active and cooling solutions, one should include the additional cost in the balance of system⁵⁴ cost.

An interesting example of passive cooling comes from a group of undergraduate MIT students (Chintapalli, Diskin & Guha 2010) who proposed a modified design of a PV module in order to increase heat dissipation. Based on (Lee et al. 2008), they chose a modified EVA composite encapsulant with a thermal conductivity larger than that of the classic EVA encapsulant (and still electrically insulating). They also changed the polyvinyl fluoride backing of traditional modules for an aluminum sheet with fins in order to enhance the heat transfer coefficient at the rear of the module. Finally, they also decided to replace flat glass with textured glass to increase heat transfer at the front of the module (because the surface area is increased by about 30%). The experimental results (Chintapalli, Diskin & Guha 2010) show that the aluminum finned substrate is the most

⁵⁴ The balance of system corresponds to all the components of a photovoltaic system other than the PV modules themselves (i.e. inverters, mounting system, wiring, ...). Price breakdowns from (Jäger-waldau 2014) show that the price of the PV modules corresponds to only 40 % of the total price of residential PV systems and about 50 % for utility scale PV systems (in Europe).

efficient among the different solutions in terms of heat dissipation. It can reduce the operating temperature of the module by about 10 °C. This value is a little less than that reported in (Cuce, Bali & Sekucoglu 2011) (≈ 17 °C under 800 W m^{-2} illumination) and also smaller than those reported in (Ross & Gonzalez 1980) which are illustrated in Fig. 41a. Note that the temperature reduction for modules with aluminum finned substrates depicted in Fig. 41a, corresponds to the open back side case (also called free-rack installation). It is also important to remember that the thermal behavior of such modules depends (similarly to any module) on the installation configuration (see Fig. 41b).

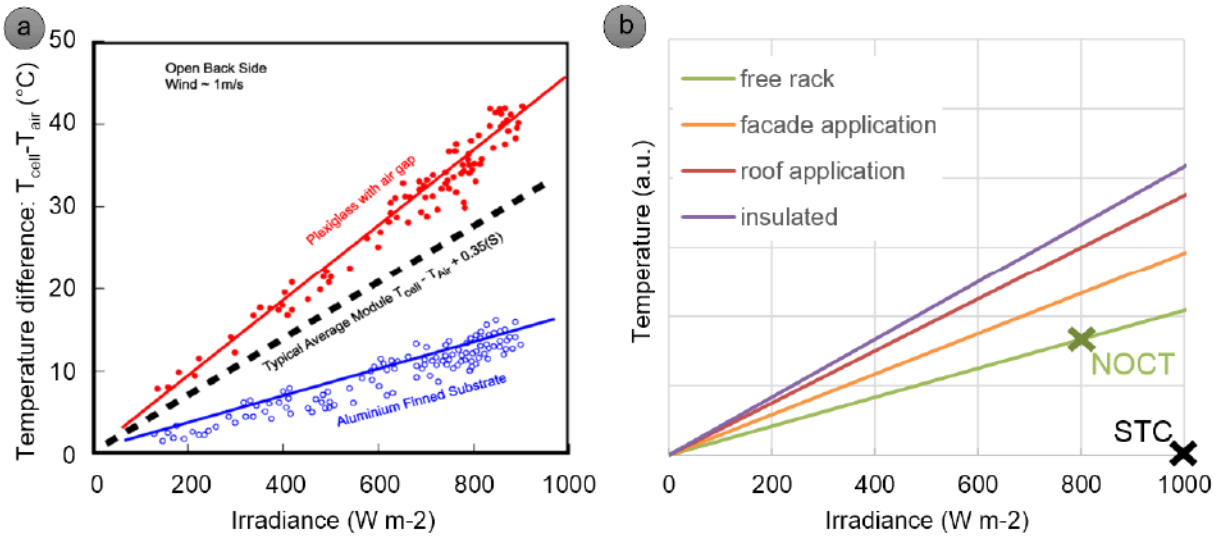


Fig. 41 Measured cell temperature dependence on solar irradiance for flat-plate photovoltaic modules: a. in open back side (free rack) configuration with different rear structures. Figure adapted from (Ross & Gonzalez 1980); b. in different mounting configurations. Figure adapted from (Bloem 2008).

Another example of passive cooling is the idea of immersing PV modules below the surface of large water basins (see Fig. 42a and for example (Rosa-Clot et al. 2010)). The main motivation for this concept of submerged PV plant is that it would remain at a low temperature because of the large heat exchange between the module and water. Other advantages claimed by Rosa-Clot *et al.* include smaller environmental impact, better stability in temperature, simpler maintenance, and the possibility of storing energy by coupling the PV plant with pumping systems between different basins. Obviously, there is also a list of disadvantages and complexities associated with such systems: there is a trade-off for the optimal depth between water temperature and water absorption of useful photons; the system is flat which is not the optimal inclination for absorbing incoming sunlight (except near the Equator); different challenges (such as water infiltration or corrosion) will probably arise because of the particular system environment... A similar

concept (taking advantage of unused water surfaces), much more developed, is that of floating PV systems. “Over the past five years, a myriad of floating systems have evolved in varying degrees for use in ponds, reservoirs, canals, rivers and oceans” (Thurston 2012). Two of these floating PV systems are shown in Fig. 42b and c. Fig. 42d illustrates another example of original idea of a passive cooling solution where the PV plant is installed in synergy with a green roof: the modules provide shadowing while the plants provide a lower ambient temperature (Witmer 2010).

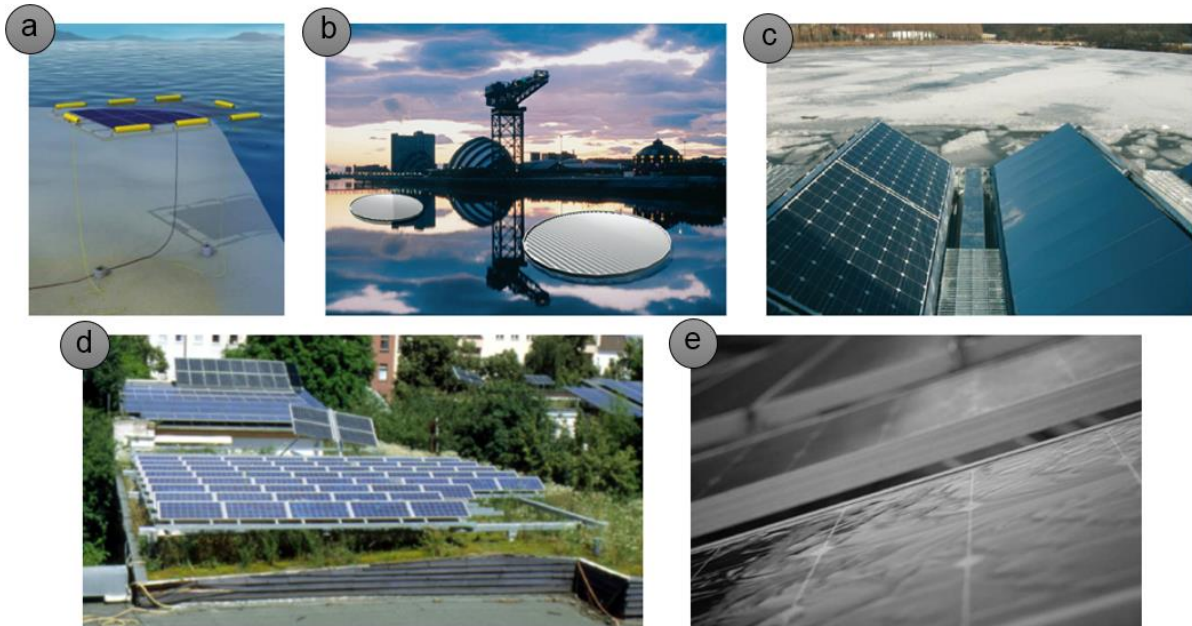


Fig. 42 Illustrations of: a. the concept of submerged PV plant. Schematic: Marco e Paolo Rosa-Clot; b. "Solar Lily Pads" with motor driven rotators on the Clyde river (in Glasgow, UK) developed by ZM Architecture. Photo: ZM ARCHITECTURE; c. Detail of the Cheongju platform built by Techwin in South Korea. Photo: Scienza Industria Tecnologia (SIT); d. PV system installed in a green roof for passive cooling (Witmer 2010); e. Active cooling by water flowing on the front surface of PV modules (Krauter 2004).

Another example of passive cooling based on device design rather than on the system environment is the concept of radiative cooling. The idea is to maximize the emission from the device in the thermal range to reduce its operating temperature. The concept is quite old as radiative exchange is the only heat dissipation mechanism available for PV devices in space. Recently, Zhu *et al.* showed that a thin layer ($\approx 100 \mu\text{m}$) of silica (topped by silica pyramids) added on top of a crystalline silicon solar cell could theoretically reduce its operating temperature by more than $15 \text{ }^\circ\text{C}$ (Zhu *et al.* 2014). This illustrates a potentially low cost passive cooling option for PV modules.

Alternatively to (or used in combination with) passive cooling, there exists a myriad of active cooling solutions. The cooling media might be air with a fan to force a flow behind the module or water pumped through a heat exchanger on the rear of the module. It was also suggested to cool the module via water flowing on its front surface (Fig. 42e, (Krauter 2004)). This water film provides the added benefit of serving as an anti-reflection layer. Krauter showed that a net gain of about 8% could be achieved taking into account the power consumed by the pumping system (Krauter 2004). However, no analysis was done to assess the economic viability of this solution. Also, the issue of water consumption (the evaporation rate is estimated to about $1 \text{ l h}^{-1} \text{ m}^{-2}$) was not addressed.

In some systems, the thermal energy extracted by the cooling media is exploited. These are called hybrid photovoltaic-thermal (PV-T) systems. The heat extracted can be used to pre-heat a domestic hot water tank (Fig. 43a) or to warm directly a building interior in building integrated PV (BIPV) applications (Fig. 43b). In the first case, which is the most common, there is a trade-off between the electrical efficiency and the “value” of the thermal source. Indeed, the temperature of the cooling fluid should be low to keep the cell cool but needs to be high enough to warm the domestic water above room temperature. Also, it is important to consider in the overall efficiency the energy required to drive the cooling fluid.

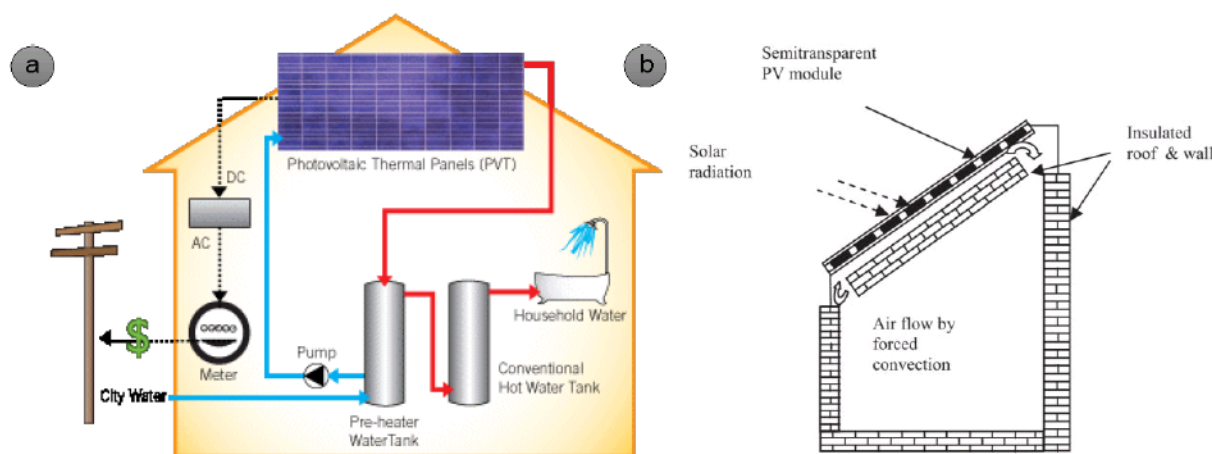


Fig. 43 Examples of hybrid PV-T systems: a. using a water flow to pre-heat domestic hot water (BossSolar 2015); b. using an air flow to heat a building interior directly (Bloem 2008).

The need for cooling is particularly important in concentrated PV applications. Indeed, as the illumination increases, so does the heat source within the device that needs to be evacuated. Royne et al. wrote a review of the different solutions suggested for cooling PV cells under concentration (Royne, Dey & Mills 2005). Fig. 44a illustrates that the thermal

resistance (defined as the inverse of the heat transfer coefficient) of the cooling system required to maintain the PV cell at a reasonable temperature decreases with increasing illumination level (the cooling medium temperature is assumed to be 25 °C). Fig. 44b shows the range of thermal resistances of different passive and active cooling technologies. As in the case of PV-T applications, the energy consumed by the cooling apparatus needs to be taken into account.

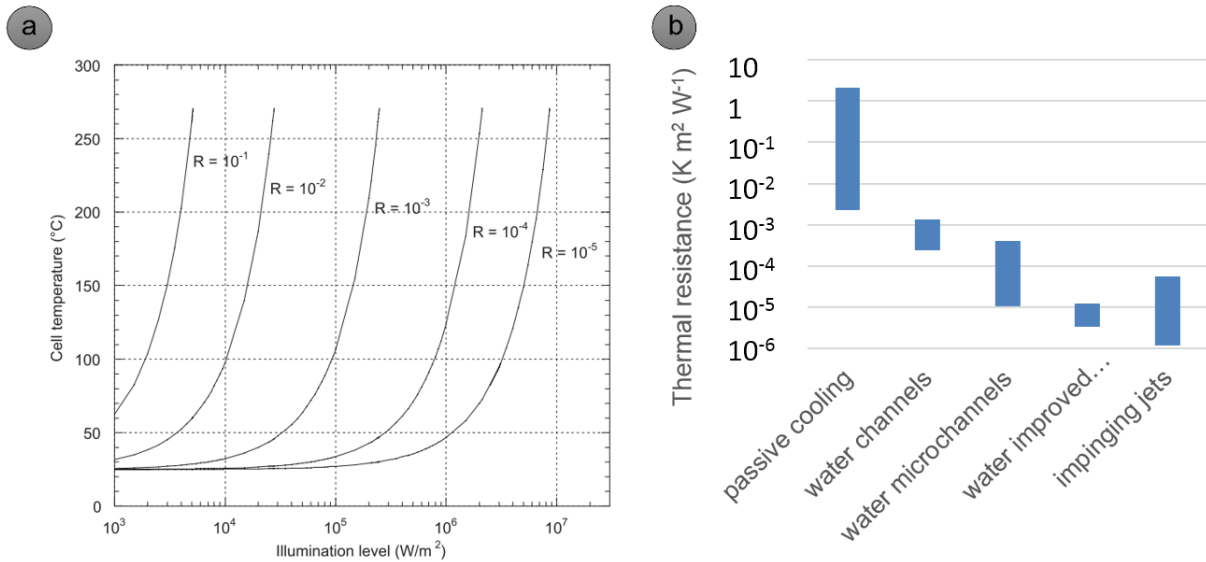


Fig. 44 a. Cell temperature as a function of illumination with different values of the thermal resistance of the cooling system. Figure from (Royne, Dey & Mills 2005); b. range of thermal resistances reported for different cooling technologies (data from (Royne, Dey & Mills 2005)).

In this section, several ways of cooling down PV systems have been presented. This literature review is not exhaustive: other examples of cooling methods can be found in (Royne, Dey & Mills 2005) and (Wu & Xiong 2014). In the literature, few works describe different approaches to deal with the temperature-induced losses in PV devices. The following section summarizes these somewhat alternative ideas.

6.2. Other approaches to reduce the temperature-induced losses of PV devices

Temperature-induced losses are especially critical for PV devices designed for space applications. This is because there is no convection in space so that the heat generated in the device can only be dissipated by thermal radiation. As we have mentioned above, radiative cooling can be increased by improving the device emissivity in the wavelength range corresponding to blackbody emission at its temperature. In 1994, Beauchamp and Tuttle-Hart submitted a patent named “UV/IR reflecting solar cell cover” (Beauchamp & Tuttle-Hart 1995) for protecting the idea of using a multilayer coating in order to reflect as much as possible of the useless incident light (i.e. in spectral regions beyond the limits of the cell response). The corresponding reduction in cell absorptance leads to a reduction of the heat absorbed in the device and ultimately a reduction of its operating temperature. This concept was also investigated for terrestrial high-concentrating photovoltaic systems (Micheli et al. 2012). For some specific space applications, the thermal management of the PV system is done at the expense of its performances. For example, it is envisaged tilting the arrays away from the Sun to prevent them from overheating during near-sun missions (Landis et al. 2004).

In 1996, Krauter and Hanitsch calculated that a gain in energy output of 0.4% could be achieved by tilting the azimuth of PV modules towards the east in order to lower the reflection in the morning when ambient temperatures are lower (Krauter & Hanitsch 1996). The tilt has to be towards the east because the ambient temperature generally lags behind solar irradiance intensity as can be observed in Fig. 45a. Krauter and Hanitsch also suggested a different idea: adding a small water tank to a module in order to increase its heat capacity so that it reaches its maximum temperature after the time of maximum incident irradiation (see Fig. 45b). Their first experimental device with a tank volume of 12 liters showed a 2.6% increase in energy yield. Their second prototype built with a much larger tank capacity resulted in improvements up to 12 % (Krauter, Hanitsch & Moreira 1996). It seems that this “heat capacity” concept provides an efficient mean to reduce the operating temperature of the PV module during the hours of maximum irradiation (and thus of important power production). However, the main drawback is the important

additional weight added to the PV unit⁵⁵ that makes installation (especially roof mounting) more difficult. Also, it is not clear in which proportion their optical optimizations (Krauter & Hanitsch 1996) participate to these values of energy yield improvements.

In the following section, we will introduce our approach which also aims at developing optimizations that pay regard to actual operating conditions.

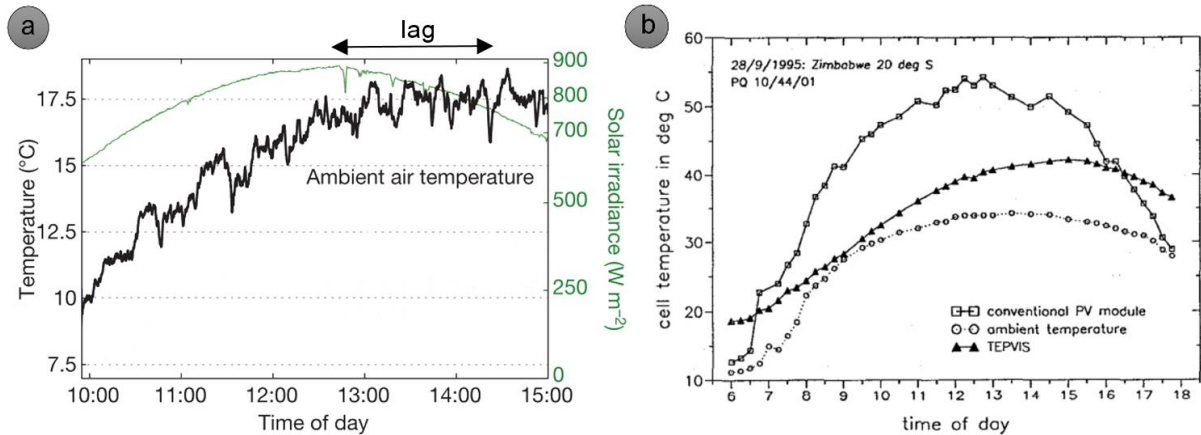


Fig. 45 Hourly variations of: a. solar irradiance and ambient temperature (Raman et al. 2014). The shift between the maximum of the solar irradiance and that of the ambient temperature is visible; b. ambient, conventional PV module and thermally and optically optimized PV module temperatures (Krauter, Hanitsch & Moreira 1996). The temperature lag and the maximum temperature reduction of the thermally and optically optimized PV module are apparent.

6.3. Our approach to reduce the temperature-induced losses of PV devices: modeling the intertwined optical, electrical and thermal mechanisms to propose device optimizations that take into account actual operating conditions

In order to investigate all the possible options to reduce the temperature-induced losses, we developed a global model of the thermal behavior of PV devices. This model is sketched in Fig. 46. The symbol Q corresponds to the heat generated within the device. The system temperature (T_c) is driven by heat source (Q) and the thermal Boundary Conditions (Thermal BCs). The thermal BCs include in particular the ambient temperature (T_e) and the global heat transfer coefficient (h). This global heat transfer coefficient takes

⁵⁵ The prototype modules weighted 200 kg (Krauter 2004).

into account conductive, convective and radiative exchanges between the system and its surroundings. Most of the ideas presented in section 6.1 correspond to improving these thermal BCs either via an increase of the heat transfer coefficient (e.g. forced convection, increase of the emissivity in the thermal range, ...) or via a reduction of the ambient temperature (e.g. floating systems, green roof, ...).

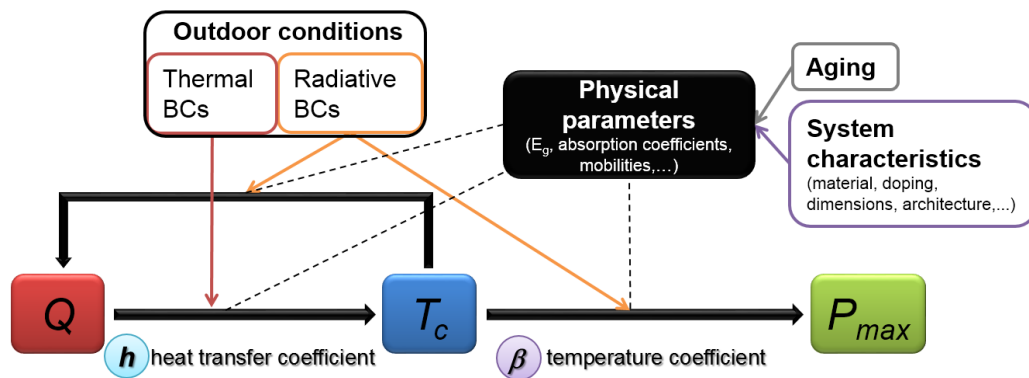


Fig. 46 Schematic of the thermal behavior of a photovoltaic device. Figure adapted from (Dupré & Vaillon 2014).

Fig. 46 shows that the heat source depends upon several physical mechanisms (e.g. the thermalization of the photogenerated electrical charges that is function of parameters such as the bandgap energy and the interband absorption coefficient). We don't list here all the physical parameters driving the different relations illustrated in Fig. 46 because this model will be described in full detail in chapter 7. Also, it can be observed that the heat source depends upon the radiative BCs which include the photon flux density of the incident radiation. This relation is illustrated by the idea developed for space cells of reflecting the useless part of the solar spectrum. This is done by adding some layers to tune the reflectivity of the device (which is a physical parameter). Interestingly, in thermophotovoltaic (TPV) applications, the reflected energy can be "recycled" by being reabsorbed in the emitter. In TPV systems, it is also possible to design the emitter in order to tune the spectrum incident on the PV device. These particularities enable several interesting design optimizations for TPV systems that will be discussed in sections 8.2 and 8.3. Another important relation in Fig. 46 is that between the system temperature and the heat source. This comes from the temperature dependences of all the physical parameters that drive the different heat generation mechanisms (e.g. the temperature dependence of the bandgap energy obviously has an impact on the thermalization source term). This feedback relation makes the problem non-linear so that it has to be solved iteratively. This will be discussed in section 8.1.

The right part of the schematic in Fig. 46 corresponds to the mechanism that was described in Part I: the impact of PV device temperature on its efficiency. It has been shown that a number of physical parameters are involved (e.g. lifetimes, absorption coefficients,...) so we believe that it might be possible to somewhat tune the temperature coefficient of a device. A lone example in the literature of such “temperature coefficient tuning” was found in a review on solar cells for space (Landis 1994): “Temperature coefficient is rarely considered as a design parameter for solar cells. From the standpoint of temperature coefficient, increasing open-circuit voltage, even at the expense of decreases in other cell parameters (for example, by increasing base doping of the cell) may result in higher power under actual space operating conditions.” Several options for modifying temperature coefficients will be presented in section 8.1. Fig. 46 also shows that the radiative BCs has an impact on the temperature coefficient. Indeed, it was shown in Part I that: 1) the light intensity modifies the open-circuit voltage (V_{oc}) and thus its temperature coefficient ($\beta_{V_{oc}}$) and 2) the spectrum (or the photon flux density) of the incident light impacts the temperature coefficient of short-circuit current ($\beta_{J_{sc}}$).

Of course, neither the thermal nor the radiative BCs are constant with time. While the BCs are as fluctuating as the weather, there are in average regular patterns in their daily and seasonal variations that enable interesting optimizations. One example is the idea suggested in (Krauter & Hanitsch 1996) of adding a water tank to a PV module in order increase its thermal capacitance and thus to delay its rise in temperature to separate it from the time of maximum insolation (Fig. 45b).

Fig. 46 also shows that both the thermal and the radiative boundary conditions are encompassed into the outdoor conditions. This means that the thermal behavior of a PV system is affected by the climate of the location it is installed in. Indeed, parameters such as ambient temperature and yearly average solar spectrum can be quite different in separate locations (see Fig. 39). This gives rise to interesting options for making the design of PV systems specific to a given location. Chapter 8 will be dedicated to the presentation of some original ideas of optimizations that take into account the actual operating conditions of PV devices. This kind of optimizations will be readily applicable as the PV industry is evolving towards products specifically adapted to the customer needs (Kurtz, Wohlgemuth, et al. 2011). The PV industry already knows about the importance of the performance under actual operating conditions. Indeed, PV customers are already focused on metrics such as energy yield rather than on Watt peak. All the companies that

have products that perform well in the field (with regard to the standard test conditions) advertise this fact (see for example Fig. 1 on page 16 or Fig. 36 on page 97). For example, Panasonic (previously Sanyo) and First Solar advertise the low temperature coefficients of their products. Alta devices claims that their devices not only have advantageous temperature coefficients but also stay cooler than conventional c-Si devices in the same operating conditions (see Fig. 47a). Their claim is based on a study made at NREL (Silverman et al. 2013). Fundamentally (in the radiative limit), it is expected that larger bandgap devices operate at lower temperature than smaller bandgap devices because the losses generating heat decrease with increasing bandgap (see Fig. 56). This will be discussed in detail in section 8.1.1. The study from NREL (Silverman et al. 2013) is really interesting in that it investigates the spectral distribution of the heat sources (see Fig. 47b and Fig. 47d). Silverman et al. observed that the heat source due to sub-bandgap photon absorption was larger for GaAs than for c-Si because of the larger bandgap of the former (see Fig. 47b) (even though they measured a higher reflectance in the IR of the GaAs module than that of the c-Si module). However, the heat source corresponding to the converted photon excess energy was much larger for the c-Si module (see Fig. 47d). They attributed this smaller heat source in the GaAs module to a smaller thermalization of interband absorbed photons (because of the lower bandgap of GaAs) and to a smaller non-radiative recombination source term (because of the high quality of the GaAs). They measured a difference of average operating temperatures of about 7°C (see Fig. 47a) and a difference of temperature coefficients of 3300 ppm K⁻¹ between the GaAs and the c-Si modules. They extrapolated that it would roughly (not taking into account the different spectral responses of the devices) correspond to an 8 % gain in energy per year for a GaAs module versus a c-Si module. While their physical interpretation is correct, their values might be biased if they compared modules with different efficiencies (indeed, GaAs modules from AltaDevices outperform significantly standard c-Si modules). Higher efficiencies lead to lower heat generation because of enhanced electrical outputs. Also, larger open-circuit voltages lead to advantageous temperature coefficients (see Part I). We believe that the differences obtained would be lower if they had compared their GaAs module to a high efficiency c-Si module. Indeed, temperature coefficients as low as -2632 ppm K⁻¹ have been reported for c-Si cells (Zhao et al. 1994) which is much lower than the value of -4100 ppm K⁻¹ measured on the c-Si module in this NREL study. To date, c-Si module efficiencies up to 22.9 % have been reported which is comparable to the best GaAs module efficiency of 24.1 % (Martin A

Green et al. 2015). Another possible bias in the NREL study is the difference in the sizes of the modules that were compared. Indeed, the GaAs module was much smaller than the c-Si module (855 cm² versus 6100 cm²). This size difference means that a different fraction of the generated heat can be dissipated through the sides of the module thus explaining to a certain extent the lower operating temperature observed for the smaller module (GaAs). While the values measured in this study might be biased, we believe that the heat generation in a device is an important design parameter when actual operating conditions are considered. We will demonstrate it through several examples in chapter 8.

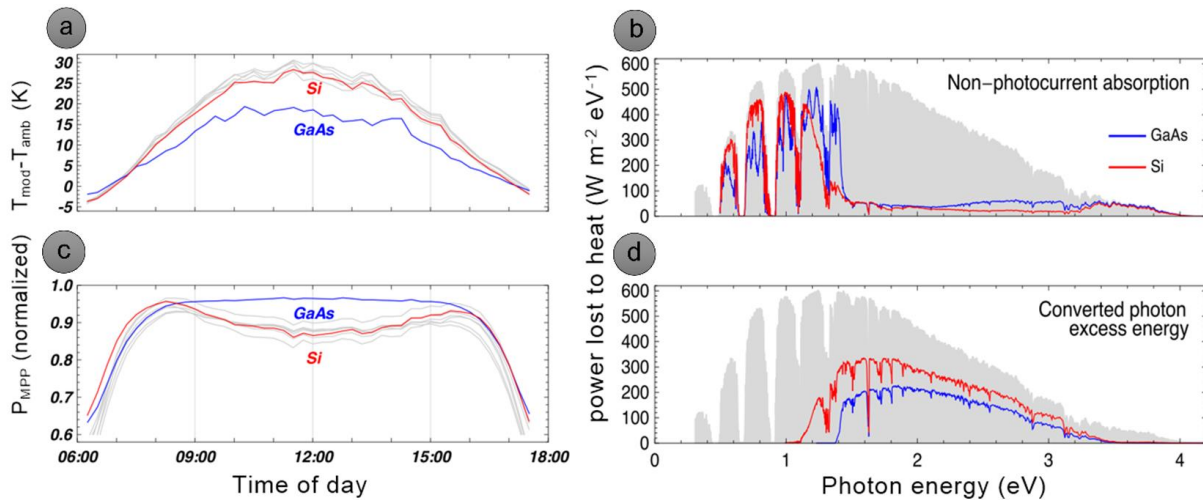


Fig. 47 Time variation of: a. excess module temperature (above ambient temperature); c. normalized maximum power output; energy distribution of the heat source in a c-Si module (in red) and a GaAs module (in blue) due to: b. parasitic absorption of photons with $E < E_g$; d. thermalization of the photogenerated carriers. Figures adapted from (Silverman et al. 2013).

We have just mentioned that several companies advertised the advantageous performances of their product under real operating conditions. However, these good field performances seem to be observed rather than designed. We found in the literature only one suggestion of optimization of the cell design that takes into account specific operating conditions. Carlson et al. made an experimental study of amorphous silicon cells (Carlson, Lin & Ganguly 2000) and concluded that their temperature behavior is dependent upon several parameters such as the device configuration, the concentration of defects in the intrinsic-layer, the thickness of the intrinsic-layer and the temperature of light soaking. In particular, they observed that the impact of the intrinsic-layer thickness on stabilized efficiencies is function of the temperature of the light soaking. This is illustrated in Fig. 48. Because of the somewhat long dynamic of annealing, one can assume that the stabilized efficiency in the field is close to the efficiency measured after an

experimental light soaking at the highest daily temperature reached by the device (Carlson, Lin & Ganguly 2000). This led Carlson et al. to conclude that the a-Si device structure (the intrinsic-layer thickness in this case) could be tuned according to the operating conditions corresponding to its installation: “In order to maximize the output power, the a-Si device structure should be tailored for the operating environment” (Carlson, Lin & Ganguly 2000). Since building integrated PV systems can reach temperatures above 90 °C (Virtuani, Pavanello & Friesen 2010), one can conclude from Fig. 48 that the a-Si cells for such systems should be designed with thicker i-layers than in the case of PV systems installed on an open-rack and operating in a cold climate. The data in Fig. 48 indicate that an a-Si module reaching 80 °C during the day can produce about 6 % more power if it is composed of cells with i-layer thicknesses of 400 nm instead of 200 nm (which is the optimum thickness if the module maximum temperature is around 40 °C). Carlson et al. also noted that one should “be able to use thinner doped layers in a-Si solar cells that will operate at elevated temperatures since the conductivity of the doped layers increases significantly with temperature”.

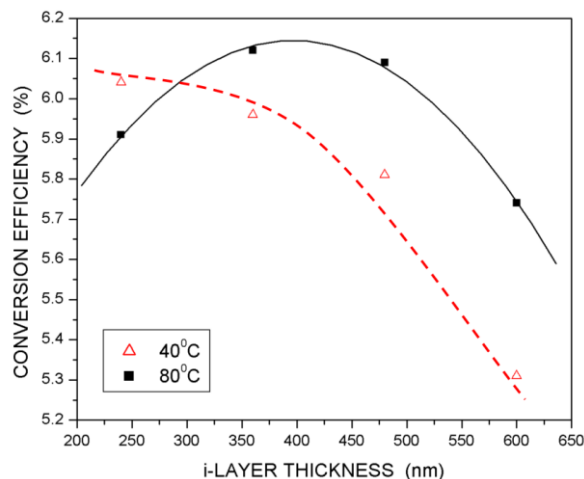


Fig. 48 Stabilized efficiencies of amorphous silicon solar cells after light soaking at 40 °C (in red) and 80 °C (in dark) as a function of intrinsic-layer thickness (Carlson, Lin & Ganguly 2000).

Part II of this manuscript aims at showing that similar optimizations that take into account the operating conditions can be found for PV devices other than those made of a-Si. The following chapter introduces a general thermal model of PV devices. This model will enable the identification of the different system characteristics (see Fig. 46) that can be optimized by using a coupled optical, electrical and thermal modeling. Chapter 8 will present examples of this kind of thermal optimizations on different system parameters (such as thicknesses of the cell and of the anti-reflection coating). Subsequently, sections 8.2 and 8.3 will illustrate that the general approach developed here can also be used for the design of solar TPV and near-field TPV systems.

7. A full thermal model of PV devices

This chapter aims at giving a detailed description of the physical mechanisms driving the thermal behavior of photovoltaic devices. By simply considering the energy balance, we know that all of the incident energy that is absorbed (i.e. neither reflected nor transmitted) and that is not converted into electricity turns into heat in the device. This is illustrated on the Sankey diagram depicted in Fig. 49 (the percentage values corresponds to the particular case of a crystalline silicon solar cell described in section 8.1, considering solar irradiation in the wavelength range $[0.3 - 1.2] \mu\text{m}$ and a cell temperature set to 25°C). To be completely exact, there is also a fraction of the incident radiative energy that is reemitted by the device. This is often negligible in today's real devices but will become more and more important as the devices' performances get closer to the radiative limit. This will be discussed in details at the end of section 7.1, which is dedicated to the presentation of the solar energy photovoltaic conversion loss processes and of the associated heat sources. In section 7.2, we will describe how the heat generated by the cell increases its operating temperature. This introduces the idea developed in chapter 8 that the heat source generated by a PV module and its specific operating conditions could be included in its optimization.

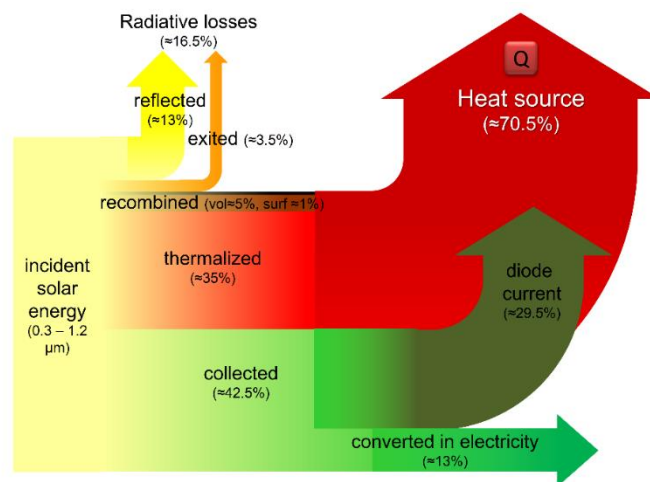


Fig. 49 Sankey diagram of the distribution of the solar energy incident upon a photovoltaic device (in the wavelength range $[0.3 - 1.2] \mu\text{m}$). The percentages reported in parentheses correspond to the case of a crystalline silicon solar cell described in section 8.1.

Fig. 49 illustrates that, in this particular example, 70.5% of the incident solar energy in the wavelength range $[0.3-1.2] \mu\text{m}$ is eventually converted into heat. Radiative (commonly called optical) losses, and electrical losses (recombinations) reduce the photoelectrical conversion efficiency and most of them contribute to the heat source. Depending on the operating conditions, this heat source is the cause of a temperature rise of the cell and thus of a thermal loss, i.e., a drop of the maximum output electrical power because the cell operates at a temperature larger than that of the ambient. Our objective is to assess in which extent thermal losses can be reduced, even at the cost of increasing radiative and/or electrical losses, in such a way that it will increase the cell efficiency when taking into consideration the operating conditions (see chapter 8). To do so, it is necessary to build an insight into the physics involved in each conversion mechanisms undergone by the incoming solar radiation and especially to look more closely at the different heat generation mechanisms. In Fig. 50, we illustrate all the existing energy conversion mechanisms taking place in a p-n junction⁵⁶. Most importantly, this representation enables to visualize directly how the radiative energy absorbed by the photogenerated electrical carriers is dissipated.

7.1. A detailed review of the energy conversion loss processes

In this section, we will discuss one by one and provide expressions for each process illustrated in Fig. 50. We will also quantify these different processes in the case of a crystalline silicon solar cell (with a given set of characteristics). This example is illustrated in Fig. 51. This representation enables to assess at a glance that, by calculating the power densities associated with the different conversion loss mechanisms, all of the incident solar power density is taken into account. Indeed, in Fig. 51, the incident solar power density corresponds to the area below the full line and the power densities of the different processes correspond to the colored areas (see Fig. 9b in Part I for a detailed description of how to read the figure). As in Part I, in order to simplify the text, in the following we will sometimes write “energy” instead of “power density” (the energy simply corresponds to the spatial and temporal integral of the power

⁵⁶ Note that similar schematics could be drawn for other PV cell architectures (such as p-i-n).

density). However, the quantified values corresponding to the example of the c-Si cell (Fig. 51) will be given in power density, knowing that the total solar irradiation power density is 1000 W m^{-2} (standard AM1.5 spectrum).

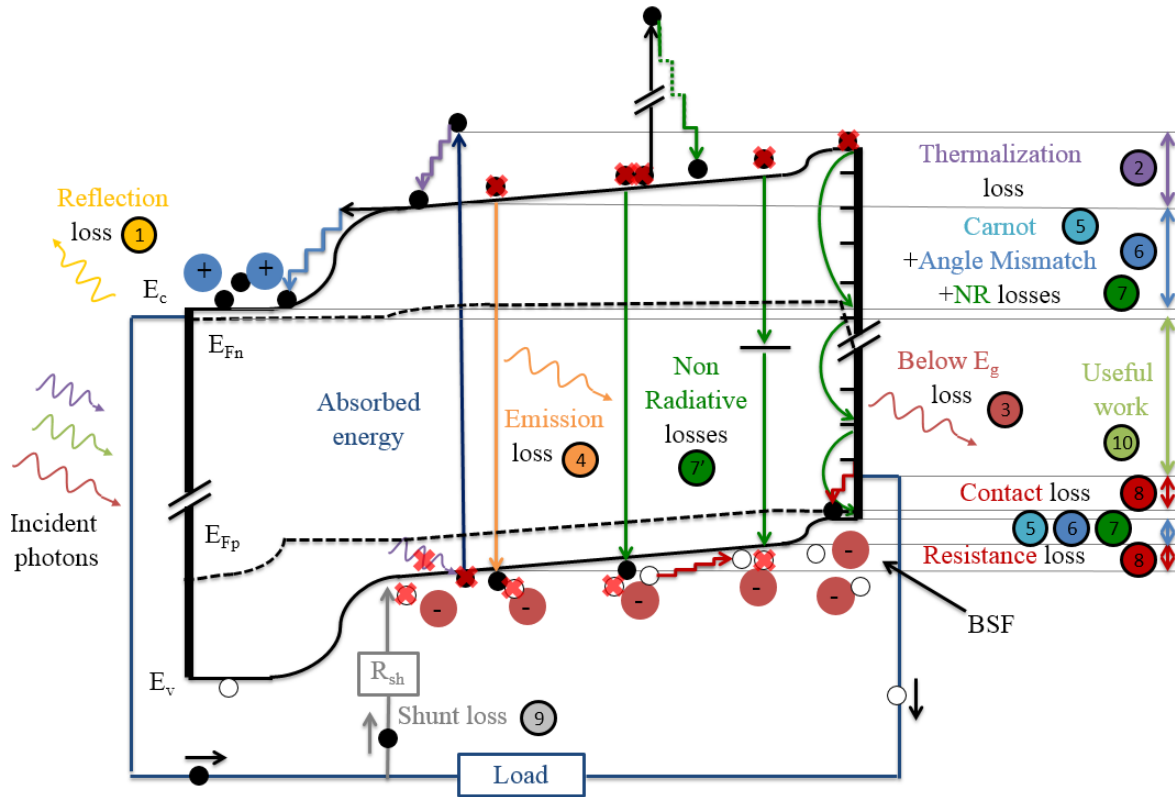


Fig. 50 p-n junction diagram showing the energy conversion loss processes in a standard single junction PV cell. Figure adapted from (Dupré, Vaillon & Green 2015b).

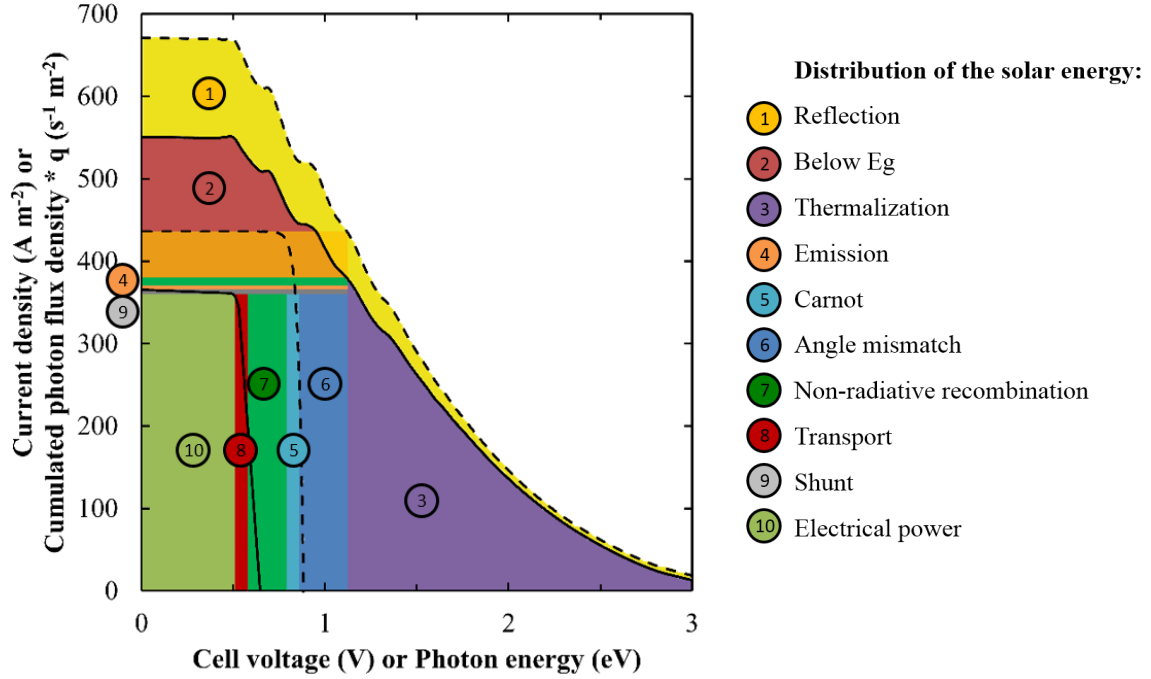


Fig. 51 Energy conversion loss processes for a c-Si cell operating at the MPP. Cumulated photon flux density of the AM1.5 spectrum (dashed line), of the transmitted fraction of this incident radiation perpendicularly through a planar c-Si surface (solid line). Ideal J-V characteristic (dashed line) and J-V characteristic of a c-Si PV cell with a planar surface (solid line). Figure adapted from (Dupré, Vaillon & Green 2015b). See Fig. 9b in Part I for a detailed description of how to read the figure.

Let us describe the different mechanisms depicted in Fig. 50 and how the energy corresponding to each of them is distributed in Fig. 51.

1 Reflection loss: a fraction of the incident photons (depicted on the left in Fig. 50) is reflected on the front surface of the device (or on the back surface and leave the cell unabsorbed). There exists several methods such as anti-reflection coatings or surface texturations that can reduce this reflection loss. Also, most of the light incident on the front metallization of a solar cell is reflected. This is one reason for the development of back-contacts solar cells. If we consider a PV module, the packing density (the area that is covered by cells divided by the total module area) has to be taken into consideration as well. In any case, it is possible to express the reflection loss (*Reflection*) as:

$$Reflection = \int_0^{\infty} R(E)PFD(E)E dE \quad (98)$$

where $R(E)$ is the spectral reflectance of the device.

The area between the cumulated photon flux density (PFD) incident on the cell (dashed line in Fig. 51) and the cumulated PFD that enters into a planar c-Si cell (full line) corresponds to the total power density of the reflected photons. Note that the areas in Fig. 51 are not directly proportional to power densities since voltage and intensity are on different scales. Also, it should be noted that Fig. 51 is simply a schematic since the values depicted are not exact for the sake of illustration. The rectangle in pale yellow illustrates the energy loss for the conversion process, i.e. the bandgap energy times the number of reflected photons that have more energy than the bandgap. In this example involving a planar c-Si surface, the reflection loss reduces the maximum short-circuit current density from 43.62 to 37.97 mA cm⁻² (-13%). Note that the reflection loss in real devices is much lower because they have anti-reflection coatings and their front surface is usually texturized (often with random pyramids).

Another optical loss is the so-called transmission loss which corresponds to the photons that pass through the cell unabsorbed (characterized by the spectral transmittance of the device $T(E)$). This loss is not depicted in Fig. 50 and not discussed in the following because in most PV modules (with the exception of bi-facial architectures), a back sheet which absorbs most of the IR photons is placed behind the cells (i.e., $T(E) \approx 0$).

2 Below E_g loss: of the incident photons that are not reflected, some don't have enough energy to excite an electron across the bandgap. These photons either leave the cell or are absorbed (by the lattice atoms or by the free-carriers or by the rear metallization...). In the case where the photons are absorbed (not depicted in Fig. 50), their energy is transferred to phonons⁵⁷ (either directly for lattice absorption or through a subsequent thermalization process in the case of free-carrier absorption): they contribute to the heat source. If the cell features a perfect rear reflector, it is easy to separate between the photons that create a heat source and those leaving the cell. Indeed, the photons that leave the cells are taken into account in the reflection loss (through the reflectance term). The photons that are not reflected in this energy range are absorbed and eventually generate heat in the cell:

$$Q_{_Below\ E_g} = \int_0^{E_g} (1 - R(E) - T(E)) PFD(E) E dE \quad (99)$$

In the example of the crystalline silicon cell (Fig. 51), the total power density of the low energy ($E < E_g$) photons is 192 W m⁻² (19.2 % of the incoming 1000 W m⁻² of the standard AM1.5

⁵⁷ Phonons correspond to modes of lattice vibrations.

spectrum). If we consider reflection, this power density (depicted in red in Fig. 51) is 141.6 W m^{-2} (16.6 % of the power density of the photons that are not reflected, i.e. 852 W m^{-2}). In an ideal scenario, all this energy eventually leaves the cell unabsorbed. However, in real modules, most of this energy contributes to heat up the module (as can be observed in Fig. 47b). It is interesting to note that reflection reduces this potential heat source.

Parasitic loss: Photons that have more energy than the bandgap can also be absorbed by the lattice atoms or by the free-carriers (not depicted in Fig. 50). In this case, these absorption mechanisms compete with interband absorption and are called parasitic absorption. Also some photons with $E \geq E_g$ can leave the cell unabsorbed if it is not sufficiently thick (with regard to its light trapping ability). The heat source corresponding to the parasitic absorption is given by:

$$Q_{_Parasitic_abs} = \int_{E_g}^{\infty} (1 - R(E) - T(E)) f_{par}(E) PFD(E) E dE \quad (100)$$

where f_{par} is the fraction of photons absorbed through the parasitic process (lattice and free-carriers). This parasitic absorption loss is neglected in the example illustrated in Fig. 51.

③ Thermalization loss: photons that excite an electrical carrier across the bandgap give away all of their energy to that carrier. However, excited carriers relax extremely quickly towards the band edges to reach their distribution of thermal equilibrium (in about 10^{-12} seconds (Würfel 2009)). During this process called thermalization, they cede the energy they have in excess of the bandgap⁵⁸ to the phonons. The associated heat source reads:

$$Q_{_Thermalization} = \int_{E_g}^{\infty} (1 - R(E) - T(E)) f_{bb}(E) PFD(E) (E - E_g) dE \quad (101)$$

where f_{bb} is the fraction of photons absorbed through the interband process. Note that because the photons that don't leave the cells have to be absorbed eventually, $f_{bb}(E) = 1 - f_{par}(E)$.

In the example of the c-Si cell (Fig. 51), the thermalization power density is 314.0 W m^{-2} (31.4 % of the incoming 1000 W m^{-2} of the standard AM1.5 spectrum). The thermalized power density of the photons that are not reflected (depicted in purple in Fig. 51) is 282.0 W m^{-2} (33.1

⁵⁸ In fact the average energy of an excited electron hole pair is roughly $E_g + 3kT_c$ (Würfel 2009). By considering only E_g , we neglect the mean kinetic energy of the carriers ($3/2 kT_c$).

% of the power density of the photons that are not reflected). Once again, it is worth noticing that reflection, while reducing the amounts of photons available to produce current, also reduces the heat source associated to the thermalization of excited carriers.

At this stage, the “excess energy” (brought by the photons absorbed through the interband process) carried by the excited carrier population corresponds to the number of excited

electrons times the bandgap energy: $E_g \int_{E_g}^{\infty} (1 - R(E) - T(E)) f_{bb}(E) PFD(E) dE$. In the

example of the crystalline silicon cell ($E_g[\text{Si}] = 1.12461$ eV at 25 °C and $f_{bb} = 1$ for $E \geq E_g$) depicted in Fig. 51, it corresponds to 50.3 % of the energy of the incident photons (AM1.5 PFD) that are not reflected.

4

Emission loss: because the carriers are excited (i.e. not in a state of thermodynamic equilibrium), the recombination rates will naturally increase. The cell voltage corresponds to the disequilibrium between electron and hole populations at either ends of the PV cell. In order to extract power from the excited carrier population, a certain disequilibrium/voltage has to be maintained in the device (see appendix 10.3). The generalized Planck’s equation (introduced in section 3.1) shows the rate of photon emission from a device caused by radiative recombination increases with the bias voltage (V):

$$Emission_rate = \frac{2\Omega_{emit}}{c^2 h^3} \int_{E_g}^{\infty} \frac{E^2}{\exp\left(\frac{E - qV}{kT_c}\right) - 1} dE \approx \frac{2\Omega_{emit}}{c^2 h^3} \exp\left(\frac{qV}{kT_c}\right) \int_{E_g}^{\infty} \frac{E^2}{\exp\left(\frac{E}{kT_c}\right)} dE \quad (102)$$

Note that a more general expression for the emission from a solar cell can be derived using Rau’s reciprocity principle (see footnote 44 in section 5.3):

$$Emission_rate_EQE = \frac{2\Omega_{emit}}{c^2 h^3} \int_0^{\infty} \frac{\overline{EQE} E^2}{\exp\left(\frac{E - qV}{kT_c}\right) - 1} dE \quad (103)$$

where \overline{EQE} is the appropriately weighted value over all angles of incident light (see section 5.3).

The energy of the emitted photons is approximately equal to the bandgap energy⁵⁹ so the power lost by emission (originally caused by radiative recombination) is:

$$Emission = E_g \times \frac{2\Omega_{emit}}{c^2 h^3} \int_{E_g}^{\infty} \frac{E^2}{\exp\left(\frac{E - qV}{kT_c}\right) - 1} dE \quad (104)$$

In the absence of parasitic absorption and non-radiative recombination, the energy lost due to radiative recombinations is equal to this emission loss. However, the radiative recombination rate can be much larger than the external photon emission rate given by eq. (102). Typically, in case of efficient light trapping, most of the photons emitted via radiative recombination are reabsorbed (in an interband or a parasitic process) within the cell and only a fraction of these photons is emitted outside the cell. For example, Fig. 52 shows the spectrally resolved probabilities of these different events for a 200- μm -thick undoped silicon wafer at 25 °C calculated in (Richter, Hermle & Glunz 2013).

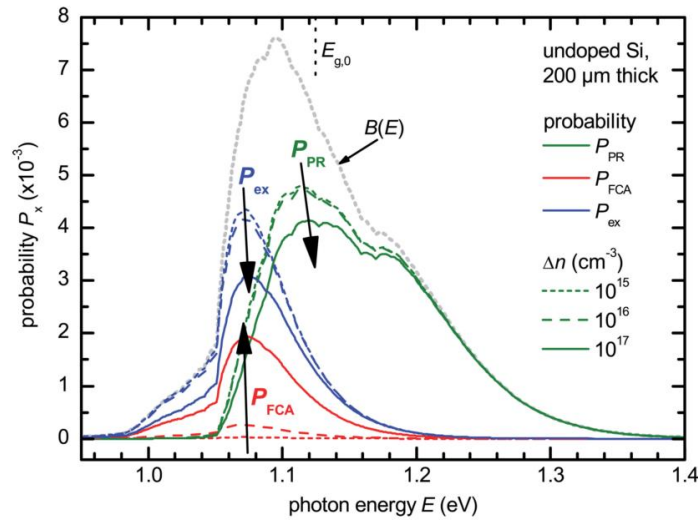


Fig. 52 Spectrally resolved probability for photon recycling P_{PR} (band-to-band transitions), Free-carrier Absorption P_{FCA} , and external emission P_{ex} of radiatively emitted photons for different injection levels Δn . Additionally shown is the normalized spectrally resolved spontaneous emission $B(E)$. Figure and legend from (Richter, Hermle & Glunz 2013). Details on the calculations can be found in the reference.

The heat source caused by the parasitic absorptions of the photons emitted via radiative recombinations in the cell is:

⁵⁹ Because the excited carriers are thermalized near the band edges, the average energy of the emitted photon is close to the bandgap energy (see the gray line in Fig. 52).

$$Q_{_Parasitic_abs_RR} = f_{par} \times RR = f_{par} \times (Emission / f_{ex}) \quad (105)$$

where RR is the total energy lost by radiative recombination, f_{par} is the fraction (or probability) of that energy that is absorbed by parasitic processes and f_{ex} is the probability that a photon emitted in the cell exits from it. Logically, the energy corresponding to radiative recombination (RR) is equal to the energy emitted out of the cell ($Emission$) divided by the fraction f_{ex} . The subscript $_RR$ indicates that this heat source corresponds to the parasitic absorption of photons emitted via radiative recombinations in the cell. Note that the parasitic absorption is dominated by Free-carrier Absorption (FCA) on this spectral range, especially when the excess carrier density (Δn) is high.

The photons that are reabsorbed in an interband process generate excited carriers that will either participate to the current or recombine either via a radiative or a non-radiative process. In the latter case, they will generate a heat source:

$$Q_{_NRR_RR} = f_{NRR} \times RR = f_{NRR} \times (Emission / P_{ex}) \quad (106)$$

where f_{NRR} is the fraction of the photons emitted via radiative recombination that generates another carrier that recombines non-radiatively. The subscript $_NRR$ indicates that this heat source stems from Non-Radiative Recombinations.

To sum up, a photon emitted via radiative recombination can either:

- leave the cell (f_{ex}),
- be absorbed by a parasitic process (f_{par}),
- be reabsorbed (interband) and generate a carrier that recombines non-radiatively (f_{NRR}),
- be reabsorbed (interband) and generate a carrier that participates to the current ($f_{current}$).

Thus, $f_{par} + f_{NRR} + f_{ex} + f_{current} = 1$.

In the example of the c-Si cell depicted in Fig. 51, we neglected parasitic absorption (f_{par}), photon recycling ($f_{current} + f_{NRR}$) and the heat sources associated to them. With these assumptions, the loss associated to radiative recombination is simply the emission loss caused by radiative recombination. Since we are detailing the energy balance at the cell's maximum power point, the energy lost by radiative emission ($Emission_{MPP}$) is given by eq. (104) with $V = V_{MPP}$:

$$Emission_{MPP} = E_g \frac{2\Omega_{emit}}{c^2 h^3} \int_{E_g}^{\infty} \frac{E^2}{\exp\left(\frac{E - qV_{MPP}}{kT_c}\right) - 1} dE \quad (107)$$

In the following, we will explain what drives the value of the voltage at the maximum power point (V_{MPP}). For now, to continue with the example of the c-Si cell depicted in Fig. 51, let us simply give the values of this emission term in different scenarios. In the radiative limit and for the AM1.5 illumination, 16 W m⁻² are emitted from the cell (1.6 % of the AM1.5 power density, $V_{MPP}=0.794$ V). In the radiative limit and for the AM1.5 illumination without the reflected photons, 13 W m⁻² are emitted from the cell (1.5 % of the power density that is not reflected, $V_{MPP}=0.790$ V). When considering all the losses described afterward, the optimal voltage (V_{MPP}) is reduced to 0.4668 V and the emission loss decreases to a negligible value: 4.6 10⁻⁵ W m⁻² (5.4 10⁻⁶ % of the power density that is not reflected). This is why the emission loss is not visible in Fig. 51.

⑤ Carnot loss: the voltage that can build in the cell is limited by the balance between generation and recombination rates. If there were no recombinations at all, all the carriers would remain excited in the conduction band and the potential energy of the carrier population would be equal to the bandgap energy. However, because there is a fundamental relation between interband absorption and emission, a solar cell necessarily emits photons. As discussed in Part I, the emission rate is minimal when the emission solid angle is equal to that of absorption of solar photons⁶⁰. In the radiative limit, the net⁶¹ recombination rate is equal to this emission rate. Also, to generate power in the load, a current has to be extracted from the device (see appendix 10.3). Interestingly, in the ideal case (radiative limit and $\Omega_{emit} = \Omega_{abs}$ ⁶²), the voltage that gives the maximum conversion efficiency (V_{MPP}) is related to the bandgap by the Carnot efficiency (Landsberg & Badescu 2000): $V_{MPP_Carnot_BB} = \frac{E_g}{q} \left(1 - \frac{T_c}{T_s}\right)$. The subscript BB indicates that this expression is derived for the incident irradiation of a blackbody at temperature T_s (where

⁶⁰ Non-concentrated direct sunlight is seen from Earth in a solid angle of 6.8 10⁻⁵ steradian. Since standard cells emit in a hemisphere, the maximum concentration factor (in air) is $\pi/6.8 \cdot 10^{-5} \approx 46200$.

⁶¹ As discussed above, the recombination rate is larger than the emission rate because emitted photons can be reabsorbed multiple times before actually exiting from the cell.

⁶² As mentioned in section 3.1, here and in the rest of the manuscript, as in (Harder & Würfel 2003), Ω corresponds to $\int \cos\theta d\Omega = \int_0^{2\pi} \int_0^\alpha \cos\theta \sin\theta d\theta d\varphi$ (where θ and φ are the polar and azimuthal angles, respectively, and α is the angle of the cone of light) because an isotropic intensity is assumed.

the subscript s stands for Sun). Note also that, as discussed in Part I, this analytical expression is derived using several approximations (see for example (Hirst & Ekins-Daukes 2011) for a discussion of the range of validity of this expression). The voltage drop between E_g/q and this “Carnot voltage” can be interpreted as the minimal price to pay to efficiently collect/separate the generated charges. Fig. 50 shows that there is a corresponding potential loss that takes place at the p-n junction (and somewhat at the back surface field that can be regarded as a selective membrane interface similarly to the p-n junction). All the carriers that circulate through the circuit (J_{MPP}) lose a fraction of their potential energy at interfaces with the selective membranes (here the p-n junction and the BSF). When going from the conduction band of the P-side to that of the N-side, the electrons accelerate by losing some of their electrical potential. Then, they quickly slow down (to their initial average thermal velocity) through collisions with the lattice atoms. This thermalization results in a heat generation term:

$$Q_{_Separation} = J_{MPP} \times (V_{bi} - V_{MPP}) \quad (108)$$

where V_{bi} is the built-in voltage of the cell (see Fig. 53). The subscript $_Separation$ symbolizes that this heat source corresponds to the loss associated to charge separation (i.e. necessary to make a current flow through the cell).

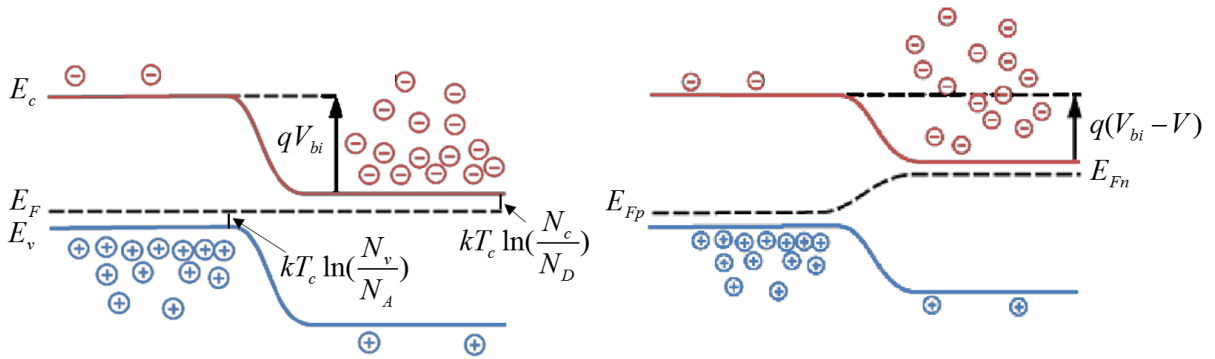


Fig. 53 Schematics of a p-n junction: a. in equilibrium; b. under an applied bias V .

For a p-n junction, $V_{bi} = \frac{E_g}{q} - \frac{kT_c}{q} \ln\left(\frac{N_c N_v}{N_A N_D}\right)$, where N_c and N_v are the effective densities of

states of the conduction and valence bands and N_A and N_D are the acceptor and donor doping densities. Thus, the built-in voltage is close to E_g/q if both sides are sufficiently doped. Consequently the potential energy lost by the excited carriers going through the p-n junction is $V_{bi} - V_{MPP} \approx E_g/q - V_{MPP}$. In this case, the heat generation associated with the minimal recombination rate in a solar cell is:

$$Q_{_Carnot_BB} = J_{MPP} \times \frac{E_g}{q} \left(\frac{T_c}{T_s} \right) \quad (109)$$

This thermalization at the p-n junction can be assimilated to Peltier heating (Breitenstein & Rakotoniaina 2005). Indeed, the voltage drop at the junction ($V_{bi} - V_{MPP}$) also corresponds to the difference of the Peltier coefficients between the P and the N doped regions ($\Pi_P - \Pi_N$). In (Pipe, Ram & Shakouri 2002), it is stated that ‘‘A material’s Peltier coefficient is related to the average energy (with respect to the Fermi energy) transported by its electrical carriers (\bar{E}_v) through $|\Pi| = \bar{E}_v / q$ ’’. The average energy of electrons in the conduction band (with respect to the quasi-Fermi energy) is ((Kittel 1996), p227):

$$\bar{E}_v = (E_C - E_{Fn} + \frac{3}{2}kT_c)^{63}, \text{ where } E_C \text{ is the conduction band edge energy and } E_{Fn} \text{ is the quasi-}$$

Fermi level of the electrons. Thus $(\Pi_P - \Pi_N) = \frac{1}{q}(E_C(P) - E_C(N)) = (V_{bi} - V_{MPP})$ (see Fig.

53). As expected, the Peltier heating at the junction reads:

$$Q_{_Peltier} = J_{MPP} \times (\Pi_P - \Pi_N) = Q_{_Separation}.$$

In the example of the c-Si cell (Fig. 51), the voltage at maximum power point cannot be

calculated from $V_{MPP_Carnot_BB} = \frac{E_g}{q} \left(1 - \frac{T_c}{T_s} \right)$ because, as already mentioned, this analytical

expression is derived for an incident spectrum from a blackbody at temperature T_s while we consider in the example the PFD of the standard AM1.5 spectrum. In this case, the maximum power point has to be found numerically. Mathematica is used to calculate the maximum of the product JV with the current density J given by the following equation:

$$\begin{aligned} J &= J_L - J_0 \exp\left(\frac{q(V + JR_s)}{kT_c}\right) - \frac{V + JR_s}{R_{sh}} \\ &= q \int_0^\infty (1 - R(E) - T(E)) f_{bb}(E) PFD(E) dE - \frac{1}{ERE} J_{0,rad} \exp\left(\frac{q(V + JR_s)}{kT_c}\right) - \frac{V + JR_s}{R_{sh}} \end{aligned} \quad (110)$$

⁶³ As mentioned before, the term $\frac{3}{2}kT_c$ corresponds to the carriers mean kinetic energy (in thermal equilibrium).

where ERE is the External Radiative Efficiency (which will be introduced later), $J_{0,rad} = q \times Emission_rate$ is the current loss associated to radiative emission, R_s and R_{sh} are the cell series and shunt resistances.

In the example illustrated in (Fig. 51), a perfect interband absorption is assumed ($f_{bb}=1$ for $E \geq E_g$) and the cell temperature (T_c) is set to 25 °C. In this ‘‘Carnot’’ configuration, $R_s=0$, $R_{sh}=\infty$, and $J_{0,rad}$ is calculated from eq. (102) with $\Omega_{emit}=1.3577 \cdot 10^{-4}$ sr (which is the solid angle of absorption of direct solar photons Ω_{abs} , see footnote 60). The maximum power point voltage (V_{MPP_Carnot}) is calculated to be 1.0588 V. It is interesting to compare the approximate analytical expression derived for a blackbody incident spectrum ($V_{MPP_Carnot_BB}$) to the voltage drop calculated numerically⁶⁴:

$$\frac{E_g[Si]}{q} - V_{MPP_Carnot} = 0.0657 \text{ V} \quad \text{to be compared with} \quad \frac{E_g[Si]}{q} \left(\frac{298.15}{5800} \right) = 0.0578 \text{ V}$$

When all the losses are taken into account (see below), the current flowing through the junction at the maximum power point is 33.89 mA cm⁻². Thus, the corresponding heat generation term ($Q_Carnot = J_{MPP} \left(\frac{E_g}{q} - V_{MPP_Carnot} \right)$) is equal to 22.3 W m⁻², which corresponds to 2.6 % of the 852 W m⁻² incident solar power density that is not reflected.

The additional recombination mechanisms (such as non-radiative processes or shunts⁶⁵) that will be described below reduce further the cell maximum power output and the voltage at which it occurs. These reductions in V_{MPP} result in an increase of the energy lost (to the phonons) at the selective membranes. Note that this energy loss is necessary to extract most of the excited carriers before they recombine so as to maximize the power output. Note also that in the case where there are transport losses (which will be described later), the voltage loss induced by charge transport ($V_{transport}$) has to be added:

$$Q_Separation = J_{MPP} \times (V_{bi} - V_{MPP} - V_{transport}) \quad (111)$$

Indeed, it is apparent in Fig. 50 that the voltage loss associated to transport resistances does not occur at the junction.

⁶⁴ At 25°C, $E_g[Si]=1.12461$ eV.

⁶⁵ Shunts can also be considered as recombination paths as they result in the de-excitation of carriers.

⑥ Angle mismatch loss: if the cell emits in a solid angle larger than the solid angle of absorption of solar photons (as is the case for the standard non-concentrated solar cells), the minimal recombination rate is larger than in the case described above (there are still only radiative recombinations). This implies that the generation/recombination balance is a function of the solid angle ratio between emission and absorption. It has been shown in Part I that, in the radiative limit and with the assumptions mentioned above, the voltage at the maximum power point is approximately equal to : $qV_{MPP_AM_BB} \approx E_g \left(1 - \frac{T_c}{T_s}\right) - k T_c \ln \left(\frac{\Omega_{emit}}{\Omega_{abs}}\right)$. The subscript $_AM$ indicates that this voltage correspond to configurations where there is an angle mismatch between absorption of collimated solar photons and cell emission. The heat generation corresponding to the voltage reduction associated to the angle mismatch (see Fig. 50) is equal to:

$$Q_AM_BB = J_{MPP} \times \frac{k T_c}{q} \ln \left(\frac{\Omega_{emit}}{\Omega_{abs}}\right) \quad (112)$$

Once again, the software Mathematica is used to find a numerical solution in our example with the AM1.5 PFD. The same conditions as in the Carnot limit are used except that the emission from the cell is now assumed to be hemispherical ($\Omega_{emit} = \pi \approx 46200 \Omega_{abs}$). This increases the dark recombination current density ($J_{0,rad}$) and thus lower the voltage at maximum power point to $V_{MPP_AM} = 0.7901$. This is 0.2687 V lower than V_{MPP_Carnot} . Once again, this value obtained numerically for an AM1.5 PFD can be compared to the analytical expression that takes into consideration a blackbody illumination: $\frac{k T_c}{q} \ln \left(\frac{\Omega_{emit}}{\Omega_{abs}}\right) = 0.2760$ V. The heat loss associated to the angle mismatch ($Q_Angle_mismatch = J_{MPP} (V_{MPP_Carnot} - V_{MPP_AM})$) is equal to 91.1 W m^{-2} (10.7 % of the incident solar power density that is not reflected, see Fig. 51).

⑦ Non-radiative recombination loss: in real PV cells, radiative recombination is not the only recombination mechanism. Several Non-Radiative Recombinations (NRR) mechanisms also impact the global generation/recombination balance of the cell. Fig. 50 illustrates the different non-radiative recombination mechanisms which have been already described in Part I. It is interesting to recall that Auger recombination is an intrinsic process that limits the ultimate

conversion efficiency of PV devices (Richter, Hermle & Glunz 2013). In all these different recombination processes the excess energy ($\approx E_g$) of the electron that goes back to the valence band is ceded to the phonons. Similarly to radiative recombinations, non-radiative recombinations reduce the current that can be extracted from the cell and limit the voltage at the maximum power point. For radiative recombination, we have separated these losses in a “current loss” (Emission) and a “voltage loss” (Carnot and Angle mismatch). For non-radiative recombination, we will use the subscripts $_J$ and $_V$ to describe the “current loss” and the “voltage loss” respectively. As in Part I, we will use the concept of External Radiative Efficiency (ERE) to quantify the non-radiative recombination losses. The ERE corresponds to the fraction of recombination events that results in the emission of a photon from the device.

Thus the rate of non-radiative recombination is: $NRR_rate = \frac{1}{ERE} \times emission_rate$. The heat generation directly associated to the NRR events is thus:

$$Q_NRR_J = E_g \times NRR_rate = E_g \left(\frac{1}{ERE} - 1 \right) \frac{2\Omega_{emit}}{c^2 h^3} \int_{E_g}^{\infty} \frac{E^2}{\exp\left(\frac{E - qV}{kT_c}\right) - 1} dE \quad (113)$$

Using the concept of External Radiative Efficiency and following the same development as in chapter 3, the following approximation can be derived (for the incident radiation of a blackbody at T_s):

$$qV_{MPP_ERE_BB} \approx E_g \left(1 - \frac{T_c}{T_s} \right) - kT_c \ln\left(\frac{\Omega_{emit}}{\Omega_{abs}}\right) - kT_c \ln\left(\frac{1}{ERE_{MPP}}\right) \quad (114)$$

It results that the heat source associated to the voltage drop caused by non-radiative recombination reads:

$$Q_NRR_V_BB = J_{MPP} \times \frac{kT_c}{q} \ln\left(\frac{1}{ERE_{MPP}}\right) \quad (115)$$

In the example depicted in Fig. 51, an ERE of 10^{-5} is assumed to mimic a commercial c-Si solar cell. Note that, in 2012, the best research c-Si cells had EREs as low as 0.56 % (Green 2012). Using once again eq. (110) (with $ERE=10^{-5}$), we calculated in our example that the non-radiative recombinations reduce V_{MPP_NRR} to 0.5054 V. Once more, it is worth noticing that the approximate analytical expression derived for a blackbody illumination gives a good approximation of the voltage drop calculated numerically. Indeed:

$$V_{MPP_AM} - V_{MPP_NRR} = 0.2847$$

using the AM1.5 solar spectrum and the diode equation, while the approximation gives with $T_c = 25^\circ\text{C}$ and $ERE = 10^{-5}$:

$$\frac{kT_c}{q} \ln\left(\frac{1}{ERE}\right) = 0.2958$$

Since the final J_{MPP} is equal to 33.89 mA cm^{-2} in the example, the heat source associated to this voltage drop ($Q_NRR_V = J_{MPP}(V_{MPP_AM} - V_{MPP_NRR})$) is 96.5 W m^{-2} (11.3 % of the incident solar power density that is not reflected, see Fig. 51).

As for the heat source corresponding to the energy directly thermalized during the non-radiative recombinations (Q_NRR_J), it cannot be calculated from eq. (113) because there is a non-null series resistance in the example. The recombination rate in the cell is always proportional to the disequilibrium in the carrier concentrations. In equilibrium, the Fermi levels of both sides of the junction are equal. Under a bias, the disequilibrium can be quantified by the difference between the quasi-Fermi levels of the majority carriers from either side of the junction ($E_{Fn}(N) - E_{Fp}(P)$). When there is no transport loss, this difference is constant through the cell and is equal to qV where V is the voltage across the cell. However, as it can be observed in Fig. 50, when there is a transport resistance, the quasi-Fermi levels of the majority carriers change across the cell so the difference ($E_{Fn}(N) - E_{Fp}(P)$) is not constant and is equal to qV only at the cell extremities. This means that the recombination rate varies across the cell and the total recombination rate is larger than if there was no transport resistance. For the calculation of the example involving the c-Si cell, the non-radiative recombination rate is estimated from eq. (110), resulting in the following approximate expression for the corresponding heat source:

$$Q_NRR_J = E_g \times NRR_rate \approx E_g \left(\frac{1}{ERE} - 1\right) \frac{J_{0,rad}}{q} \exp\left(\frac{q(V + JR_s)}{kT_c}\right) \quad (116)$$

The result is 22.5 W m^{-2} (2.6 % of the incident solar power density that is not reflected, see Fig. 51). Note that this value is somewhat overestimated because the difference between the quasi-Fermi levels of the majority carriers is smaller than $q(V + JR_s)$ in some parts of the cell (see Fig. 50).

8 Transport loss: in real solar cells, the transport of electrical carriers is not a lossless process. Along their paths, the carriers lose some of their potential energy through collisions with the lattice atoms or other carriers (as illustrated in Fig. 50). This corresponds to a potential loss proportional to the cell series resistance (R_s) and the flow of carriers ($V_{series} = R_s \times I$). The corresponding energy loss is also known as Joule heating (RI^2) and reads at the maximum power point:

$$Q_{Series} = R_s \times J_{MPP}^2 \quad (117)$$

Note that the series resistance (R_s) of a solar cell comes mainly from the semiconductor bulk resistance, that of the metallic contacts and interconnections and from the contact resistances between the semiconductor and the contacts (Green 1982).

In the example depicted in Fig. 51, a series resistance of $1.1 \Omega \text{ cm}^2$ is assumed. This value is particularly large to illustrate clearly the impact of series resistances on the shape of the J-V curve. This transport resistance results in a voltage loss of 0.0373 V and a corresponding heat generation of 12.6 W m^{-2} (1.5 % of the incident solar power density that is not reflected, see Fig. 51).

9 Shunt loss: as it has been mentioned before, shunt paths can be assimilated to recombination paths as they also result in the de-excitation of electrons (see Fig. 50). The shunt resistance (R_{sh}) of a solar cell is driven by “leakage across the p-n junction around the edge of the cell and in non-peripheral regions in the presence of crystal defects and precipitates of foreign impurities in the junction region” (Green 1982). Loss rates via shunt paths increase linearly with increasing bias/voltage (as eq. (118) indicates), contrary to most recombination rates which increase exponentially with voltage. The result of these different voltage dependences is that shunt paths effectively reduce J_{sc} and J_{MPP} but don’t impact V_{MPP} or V_{oc} (for common shunt resistance values). Thus, the heat source associated to shunt paths is:

$$Q_{Shunts} = E_g \times shunt_rate \quad (118)$$

Once again, we use the single-diode model (eq. (110)) to calculate the shunt loss rate in the example of the crystalline silicon solar cell (Fig. 51): $shunt_rate = \frac{V + JR_s}{R_{sh}}$. The shunt resistance (R_{sh}) value chosen is $240 \Omega \text{ cm}^2$ which is purposely very low in order to illustrate

clearly the effect of R_{sh} on the shape of the J-V characteristic. At the maximum power point, the shunt rate is equal to 2.10 mA cm^{-2} . The corresponding heat source is equal to 25.2 W m^{-2} (3.0 % of the incident solar power density that is not reflected, see Fig. 51).

10 Electrical power: at the maximum power point, the electrical carriers that did not recombine on their way or take shunt paths (J_{MPP}) flow through the load where they dissipate the excess potential energy they have (V_{MPP}). This result in an electrical power output (P_{MPP}):

$$P_{MPP} = J_{MPP} \times V_{MPP} \quad (119)$$

In our c-Si cell example, the maximum output electrical power of the cell is depicted by the pale green rectangle in Fig. 51. It is equal to 158.2 W m^{-2} , which corresponds to an efficiency of 18.6 % with regard to the incident solar power density that is not reflected. With regard to the total incident solar power density of the AM1.5 spectrum (1000 W m^{-2}), it corresponds to an efficiency of 15.8 %.

The expressions of the different mechanisms depicted in Fig. 50 and Fig. 51 are gathered in Table 4 while Table 5 displays the power densities and the relative fractions of these different mechanisms. The balances show that all of the incident energy is distributed in the different terms (the balances are not exactly zero because of the approximation done in eq. (116) and also possibly because of the rounding of values in the calculations; the relative error is smaller than 0.2%). In Fig. 54, pie charts are plotted to visualize the fractions of the incident power that correspond to the different mechanisms. Fig. 54a shows the percentages relative to the incident solar power density while Fig. 54b shows the percentages relative to the incident solar power density that is not reflected as in Fig. 51.

It is also possible to check the balance of the excited carrier population. The rate of interband absorption (which is also the rate of excited carrier generation) has to be equal to the sum of the current extracted and the recombination rates (radiative, non-radiative and via shunts). Indeed, in the example of the c-Si cell:

$$\begin{aligned} & Abs_bb - rec_R - rec_NRR - rec_shunts - J_{MPP} \\ & = 37.97 - 0 - 2.00 - 2.10 - 33.89 = -0.02 \text{ mA cm}^{-2} \approx 0 \end{aligned}$$

The energy balance also requires that the sum of the voltage drops correspond to the bandgap energy divided by the elementary charge, which is successfully checked in the example:

$$\frac{E_g [Si]}{q} - \Delta V_{Carnot} - \Delta V_{angle\ mismatch} - \Delta V_{ERE} - \Delta V_{R_s} - V_{mpp} \\ = 1.12461 - 0.0658 - 0.2687 - 0.2847 - 0.0373 - 0.4668 = 0.0013 \text{ V} \approx 0$$

Table 4 Expressions for the different terms of the full thermal model for PV devices.

incident power density	$Incident\ power = \int_0^{\infty} PFD(E)E\ dE$
power density not reflected	$\int_0^{\infty} PFD(E)E\ dE - \int_0^{\infty} R(E)PFD(E)E\ dE$
Reflection	$Reflection = \int_0^{\infty} R(E)PFD(E)E\ dE$
Transmission	$Transmission = \int_0^{\infty} T(E)PFD(E)E\ dE$
Below Eg	$Q_{\text{Below } E_g} = \int_0^{E_g} (1 - R(E) - T(E))PFD(E)E\ dE$
Thermalization	$Q_{\text{Thermalization}} = \int_{E_g}^{\infty} (1 - R(E) - T(E))f_{bb}(E)PFD(E)(E - E_g)\ dE$
Parasitic absorption	$Q_{\text{parasitic abs}} = \int_{E_g}^{\infty} (1 - R(E) - T(E))f_{par}(E)PFD(E)E\ dE$
Emission	$Emission_{MPP} = E_g \frac{2\Omega_{emit}}{c^2 h^3} \int_{E_g}^{\infty} \frac{E^2}{\exp\left(\frac{E - qV_{MPP}}{kT_c}\right) - 1} dE$
Carnot	$Q_{\text{Carnot}} = J_{MPP} \left(\frac{E_g}{q} - V_{MPP_Carnot} \right)$
Angle mismatch	$Q_{\text{Angle_mismatch}} = J_{MPP} (V_{MPP_Carnot} - V_{MPP_AM})$
NRR_V	$Q_{\text{NRR_V}} = J_{MPP} (V_{MPP_AM} - V_{MPP_NRR})$
NRR_J	$Q_{\text{NRR_J}} = E_g \times NRR_rate \approx E_g \left(\frac{1}{ERE} - 1 \right) \frac{J_{0,rad}}{q} \exp\left(\frac{q(V + JR_s)}{kT_c}\right)$
Transport	$Q_{\text{series}} = R_s \times J_{MPP}^2$
Shunt	$Q_{\text{shunts}} = E_g \times \frac{V_{MPP} + J_{MPP}R_s}{R_{sh}}$
Electrical power	$P_{MPP} = J_{MPP} \times V_{MPP}$

Table 5 Distribution (power densities and relative fractions) of the incident solar irradiance.

			Power density (W.m ⁻²)	% of the incident power density	% of the incident power density not reflected	
		incident power density	1000	100.0		
		incident power not reflected	852		100.0	
incident power density	not absorbed	Reflection	148	14.8		
	absorbed	heat generation	Below Eg	141.6	14.2	16.6
			Thermalization	282	28.2	33.1
			Emission	0	0.0	0.0
			Carnot	22.4	2.2	2.6
			Angle mismatch	91.1	9.1	10.7
			NRR_V	96.5	9.7	11.3
			NRR_J	22.5	2.3	2.6
			Transport	13.8	1.4	1.6
			Shunt	25.2	2.5	3.0
			Electrical power	158.2	15.8	18.6
				Balance	-1.3	-0.1

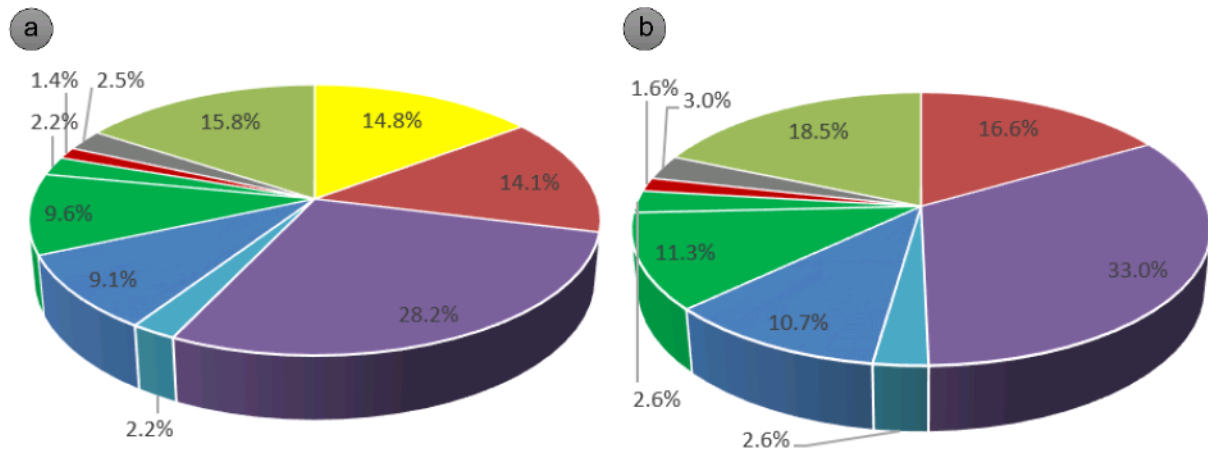


Fig. 54 Distribution of: a. the incident solar power density; b. the incident solar power density that is not reflected. Each part of these pie charts corresponds to the term from the same colour in Table 5.

An interesting remark about the heat source terms described previously concern their bias dependences. Indeed, most of the mechanisms that generate heat in the device are function of the voltage bias. In the following discussion, it must be kept in mind that the systematic heat source associated to the thermalization of photogenerated carriers and the heat source due to parasitic absorption of photons with $E < E_g$ will not be considered (the latter heat source is not systematic since it can be eliminated through infrared (IR) reflection for example). In short-circuit condition ($V_{sc}=0$), most of the excited carriers do not recombine

and through the cell and the load, $J_{sc} \approx J_{ph}$, where J_{ph} is the photogenerated current density. Since $V_{sc}=0$, the electrical energy output is null. All of the energy absorbed by the carriers (from the incident solar photons) is dissipated in Peltier heating at the p-n junction and in Joule heating through the cell. To be exact, there is a fraction of the energy carried by the photogenerated electrical carriers that is not dissipated into heat but that is emitted out of the cell via radiative recombination processes. However, this fraction is negligible in short-circuit even in the radiative limit (because $V_{sc}=0$, see eq. (102)).

In open-circuit condition ($V=V_{oc}$ and $J_{oc}=0$), the voltage is such that the recombination rate balances the generation rate. Thus there isn't any current flowing through the cell and the load. Once again, the electrical energy output is null, this time because $J_{oc}=0$. All of the energy carried by the photogenerated carriers is lost via the different recombination processes. All of these processes result in heat generation except for radiative recombination that can also result in emission from the cell. If the radiative recombination rate is negligible compared to the non-radiative recombination rate ($ERE < 10^{-3}$), the heat generation corresponds to all of the absorbed solar energy as in the short-circuit configuration. However, when the cell radiative quality is high enough ($ERE > 10^{-3}$), the heat generation can be significantly lower than the absorbed solar energy because a significant fraction of the absorbed energy is emitted by the cell. In the extreme case (the radiative limit: $ERE=1$), in open-circuit, all of the absorbed solar energy (minus the thermalization term as mentioned above) is eventually reemitted so there is no heat source in the cell apart from that resulting from thermalization and eventually from parasitic absorption (of photons above and below E_g).

These considerations are worth being noticed but the heat generation of crucial importance for cell operation is that at the maximum power point ($V=V_{MPP}$). In this configuration, some of the absorbed energy is converted into electricity, thus the heat source is smaller than in open and short-circuit conditions. In our c-Si cell example, the heat source at MPP is 18.6 % lower than in short circuit and open-circuit. This fraction corresponds to the percentage of energy absorbed that is converted into electrical power because the radiative recombinations are negligible ($ERE=10^{-5}$) and it is assumed that all of the photons below E_g are absorbed and contribute to heat the cell. Our argument is that the heat source in a PV cell is lower at MPP than in open-circuit and short-circuit conditions (especially for high efficiency cells where a large fraction of the absorbed energy is turned into electricity).

7.2. Temperature of the cell in a given environment

All the physical mechanisms resulting in the generation of heat in a PV cell have been described above. The temperature of the cell results from a balance between this heat source and the heat lost to the cell's environment. There are three types of heat transfer: conductive, convective and radiative. Several examples of cooling solutions using alternatively these different heat loss mechanisms have been presented in Chapter 6.

Conductive and convective heat transfer can be described by the following equation:

$$Q_{cond+conv} = -h(T_c - T_e) \quad (120)$$

where T_c and T_e are the temperature of the cell and the environment and h is a global heat transfer coefficient (in $\text{W m}^{-2} \text{K}^{-1}$). It is worth noticing that these heat transfer mechanisms increase linearly with the difference between the cell temperature and that of its environment. Radiative heat transfer has a different dependence on the cell temperature. In the case of gray emission and absorption, it depends on the difference between the cell temperature to the fourth power and the environment temperature to the fourth power:

$$Q_{rad} = -\varepsilon \sigma (T_c^4 - T_e^4) \quad (121)$$

where ε is the cell total emittance and σ is the Stefan-Boltzmann constant. More generally:

$$Q_{rad} = -\int_0^{\infty} \varepsilon(E) \times E \times (PFD(BB(T_c)) - PFD(BB(T_e))) dE \quad (122)$$

where $BB(T)$ is the emission from a blackbody (Planck function) at temperature T .

The heat dissipation from a solar cell depends on the heat transfer coefficient, the cell emittance, the temperature of the environment, and that of the cell itself. For a specific system in a given configuration, these parameters are fixed and the cell temperature depends on the heat generation terms described above. This is illustrated in the schematic in Fig. 46. This schematic also shows that the heat source is a function of the cell temperature (as shown in 7.1). This feedback relation implies that the operating temperature and thus the operating efficiency of a PV cell have to be calculated iteratively. In Chapter 8, several examples of original optimizations that take into account the thermal balance of the PV cell/device will be presented.

7.3. Revisiting the Normal Operating Conditions Temperature (NOCT)

In section 7.1, it has been observed that the heat source within a cell is lower at its maximum power point than it is in open and short-circuit conditions. Thus the operating temperature of a cell is also lower at MPP than in open-circuit (see section 7.2). These observations lead us to suggest a modification in the definition of the Normal Operating Conditions Temperature (NOCT). NOCT is defined as the temperature reached by the open-circuited cells in a module mounted on an open-rack with a wind velocity of $1 \text{ m}\cdot\text{s}^{-1}$, an ambient air temperature of 20°C and under a 800 W m^{-2} illumination (Ross & Gonzalez 1980). These conditions have been chosen so that the annual energy produced by a module is well approximated by its efficiency at NOCT, times the average irradiance incident on the module (in kWh/year) at the location of interest (Ross, R. G. & Smokler 1986). However, it is interesting to notice in (Ross & Gonzalez 1980) that the locations used to define these conditions (Albuquerque, Cap. Hat., Omaha, Miami) are not representative of all the climates/operating conditions that can be found worldwide. Thus, the NOCT is simply an indicator of the quality of the thermal design of the module (how efficiently it evacuates the heat it generates). From the argument above, we suggest that it could be interesting to define the NOCT as the temperature reached by a module at its maximum power point rather than in open-circuit (still in a given set of outdoor conditions). A similar suggestion was written in (Couderc et al. 2014). This would include the impact of the conversion efficiency of the device in the value of the NOCT. Thus the NOCT would correspond more closely to the temperature reached by the module in normal operating conditions since PV modules operate at MPP. Another suggestion is to define several NOCTs for different sets of outdoor conditions (ambient temperature, illumination, wind speed, ...) representative of specific climates and for different mounting configurations. This would motivate specific designs of PV modules that take into account the operating conditions.

In the following chapter, we will give some examples demonstrating that several parameters of a PV cell can be optimized by considering different sets of operating conditions and solving the coupled thermal, electrical and radiative/optical problems.

8. Beyond STC: optimizations of PV devices that take into account actual operating conditions

Nowadays, to our knowledge, the design of PV systems is always made considering the Standard Test Conditions (STC). The reason behind this is that the efficiency of PV products is rated in these STC. However, the operating conditions of PV systems vary according to the installation locations and usually differ significantly from the STC (see chapter 1). In the present chapter, based on the previous analysis of the physics of the thermal behavior of PV devices, we will show through some examples that it is possible to take into account the (mean) operating conditions of PV cells to optimize their design.

Fig. 55 reminds the general schematic of the thermal behavior of a PV device introduced in chapter 6. In chapter 7, the different mechanisms generating heat within the cell have been described. The relations between the operating temperature and the heat source and the outdoor/operating conditions have also been described. The complex relation between a cell efficiency and its operating temperature has been explored in detail in Part I. It has been shown that a large number of parameters are driving these different relations. The following section will provide some examples of optimization of different parameters in the case of standard PV cells. Subsection 8.1.1 will illustrate the impact of the cell bandgap on the thermal behavior of PV devices in different configurations. Subsection 8.1.2 will present the impact of the operating conditions on the optimization of some design characteristics of a PV cell: its thickness and the thickness of the anti-reflection coating (ARC) in the case of a crystalline silicon cell (c-Si) cell. Subsection 8.1.3 will provide some original ideas to tune the temperature coefficients of PV cells. Then sections 8.2 and 8.3 will demonstrate that our approach can also be applied to solar TPV and near-field TPV systems.

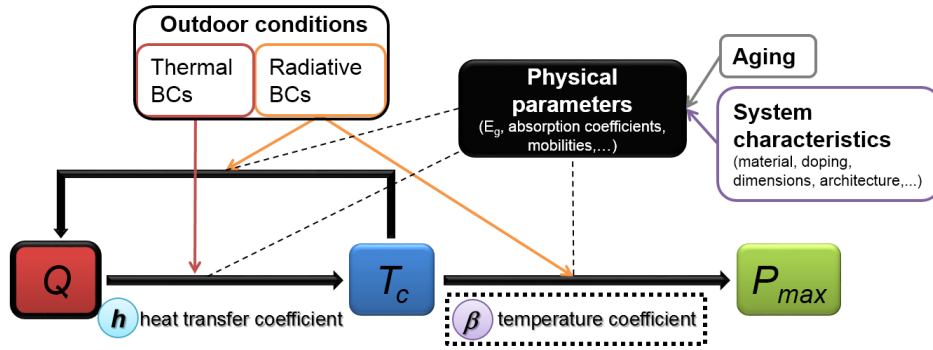


Fig. 55 Schematic of the thermal behavior of photovoltaic devices. Figure adapted from (Dupré & Vaillon 2014).

8.1. Global optimizations of standard solar PV systems

8.1.1. A thermal engineering vision on solar PV system performances

Let us illustrate the relations shown in Fig. 55 for a photovoltaic system in a simple and somewhat idealistic configuration. Let us assume that all of the useful photons ($E \geq E_g$) are absorbed and excite an electrical carrier across the bandgap and all of the photons with less energy than the bandgap (the so-called Below E_g term) are reflected. In this case, all of the incident energy generates either heat or output power except for the terms “Below E_g ” and “Emission” (described in chapter 7). Fig. 56a shows the distribution of the incident solar energy in the radiative limit calculated from the approximate expressions detailed in section 3.1 (in particular, an incident radiation from a blackbody at 5800 K is assumed here). The different losses within the area bounded by the bold line are those that generate heat in the cell. It is apparent that the heat source is smaller for larger bandgap cells (in this configuration where all of the useless photons (Below E_g) are reflected and thus are not absorbed by parasitic processes). This is mainly due to the reduction of the “Thermalization” energy with increasing bandgap. The relative contribution of the loss associated to the angle mismatch between absorption and emission also diminishes when the bandgap increases. This is because the associated voltage reduction, $\frac{kT_c}{q} \ln\left(\frac{\Omega_{emit}}{\Omega_{abs}}\right)$, does not depend on the bandgap. Another important feature in Fig. 56 is the dotted line which corresponds to the temperature coefficient of the maximum efficiency. It is

calculated numerically using the expressions introduced in chapter 3. Fig. 56a shows that temperature sensitivity of PV cells fundamentally decreases⁶⁶ (improve) with increasing bandgap. As discussed in Part I, this is due to the reduction of the losses affecting the generation-recombination balance of the cell.

In short, Fig. 56a shows that the heat source generated in a PV device⁶⁷ and its temperature sensitivity decreases (improves) with increasing bandgap. These two combined effects modify the efficiency expected in real operating conditions. Indeed, larger heat sources lead to larger operating temperatures which reduce the conversion efficiencies according to the temperature coefficients. Fig. 57 shows the results of a calculation of the operating temperature and the resulting efficiency in a given configuration (outdoor condition). In this example, a global heat transfer coefficient h of $10 \text{ W m}^{-2} \text{ K}^{-1}$ is assumed. The operating temperature of the cell (T_c) is calculated from $Q_{generated} = h (T_e - T_c)$ where $Q_{generated}$ is the heat source in the cell⁶⁸ and T_e is the temperature of the environment which is set to $25 \text{ }^\circ\text{C}$. The maximum efficiency (η_{max}) at the operating temperature (T_c) is then determined using the temperature coefficient $\beta_{\eta_{max}}$ showed in Fig. 56 via the expression $\eta_{max}(T_c) = \eta_{max}(25^\circ\text{C}) + 10^{-6} \beta_{\eta_{max}} \times (T_c - 25^\circ\text{C}) \times \eta_{max}(25^\circ\text{C})$. In Fig. 57, the results corresponding to the radiative limit ($ERE=1$) are plotted in dashed lines. The efficiencies assuming that the cell temperature is equal to $25 \text{ }^\circ\text{C}$ are plotted in green. This green line corresponds to the Shockley-Queisser limit. The efficiencies at the calculated operating cell temperatures (in the arbitrary set of conditions described above) are plotted in red. The dashed blue line corresponds to the operating cell temperatures calculated in this configuration. As expected, the operating temperature follows the same trend as the heat source (depicted in Fig. 56). Fig. 57 shows that the bandgap that leads to the maximum conversion efficiency is different from that in the Shockley-Queisser limit if the thermal operating conditions are taken into account. Of course, this shift depends on the thermal boundary conditions as is illustrated in Fig. 58 which shows cell operating temperatures and efficiencies for different values of the heat transfer coefficient. If the heat transfer coefficient is large enough, the heat generated in the cell does not bring the cell operating temperature above that of the environment. In this case, there is no interest in reducing the heat generated in the device. However, in the field, PV modules operating

⁶⁶ They decrease in absolute values since they are negative.

⁶⁷ In this specific configuration where all the photons with $E < E_g$ are reflected.

⁶⁸ Note that, for the sake of simplicity, the heat dissipated by radiation is neglected in this calculation.

temperatures rise significantly above ambient. Thus, their efficiencies could be enhanced by reducing the heat source.

Fig. 56b shows the distribution of the incident solar energy assuming a device external radiative efficiency of 10^{-5} to mimic a recent commercial cell (for indication, $V_{oc}[\text{Si}@ERE=10^{-5}] \approx 0.51$ V, see section 7.1). The additional loss terms (compared to Fig. 56a) are due to the non-radiative recombinations. Similarly to the losses associated to radiative recombinations (“Angle mismatch” in particular), these additional losses decrease with increasing bandgap. Since these losses both increase the heat source and increase (make worse) the temperature sensitivity of PV cells (compared to the radiative limit configuration, $ERE = 1$), they magnify the impact of considering the cell thermal operating conditions. This is illustrated by the full lines in Fig. 57. Once again the green line corresponds to a “standard” calculation of the efficiency that assumes that the cell temperature is set to 25 °C (which correspond to the STC). Of course, the efficiencies in this case are lower than those in the radiative limit presented above and depicted by the dashed lines. The red line corresponds to a calculation of the efficiency at the operating cell temperature derived from the heat source (see Fig. 56b) and a set of operating conditions (here, $T_e = 25$ °C and $h = 10$ W m⁻² K⁻¹). The important point for this analysis is that the gap between the green line and the red line in Fig. 57 is larger in this case (full lines, $ERE = 10^{-5}$) than in the radiative limit (dashed lines, $ERE = 1$). This means that it is especially important to consider the thermal behavior of PV modules with poor conversion efficiencies. This is because cells with poor conversion efficiencies have lower (worse) temperature coefficients (as discussed in Part I) and generate more heat since their electrical outputs are lower.

Fig. 57 also depicts the efficiencies corresponding to the bandgaps of c-Si and CdTe in the different scenarios presented above. It illustrates that while these two materials have similar efficiencies in the Shockley-Queisser limit, their thermal behaviors are quite different. These different thermal behaviors result in an advantage when considering the operating conditions for CdTe (because it has a larger bandgap than c-Si). However, Fig. 57 shows that cells made of c-Si and CdTe with EREs equal to 10^{-5} have different efficiencies at 25°C. Also, the values in Fig. 57 are calculated using the incident photon flux density from a blackbody. In order to be representative of the standard test conditions, we calculated numerically (as in section 7.1) the heat sources, the operating temperatures and the efficiencies resulting from a 1000 W m⁻² AM1.5 photon flux density. The results

are plotted in Fig. 59. In order to compare two devices with the same rated performances, we calculated that the efficiency of a c-Si cell with an ERE of 10^{-5} is equal to that of a CdTe cell with an ERE of $2.2 \cdot 10^{-7}$. Fig. 59 illustrates that, in these conditions ($ERE=10^{-5}$ and $2.2 \cdot 10^{-7}$ respectively), the c-Si cell operates at a temperature of 94 °C and an efficiency of 14.5 % while the CdTe cell operates at a temperature of 69 °C and an efficiency of 17.9 %. This somewhat rough calculation explains the advantageous energy yield advertised by First Solar which is a CdTe module manufacturer (Strevel et al. 2012). This analysis also show that improving module efficiencies result in improved energy yield in the field through the improvement of the temperature coefficients and the reduction of the generated heat sources. In its second quarter earnings call of 2015 (First Solar 2015), First Solar indicated that, based on their module efficiency roadmap, the company is expecting a significant increase of the energy advantage of their modules by the end of 2017. As for the crystalline silicon PV industry, we believe that the energy yield of industrial c-Si modules should also increase with the transition to Passivated Emitter and Rear Cell (PERC) technology⁶⁹ (Green 2015b). Note that the analysis presented above is unrealistic in that, as we have mentioned above, the assumption that all of the energy of the photons with $E < E_g$ does not generate heat in the device does not correspond to real devices⁷⁰ (see Fig. 47c). Also, this calculation, in order to be generic, does not consider all of the temperature dependent losses in present commercial solar cells (discussed in Part I). Several parameters other than the bandgap have an influence on the heat source generated within a PV cell and its temperature coefficient. For example, the following subsection will show for a crystalline silicon cell that the thickness of the cell and that of the anti-reflection coating can be optimized by considering the real operating conditions of the cell.

⁶⁹ The energy yield is expected to increase with the transition to PERC for two reasons: because STC efficiencies will be larger and because the temperature-induced losses will be lower. Indeed, larger open-circuit voltages will lead to corresponding better temperature coefficients. Additionally, the operating temperatures will be lower due to reduced heat sources because: 1. of the increased efficiencies; 2. of the increased reflection of the back-surfaces that will reduce the parasitic absorption of photons with $E < E_g$.

⁷⁰ Note that it is possible to do similar analyses assuming different hypotheses on the reflection of photons with $E < E_g$.

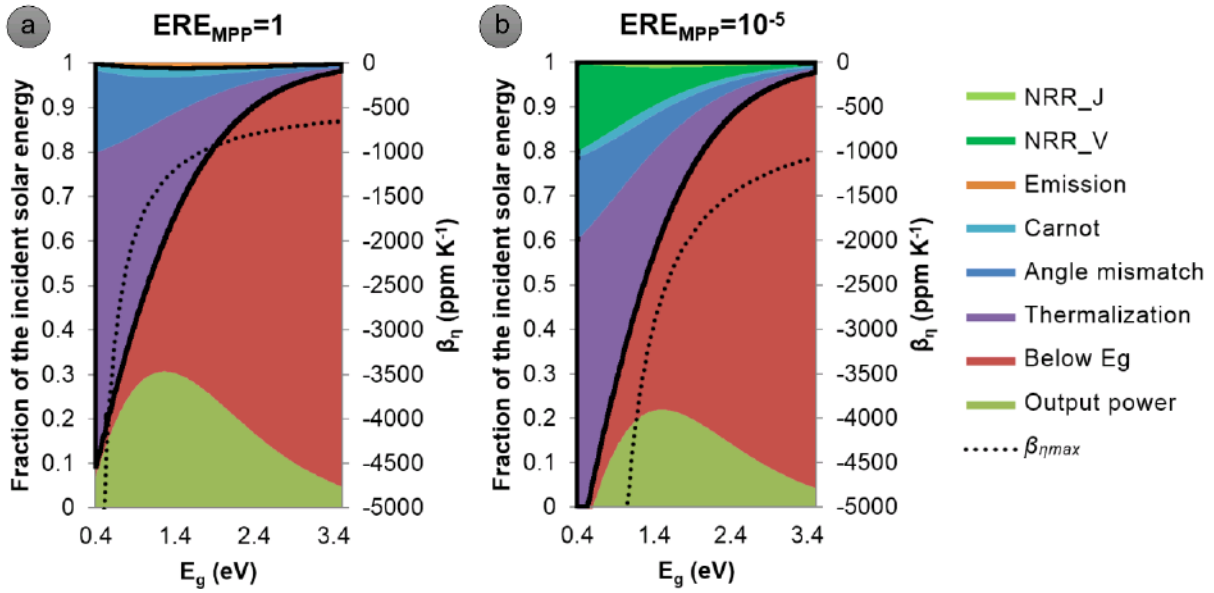


Fig. 56 Distribution of the incident solar radiation at the maximum power point for PV conversion at 300 K as a function of bandgap energy under one Sun illumination: a. in the radiative limit (as in (Hirst & Ekins-Daukes 2011)); b. considering an external radiative efficiency equal to 10^{-5} . The dotted line corresponds to the temperature coefficient calculated as a function of bandgap. The legend on the right describes the color code of the losses on both graphs.

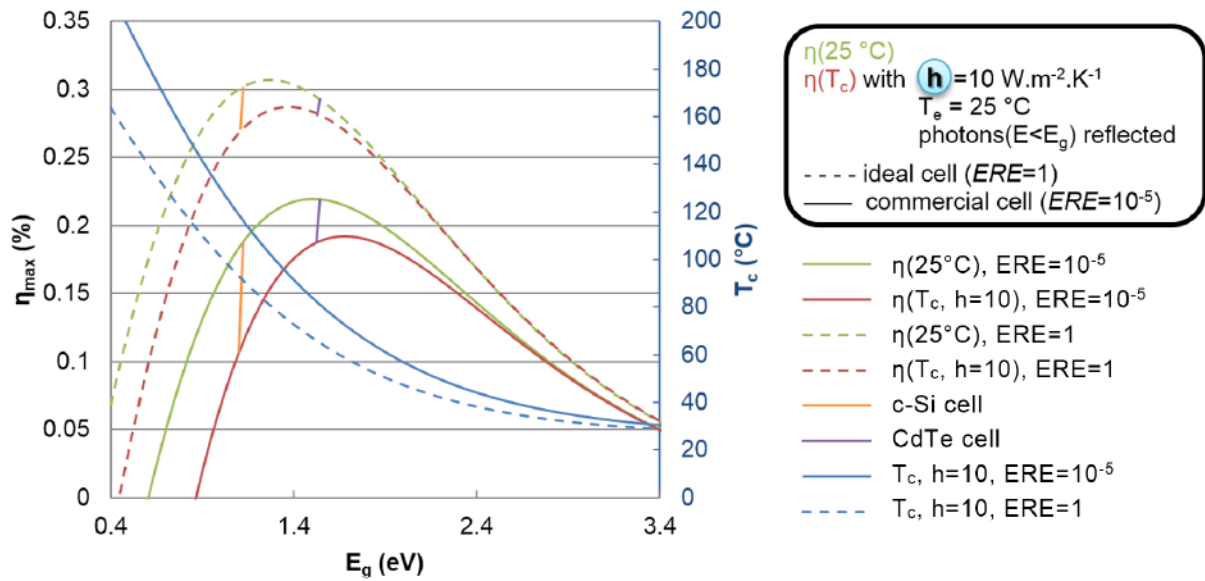


Fig. 57 Illustration of the impact of the bandgap on cell operating temperature and efficiency for an ideal cell (dotted lines) and a commercial cell (full lines). The operating temperature is plotted in blue and is derived from the heat sources depicted in Fig. 56 and an heat transfer coefficient $h=10 \text{ W m}^{-2} \text{ K}^{-1}$. The efficiencies corresponding to these operating temperatures are plotted in red while the efficiencies assuming that the cell operates at 25 °C are plotted in green. Also shown are the efficiencies of a c-Si (orange) and a CdTe (purple) cells in the different configurations.

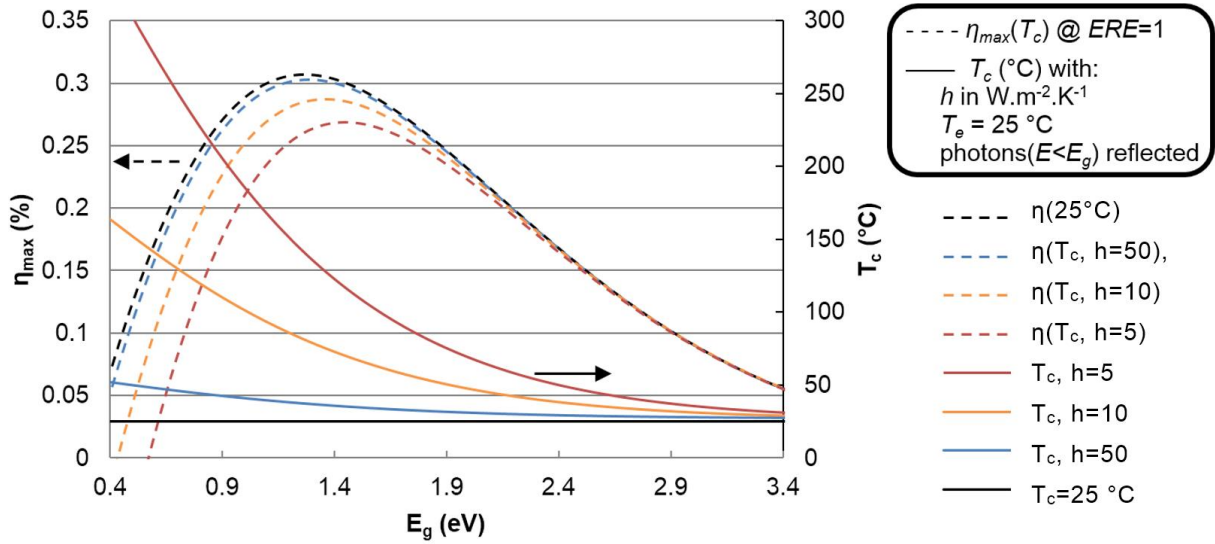


Fig. 58 Impact of the heat transfer coefficient on the cell operating temperature and the maximum efficiency in the radiative limit ($ERE=1$).

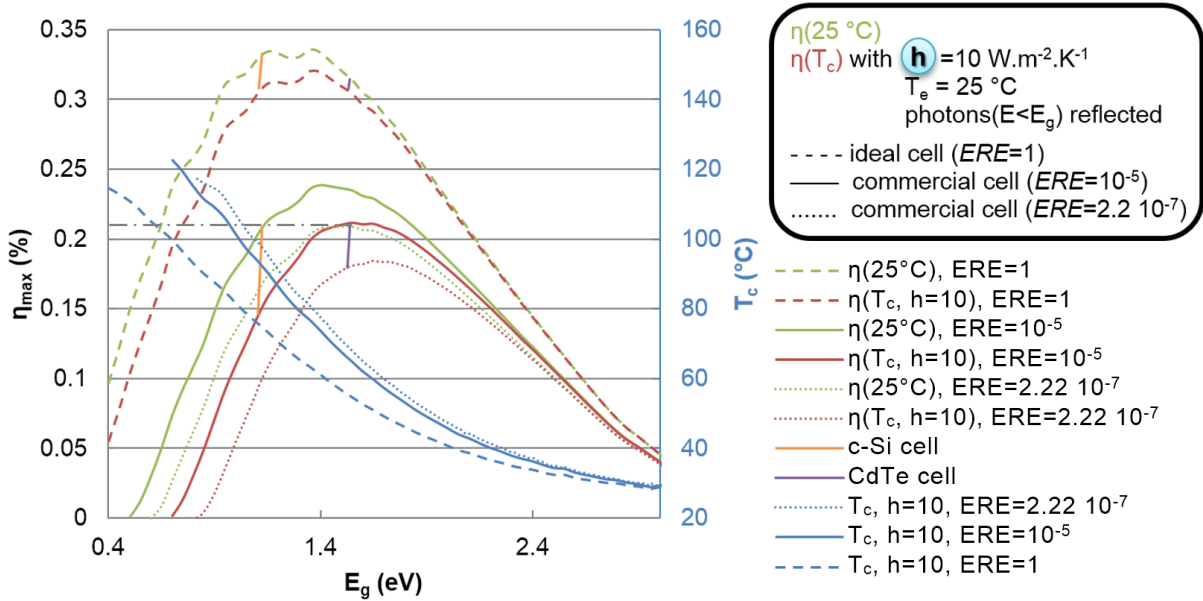


Fig. 59 Illustration of the impact of the bandgap on cell operating temperature and efficiency for an ideal cell (dotted lines), a cell with $ERE=10^{-5}$ (full lines) and a cell with $ERE=2.22 \cdot 10^{-7}$ (dotted lines) for an AM1.5 photon flux density. The operating temperatures are plotted in blue and are derived from the heat sources explained in the text and a heat transfer coefficient $h=10$ $W m^{-2} K^{-1}$. The efficiencies corresponding to these operating temperatures are plotted in red while the efficiencies assuming that the cell operates at 25 °C are plotted in green.

8.1.2. Original optimizations of the cell and ARC thicknesses of a c-Si solar cell

As we have mentioned, the design of PV systems is always made considering the Standard Test Conditions (STC). The ordinary admitted primary design rules which guide the research efforts are the following: maximizing the capture of light that generates electron-hole pairs (i.e., reducing the optical losses); minimizing the recombination of charges so that a maximum of them are collected (i.e., reducing the electrical losses). In this subsection, we will give some indications that a third criterion could be added in the design of PV cells: reducing the thermal losses. Indeed, it is well known that any temperature increase of a solar cell leads to a decrease of its maximum output power (see Part I). The usual approach to mitigate this effect is to find ways of cooling photovoltaic systems (see section 6.1). However, these methods for minimizing heat losses are but “add-on” to the photovoltaic (PV) system. The approach we propose consists in solving the coupled optical-electrical-thermal problem in order to find optimums (for different PV device parameters) that take into account a given set of operating conditions. This idea is in line with recent studies that emphasize the importance of considering the real operating conditions (Makrides, Zinsser, Norton, et al. 2012) and ultimately to design photovoltaic cells and systems in accordance to them (Kurtz, Wohlgemuth, et al. 2011).

In the following, we will consider two PV cell’s characteristics, the thickness of the cell (case A) and the thickness of the Anti-Reflection Coating (ARC) (case B), and calculate their influences on the cell conversion efficiency when the thermal problem is taken into consideration (see Fig. 55).

All the results in this subsection were obtained using a lab-made simulation tool (based on developments described in (Vaillon et al. 2006)⁷¹ and somewhat extended since then) that solves the coupled electrical, radiative, and thermal transport problems for a c-Si cell as a function of irradiation and thermal conditions. It is important to specify that we

⁷¹ We provide here some errata to the initial paper introducing the simulation tool (Vaillon et al. 2006): the parameter A_d in the expression of the interband absorption coefficient was incorrectly copied (in Table 1) from (Rajkanan, Singh & Shewchun 1979); the correct value is $1.052 \cdot 10^6$ instead of $1.052 \cdot 10^{-6}$. The surface recombination term was added while it ought to be subtracted in the thermal boundary condition and the thermal balance. In the expression of the free carrier absorption coefficient (k_{rc}) from Clugston & Basore (Clugston & Basore 1997) (equation 29) 10^4 should be replaced by 10^{-4} .

realized later, thanks to some of the research made at a later stage during this thesis, that the simulation tool was flawed. Indeed, it calculated the heat source generated as the sum of the thermalized energy and the energy directly lost through bulk and surface recombination in short-circuit ($V=0$). Several heat sources were missing (see the full thermal model of PV devices described in chapter 7). The energy thermalized by the carriers while crossing the p-n junction was not taken into account. Additionally, as explained in section 7.1, the recombination rate at MPP is much larger than that in short-circuit. However, keeping in mind that the numbers are biased because some heat sources were missing, the principles of the methodology presented afterwards are sound. Thus, we will present some results here to illustrate the concept of optimizations that take into account the system operating conditions.

The case of a standard single p-n junction crystalline silicon (c-Si) cell was selected because this technology is mature enough and, thus, all required properties and their dependences on temperature are available. The configuration considered is that of a non-encapsulated cell coated with an anti-reflection layer of silicon mono-nitride (SiN). The relevant parameters for the subsequent analyses (cell characteristics and boundary conditions) are provided in Fig. 60. The electrical (recombination velocities S_h and S_e) and radiative boundary conditions are, respectively, prescribed at the front and at the back of the cell. A fully direct AM1.5D solar irradiation with normal incidence is selected. As for the thermal boundary conditions, the external temperatures ($T_{ext,f}$ and $T_{ext,b}$) are set to 25 °C whereas the two heat transfer coefficients (h_f , h_b) [$\text{W m}^{-2} \text{K}^{-1}$] values are set to correspond to various Thermal Conditions (TC). TC1 is a condition where the temperature of the cell is set to 25 °C ($h_f = h_b = 5 \cdot 10^4 \text{ W m}^{-2} \text{K}^{-1}$). TC2 is a condition corresponding to a light breeze at the front and natural convection at the back of the cell ($h_f = 14 \text{ W m}^{-2} \text{K}^{-1}$, $h_b = 5 \text{ W m}^{-2} \text{K}^{-1}$). TC3 is a condition corresponding to natural convection at the front and insulation at the back of the cell ($h_f = 5 \text{ W m}^{-2} \text{K}^{-1}$, $h_b = 0 \text{ W m}^{-2} \text{K}^{-1}$). These different thermal conditions enable to apprehend the way outdoor and/or cooling conditions affect the optimums of the different system characteristics.

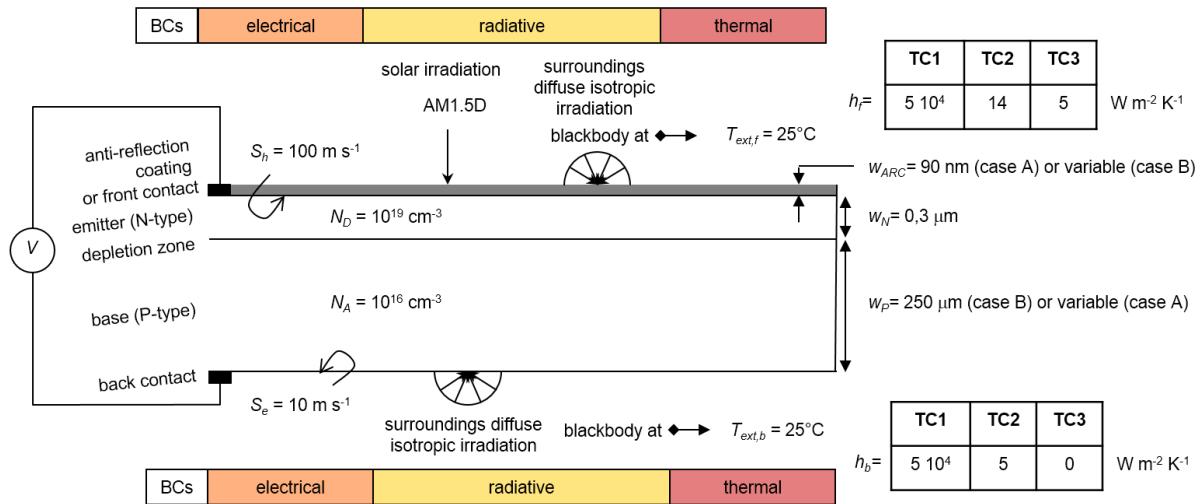


Fig. 60 Scheme of the studied configuration, boundary conditions, and parameters relevant to the analysis. Figure from (Dupré & Vaillon 2014).

Several cell parameters would be worth taking into consideration: at first, one after the other to properly understand their individual impact, and eventually all together to make a comprehensive optimization. For the sake of illustration, two cases are detailed in this subsection. In case A, the thickness of the P-layer (base) of the cell (w_P) is the variable parameter. In case B, it is the anti-reflection coating thickness (w_{ARC}).

First, the optimization of the cell thickness is analysed (case A). Since a diminution of the cell thickness would decrease the costs, research was carried out from an electrical and optical perspective to understand how the efficiency depends on it (see, for example, (Sah, Yamakawa & Lutwack 1982)). Of course, the optimum cell thickness depends on the cell optical design (such as textured surfaces or other light confinement schemes (Atwater & Polman 2010)). Here in case A, a thermal viewpoint is introduced: performances of the c-Si cell in different thermal conditions are analysed using the simulation code while the thickness of the base layer (w_P) is varied. The emitter thickness (w_N) is prescribed at $0.3 \mu\text{m}$ and results are reported as a function of the cell thickness (w , varying from 10 to $500 \mu\text{m}$) in Fig. 61. The maximum-related difference in maximum output power is reported as a function of the thickness of the cell for the three thermal conditions.

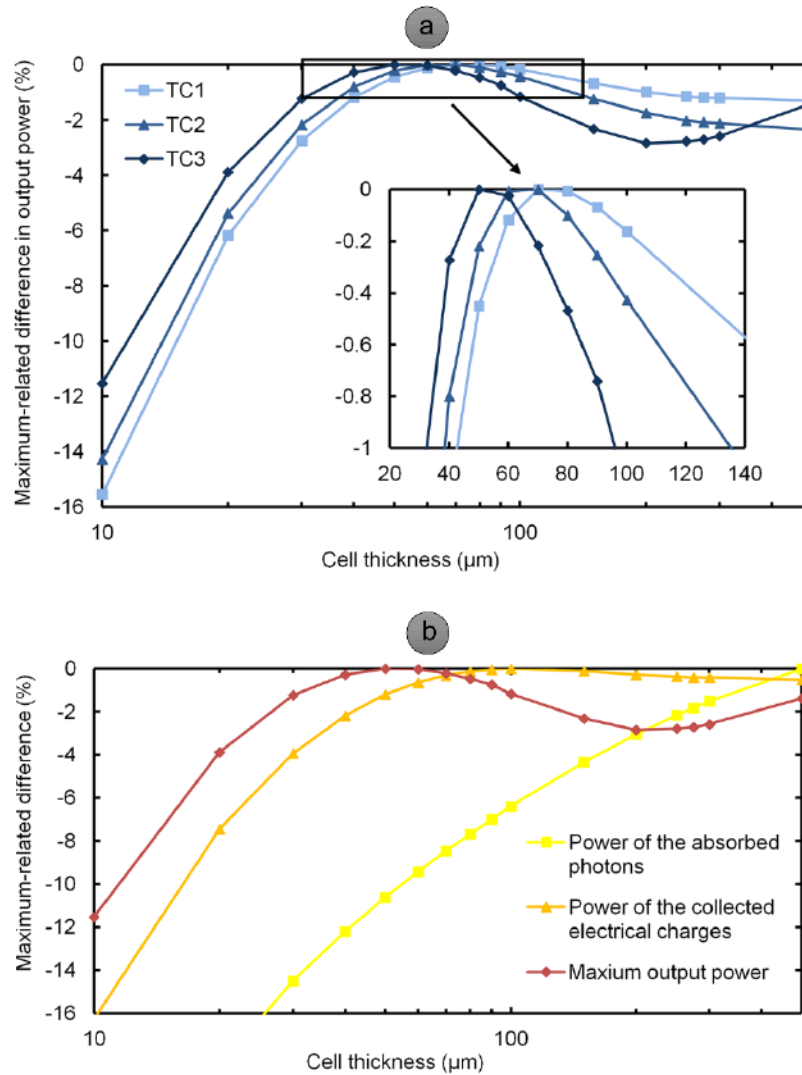


Fig. 61 Maximum-related difference as a function of the cell thickness in: a. maximum output power under the three thermal conditions (TC1, TC2, and TC3; see Fig. 60); b. power of the absorbed photons, power of the collected electrical charges (at $V=0$), and maximum output power in the case of TC3. Figure from (Dupré & Vaillon 2014).

In Fig. 61a, the maximum-related difference in maximum output power is reported as a function of the thickness of the cell for the three thermal conditions. When the temperature of the cell is maintained at 25 °C (TC1, black lines), the optimum cell thickness is about 75 μm . It is shifted to smaller values in the case of TC2 (65 μm) and TC3 (55 μm). In the Thermal Condition 1, as the heat transfer coefficient is huge, the variation of internal heat sources as a function of the cell thickness does not impact the cell temperature. In the other cases, the internal heat sources play a more important role. The reason for the decrease of optimum cell thickness in the case of TC2 and TC3 can

be explained using Fig. 61b and Fig. 62⁷². Fig. 61b displays the power of the absorbed photons, the power of the collected electrical charges (at $V=0$), and the maximum output power in the case of TC3. Fig. 62 shows the impact of the cell thickness on the spectral distributions in the range of [0.3–1.2] μm of the different transformations of the incident power in the case of TC3. In Fig. 61b, logically, the power of the absorbed photons increases together with cell thickness as more and more photons get absorbed. Note that, in current c-Si cells, most of the useful photons are absorbed in much thinner cells⁷³ thanks to textured surfaces that increase the mean optical path length. Fig. 61b shows that the power of the collected electrical charges (at $V=0$) increases with cell thickness until about 90 μm and decreases afterward. This is because, as shown in Fig. 62, carriers photogenerated in the rear of the cell (by long wavelength photons) are likely to recombine before reaching the p-n junction (and contribute to the “collected power”). These recombinations depend on the spatial generation rates (and thus on the cell optical configuration) and on the carriers diffusion lengths (and thus on several parameters such as doping and defects concentrations, temperature, mobilities). Finally, Fig. 61b shows that the optimum of maximum output power in the case of TC3 is reached at a smaller cell thickness than that corresponding to the optimum of the collected electrical charges. This is because, as can be observed in Fig. 62, the heat generated in the cell increases with increasing cell thickness because there is more absorption and thus more thermalization and also because the recombined power increases with cell thickness. Another way to put it is that increasing the cell thickness increases the short-circuit current (until a certain thickness) but also increases the heat generated within the cell. The augmentation of heat generation induces an increase of the cell operating temperature and a corresponding reduction of the maximum power. Of course, the impact of the heat source on the temperature is linked to the thermal boundary conditions. This explains why, in Fig. 61a, the optimum value of the cell thickness is smaller when the heat transfer coefficient considered is smaller ($h_{TC1} > h_{TC2} > h_{TC3}$). Eventually, the zoom in Fig. 61a shows that, in the thermal condition TC3, a cell with a “thermally optimized” thickness would produce 0.4% more than if its thickness was optimized considering a cell temperature set to 25°C. As we have mentioned, these calculations are flawed (incorrect heat source) and somewhat

⁷² An animated version of this figure illustrating more cell thicknesses is available online, [URL: <http://dx.doi.org/10.1063/1.4828367.1>].

⁷³ The average wafer thickness of commercial c-Si cells was 180 μm in 2012 (Fraunhofer 2014).

unrealistic (no texturation, no encapsulation, ...). However, we expect that a correct modeling would show similar shifts in the optimum values when considering the thermal equilibrium of the cell (because the correct heat source would show a similar trend as a function of wavelength to that considered here).

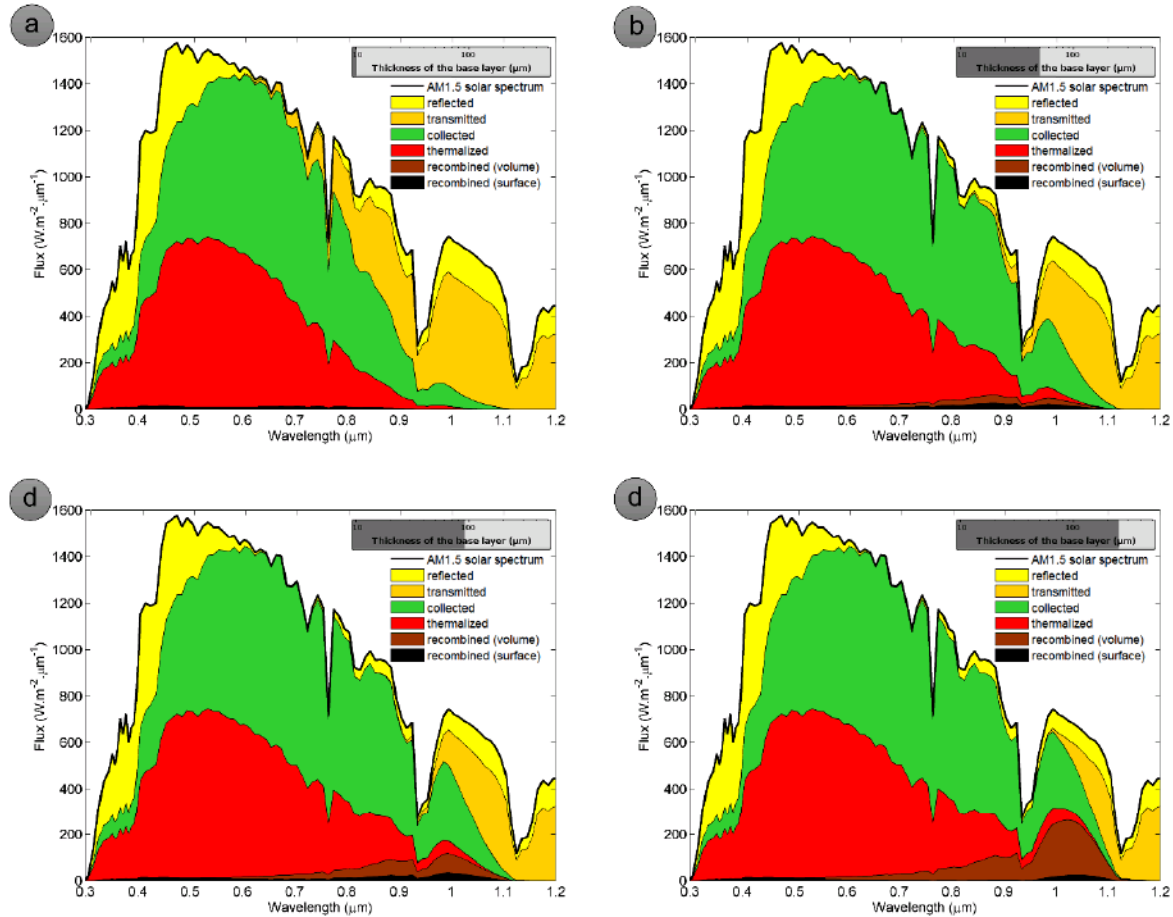


Fig. 62 Transformations of the incident power, at $V=0$, as a function of wavelength in the case of TC3 for a cell thickness of: a. $10 \mu\text{m}$; b. $50 \mu\text{m}$; c. $90 \mu\text{m}$; d. $115 \mu\text{m}$. Figure adapted from (Dupré & Vaillon 2014).

Secondly, the optimization of the anti-reflection coating thickness is analysed (case B). Research towards the reduction of the optical losses was intensively conducted in many different directions: anti-reflection coatings (Zhao & Green 1991; Chen 2001; Sun, Jiang & Jiang 2008), surface texturizations (Campbell & Green 1987; Baker-Finch & McIntosh 2011), photonic nano-structures, and plasmonics (Atwater & Polman 2010). Optical and sometimes electrical design criteria are considered in these studies while thermal rules are lacking. Here in case B, the thermal perspective is again introduced in a simple configuration. Performances of the c-Si cell are analysed in different thermal conditions

when varying the thickness of the SiN anti-reflection coating (while the thickness of the cell is set constant, $w = 250 \mu\text{m}$).

Results are reported in Fig. 63a. The optimum ARC thickness increases when the heat transfer coefficient decreases ($h_{TC1} > h_{TC2} > h_{TC3}$). The reason for this shift in optimum thickness can be explained using Fig. 63b and Fig. 64⁷⁴. Fig. 63b displays the power of the absorbed photons, the power of the collected electrical charges (at $V=0$), and the maximum output power in the case of TC3. Fig. 64 shows the impact of the ARC thickness on the spectral distributions in the range of $[0.3-1.2] \mu\text{m}$ of the different transformations of the incident power in the case of TC3. Fig. 64 shows that changing the ARC thickness corresponds to changing the wavelength at which the reflection is minimal. When the ARC thickness increases, so does the wavelength at which normal reflection is zero. In Fig. 63b, the maximum of the yellow line gives the ARC thickness that enables the absorption of the maximum useful photons ($E \geq E_g$). The maximum of the orange line, which corresponds to the maximum carrier collection (at $V=0$), is found for a smaller ARC thickness (than the maximum of the yellow line). This is because, as can be observed in Fig. 64, carriers generated by long wavelength photons are more likely to recombine. The maximum of the red line in Fig. 63b, which corresponds to the maximum output power when the cell temperature is considered, is found for larger ARC thickness (than the maximum of the orange line). This is because the heat generated in the cell by small wavelength (large energy) photons is larger than that generated by long wavelength (small energy) photons. This effect is mainly⁷⁵ due to the thermalization of the energy in excess of the bandgap. Because of this phenomenon, it is more interesting to absorb photons that don't have much energy in excess of the bandgap. This explains the observed shift of the optimum ARC thickness between the orange and the red lines in Fig. 63b. As explained for case A, the impact of the heat source on the cell temperature (and thus on its output power) is function of the heat transfer coefficient. This clarifies why we observe in Fig. 63a that the optimum ARC thickness increases when the heat transfer coefficient decreases ($h_{TC1} > h_{TC2} > h_{TC3}$). Finally, Fig. 63a shows that, in the thermal condition TC3, a cell with a "thermally optimized" ARC thickness would produce 0.4% more power than a

⁷⁴ An animated version of this figure illustrating more ARC thicknesses is available online, [URL: <http://dx.doi.org/10.1063/1.4828367.2>].

⁷⁵ In Fig. 64, the heat source due to the recombination of carriers generated by long wavelength photons is quite important. This is because the thickness of the cell chosen in this example is much larger than the carrier diffusion length (which is hopefully not the case of all solar cells).

cell with an ARC designed in the STC (in particular, a cell temperature of 25 °C). As we have already mentioned, these calculations are flawed and not really representative of present commercial c-Si cells. However, since the correct heat source would have a similar wavelength dependence, we expect that a full modeling of the heat source would demonstrate this kind of shift of the optimum ARC thickness as a function of the cell operating conditions. These shifts of the optimum ARC thickness result from the combined impacts of the internal heat source (Q), the thermal conditions (h and T_{ext}), and the temperature coefficient (β). In other words, the design of anti-reflection solutions may benefit from including the minimization of the internal heat source in the design criteria and taking into account the outdoor conditions⁷⁶.

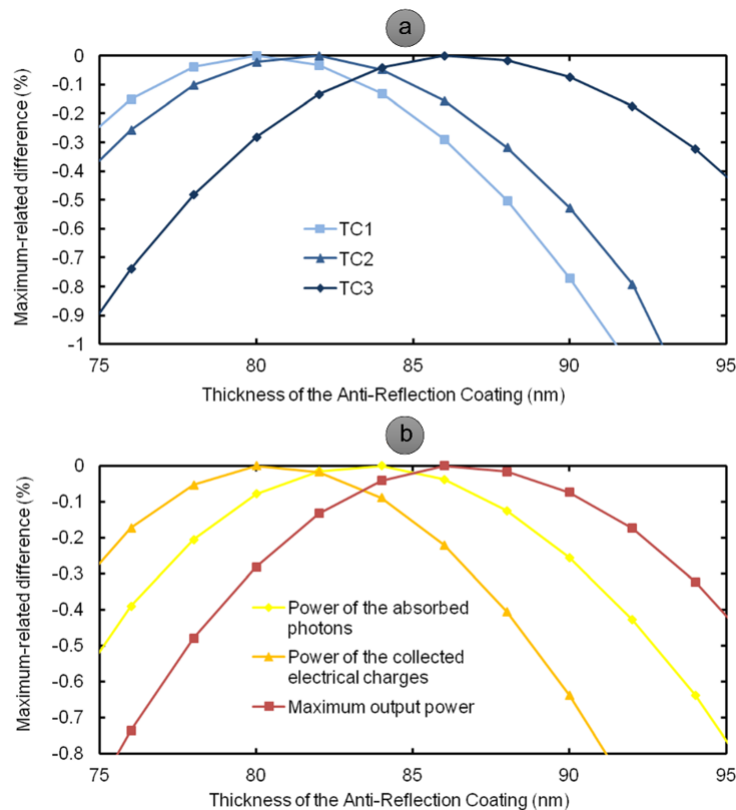


Fig. 63 Maximum-related difference as a function of the ARC thickness in: (a) maximum output power under the three thermal conditions (TC1, TC2, and TC3; see Fig. 60); (b) power of the absorbed photons, power of the collected electrical charges (at $V=0$), and maximum output power in the case of TC3. Figure from (Dupré & Vaillon 2014).

⁷⁶ This thermal engineering might be especially important for space cells. Indeed, the solar spectrum in space contains some really energetic photons (that are filtered by Earth's atmosphere). Furthermore, the heat dissipation of space cells is limited to radiative cooling. Thus it could be interesting to reflect completely the UV photons whose absorption increases slightly the short-circuit current but increases significantly the heat source.

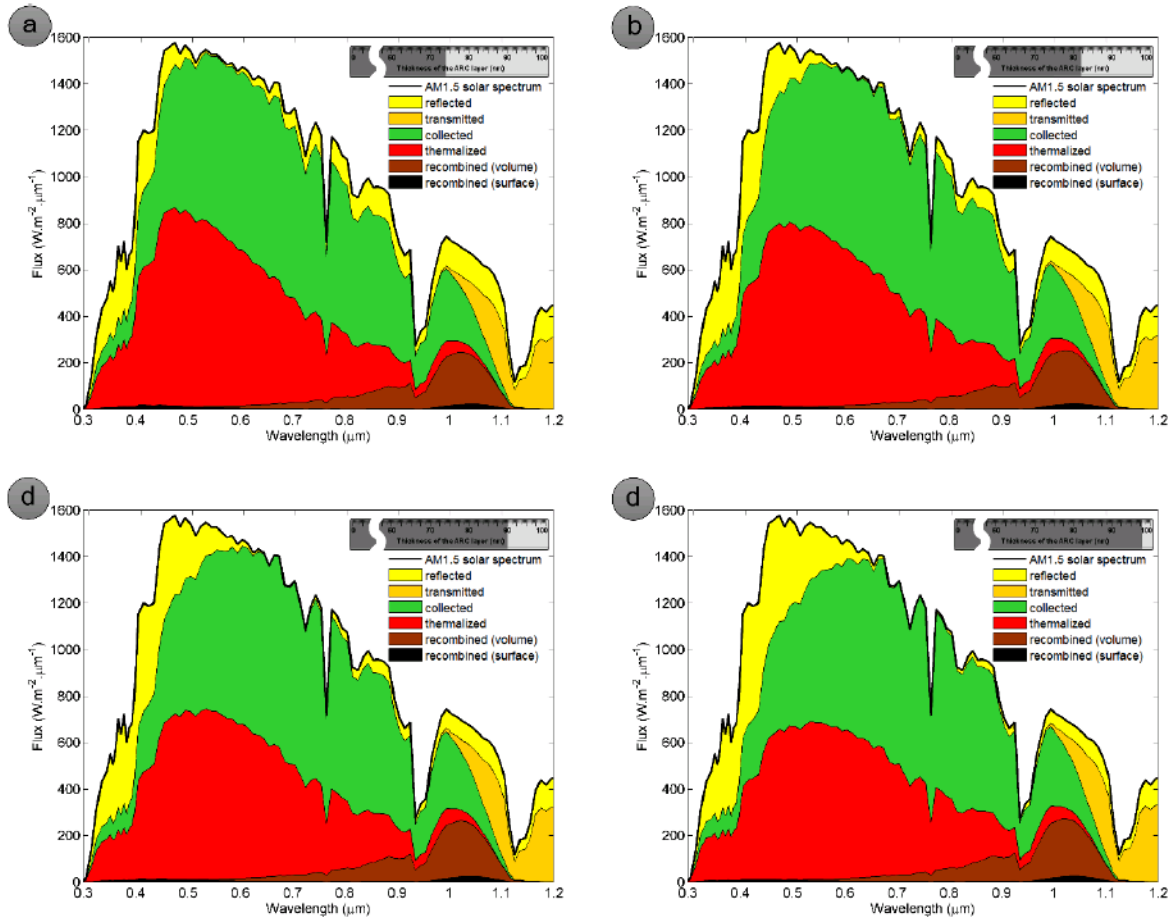


Fig. 64 Transformations of the incident power, at $V=0$, as a function of wavelength in the case of TC3 for an ARC thickness of: a. 74 nm; b. 82 nm; c. 90 nm; d. 98 nm. Figure adapted from (Dupré & Vaillon 2014).

This section has illustrated that the usual electrical and optical optimizations may be modified when a thermal criterion arbitrates. It has been shown that considering the minimization of the internal heat source, in addition to the minimization of the optical and electrical losses, modifies the optimum of the two parameters that have been studied, namely the cell thickness and the anti-reflection coating thickness. There are several other parameters that would be worth taking into consideration (doping concentrations, back surface reflector quality,...) and it would be interesting eventually to make a comprehensive optimization by considering all these different parameters simultaneously. When including a thermal criterion, the optimum of these parameters depends on outdoor conditions and might be chosen accordingly.

These “thermal optimizations” enable enhancements of the conversion efficiency through a reduction of the device operating temperature (caused by a reduction of the internal heat source). It is interesting to note that reducing the operating temperature has also a

beneficial impact on the cell durability⁷⁷. Another beneficial “side-effect” of reducing the heat source and thus the maximum temperature reached by a PV module is that it increases the number of modules that can be connected in series to one inverter. Indeed, inverters can operate on a limited range of voltage (they have low-voltage shut-down thresholds and are damaged if the voltage exceeds their high-voltage thresholds). Since they have to operate in any operating conditions, the number of modules they can manage depends on their voltage range of operation and on the maximum and the minimum temperatures reached by the modules on the course of a year (see Fig. 65). Thus limiting the maximum temperatures reached by PV modules enable to reduce the number of inverters required for a given power production. This could correspond to a significant economic gain since inverters account for about 7 % of the total price per Watt peak of utility-scale PV systems including permits, insurances, engineering, construction, etc. (Jäger-waldau 2014).

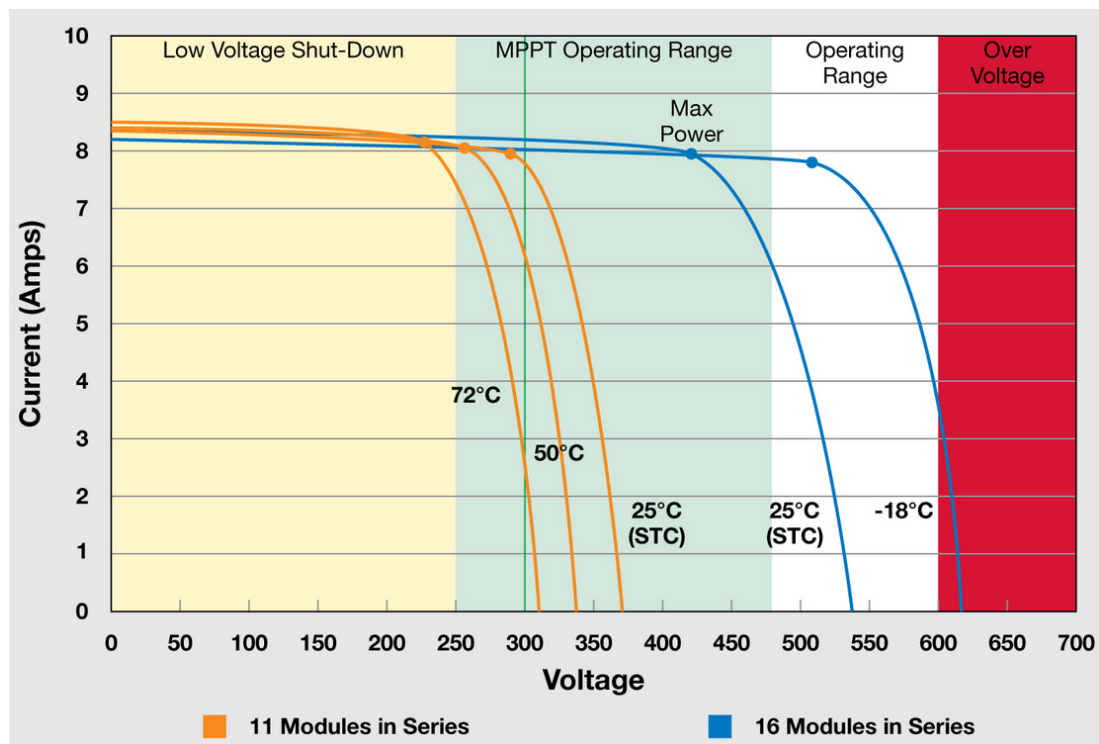


Fig. 65 Illustration of the operating range of an inverter and light I-V characteristics at different temperatures of 11 modules in series (in orange) and 16 modules in series (in blue). Figure from (HomePower 2015).

⁷⁷ We don't know if this information is up to date but in 2014, Zhu and coworkers quoted the work of Otth and Ross (Otth & Ross 1983): “the aging rate of a solar cell array doubles for every 10 K increase in its operating temperature” (Zhu et al. 2014).

8.1.3. Opportunities for tuning the temperature coefficients of PV cells

In the previous subsection (8.1.2), we have presented some examples of optimizations that consider the minimization of the heat source (and thus of the cell temperature) as a thermal criterion. Another possible “thermal criterion” appears on the general graph of the thermal problem in PV devices depicted in Fig. 55: the minimization of the temperature coefficient of the conversion efficiency. In this subsection, we will present different ideas for tuning the temperature coefficient of PV devices.

In Part I, it has been shown that the temperature coefficient of open-circuit voltage is clearly dependent (in most cases) on the open-circuit voltage (see Fig. 33). This is because the open-circuit voltage is an indication of the generation-recombination balance of the cell and because recombination rates increase (in general⁷⁸) with cell temperature. Also, the temperature coefficient of the open-circuit voltage accounts for the major part of the temperature sensitivity ($\beta_{\eta_{max}}$ or equivalently $\beta_{P_{max}}$) of good quality cells (Green 2003). This explains the quite good correlation observed on measurements between the temperature coefficient of maximum power of c-Si cells and their open-circuit voltages (see Fig. 66). This observation confirms a statement made by Green and co-workers already in 1982: “As the open-circuit voltage of silicon solar cells continues to improve, one resulting advantage, not widely appreciated, is reduced temperature sensitivity of device performance” (Green, Emery & Blakers 1982). Increasing open-circuit voltage can be achieved through the reduction of the defects concentration in the material. It can also be achieved by improving the generation-recombination balance via the concentration of light upon the device (see for example (Braun, Katz & Gordon 2012)) or by limiting the emission angle from device (Kosten et al. 2013).

⁷⁸ Radiative, Auger and most SRH recombination rates increase with increasing device temperature. However, certain defects such as the metastable defects in standard boron-doped Czochralski silicon have capture cross sections that decreases with temperature leading to a positive temperature dependence of carrier lifetimes (Rein & Glunz 2003).

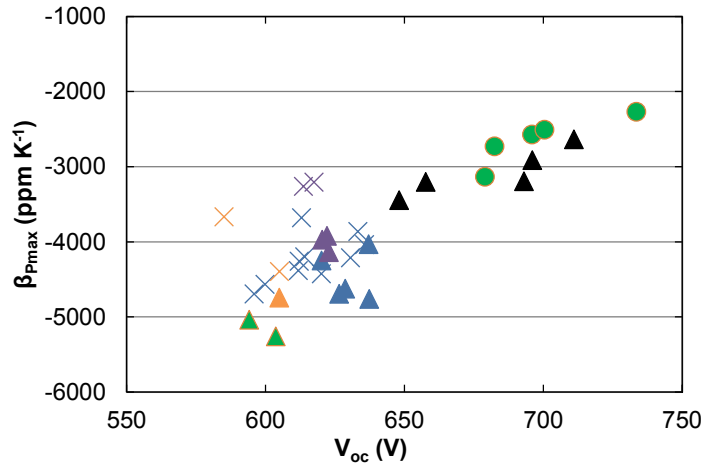


Fig. 66 Temperature coefficient of conversion efficiency as a function of open-circuit voltage. Green circles represent HIT solar cells (Mishima et al. 2011). Triangles represent conventional homo-junction c-Si solar cells: green (Mishima et al. 2011), blue (Ponce-Alcántara et al. 2014), purple (Tanay et al. 2011), orange (Xiao et al. 2014), black (Green, Emery & Blakers 1982; Green, Blakers & Osterwald 1985; Zhao et al. 1994). The x's represent solar cells made from compensated silicon feedstock: same color code.

It can be observed in Fig. 66 that the correlation between $\beta_{P_{max}}$ and V_{oc} is not really obvious for cells with relatively low open-circuit voltage. This is because additional loss mechanisms can be significant in these lower quality devices. For example, we have observed experimentally in section 5.2 that c-Si cells that suffer from incomplete light collection have large temperature coefficients of short-circuit current because they benefit especially from the positive temperature dependence of the absorption coefficient of crystalline silicon. Also, we have shown in section 5.6 that the temperature coefficient of the short-circuit current plays an important role in the overall temperature sensitivity of commercial c-Si cells (made from standard and compensated silicon feedstock). Amorphous silicon devices have particularly good temperature sensitivities because their temperature coefficients of fill factor is impacted by resistances that decrease with temperature or ‘mobility-lifetime’ products that increase with temperature (Green 2003). More generally, any loss mechanism that decreases with increasing temperature results in favorable temperature coefficients. For example, it was noticed in (Seif et al. 2015) that silicon heterojunction cells containing layers that impede carrier transport more at room temperature than at larger temperatures benefit from advantageous TC of their fill factor. Seif et al. even suggested that β_{FF} could be improved adding layers reducing the carrier transport at room temperature. Similarly, one could think of designing cells with incomplete light collection at room temperature in order to boost the temperature

coefficient of the short-circuit current. Of course, these ideas correspond to “adding losses” and thus reducing the device efficiency at room temperature and above.

In chapter 3, it has been shown that larger bandgap materials have fundamentally lower temperature coefficients. The advantageous temperature coefficients advertised by First Solar (manufacturer of CdTe modules, $E_g[\text{CdTe}] = 1.54 \text{ eV} > E_g[\text{Si}]$) and Alta Devices (manufacturer of GaAs modules, $E_g[\text{GaAs}] = 1.43 \text{ eV} > E_g[\text{Si}]$) prove that it also happens to be true for commercial devices. Of course, these temperature coefficients also depend on device quality as discussed in section 4.1.

In section 8.1, several possibilities of “thermal” optimizations of solar PV devices have been presented. In the following sections, it will be demonstrated that the same approach can be applied to other kinds of photovoltaic converters.

8.2. Global optimizations of solar TPV systems

Photovoltaic systems that convert into electricity the radiation of hot bodies other than the Sun (such as furnaces, motor engines,...) are called ThermoPhotoVoltaic (TPV) converters. Solar TPV (STPV) systems are a particular kind of TPV devices where the hot body temperature is maintained via the absorption of solar radiation. We chose a solar TPV system rather than a TPV system to exemplify our approach because in TPV converters there is a trade-off between power density and conversion efficiency whose optimum depends specifically on the application. Still, in solar TPV systems, many parameters can be adjusted to reach optimum efficiencies. Additional parameters (in comparison to standard solar PV devices) include the geometry of the system and often spectral filters. Recently, Datas and Algora wrote a really comprehensive article proposing a global optimization of solar TPV systems (Datas & Algora 2013). This article extends one of their previous work (Datas & Algora 2010) and proposes an optimization of STPV systems that includes in addition to the cell bandgap, geometrical considerations (sunlight concentration factor, absorber-to-emitter and emitter-to-cell area ratios, emitter-to-cells and cells-to-cells view factors), spectral tuning considerations (through an

absorber and an emitter cutoff energy) and non-ideality (by considering different reflectivities of the back surface reflector).

Theoretically⁷⁹, an STPV system can operate up to 85.4 % efficiency (Harder & Würfel 2003; Datas & Algora 2013). This value is largely above the maximum of the Shockley-Queisser limit for solar PV cells (41 % for full concentration). This can be achieved (theoretically) because, in TPV systems, it is possible to tune the spectrum of radiation incident on the PV converter. An ideal PV cell receiving nearly-monochromatic light with a wavelength corresponding to its bandgap energy will operate near the Carnot limit. However, limiting the emission from the hot body to the cell increases its temperature and causes its emission towards the environment (towards the Sun in the optimal case) to increase. It is possible to increase the ratio of the power emitted towards the cell to the power emitted towards the environment by increasing the emitter-to-absorber area ratio. To reach the optimal efficiency, it is also necessary to make sure that the cell-to-emitter and the emitter-to-cell view factors are equal to one. These requirements correspond to complicated three-dimensional shaped emitter structures (Harder & Würfel 2003). In this section, we study the simpler configuration of a planar STPV system where the absorber-emitter area ratio is equal to one. For the sake of simplicity, the case of a single junction PV cell is selected. The configuration analysed in this section is illustrated in Fig. 67. In the same configuration, Datas and Algora calculated that the optimal efficiency is 45.3 % (Datas & Algora 2013). This result was obtained for an absorber temperature of 1060 K corresponding to a sunlight concentration factor of 4.4. Datas and Algora noted that, while this efficiency is lower than the theoretical maximum efficiency of STPV system (85.4 %), the requirements (a concentration factor of 4.4 instead of 46200 which corresponds to maximum concentration and a temperature of the absorber of 1060 K instead of 2544 K (Harder & Würfel 2003)) and the geometrical simplicity make its practical implementation more realistic.

⁷⁹ The best experimental efficiency reported to date for solar TPV system is only 3.2 % (Lenert et al. 2014). This low value should be considered with caution as very little research was dedicated to the development of this technology.

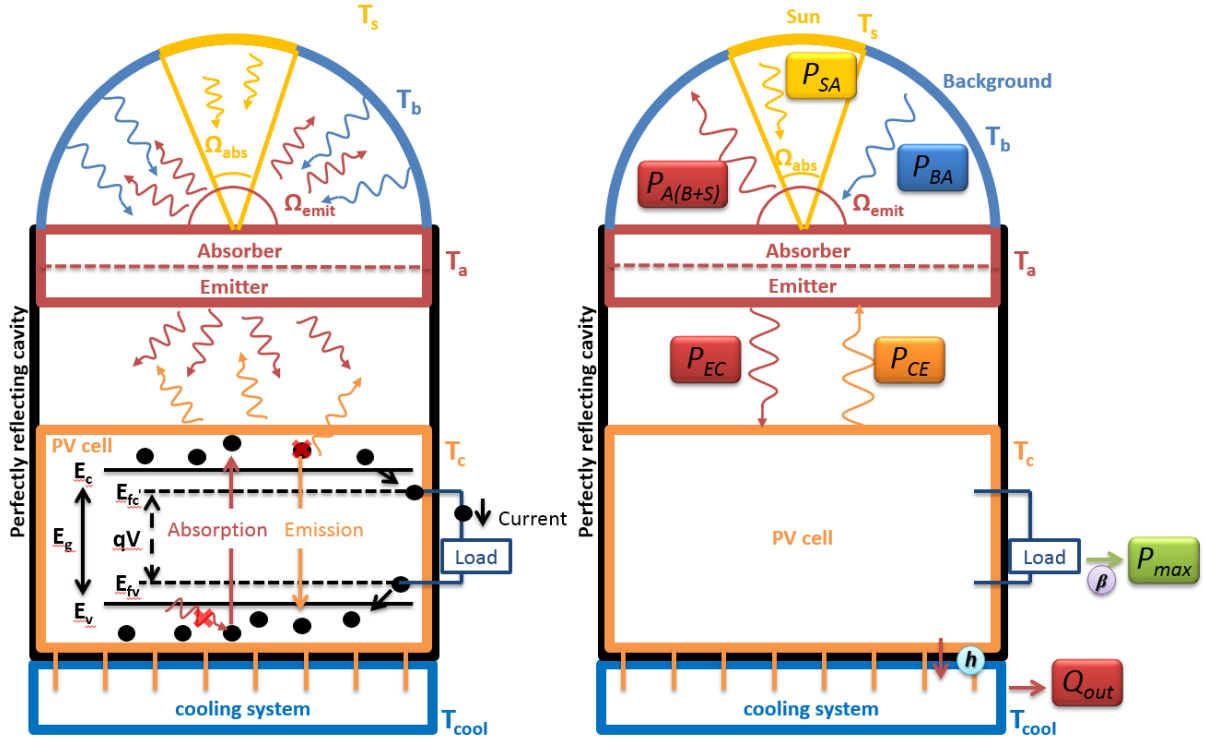


Fig. 67 Schematics of the planar solar TPV system considered in the analysis.

Let us describe in detail the configuration analysed which is similar to that of the planar STPV system with a single junction cell described in (Datas & Algora 2013). The sun, the environment, the absorber, the emitter and the cell are assumed to be blackbody thermal radiators, unless specified otherwise for specific spectral intervals. Thus the photon flux densities and the power densities exchanged per unit energy (E) and per unit solid angle (Ω) are described respectively by the following equations (see section 3.1):

$$n(E, \Omega, T, \mu) = \frac{2\Omega}{c^2 h^3} \frac{E^2}{\exp\left(\frac{E - \mu}{kT}\right) - 1} \quad (123)$$

$$p(E, \Omega, T, \mu) = \frac{2\Omega}{c^2 h^3} \frac{E^3}{\exp\left(\frac{E - \mu}{kT}\right) - 1} \quad (124)$$

where T is the body temperature, μ its chemical potential (Würfel 1982) and Ω is, as in (Harder & Würfel 2003), referred to as a solid angle but it is an integral over the solid angle of the polar angle cosine (see footnote 14 in section 3.1). Then, the spectrally integrated photon flux densities and the power densities read:

$$N(E_{\min}, E_{\max}, \Omega, T, \mu) = \frac{2\Omega}{c^2 h^3} \int_{E_{\min}}^{E_{\max}} \frac{E^2}{\exp\left(\frac{E - \mu}{kT}\right) - 1} dE \quad (125)$$

$$P(E_{\min}, E_{\max}, \Omega, T, \mu) = \frac{2\Omega}{c^2 h^3} \int_{E_{\min}}^{E_{\max}} \frac{E^3}{\exp\left(\frac{E - \mu}{kT}\right) - 1} dE \quad (126)$$

where E_{\min} and E_{\max} are the lower and the upper integration limits, respectively.

The main incident source of radiation is the Sun whose temperature (T_s) is assumed to be 6000 K. In this analysis, for the sake of simplicity, we set the concentration factor to 4.4 (which corresponds to the optimal value calculated in a similar configuration in (Datas & Algora 2013)). This corresponds to an incident solid angle (Ω_s) of $4.4 \times 6.8 \cdot 10^{-8}$. In the remaining of the hemisphere ($\Omega_e = \pi - 4.4 \times 6.8 \cdot 10^{-8}$)⁸⁰, the absorber receives a photon flux from the environment whose temperature (T_e) is set to 300 K. Note that this contribution is almost negligible.

The absorber is characterized by its temperature (T_a) and an optimized cutoff energy ($E_{\min} = E_{ca}$), i.e. energy below which photons are not absorbed (they are reflected). This optimum cutoff energy corresponds to the energy at which the power radiated from the absorber to the outdoor which comprises the Sun and the Background ($p_{A(B+S)}$) is equal to the power radiated from the outdoor to the absorber: $p_{A(B+S)}(E_{ca}) = p_{SA}(E_{ca}) + p_{BA}(E_{ca})$. This optimization of the absorber cutoff energy is illustrated in Fig. 68. It can be observed that if the cutoff would be smaller than E_{ca} , additional photons with energy smaller than E_{ca} would be allowed to be absorbed, but there would be in comparison more additional power lost by emission towards the environment (and thus the absorber-emitter equilibrium temperature would be lower). In the opposite configuration (cutoff larger than E_{ca}) the loss in absorbed power from the Sun would be detrimental to the absorber-emitter equilibrium temperature.

⁸⁰ According to the definition of the solid angle applying in this manuscript, the integral over 2π sr (the hemisphere) of the polar angle cosine is π .

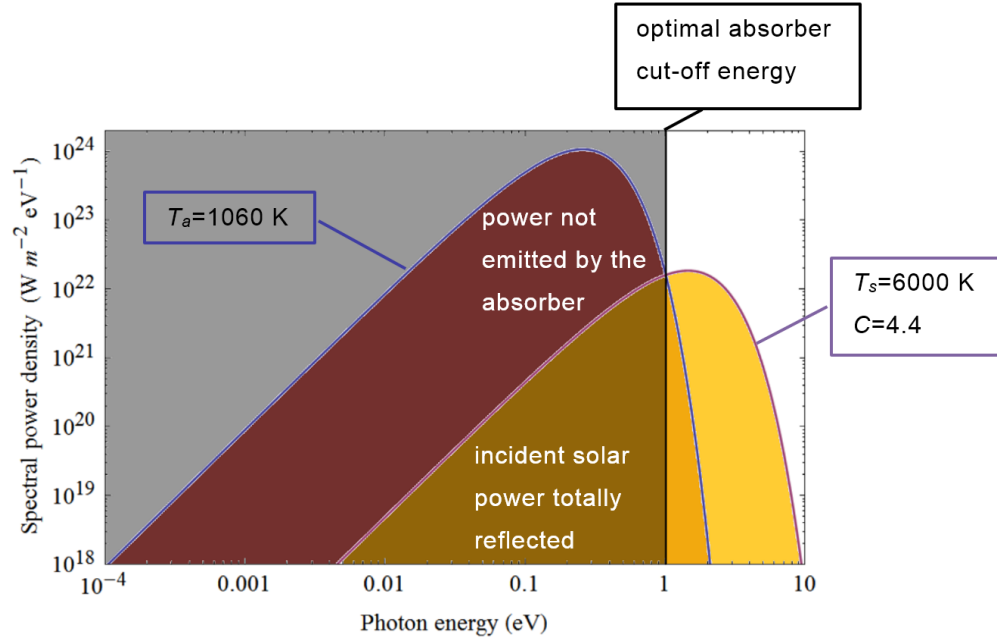


Fig. 68 Spectral power density plotted versus photon energy of a blackbody at $T_a=1060$ K emitting in a hemisphere, $\Omega_{\text{emit}}=\pi$, (blue line) and from the Sun modeled by a blackbody at $T_s=6000$ K with a concentration factor of 4.4, $\Omega_{\text{abs}}=4.4 \times 6.7 \cdot 10^{-8}$ (purple line). The optimal cutoff energy for the absorber is shown by the black vertical line. Note that this is a log-log plot so the areas are not proportional to the corresponding power densities.

The emitter temperature is the same as the absorber (T_a) but the cutoff energy ($E_{\min}=E_{ce}$) is different and is set equal to the cell bandgap energy: $E_{ce}=E_g$. This way, only photons with $E \geq E_g$, which can generate electrical carriers, are emitted towards the cell. It is equivalent to assume no cutoff energy for the emitter and that all photons with $E < E_g$ are reflected back towards the emitter (which is the configuration modeled in (Datas & Algora 2013)).

It is initially assumed that the PV cell is a single junction with bandgap (E_g) and operates in the radiative limit ($ERE=1$). There is no shading loss and no reflection loss so that all the incident photons enter into the cell. Additionally, it is assumed that all the photons with $E \geq E_g$ are absorbed by the cell and generate one (and only one) excited electrical carrier. In these conditions, the current that can be extracted (J) is equal to the difference between the absorbed and emitted photon fluxes:

$$J(E_g, T_a, T_c, V) = q(N_{EC} - N_{CE}) = q(N(E_g, \infty, \pi, T_a, 0) - N(E_g, \infty, \pi, T_c, qV)) \quad (127)$$

The excited electrical carriers are assumed to have infinite mobilities so that there is no transport loss and the chemical potential inside the cell (μ) is constant and equal to qV where V is the voltage across the cell. The voltage at maximum power point can either be

calculated numerically (as in section 7.1) or be approximated using the analytical expression introduced in section 3.1:

$$V_{MPP} \approx \frac{E_g}{q} \left(1 - \frac{T_c}{T_a} \right) - \frac{kT_c}{q} \ln \left(\frac{\Omega_{emit_cell}}{\Omega_{abs_cell}} \right) \quad (128)$$

where T_c and T_a are respectively the cell and the absorber (emitter) temperatures and Ω_{abs_cell} and Ω_{emit_cell} are respectively the solid angles of absorption and emission of the cell. In this configuration, the view factor between the cell and the emitter is assumed to

be one, thus $V_{MPP} \approx \frac{E_g}{q} \left(1 - \frac{T_c}{T_a} \right)$. The maximum output power of the PV cell is given by:

$$P_{MPP} = V_{MPP} \times J_{MPP} \approx \frac{E_g}{q} \left(1 - \frac{T_c}{T_a} \right) \left(q N \left(E_g, \infty, \pi, T_a, 0 \right) - N \left(E_g, \infty, \pi, T_c, E_g \left(1 - \frac{T_c}{T_a} \right) \right) \right) \quad (129)$$

It is only function of the bandgap and of the cell and absorber temperatures. The absorber temperature is calculated by solving the power balance of the absorber-emitter subsystem:

$$P_{SA} + P_{BA} + P_{CE} = P_{A(S+B)} + P_{EC}$$

$$\left(\begin{array}{c} P(E_{ca}, \infty, 4.4 \times 6.8 \cdot 10^{-8}, T_a, 0) \\ + \\ P(E_{ca}, \infty, \pi - (4.4 \times 6.8 \cdot 10^{-8}), T_b, 0) \\ + \\ P(E_g, \infty, \pi, T_c, E_g \left(1 - \frac{T_c}{T_a} \right)) \end{array} \right) = \left(\begin{array}{c} P(E_{ca}, \infty, \pi, T_a, 0) \\ + \\ P(E_g, \infty, \pi, T_a, 0) \end{array} \right) \quad (130)$$

In (Datas & Algora 2013), the cell temperature, T_c , is set to 300 K. In practice, a cooling system is required since there is heat generated within the cell (Q). Indeed, even though the cell operates in the radiative limit, heat is generated at the junction (see the Carnot term in section 7.1) and in the whole cell from thermalization of the excited electrical carriers (see the Thermalization term in section 7.1). In this work, we propose a method to take into account the cell temperature. This way, it is possible to design a real STPV system where the cooling system is defined (by a finite heat transfer coefficient and a temperature of the cooling fluid) or to take into account the power cost of cooling down the cell. Similarly to the absorber temperature, the cell temperature is calculated by solving the power balance of the cell:

$$P_{EC} = P_{CE} + P_{MPP} + Q_{MPP}$$

$$P(E_g, \infty, \pi, T_a, 0) = \left(\begin{array}{c} P\left(E_g, \infty, \pi, T_c, E_g\left(1 - \frac{T_c}{T_a}\right)\right) \\ + \\ \frac{E_g}{q}\left(1 - \frac{T_c}{T_a}\right)\left(qN\left(E_g, \infty, \pi, T_a, 0\right) - N\left(E_g, \infty, \pi, T_c, E_g\left(1 - \frac{T_c}{T_a}\right)\right)\right) \\ + \\ h(T_c - T_{cool}) \end{array} \right) \quad (131)$$

where h is the heat transfer coefficient between the cell and the cooling fluid and T_{cool} is the temperature of the cooling fluid. Q_{MPP} is the heat density that must be extracted from the cell by the cooling device when the cell operates at its maximum power point.

Calculating the cell temperature complicates the resolution of the power balance of the overall STPV system because the absorber-emitter and the cell temperature are interdependent. Thus, an iterative process is required to converge towards the values corresponding to the equilibrium state.

As a first original result, we calculate the cooling requirements necessary to reach the efficiency of 45.3 % calculated in this configuration in (Datas & Algora 2013). No iterative process is required in this calculation. We set (arbitrarily) T_{cool} to 290 K ($\sim 15^\circ\text{C}$) and calculate h by solving eq. (148) with $T_c=300$ K. The result is $h=230.5 \text{ W m}^{-2} \text{ K}^{-1}$. This corresponds to a heat density that needs to be evacuated equal to 2350 W m^{-2} .

Datas and Algora calculated that in the configuration presented above, with a cell temperature set to 300 K, the optimum bandgap energy of the PV cell is 0.605 eV. We obtained the same optimal value as shown by the maximum of the dashed blue line in Fig. 69. The second original result of this analysis is the calculation of the optimal bandgap taking into account the cell equilibrium temperature for different settings of the cooling system. The normalized power output of the STPV system and the cell temperature are plotted in Fig. 69 for an arbitrary cooling medium temperature of 290 K and a heat transfer coefficient of $50 \text{ W m}^{-2} \text{ K}^{-1}$ (orange line) and $20 \text{ W m}^{-2} \text{ K}^{-1}$ (red line). Fig. 69 illustrates that taking into account the cell thermal behavior has an impact on the optimum parameters of the STPV systems. Indeed, the optimal bandgap of the cell shifts from 0.605 eV when the cell temperature is kept at 300 K, to 0.680 eV when the cell temperature is regulated with a given cooling system ($T_{cool}=290$ K and $h=50 \text{ W m}^{-2} \text{ K}^{-1}$), and to 0.815 eV

with a less efficient cooling system ($T_{cool}=290$ K and $h=20$ W m⁻² K⁻¹). The reason for this shift is the same as that explaining the shift observed in case B in subsection 8.1.2. Indeed when the thermal problem is taken into account, it becomes interesting to reduce the heat generated in the cell (and especially when the heat transfer coefficient is small). Larger bandgap cells generate less heat as the Thermalization term is reduced. This is the reason why the cell temperatures plotted in Fig. 69 decrease with increasing bandgap. Note that Fig. 69 only shows the output power and the cell temperature (because they are the most relevant parameters to our analysis), but the absorber-emitter temperature and the optimal cutoff energy of the absorber varies with the cell bandgap (they were calculated for each point). For information, the values of the different optimum parameters of the planar STPV system in each configuration are gathered in Table 6.

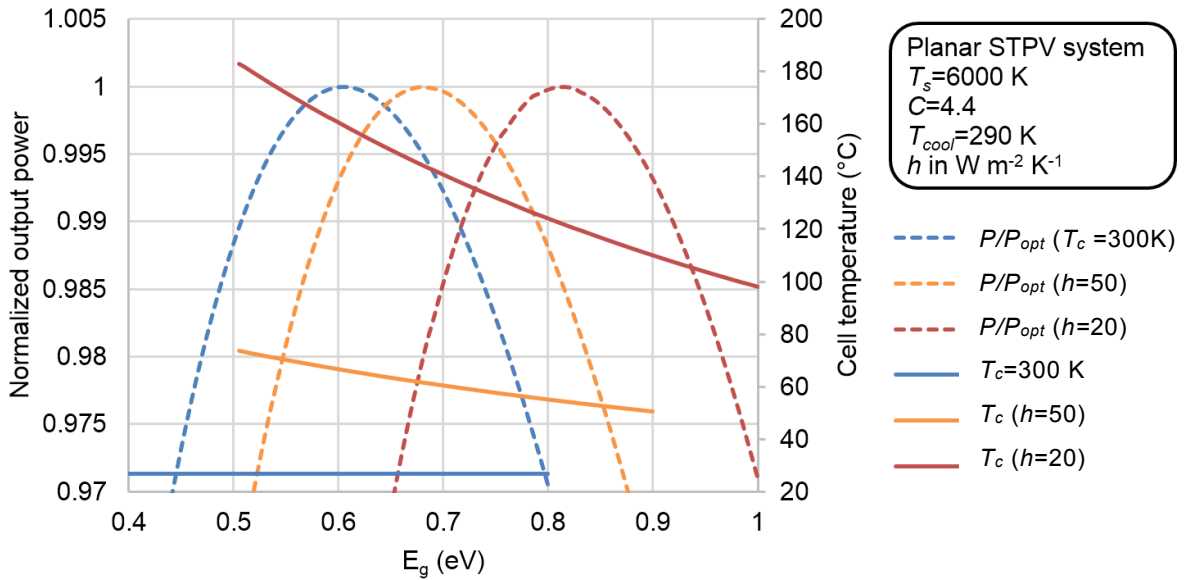


Fig. 69 Normalized output power (dashed lines) and cell temperature (full line) as a function of bandgap energy: when the cell temperature is kept at 300 K (in blue), when the cell temperature is regulated with a given cooling system ($T_{cool}=290$ K and $h=50$ W m⁻² K⁻¹) (in orange), when the cell temperature is regulated with a less efficient cooling system ($T_{cool}=290$ K and $h=20$ W m⁻² K⁻¹) (in red). The configuration of the system is described in the text and summarized in the boxed text. For simplicity, in the legend, P_{max} is noted P and $P_{opt}=\max(P_{max})$.

Table 6 Optimum values of the parameters of a planar STPV system with $C=4.4$ and $T_{COOL} = 290$ K for different thermal boundary conditions.

	η_{STPV} (%)	P_{opt} (W m ⁻²)	E_g (eV)	T_c (°C)	T_a (°C)	E_{ca} (eV)
$T_c=300$ K	45.3	3163	0.605	27	786	1.010
$h=50$ (W m ⁻² K ⁻¹)	42.9	2997	0.680	62	849	1.087
$h=20$ (W m ⁻² K ⁻¹)	38.7	2702	0.815	122	958	1.224

The third original result of this analysis is the investigation of the impact of the cell non-ideality using the concept of External Radiative Efficiency (ERE) introduced in section 4.1. The ERE corresponds to the fraction of recombinations that ends up in the emission of a photon from the cell. In the radiative limit, $ERE=1$ and in the presence of non-radiative recombination $ERE<1$ (see (Green 2012) for the values of the ERE of the best PV cells made of different semiconductors). Using the concept of ERE , an analytical expression for the voltage at maximum power point can be derived (see section 7.1):

$$V_{MPP} \approx \frac{E_g}{q} \left(1 - \frac{T_c}{T_a} \right) - \frac{k T_c}{q} \ln \left(\frac{1}{ERE} \right) \quad (132)$$

Note that the voltage at maximum power point could also be calculated numerically as in the example of section 7.1. This analytical expression, eq. (132), shows that the voltage at maximum power point decreases together with the cell ERE . This has two main consequences: it reduces the power density emitted from the cell towards the emitter; it increases the heat generated within the cell (because $E_g/q - V_{MPP}$ is larger and because of the heat source associated to the non-radiative recombinations increases).

Fig. 70 shows normalized output powers and cell temperatures as a function of bandgap energy for different values of the ERE . It can be observed that the optimum bandgap energy increases as the ERE decreases. This is due to the fact that the heat generated increases when the ERE decreases so the bandgap has to be larger in order to reduce the thermalization heat generation so that the cell is kept at a “reasonable” temperature. Additionally, the cell operating temperature has an even larger impact on the output power as the ERE decreases because the temperature coefficient gets worse with decreasing ERE (see section 4.1). As in Fig. 69, it can be observed in Fig. 70 that the cell temperature decreases with increasing bandgap. It is consistent with the fact that the thermalization heat source decreases with increasing bandgap. In Fig. 70, the cell temperature follows the same trend in the different configurations. This is because the thermal boundary conditions (T_{cool} and h) are set to the same values. Surprisingly, for the four different values of the ERE , the optimum bandgap corresponds to a cell temperature that only varies between 62 and 66 °C (see Table 7). Another initially surprising observation is that the shift of the optimum bandgap is larger when the ERE is varied from 1 to 10^{-1} than from 10^{-1} to 10^{-2} and from 10^{-2} to 10^{-3} . This can be explained by considering the power balance

of the absorber-emitter. The power emitted by the cell towards the emitter is equal to 1448 W m^{-2} when the ERE is equal to 1 and would remain equal to this value times the ERE if the other parameters (bandgap, cell and absorber temperatures) did not change in the other configurations (the values of the power actually emitted by the cell can be found in Table 7). Thus, the change from 1 to 10^{-1} has a significant impact on the energy balance of the absorber-emitter while the other drops of the ERE do not. For EREs smaller than 10^{-1} the variations of the optimum parameters are mainly due to the increase of the heat generated in the cell associated to the non-radiative recombination rate.

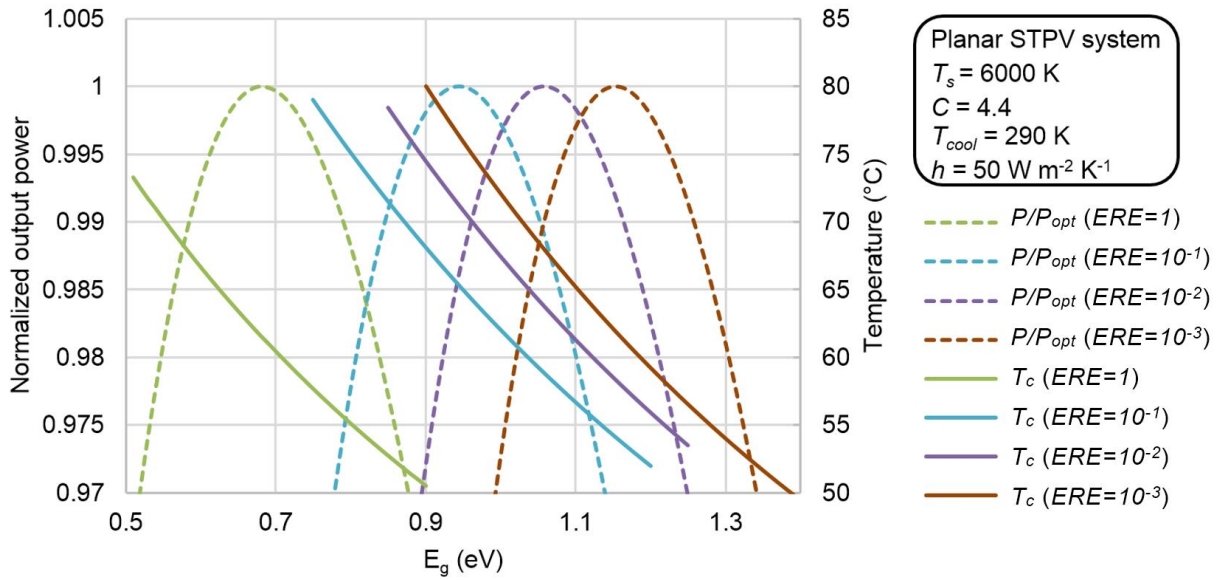


Fig. 70 Normalized output power (dashed lines) and cell temperature (full line) as a function of bandgap energy: when the cell $ERE=1$ (in green), when the cell $ERE=10^{-1}$ (in turquoise), when the cell $ERE=10^{-2}$ (in purple), when the cell $ERE=10^{-3}$ (in brown). The configuration of the system is described in the text and summarized in the boxed text.

Table 7 Optimum values of the parameters of a planar STPV system with $C=4.4$, $T_{COOL} = 290 \text{ K}$ and $H = 50 \text{ W m}^{-2} \text{ K}^{-1}$ for different values of the cell External Radiative Efficiency (ERE).

	$\eta_{STPV} (\%)$	$P_{opt} (\text{W m}^{-2})$	$E_g (\text{eV})$	$T_c (^\circ\text{C})$	$T_a (^\circ\text{C})$	$E_{ca} (\text{eV})$	$P_{CE} (\text{W m}^{-2})$
$ERE=1$	42.9	2997	0.68	62	849	1.087	1449
$ERE=10^{-1}$	30.1	2100	0.94	66	1021	1.304	91
$ERE=10^{-2}$	26.3	1839	1.06	64	1104	1.416	8
$ERE=10^{-3}$	23.6	1647	1.15	62	1165	1.501	7

In this subsection, we have presented an analysis of a planar STPV system that includes the thermal equilibrium of the PV cell. The results demonstrate the impact of the thermal boundary conditions on the optimum set of parameters for STPV power generation.

Additionally, it has been shown that the cell quality (quantified by its External Radiative Efficiency) impacts the STPV conversion efficiency both directly and through the thermal balance of the overall system. In the following subsection, another example of the importance of thermal considerations for optimizing PV systems will be given in the case of a near-field TPV converter.

8.3. Global optimizations of near-field thermophotovoltaic systems

Near-field thermophotovoltaic (NF TPV) systems are TPV converters with the emitter and the cell separated by a sub-wavelength vacuum gap (Whale & Cravalho 2002). At such a distance the transfer of thermal radiative energy can reach values orders of magnitude larger than that predicted for blackbodies because of the additional contribution of evanescent waves (Mulet et al. 2002). This so-called near-field enhancement is interesting for TPV applications as it can enable a better trade-off between efficiency and power density. This trade-off stems from the fact that the optimum conversion efficiency of a TPV system is achieved for a monochromatic irradiation upon the cell but a filtered monochromatic irradiation generally carries much less power than a broadband thermal irradiation. Thus it is interesting to find ways to transfer large power densities on small spectral intervals. This can be achieved by increasing the emitter-to-absorber area ratio (Harder & Würfel 2003) or alternatively, in the case of NF TPV, it is achieved through near-field radiative enhancement. Moreover, by using materials supporting surface polaritons, it is possible to spectrally tune thermal radiation in the near field and make it almost monochromatic (Mulet et al. 2002). The near-field enhancement enables to use simple geometrical (planar) configurations but it adds the really challenging requirement of separating two bodies by a sub-micron vacuum gap.

Numerical studies predicted a potential power output enhancement by a factor of 20 to 30 in NF TPV systems, but most of these modeling efforts only accounted for the optical (radiative) losses in the cell (Narayanaswamy & Chen 2003; Laroche, Carminati & Greffet 2006; Ilic et al. 2012; Simovski et al. 2013; Messina & Ben-Abdallah 2013; Svetovoy & Palasantzas 2014). Radiative and electrical losses in NF TPV power generators were considered for the first time by Park et al. (Park et al. 2008). A device consisting of a

tungsten radiator at 2000 K and an indium gallium antimonide ($\text{In}_{0.18}\text{Ga}_{0.82}\text{Sb}$) cell maintained at 300 K was modeled. Results revealed that electrical losses induce a drop in conversion efficiency by 5 to 10%. Francoeur et al. were the first to analyse the impacts of the coupled radiative, electrical and thermal losses on the performances of a NF TPV system made of a tungsten radiator maintained at 2000 K and an $\text{In}_{0.18}\text{Ga}_{0.82}\text{Sb}$ cell (Francoeur, Vaillon & Mengüç 2011). Results showed that the broadband enhancement of the radiative flux in the near field does not automatically lead to improved performance due to large heat generation in the cell and a corresponding increase of its temperature inducing a significant drop of the power output. It was found that a thermal management system with an extremely large heat transfer coefficient of $10^5 \text{ W m}^{-2} \text{ K}^{-1}$ was required to maintain the cell at room temperature for nanometer-size gaps in order to obtain performances similar to those of Park et al. It is thus clear that taking into consideration the cell thermal equilibrium is critical when designing NF TPV power generators. Fig. 71 illustrates the reduction of the near-field enhancement associated to the thermal equilibrium of the cell (for different values of the heat transfer coefficient) for a NF TPV system made of a tungsten radiator maintained at 2000 K and an $\text{In}_{0.18}\text{Ga}_{0.82}\text{Sb}$ cell.

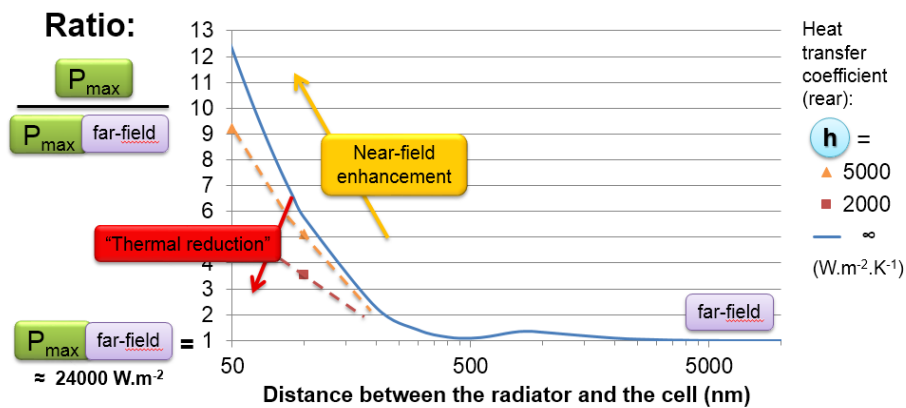


Fig. 71 Power output (normalized to its value in the far field) plotted as a function of the distance between the radiator and the cell for different values of the heat transfer coefficient of the cooling system of the cell. This graph illustrates that the near-field enhancement is reduced for realistic values of the heat transfer coefficient. Calculations from the work reported in (Francoeur, Vaillon & Mengüç 2011).

In a recent study, based on the modeling developed in (Francoeur, Vaillon & Mengüç 2011), we analysed the impacts of radiative, electrical and thermal losses on the performances of NF TPV power generators consisting of a gallium antimonide cell paired

with a broadband tungsten or a radiatively-optimized Drude radiator⁸¹ (Bernardi et al. 2015). The results show that the key limiting factors for the Drude and tungsten-based devices are respectively the recombination of electron-hole pairs at the cell surface and the thermalization subsequent to the absorption of photons with energies larger than the cell bandgap. Additionally, a guideline for designing a high energy cutoff above which radiation from the emitter has a net negative effect on NF TPV power output due to the thermal losses is proposed. It is summarized hereafter.

The characteristics of the modeled system are presented in Fig. 72. The NF TPV device consists of a tungsten radiator at 2000 K and an indium gallium antimonide ($\text{In}_{0.18}\text{Ga}_{0.82}\text{Sb}$) cell at temperature T_c separated by a vacuum gap of 10 nm. The cooling device is characterized by a heat transfer coefficient, $h=10^4 \text{ W m}^{-2} \text{ K}^{-1}$, and a temperature of the cooling medium, $T_{cool} = 293 \text{ K}$ ($\sim 20 \text{ }^\circ\text{C}$). The cell temperature is determined by calculating the power densities of the heat sources generated within the cell (Q) and the heat flux exchanged by the cell with the cooling system (Q_{out}). In order to avoid the parasitic absorption of the photons with $E < E_g$, a low energy cutoff is set to 0.66 eV which is equal to the cell bandgap energy at 448 K⁸². The value of the high energy cutoff is varied and the resulting cell temperature and maximum output electrical power (P_{max}) are shown in Fig. 73a. It can be observed that the output electrical power reaches a maximum for an optimal high energy cutoff of about 1.45 eV. This optimum is the result of a trade-off between the useful radiation power and the heat associated to the thermalization of the photogenerated electrical carriers. On the one hand, reflecting photons causes the number of excited carriers to decrease but, on the other hand, it causes a decrease of the heat generated which induces a lower cell temperature and thus a lower temperature-induced electrical power reduction. This explains why, in Fig. 73b, when the high energy cutoff increases, the cell current, J_{max} , increases (because less photons reflected) while the cell voltage, V_{max} , decreases (because the cell temperature increases as can be seen in Fig. 73a).

⁸¹ The optimization consists of designing a fictitious material with a dielectric function described by a Drude model and tuning the parameters of this model to maximize radiation transfer towards the cell for energies larger than the cell bandgap. The surface polariton resonance is tuned at a frequency corresponding to a radiation energy slightly larger than the bandgap.

⁸² This was done for simplicity as the optimum low energy cut-off is always equal to the cell bandgap and thus varies with cell temperature.

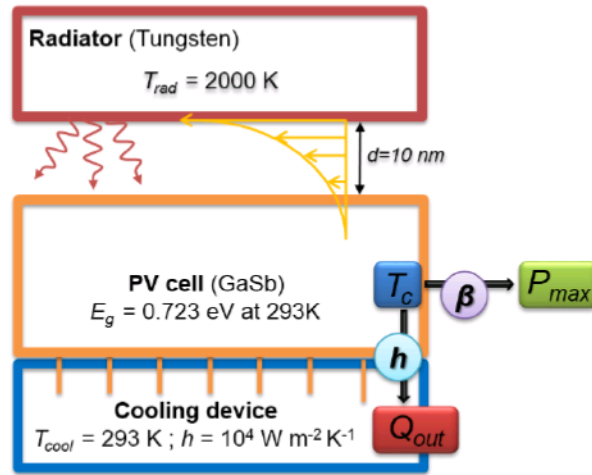


Fig. 72 Schematic of the configuration selected for this study of a high energy cutoff of spectral radiation emitted by the radiator (whose results are shown in Fig. 73).

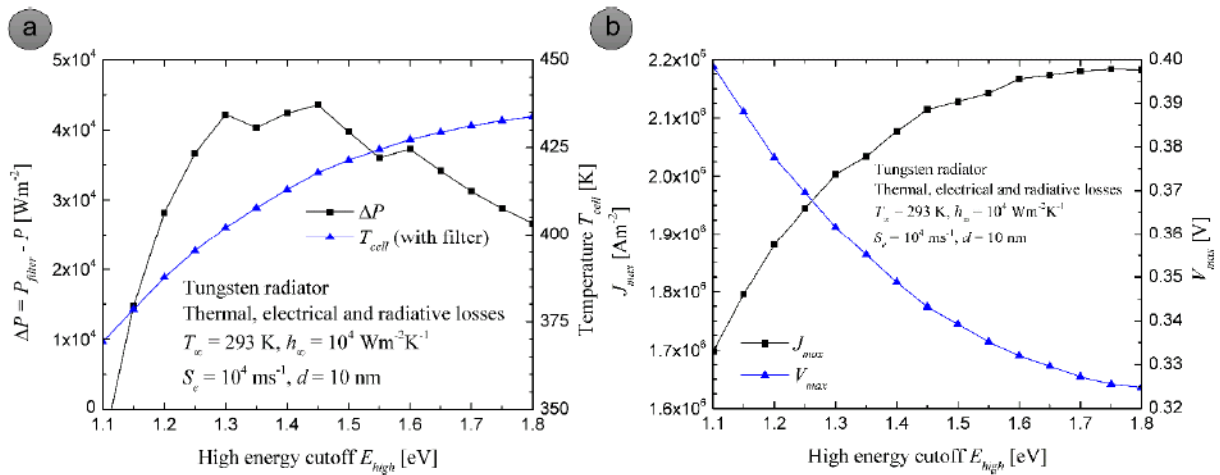


Fig. 73 a. Difference of power output with and without filter ΔP and cell temperature T_{cell} (T_c throughout this manuscript) as a function of the high energy cutoff E_{high} (the low energy cutoff is fixed at 0.66 eV); b. current (J_{max}) and voltage (V_{max}) at maximum power output as a function of the high energy cutoff E_{high} . Figures from (Bernardi et al. 2015).

The underlying reason for the optimum observed in Fig. 73a is that there is a photon energy at which the ratio of heat generated to useful work becomes detrimental for the system efficiency. Indeed, photons with energy larger than the bandgap⁸³ whose absorption leads to an important heat generation with a corresponding increase of the cell temperature might be better reflected completely than absorbed even though they would otherwise generate additional electrical carriers. It is possible to define a corresponding

⁸³ Again, photons with energy smaller than the cell bandgap ($E < E_g$) are assumed to be totally reflected (low-energy cut-off).

threshold for the ratio of heat generated to useful work under which it is profitable to reflect the incident photons. Of course, this threshold depends on the heat transfer coefficient (h) and the cell temperature coefficient (β). Let us illustrate this with a simple example. Fig. 74 shows the ratio of heat generated to useful power as a function of photon energy for a single junction PV cell. The purple area corresponds to the fraction of the incident photon energy in excess of the cell bandgap (it corresponds to the Thermalization term introduced in Chapters 2 and 7). The red area corresponds to the fraction of the incident photon energy that results in heat generation (from mechanisms other than Thermalization). It is plotted as a straight line because this heat generation is equal to a given fraction of the cell bandgap energy for all the generated carriers (we assume here that recombinations do not depend upon the position in the cell where absorption takes place and thus do not depend on the wavelength of the absorbed photons). It should be noted that this fraction depends on the recombination rate and increases when the cell ERE decreases (not illustrated). If we neglect thermal emission from the cell, all the heat generated (Q) has to be evacuated via the cooling system, thus:

$$T_c = T_{cool} + \frac{Q}{h} \quad (133)$$

In this configuration, an increase of the heat source (ΔQ) corresponds to an increase of the cell temperature:

$$\Delta T_c = \frac{\Delta Q}{h} \quad (134)$$

Also, introducing the cell absolute temperature coefficient:

$$\beta_{abs} = \frac{P(T_c) - P(T_{c,ref})}{T_c - T_{c,ref}} \quad (135)$$

an increase of the cell temperature can be associated directly to a drop in efficiency:

$$\Delta P_{max} = \beta_{abs} \Delta T_c \quad (136)$$

By combining these equations, an increase of the heat source can be associated to a power loss:

$$\Delta P = \beta_{abs} \frac{\Delta Q}{h} \quad (137)$$

From this equation, it is possible to evaluate the fraction of heat generated to output power above which photon absorption is detrimental to the cell efficiency. Let us denote the fraction of the incident photon energy that results in heat (F_Q) and the fraction that results in output power (F_P). The condition for the photon absorption to be profitable reads:

$$F_P + \beta_{abs} \frac{F_Q}{h} > 0 \quad (138)$$

Since $F_Q = 1 - F_P$ in this configuration, it results in the condition:

$$F_P > F_{P_threshold} = \frac{1}{1 - h / \beta_{abs}} \quad (139)$$

This equation, while derived in a very specific configuration, is meaningful because it shows why there is an optimum cutoff energy and how this optimum depends on the heat transfer coefficient and on the temperature coefficient⁸⁴.

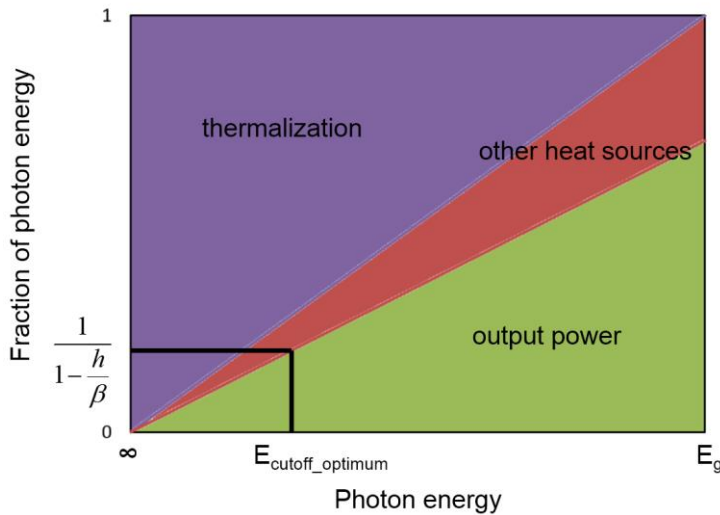


Fig. 74 Schematic showing the optimal cutoff energy in a simplistic configuration.

In this subsection, we have demonstrated that our approach that consists in considering the thermal equilibrium of PV cells could also benefit to the design and optimization of NF TPV devices.

⁸⁴ For example, assuming realistic values for a standard single junction c-Si solar cells ($\beta_{abs} = -0.8 \text{ W m}^{-2} \text{ K}^{-1}$ and $h = 10 \text{ W m}^{-2} \text{ K}^{-1}$), eq. (146) gives $F_{P_threshold} = 7.4\%$. This fraction indicates the ratio of useful to incident power below which photon absorption is detrimental to the cell performances.

9. General conclusions

This Ph.D. thesis manuscript has presented an investigation of the physics of the thermal behavior of photovoltaic devices. In Part I, a thorough analysis based on device physics of the relation between device temperature and conversion efficiency has been presented. In Part II, a complete model of the heat generation mechanisms in PV systems has been proposed. Then, the different parameters that impact the relation between the heat source and the device temperature have been identified. Finally, several examples have been presented in order to illustrate the original approach presented in this manuscript that consists in taking into account the real operating conditions of a PV device for its design.

9.1. Conclusions and prospects for the research on the physics of the temperature coefficients of PV devices

In the first part of this thesis manuscript, a detailed study of the temperature coefficients of photovoltaic devices has been presented.

In chapter 2, a brief summary of the most relevant literature on this topic has been provided. This overview of the state-of-the-art has highlighted that, while it is long known that the conversion efficiency of any PV device is negatively affected by its temperature, some of the underlying physics remains to be clarified.

In chapter 3, the theoretical reasons why photovoltaic conversion is fundamentally affected by the device temperature have been detailed. Following previous works, this has been demonstrated both from a detailed balance analysis and from a thermodynamic argument. The temperature dependences of the fundamental losses for single junction solar cells have been examined and fundamental temperature coefficients have been calculated. Then, the impacts on temperature coefficients of the incident spectrum and of the temperature dependences of semiconductors bandgaps have been highlighted. It has been shown that perovskite based solar cells will ultimately (i.e. in the radiative limit)

have peculiar temperature sensitivities because of the unusual behavior of the bandgaps of perovskite semiconductor compounds. For some semiconductors, the radiative limit cannot be reached. For example, crystalline silicon solar cells are intrinsically limited by Auger recombination (in addition to radiative recombination). The temperature coefficient calculated in this intrinsic limit for crystalline silicon based devices is -2380 ppm K^{-1} which is larger than the value of the temperature coefficient calculated in the radiative limit (-1582 ppm K^{-1}). Also, this value is significantly smaller than the commonly assumed value for existing c-Si devices ($\sim -4000 \text{ ppm K}^{-1}$).

In chapter 4, the temperature coefficients of real solar cells (which do not operate in the radiative limit) have been discussed. All the additional loss mechanisms that limit the efficiency of present commercial cells have been introduced. These loss mechanisms have been depicted on a p-n junction diagram and on a graph showing the cumulated photon flux density as a function of photon energy together with a J-V characteristic. Because the cell parameters V_{oc} , J_{sc} , and FF depend on different sets of physical mechanisms, the analysis of the temperature coefficient (TC) of the cell efficiency has been separated into that of the TCs of V_{oc} , J_{sc} and FF . It has been shown that the temperature sensitivity of open-circuit voltage is connected to the balance between generation and recombination of carriers and the temperature dependence of this balance. A general expression that relates the temperature sensitivity of a cell open-circuit voltage ($\beta_{V_{oc}}$) to the cell external radiative efficiency (ERE) has been proposed. Also, it has been shown that the temperature coefficient of open-circuit voltage could be used to identify the dominant recombination processes in a PV device. The influence of bandgap temperature dependence and incident spectrum on the temperature sensitivity of short-circuit current ($\beta_{J_{sc}}$) has been demonstrated. The theoretical expression for $\beta_{J_{sc}}$ that has been used is interesting in that it enables to separate these material related effects from device related effects that are taken into account by the collection fraction parameter. Then, several expressions for the temperature coefficient of the fill factor (β_{FF}) have been presented. The temperature behavior of the fill factor can be complex because it depends on the generation-recombination balance at maximum power point and thus it is also a function of the transport mechanisms. It is worth keeping in mind that measurements of β_{FF} can also provide information on the device physics and in particular on the transport mechanisms.

In chapter 5, an experimental assessment of the theoretical expressions (introduced in chapter 4) in the case of crystalline silicon solar cells have been presented. The details of the measurements realized at the University of New South Wales (UNSW) on c-Si cells have been provided. The results have validated that the external radiative efficiency of PV cells plays a significant role in the temperature dependence of open-circuit voltage. It has also been observed that, because of the indirect bandgap of silicon, cells with small collection fraction exhibit specific temperature sensitivities of short-circuit current and open-circuit voltage. Additionally, the experimental results have highlighted that the validity of the theoretical expression of β_{FF} from (Zhao et al. 1994) is limited to cells with small series resistances and very large shunt resistances. Finally, analyses of experimental data from the literature have demonstrated that the temperature sensitivities of silicon heterojunction cells and cells made from compensated silicon are similar to that of “standard” homo-junction crystalline silicon cells and are well described by the same expressions.

The work described in Part I of the thesis manuscript opens up a number of prospects. The investigation of the fundamental causes for the temperature sensitivity of solar cells presented in chapter 3 can be extended to any kind of radiative energy conversion (e.g. thermophotovoltaic concepts). Also, it might be interesting to investigate the physics of the temperature coefficients of perovskite based solar cells to determine whether this kind of solar cell is likely to operate with interesting temperature sensitivities as predicted in the radiative limit (see section 3.2). Theoretically, the temperature coefficient of the open-circuit voltage enables to identify the dominant recombination mechanisms in a solar cell (see section 4.1). This has been proven experimentally for Cu(InGa)Se₂ cells in (Grover & Li 2015). It might be interesting to apply the approach from Grover et al. (Grover et al. 2013; Grover & Li 2015) to “standard” homo-junction crystalline silicon cells in order to obtain a quantitative evaluation of the recombinations in the different regions of the cells from the value of the temperature coefficient of the open-circuit voltage. In a future work, it could also be interesting to investigate the effects of the temperature dependences of lifetimes related to known defects in silicon (iron, B-O complexes, ...) on the temperature coefficient of the open-circuit voltage through the parameter γ (see section 4.1). This could enable the identification of the defects present in a solar cell from temperature dependent measurements. Another potential follow-up of this research work would be to derive a more general expression for the temperature coefficient of the fill factor that would take

into account the temperature dependences of the ideality factor and the series and shunt resistances (see section 5.4). Finally, sections 5.5 and 5.6 have shown that additional research on the temperature coefficients of silicon heterojunction cells and cells made from compensated silicon would enable to predict how the temperature coefficients of these technologies are likely to evolve in the coming decades.

The understanding of the parameters that govern the temperature coefficients of solar cells suggests that new guidelines could be derived for the design of PV cells. In order to propose optimizations that take into account the thermal behavior of PV devices, the mechanisms that drive their operating temperature have been investigated in Part II.

9.2. Conclusions and prospects for the research on the thermal optimizations of PV devices

The second part of this thesis manuscript has presented an original approach for the design of PV systems that takes into account the system operating conditions. This approach consists in calculating the cell temperature from its power balance. This way, it is possible to take into account the output power penalty associated to heat generation within the cell. Indeed, the cell temperature is related to the heat generation via the heat transfer coefficient, and the output power is linked to the cell temperature by the temperature coefficient.

In chapter 6, the approaches commonly used to deal with temperature-induced losses in PV devices have been reviewed. Most of them consist in implementing either passive or active cooling strategies (see section 6.1). The rare approaches that do not consist in adding a cooling system but in somehow tuning the thermal design of the PV system have also been reported (see section 6.2). Finally, our approach that takes into account the system operating conditions has been introduced (see section 6.3).

In chapter 7, a complete thermal model of PV systems has been proposed (see section 7.1). This model describes all the different loss mechanisms that can reduce the power output of a PV cell. Analytical expressions have been given for the different loss terms. It has been demonstrated, by calculating numerically all the losses for an arbitrary c-Si cell, that all the incident power is correctly accounted for when using the suggested

expressions. In section 7.2, the different heat dissipation mechanisms have been briefly presented. Finally, we have suggested that measuring Nominal Operating Cell Temperatures (NOCTs) at MPP rather than in short-circuit would make this parameter more relevant for the quantification of the “thermal quality” of PV modules (see section 7.3).

When the heat source is properly defined (see chapter 7), it is possible to include it as a design criterion in the optimization of PV systems. This is what has been illustrated in chapter 8 via several examples in different configurations. It has been shown that, when including a thermal criterion, the optimum set of parameters is different from that obtained through a more common electrical and optical modeling of the PV system. In section 8.1, examples of global optimizations (that include optical, electrical and thermal criteria) have been given in the case of standard solar PV systems. It has been demonstrated that taking into account the thermal operating conditions of solar cells leads to changes of the optimum set of parameters for PV conversion (the examples have included the bandgap, the cell thickness and the thickness of the anti-reflection coating). Additionally, some opportunities for tuning the temperature coefficient of a PV device have been presented. In section 8.2, it has been demonstrated that the design of solar thermophotovoltaic (STPV) devices can also benefit from the original optimization guidelines described in this manuscript. Indeed, it has been shown via a complete modeling that taking into account the global thermal balance of the STPV system results in optimum bandgaps that depend upon the thermal boundary conditions. Additionally, it has been shown that the cell quality (quantified by its External Radiative Efficiency) impacts the STPV conversion efficiency both directly and through the thermal balance of the overall system. These conclusions are particularly important because they will enable to design optimally experimental (non-ideal) STPV devices. Finally, it has been shown in section 8.3 that modeling the intertwined optical, electrical and thermal mechanisms is also especially important for designing near-field TPV systems.

Part II of this manuscript has described an original approach for the design of photovoltaic systems. The principles of a thermal design of solar cells have been exposed and discussed. The main idea is that adding a thermal criterion to the optical and electrical ones in the optimization of PV devices would enable an enhancement of their efficiency under real operating conditions. In the case of crystalline silicon cells, it has been shown that the cell thickness and the anti-reflection coating thickness can be tuned in order to reduce

the cell heating as much as possible without degrading significantly its optical and electrical properties, thus increasing its performances under real operating conditions. However, there are much more parameters that would be worth taking into consideration (doping concentrations, back surface reflector quality, etc) and it would be interesting eventually to make a comprehensive optimization by considering all these different parameters simultaneously. Of course, when including a thermal criterion, the optimum set of parameters depends on outdoor conditions. Thus, it would also be interesting to propose different “thermally optimized” designs of PV cells specific to given locations or climates. For example, considering space applications could lead to very specific designs because the operating conditions (temperature and irradiance) can be particularly exotic and the heat dissipation is limited in space. Furthermore, space cells already feature UV and IR reflectors whose optimum cutoff energies could be optimized as shown for TPV systems in sections 8.2 and 8.3. These sections also pave the way for future works aiming at the complete design of experimental TPV systems (standard, solar or near-field).

We hope that this Ph.D. thesis work has contributed to better understand the physics of the thermal behavior of PV devices and to open up new design possibilities.

10. Appendices

10.1. Evaluating PV potential in the world taking into account thermal effects

When choosing an appropriate location to install PV devices, one would obviously look for places with important yearly solar irradiation (Fig. 75).

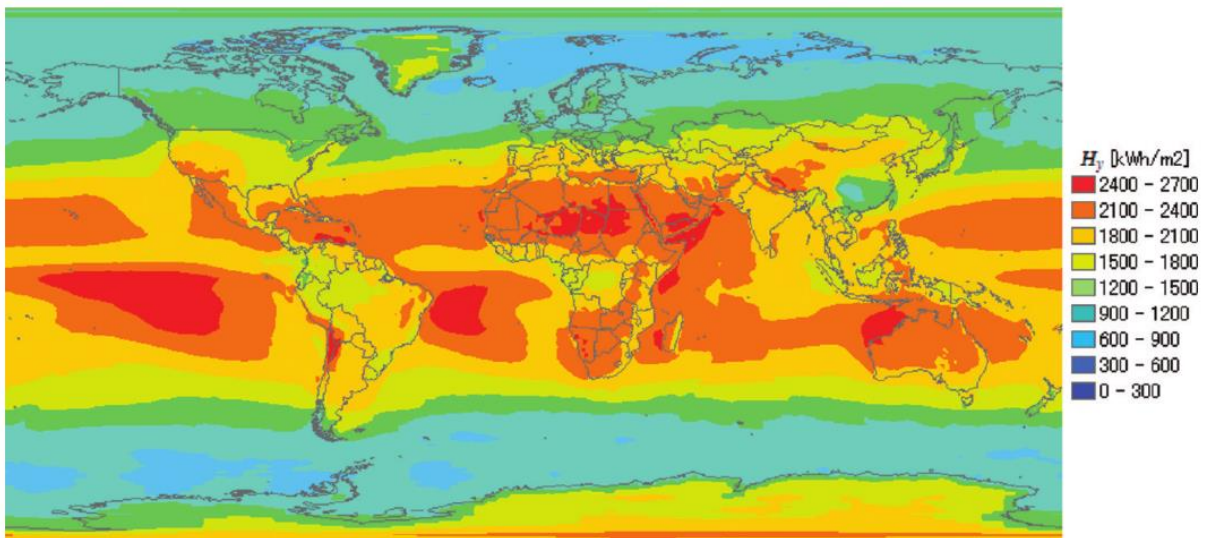


Fig. 75 Global map of annual total irradiation on Equator-pointed surfaces tilted at the latitude angle (Kawajiri, Oozeki & Genchi 2011).

Also, since efficiencies of PV devices decrease when their temperatures rise, one would also want a low temperature environment (Fig. 76).

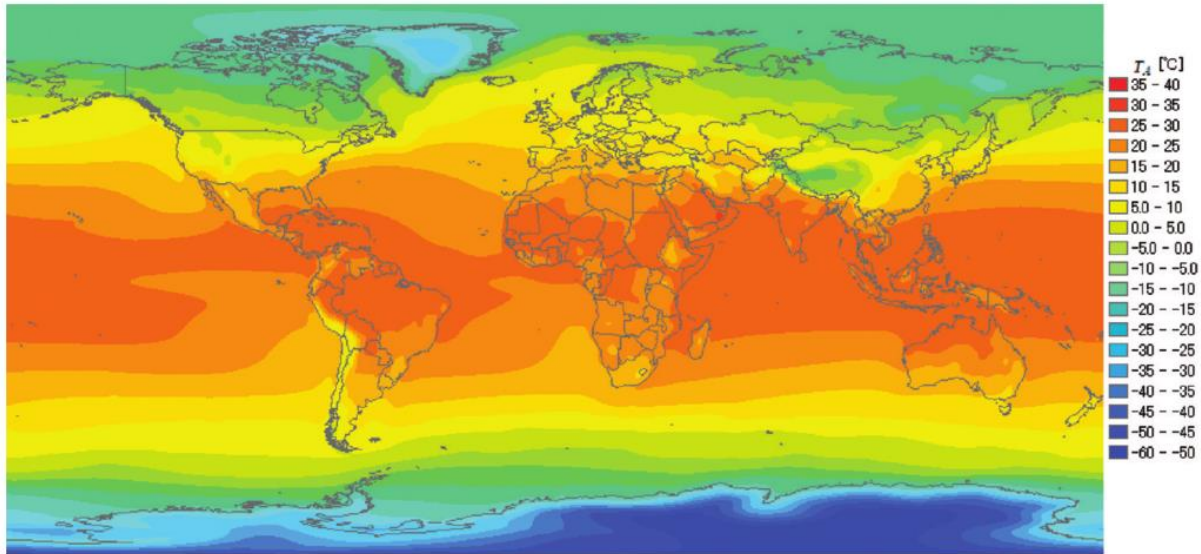


Fig. 76 Global map of yearly average ambient temperature (Kawajiri, Oozeki & Genchi 2011).

Using a simple correlation to relate the outdoor temperature to that of a standard c-Si module mounted on a platform (open-rack) together with a unique temperature coefficient, Kawajiri et al. (Kawajiri, Oozeki & Genchi 2011) mapped the effect of temperature on PV potential in the world (Fig. 77).

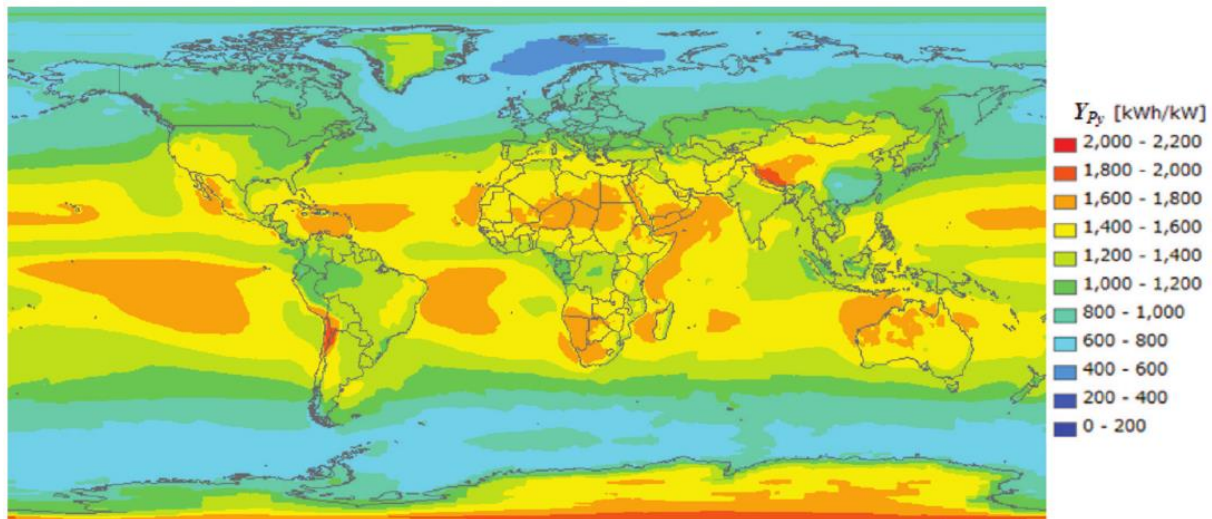


Fig. 77 Global potential map of PV energy generation by c-Si modules considering temperature effects (Kawajiri, Oozeki & Genchi 2011).

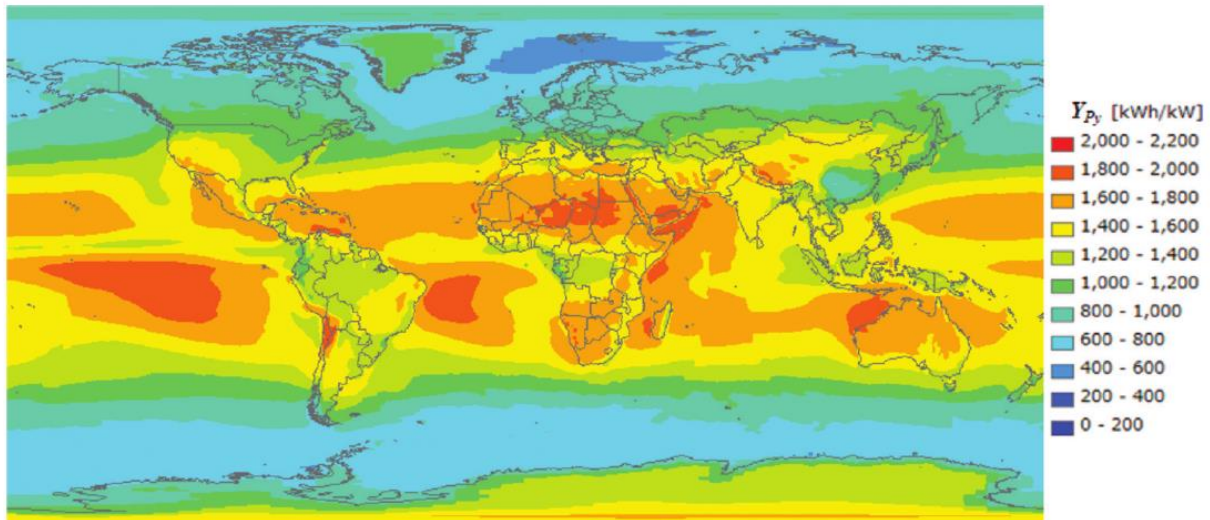


Fig. 78 Global potential map of PV energy generation by c-Si modules without considering temperature effects (Kawajiri, Oozeki & Genchi 2011).

Fig. 78 shows a map of the potential of PV energy generation that does not consider any thermal effect (as if modules operated everywhere and constantly at 25°C). Comparing Fig. 77 and Fig. 78, it is clear that the potential of PV energy generation is impacted by the consideration of ambient temperature. Several places with high yearly irradiation (like deserts) that were though interesting for PV are shown to be less attractive because of large operating temperatures. On the other hand, places at high elevations (such as the Himalayas), are shown to have a huge potential in terms of PV operation because of particularly good irradiance/temperature ratios. Of course, this really rough approach is only aimed at illustrating the importance of considering the thermal behavior. In reality, the temperature of a module is impacted by other parameters such as mounting configuration and wind speed. One could include these parameters using empirical correlations (Skoplaki & Palyvos 2009b) and wind speed data (Fig. 79). However, these irradiation, temperature and wind speed data are averaged values and a realistic energy potential could only be determined with the detailed knowledge of these data as a function of time. Furthermore, there are a number of other phenomena such as partial shading due to snow (in mountains) or staining (in deserts) that can also impact the real energy yield of a PV plant. It is complicated to gather all these data for the whole world but the accurate prediction of potential of PV in a given location is the challenge faced by engineers before establishing any large PV installation.

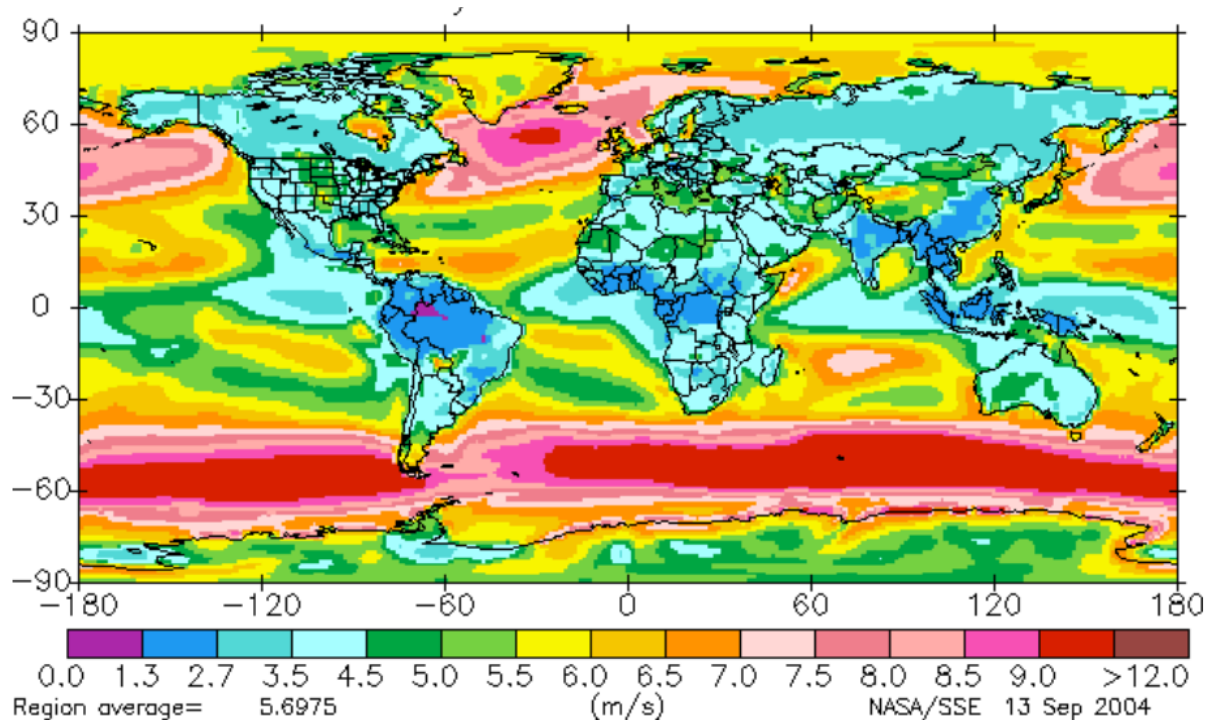


Fig. 79 Annual 10m wind speed for terrain similar to airports July 1983 - June 1993 (Whitlock, Brown & Chandler 2006).

10.2. On the temperature dependence of the diode saturation current

In the literature, the following expression is often used for the diode saturation current density of a solar cell (Green 1982):

$$J_0 = CT^\gamma \exp\left(-\frac{E_{g0}}{kT_c}\right) \quad (140)$$

It is important to explain this expression of the diode saturation current density because it is the basis of many works dealing with temperature coefficients (Fan 1986; Landis 1994; Friedman 1996; Yoon & Garboushian 1994). The diode saturation current density, J_0 , is a fundamental parameter of solar cells. It corresponds to the diffusion current density of carriers in the reverse diode direction when no voltage is applied and balances the drift current density at the p-n junction (Fig. 80a). Under an applied forward bias V , the potential at the junction is lowered and the concentration of carriers with enough energy to diffuse across it, is increased by $\exp(qV/kT_c)$ (Fig. 80b). This explains the form of the famous ideal diode law (Shockley 1948):

$$J = J_0 \left(\exp\left(\frac{qV}{kT_c}\right) - 1 \right) \quad (141)$$

The principle of superposition states that for a linear system, the response to several excitations corresponds to the sum of the response caused by each individual excitation. In the case of a solar cell, the excitations are that caused by the light and that caused by the voltage. Assuming linearity (which is usually valid under low injection conditions: majority carrier concentrations much larger than minority carrier concentrations), the principle of superposition tells us that the current density that can be drawn from a solar cell (J) equals that photogenerated (J_{ph}) minus that recombined (which corresponds to that flowing in reverse bias through the diode in the dark, Eq. (141):

$$J = J_{ph} - J_0 \left(\exp\left(\frac{qV}{kT_c}\right) - 1 \right) \quad (142)$$

This expression illustrates the name commonly given to the parameter J_0 (diode or dark saturation current density). Indeed, in the dark and under a large reverse bias, the current should saturate towards the value J_0 . However, the parameter J_0 has a more profound

physical signification: it is proportional to the recombination rate in thermal equilibrium (with no applied bias). It is used to describe the strength of the recombination mechanisms independent of the bias condition. Because the value of the bias corresponds to the magnitude of the disequilibrium, the recombination rate can often be written as the product of J_0 and $\exp\left(\frac{qV}{kT_c}\right)$. However, the situation can be more complex because different recombination mechanisms have different bias dependences. The reader can find a really interesting discussion on the physical meaning of the parameter J_0 and an analysis of different recombination scenarios in (Cuevas 2014).

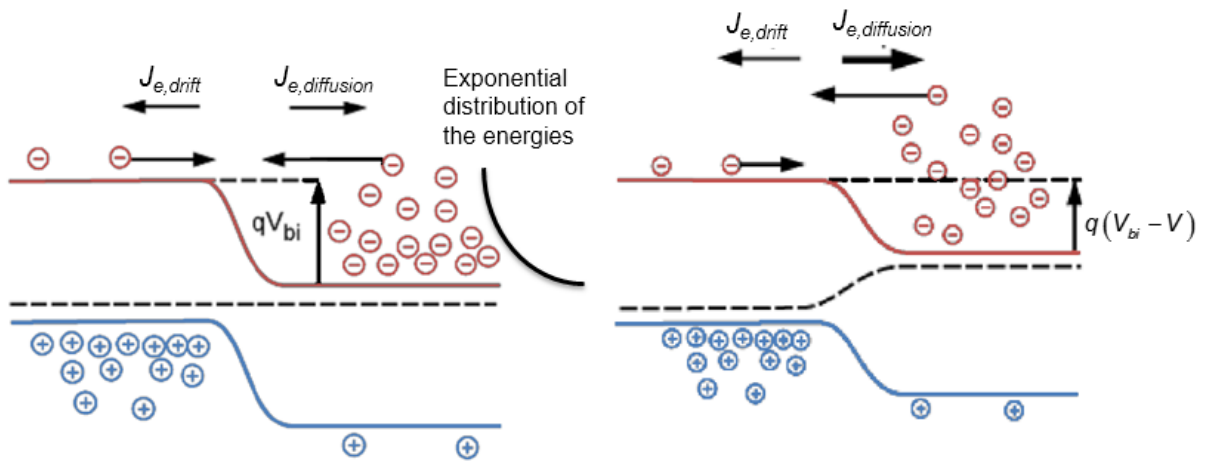


Fig. 80 p-n junction diagram in the dark under a. no bias b. an external bias V . Figure adapted from a document by Bill Wilson under a licence Creative Commons Attribution License (by 1.0) http://cnx.org/contents/8c8d95ff-8ac8-421c-a009-6bff6b862903@14/P-N_Junction:_Part_I.

Under a number of assumptions (detailed in (Green 1982)), J_0 can be derived easily from the carrier transport equations (Green 1982), p. 81:

$$J_0 = q \left(\frac{D_e}{L_e} \frac{1}{N_A} F_P + \frac{D_h}{L_h} \frac{1}{N_D} F_N \right) n_i^2 \quad (143)$$

F_P and F_N are factors that account for the finite dimensions of the P and N regions respectively and are thus function of the surface recombination velocities. $D_{e,h}$ and $L_{e,h}$ are the diffusion coefficients and the diffusion lengths of the electrons and holes. $N_{A,D}$ are the doping concentrations of acceptors and donors. n_i is the intrinsic carrier concentration which is maybe the most crucial parameter in cell modeling. It corresponds to the concentration of carriers that are thermally excited from the valence band to the conduction band in an intrinsic material (i.e. non doped). For a non-degenerate

semiconductor (i.e. where the Fermi energy is at least $3kT_c$ away from either band edge), the product of the electron and hole intrinsic concentrations is given by (Green 1982):

$$n_i^2 = N_c N_v \exp(-E_g / kT_c) \quad (144)$$

where N_c and N_v are the number of effectively available states in the conduction and valence bands.

Comparing eq. (140) with eqs. (143) and (144), we observe that the γ term is supposed to describe the temperature dependence of the product of a lot of parameters that are temperature dependent (namely N_c , N_v , F_P , F_N , D_e , D_h , L_e , L_h , N_A and N_D).

- The densities of states can be calculated by solving the Schrödinger equation assuming the simple particle-in-a-box model (Zeghbrouck 2011). Using also the Boltzmann probability function (instead of the Fermi-Dirac probability function since we consider a non-degenerate semiconductor), the product of effectively available states in the conduction and valence band $N_c N_v$ is:

$$N_c N_v = 4(2\pi kT_c / h^2)^3 (m_e^* m_h^*)^{3/2} \quad (145)$$

where m_e^* and m_h^* are the effective masses of the electrons and the holes.

- F_P and F_N are temperature dependent because of the temperature dependence of the surface recombination velocities.
- The diffusion coefficients D_e , D_h are related to the carrier mobilities by the Einstein relations:

$$D_{e,h} = \mu_{e,h} \frac{kT_c}{q} \quad (146)$$

The thermal energy kT_c which causes the random motion of carriers is logically present in the equation of the diffusion coefficient. Also, the mobilities of the carriers are function of temperature and these temperature dependences are themselves function of the doping concentrations (because doping impacts the carrier equilibrium concentrations).

- The diffusion lengths (L_e , L_h) correspond to the average distances traveled by excited carriers before their recombination. They depend on the diffusion coefficients (D_e , D_h) and the lifetimes of the carriers (τ_e , τ_h):

$$L_{e,h} = \sqrt{D_{e,h}\tau_{e,h}} \quad (147)$$

Lifetimes are also temperature dependent because the different existing recombination mechanisms are function of the cell temperature (Schenk 1992; Trupke et al. 2003; Huldt, Nilsson & Svantesson 1979).

- Eventually, the dopant concentrations N_A and N_D may depend on temperature in the case of incomplete ionization of the dopants in the range of temperature of interest.

In several works (Nell & Barnett 1987; Friedman 1996), the temperature dependence of $\frac{D_e}{L_e} \frac{1}{N_A} F_p$ (in eq. (143)) is neglected and it is assumed that the temperature dependence of J_0 is driven by that of n_i^2 (neglecting eventual temperature dependences of the effective masses):

$$J_0 = CT^3 \exp\left(-\frac{E_{g0}}{kT_c}\right) \quad (148)$$

where C is a constant supposed independent of the temperature.

One can also find in the literature additional parameters in the diode saturation current density equation (Fan 1986; Yoon & Garboushian 1994). For example, the following equation was initially proposed by Fan (Fan 1986) and served as the basis for several works on temperature coefficients (Landis 1994; Friedman 1996; Yoon & Garboushian 1994):

$$J_0 = CT_c^{3/a} \exp\left(-\frac{E_g}{bkT_c}\right) \quad (149)$$

where C is an empirical parameter related to the material the cell is made of and a, b are “empirical parameters depending on the quality of the cell material and junction” (Fan 1986). Unfortunately these parameters are sometimes extracted from fits and are not directly correlated to any physical mechanisms. As demonstrated by Green (Green 2003), such analyses can lead to systematic errors in the modeling. From the number of temperature dependent parameters listed above, we understand the complexity of the temperature dependence of the diode saturation current density.

It is noteworthy that the expression of diode saturation current given by Eq. 69 corresponds to a scenario where recombinations mainly occur in the quasi-neutral regions (i.e. in the bulk) or at the surfaces. Several expressions have been derived for different limiting scenarios. For example, if the recombinations are mostly happening in the depletion region, the diode saturation current can be written as (Siefer & Bett 2012):

$$J_{02} = \frac{n_i W_d k T_c}{2(V_d - V) \tau_{n0}} \quad (150)$$

where W_d is the width of the depletion zone, V_d is the diffusion voltage and τ_{n0} is the minimum electron lifetime. This expression shows a different temperature dependence than that discussed above (Eq. 69). A detailed discussion of these different scenarios is presented in section 4.1.

10.3. Analogy between a photovoltaic cell and a leaky bucket feeding a water wheel

The analogy illustrated in Fig. 81 was inspired by a lecture from Prof. Yablonovitch at the International School of Solid State Physics 56th course “Materials for Renewable Energy”(Yablonovitch 2012). We modified it so that it could explain better some physical mechanisms of solar cell operation. In this analogy, a photovoltaic device is compared with a leaky bucket. This leaky bucket is connected to a water wheel whose mechanical resistance represents the electrical resistance of the load connected to the solar cell. The power dissipated in the wheel is equal to the product of the water flow (that is the analog of the electrical current) and the pressure head in the bucket (that compares to the voltage across the solar cell). Representing the carriers excited into the conduction band by solar photons, water flows into the bucket by a “shower head powered by the Sun”. The bucket leaks through its sidewalls to represent the recombination of excited carriers. The more water is in the bucket, the more water leaks from the sides (just like recombination rates increase when the cell voltage increases). It is clear in this analogy that the amount of water in the bucket (\equiv cell voltage) depends on the balance between water flowing in by the hose (\equiv photogeneration) and water flowing out by its sides or through the water wheel (\equiv recombination and output current). To transfer the maximum power into the wheel, its resistance needs to be adjusted so that it is not too low to maintain some pressure in the bucket but not too high to prevent excessive leaking from it. When the outlet to the waterwheel is open and the resistance of the wheel is negligible –short-circuit configuration– the bucket does not fill and almost all the water entering through the shower head directly exits through the waterwheel ($J_{sc} \approx J_{photogenerated}$). When the outlet to the waterwheel is closed –open-circuit configuration– the bucket fills with water until the flow leaking through the sides equals that entering from the shower head. This illustrates why the open-circuit voltage indicates the balance between photogeneration and recombination rates. If you could completely prevent the leaking (\equiv the recombination), the bucket would be filled with all the water (\equiv all the carriers in an excited state, $V = E_g$). However, the amount of water is ultimately limited further ($V \leq E_g(1 - T_c/T_s)$) because there is a minimum recombination rate since photon absorption and emission are reciprocal mechanisms (this reciprocity is not depicted by the analogy).

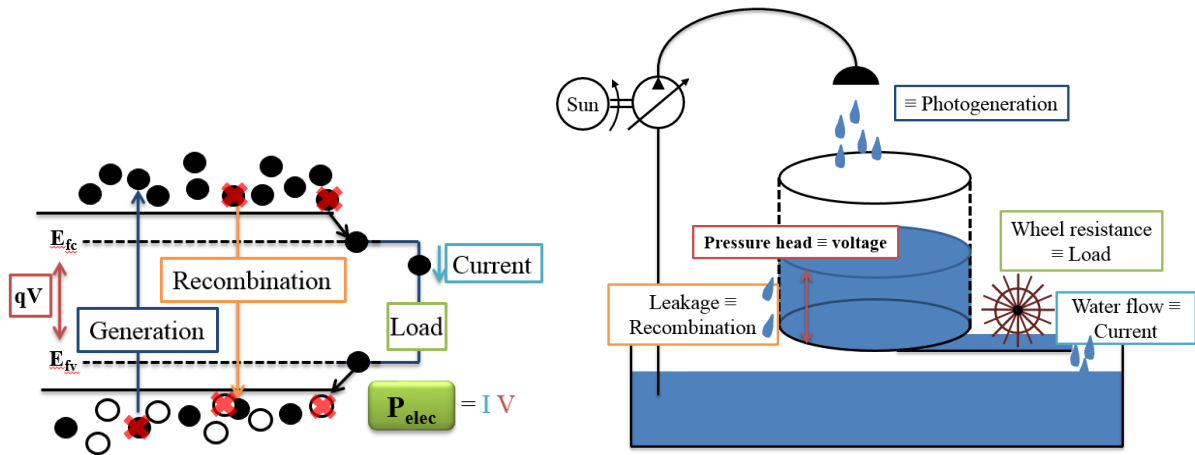


Fig. 81 Hydraulic analogy of the operating principles of a solar cell.

10.4. Extrapolation of the integral rate of spontaneous emission from a c-Si cell from the experimental data of (Trupke et al. 2003)

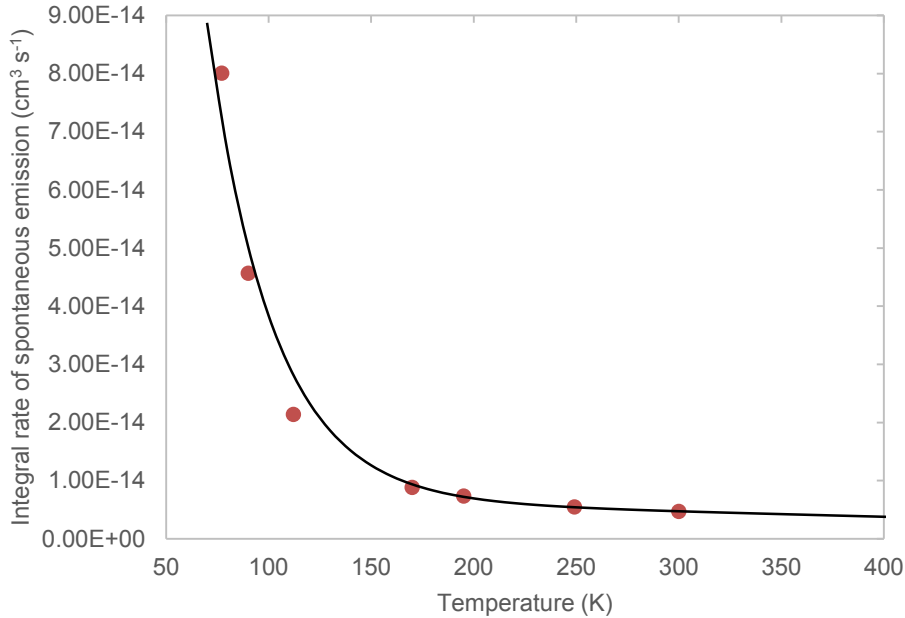


Fig. 82 Extrapolation (black line) of the integral rate of spontaneous emission from a c-Si cell based on the experimental data (red dots) of (Trupke et al. 2003), Table 1. The experimental data were fitted using Origin and adding some weights to have the exact value at 300 K and a reasonable extrapolation on the 300-400 K range. The (completely unphysical) equation of the fit is:

$$B_{low}(T) = 7.41 \cdot 10^{-13} \times \exp\left(-\frac{T}{31.8}\right) + 7.35 \cdot 10^{-15} - 8.92 \cdot 10^{-18} T$$

10.5. Matlab code to extract the simple diode model parameters (R_s , R_{sh} , n , I_0 , I_{ph}) from light I-V curves

The program consists of two files (IVFIT.m and OneDiodeModel.m) and extracts the simple diode model parameters (R_s , R_{sh} , n , I_0 , I_{ph}) from a light I-V curve contained in an excel file. It requires the following Matlab packages:

- Symbolic Math Toolbox (for the *lambertw* function)
- Optimization Toolbox (for *lsqnonlin*)

The program uses *lsqnonlin* to solve the nonlinear least-squares curve fitting problem between the experimental light I-V data and an approximated explicit analytical expression of the single-diode model (eq (8)⁸⁵ in (Zhang et al. 2011)).

```
IVFIT.m :
clear all
clc
close all
global V I Voc Isc T kB q
kB = 1.3806488E-23;
q = 1.60217657E-19;
%%%%%%%%%%%%%%%%%%%%%%%%%%%%%%%%%%%%%%%%%%%%%%%%%%%%%%%%%%%%%%%%%%%%%%%%
%The IV data (I and V), the cell temperature (T), the open-circuit voltage (Voc) and the short-circuit current (Isc)
are extracted from an excel file
T=xlsread('Excel file.xlsx',1,'B8');
V=xlsread('Excel file.xlsx',1,'A21:A300');
I=xlsread('Excel file.xlsx',1,'B21:B300');
Voc=xlsread('Excel file.xlsx',1,'B10');
Isc=xlsread('Excel file.xlsx',1,'B21');

%The initialization parameters for the ideality factor (n0), the series resistance (Rs0), shunt resistances (Rsh0) are
also extracted from the excel file. They were calculated from the data using the 5 points analytical method described
in Chan&Phang_1987_Analytical methods for the extraction of solar-cell single- and double-diode model parameters
from I-V characteristics
n0=xlsread('Excel file.xlsx',1,'E14');
Rs0=xlsread('Excel file.xlsx',1,'F17');
Rsh0=xlsread('Excel file.xlsx',1,'D19');
```

⁸⁵ There are two missing brackets in Eq. 8 of (Zhang et al. 2011): one should read ...

$$\exp\left(\frac{q}{nkT_c}\left(R_s I_{SC} + \frac{R_{sh} V}{R_{sh} + R_s}\right)\right) \dots$$

```

b0=[n0, Rs0, Rsh0];
b=lsqnonlin(' OneDiodeModel',b0) %b=[n,Rs,Rsh]

n=b(1)
Rs=b(2)
Rsh=b(3)

%eq (7a) in Zhang_2011. Assumption: eq (6) is true
I0=(Isc+(Rs*Isc-Voc)/Rsh)*exp(-q*Voc/(n*kB*(T+273.15)))
%eq (7b) in Zhang_2011. Assumption: eq (6) is true
Iph=Isc+Rs*Isc/Rsh-I0

%plot of the experimental IV curve together with the fits obtained from eq (2) and eq (8) in Zhang_2011
figure
plot(V,I)
hold on
Vfit = linspace(0,Voc,50)';
%-1*eq (2) in Zhang_2011
Ifit=-(Vfit./Rs-
Rsh.*(Rs.*Iph+Rs.*I0+Vfit)/(Rs.*(Rsh+Rs))+n.*kB.*(T+273.15)./(q.*Rs).*lambertw(q.*Rs.*I0.*Rsh./((Rs+Rsh).*
n.*kB.*(T+273.15)).*exp(Rsh.*q.*(Rs.*Iph+Rs.*I0+Vfit)./(n.*kB.*(T+273.15).*(Rs+Rsh)))));
stem(Vfit,Ifit)
%-1*eq (8) in Zhang_2011
Ifit2=-((n.*kB.*(T+273.15)./(q.*Rs).*lambertw(q.*Rs./((n.*kB.*(T+273.15)).*(Isc-Voc)/(Rs+Rsh)).*exp(-
q.*Voc./((n.*kB.*(T+273.15)).*exp(q./((n.*kB.*(T+273.15)).*(Rs.*Isc+Rsh.*Vfit)/(Rsh+Rs)))))+Vfit./Rs-Isc-
(Rsh.*Vfit)/(Rs.*(Rsh+Rs))));
stem(Vfit,Ifit2)
savefig('FIT IV curve.fig')

OneDiodeModel.m
function y=OneDiodeModel(b)

global V I Voc Isc T kB q

%-1*eq (8) in Zhang_2011
Ionediodemodel=-((b(1).*kB.*(T+273.15)./(q.*b(2)).*lambertw(q.*b(2)./(b(1).*kB.*(T+273.15)).*(Isc-
Voc./((b(2)+b(3))).*exp(-
q.*Voc./((b(1).*kB.*(T+273.15)).*exp(q./((b(1).*kB.*(T+273.15)).*(b(2).*Isc+b(3).*V./((b(3)+b(2))))))+V./b(2)-Isc-
(b(3).*V)./(b(2).*(b(3)+b(2))))));
y=Ionediodemodel-I;

```


Bibliography

- Ali, B., Murray, R., Hegedus, S.S. & Ismat Shah, S., 2012. Analysis of voltage and temperature dependent photocurrent collection in p3ht/pcbm solar cells. *Journal of Applied Physics*, 112, pp.1–11.
- Altermatt, P.P., 2011. Models for numerical device simulations of crystalline silicon solar cells - a review. *Journal of computational electronics*, 10(3), pp.314–330.
- Altermatt, P.P., Geelhaar, F., Trupke, T., Dai, X., Neisser, A. & Daub, E., 2005. Injection dependence of spontaneous radiative recombination in c-Si: Experiment, theoretical analysis, and simulation. In *Proceedings of the 5th International Conference on Numerical Simulation of Optoelectronic Devices*. pp. 47–48.
- Altermatt, P.P., Schmidt, J., Heiser, G. & Aberle, A.G., 1997. Assessment and parameterisation of Coulomb-enhanced Auger recombination coefficients in lowly injected crystalline silicon. *Journal of Applied Physics*, 82(10), pp.4938–4944.
- Araújo, G.L. & Martí, A., 1994. Absolute limiting efficiencies for photovoltaic energy conversion. *Solar Energy Materials and Solar Cells*, 33(2), pp.213–240.
- Atwater, H. & Polman, A., 2010. Plasmonics for improved photovoltaic devices. *Nature materials*, 9(3), pp.205–13.
- Baker-Finch, S.C. & McIntosh, K.R., 2010. A freeware program for precise optical analysis of the front surface of a solar cell. In *35th IEEE Photovoltaic Specialists Conference (PVSC)*. IEEE, pp. 2184–2187.
- Baker-Finch, S.C. & McIntosh, K.R., 2011. Reflection of normally incident light from silicon solar cells with pyramidal texture. *Progress in Photovoltaics: Research and Applications*, (October 2010), pp.406–416.
- Baldasaro, P.F., Reynolds, J.E., Charache, G.W., DePoy, D.M., Ballinger, C.T., Donovan, T. & Borrego, J.M., 2001. Thermodynamic analysis of thermophotovoltaic efficiency and power density tradeoffs. *Journal of Applied Physics*, 89(6), pp.3319–3327.
- Basore, P., 1994. Defining terms for crystalline silicon solar cells. *Progress in Photovoltaics: Research and Applications*, 2(January), pp.177–179.
- Bauer, T., 2013. *Thermophotovoltaics Basic Principles and Critical Aspects of System Design*, Berlin: Springer Berlin.
- Beard, M.C., 2011. Multiple exciton generation in semiconductor quantum dots. *Journal of Physical Chemistry Letters*, 2(11), pp.1282–1288.

- Beauchamp, W.T. & Tuttle-Hart, T., 1995. Patent n° US5449413 A - “UV/IR reflecting solar cell cover.”
- Bernardi, M.P., Dupré, O., Blandre, E., Chapuis, P.-O., Vaillon, R. & Francoeur, M., 2015. Impacts of propagating, frustrated and surface modes on radiative, electrical and thermal losses in nanoscale-gap thermophotovoltaic power generators. *Scientific Reports*, 5.
- Bird, R.E., Hulstrom, R.L., Kliman, a W. & Eldering, H.G., 1982. Solar spectral measurements in the terrestrial environment. *Applied optics*, 21(8), pp.1430–1436.
- Bird, R.E. & Riordan, C., Webpage from NREL’s website offering the download of the “SPCTRAL2” software. Available at: <http://rredc.nrel.gov/solar/models/spectral/SPCTRAL2/>.
- Bloem, J.J., 2008. Evaluation of a PV-integrated building application in a well-controlled outdoor test environment. *Building and Environment*, 43(2), pp.205–216.
- BossSolar, 2015. Combination Hot Water & PV. Available at: <http://www.bosssolar.com/combination-hot-water-pv/>.
- Braun, A., Katz, E.A. & Gordon, J.M., 2012. Basic aspects of the temperature coefficients of concentrator solar cell performance parameters. *Progress in Photovoltaics: Research and Applications*, 21, pp.1087–1094.
- Breitenstein, O., Altermatt, P., Ramspeck, K. & Schenk, A., 2006. The origin of ideality factors $n > 2$ of shunts and surfaces in the dark I-V curves of solar cells. In *21st European Photovoltaic Solar Energy Conference*. pp. 625–628.
- Breitenstein, O. & Rakotoniaina, J.P., 2005. Electrothermal simulation of a defect in a solar cell. *Journal of Applied Physics*, 97.
- British Petroleum, 2015. *BP Statistical Review of World Energy 2015*,
- Brown, A.S. & Green, M.A., 2002. Impurity photovoltaic effect: Fundamental energy conversion efficiency limits. *Journal of Applied Physics*, 92(3), pp.1329–1336.
- Brown, L., 2009. *PLAN B 4.0, Mobilizing to Save Civilization*,
- Bullis, W. & Brewer, F., 1968. Temperature coefficient of resistivity of silicon and germanium near room temperature. *Solid-State Electronics*, 11, pp.639–646.
- Campbell, P. & Green, M.A., 1987. Light trapping properties of pyramidally textured surfaces. *Journal of Applied Physics*, 62(1), pp.243–249.
- Carlson, D.E., Lin, G. & Ganguly, G., 2000. Temperature dependence of amorphous silicon solar cell PV parameters. In *Twenty-Eighth IEEE Photovoltaic Specialists Conference*.
- Chan, D.S.H. & Phang, J.C.H., 1987. Analytical methods for the extraction of solar-cell single- and double-diode model parameters from I-V characteristics. *IEEE*

- Transactions on Electron Devices*, 34(2), pp.286–293.
- Chen, D., 2001. Anti-reflection (AR) coatings made by sol–gel processes: A review. *Solar Energy Materials and Solar Cells*, 68(3-4), pp.313–336.
- Chintapalli, M., Diskin, M. & Guha, I., 2010. Improving solar cell efficiency: a cooler approach. Available at: http://web.mit.edu/3.042/team5_10/Poster.html.
- Clugston, D.A. & Basore, P.A., 1997. Modelling free-carrier absorption in solar cells. *Progress in Photovoltaics: Research and Applications*, 5(4), pp.229–236.
- Couderc, R., Lemiti, M., Amara, M., Lyon, D. & Lyon, I. De, 2014. Impact of the bias on the temperature of silicon solar cells under operating conditions. In *40 th IEEE Photovoltaic Specialist Conference*. pp. 2463–2466.
- Cuce, E., Bali, T. & Sekucoglu, S. a., 2011. Effects of passive cooling on performance of silicon photovoltaic cells. *International Journal of Low-Carbon Technologies*, 6, pp.299–308.
- Cuevas, A., 2014. The recombination parameter J_0 . *Energy Procedia*, 00, pp.53–62.
- D’Innocenzo, V., Grancini, G., Alcocer, M.J.P., Kandada, A.R.S., Stranks, S.D., Lee, M.M., Lanzani, G., Snaith, H.J., et al., 2014. Excitons versus free charges in organo-lead tri-halide perovskites. *Nature communications*, 5, pp.1–6.
- Datas, A. & Algora, C., 2010. Detailed balance analysis of solar thermophotovoltaic systems made up of single junction photovoltaic cells and broadband thermal emitters. *Solar Energy Materials and Solar Cells*, 94(12), pp.2137–2147.
- Datas, A. & Algora, C., 2013. Global optimization of solar thermophotovoltaic systems. *Progress in Photovoltaics: Research and Applications*, 21(5), pp.1040–1055.
- Deceglie, M.G., Silverman, T.J., Marion, B. & Kurtz, S.R., 2014. Metastable changes to the temperature coefficients of thin-film photovoltaic modules. In *40th IEEE Photovoltaic Specialist Conference*. Honolulu, HI: IEEE, pp. 337–340.
- Dey, P., Paul, J., Bylsma, J., Karaiskaj, D., Luther, J.M., Beard, M.C. & Romero, A.H., 2013. Origin of the temperature dependence of the band gap of PbS and PbSe quantum dots. *Solid State Communications*, 165, pp.49–54.
- Dupré, O. & Vaillon, R., 2014. Optimizations of photovoltaic cells including the minimization of internal heat sources. *Journal of Renewable and Sustainable Energy*, 6(1), p.011201.
- Dupré, O., Vaillon, R. & Green, M.A., 2015a. Experimental assessment of temperature coefficient theories for silicon solar cells. *IEEE Journal of Photovoltaics*, pp.1–5.
- Dupré, O., Vaillon, R. & Green, M.A., 2015b. Physics of the temperature coefficients of solar cells. *Solar Energy Materials and Solar Cells*, 140, pp.92–100.
- Emery, K., 2008. Photovoltaic Test Performance: Laboratory Test Procedures Measure

- Photovoltaic Cells and Modules According to International Standards. *Photonics Spectra*, 42(6), pp.76–80.
- Emery, K., Burdick, J., Caiyem, Y., Dunlavy, D., Field, H., Kroposki, B., Moriarty, T., Ottoson, L., et al., 1996. Temperature dependence of photovoltaic cells, modules and systems. In *25th IEEE Photovoltaic Specialists Conference*. IEEE, pp. 1275–1278.
- Even, J., Pedesseau, L., Dupertuis, M. a., Jancu, J.M. & Katan, C., 2012. Electronic model for self-assembled hybrid organic/perovskite semiconductors: Reverse band edge electronic states ordering and spin-orbit coupling. *Physical Review B - Condensed Matter and Materials Physics*, 86(20), pp.3–6.
- Fan, J., 1986. Theoretical temperature dependence of solar cell parameters. *Solar cells*, 17, pp.309–315.
- First Solar, 2015. *First Solar Q2'15 Earnings Call*,
- First Solar, 2014. First Solar Series 3 Black Plus TM PV Module.
- Fischer, D., Bichsel, F., Bruijn, S. De, Goulpie, P., Sansonnens, L., Ziegler, Y., Closset, A., Yverdon, C.-, et al., 2009. Positive effective temperature coefficient of power of +0.75%/°C in flexible a-Si modules in building integrated installations. In *24th European Photovoltaic Solar Energy Conference*. pp. 3505–3508.
- Francoeur, M., Vaillon, R. & Mengüç, M.P., 2011. Thermal impacts on the performance of nanoscale-gap thermophotovoltaic power generators. *IEEE transactions on Energy Conversion*, 26(2), pp.686–698.
- Fraunhofer, 2014. *Photovoltaics Report*,
- Friedman, D.J., 1996. Modelling of tandem cell temperature coefficients. In *25th IEEE Photovoltaic Specialists Conference*. IEEE, pp. 89–92.
- Green, M.A., 2015a. 2015 SEMI Roadmap for Photovoltaics: What's Hot and What's Not? Available at: <http://www2.pv.unsw.edu.au/videos/Martin-Green-4June2015/seminar.php> [Accessed June 25, 2015].
- Green, M.A., 2003. General temperature dependence of solar cell performance and implications for device modelling. *Progress in Photovoltaics: Research and Applications*, 11(5), pp.333–340.
- Green, M.A., 1990. Intrinsic concentration, effective densities of states, and effective mass in silicon. *Journal of Applied Physics*, 67(6), pp.2944–2954.
- Green, M.A., 1999. Limiting efficiency of bulk and thin-film silicon solar cells in the presence of surface recombination. *Progress in Photovoltaics: Research and Applications*, 330(November 1998), pp.327–330.
- Green, M.A., 2012. Radiative efficiency of state of the art photovoltaic cells. *Progress in Photovoltaics: Research and Applications*, 20, pp.472–476.

- Green, M.A., 2008. Self-consistent optical parameters of intrinsic silicon at 300K including temperature coefficients. *Solar Energy Materials and Solar Cells*, 92(11), pp.1305–1310.
- Green, M.A., 1995. *Silicon Solar Cells: Advanced Principles & Practice*, UNSW Photovoltaics.
- Green, M.A., 1981. Solar cell fill factors: General graph and empirical expressions. *Solid-State Electronics*, (2), pp.2–3.
- Green, M.A., 1982. *Solar cells: operating principles, technology, and system applications*, Prentice-Hall, Englewood Cliffs, NJ.
- Green, M.A., 2015b. The Passivated Emitter and Rear Cell (PERC): From conception to mass production. *Solar Energy Materials and Solar Cells*, 143, pp.190–197.
- Green, M.A., 2001. Third generation photovoltaics: Ultra-high conversion efficiency at low cost. *Progress in Photovoltaics: Research and Applications*, 9(2), pp.123–135.
- Green, M.A., Blakers, A.W. & Osterwald, C.R., 1985. Characterization of high-efficiency silicon solar cells. *Journal of Applied Physics*, 58(11), p.4402.
- Green, M.A., Emery, K. & Blakers, A.W.W., 1982. Silicon solar cells with reduced temperature sensitivity. *Electronics Letters*, 18(2), pp.97–98.
- Green, M.A., Emery, K., Hishikawa, Y., Warta, W. & Dunlop, E.D., 2015. Solar cell efficiency tables (Version 45). *Progress in Photovoltaics: Research and Applications*, 20(Version 45), pp.1–9.
- Green, M.A., Ho-Baillie, A. & Snaith, H.J., 2014. The emergence of perovskite solar cells. *Nature Photonics*, 8(7), pp.506–514.
- Green, M.A., Keevers, M.J., Thomas, I., Lasich, J.B., Emery, K. & King, R.R., 2015. 40% efficient sunlight to electricity conversion. *Progress in Photovoltaics: Research and Applications*, 23(6), pp.685–691.
- Grover, S. & Li, J. V., 2015. Theory and analysis of temperature coefficient of open-circuit voltage (dVOC/dT) in heterojunction solar cells. In *42nd IEEE Photovoltaic Specialists Conference*. New Orleans.
- Grover, S., Li, J. V., Young, D.L., Stradins, P. & Branz, H.M., 2013. Reformulation of solar cell physics to facilitate experimental separation of recombination pathways. *Applied Physics Letters*, 103(9).
- Hacke, P., Terwilliger, K., Smith, R., Glick, S., Pankow, J., Kempe, M., Kurtz, S., Bennett, I., et al., 2011. System Voltage Potential- Induced Degradation Mechanisms in PV Modules and Methods for Test Preprint. In *37th IEEE Photovoltaic Specialists Conference*.
- Harder, N. & Würfel, P., 2003. Theoretical limits of thermophotovoltaic solar energy

- conversion. *Semiconductor science and technology*, 15(5), pp.S151–S157.
- Helmers, H., Schachtner, M. & Bett, A.W., 2013. Influence of temperature and irradiance on triple-junction solar subcells. *Solar Energy Materials and Solar Cells*, 116, pp.144–152.
- Henry, C.H., 1980. Limiting efficiencies of ideal single and multiple energy gap terrestrial solar cells. *Journal of Applied Physics*, 51(8), pp.4494–4500.
- Hirst, L.C. & Ekins-Daukes, N.J., 2011. Fundamental losses in solar cells. *Progress in Photovoltaics: Research and Applications*, 19(3), pp.286–293.
- Holt, D.B. & Yacobi, B.G., 2007. *Extended Defects in Semiconductors: Electronic Properties, Device Effects and Structures*, Cambridge University Press.
- HomePower, 2015. Effect of operating temperature on inverter requirements. Available at: <http://www.homepower.com/accounting-photovoltaic-cell-temperature> [Accessed August 9, 2015].
- Huldt, L., Nilsson, N.G. & Svantesson, K.G., 1979. The temperature dependence of band-to-band Auger recombination in silicon. *Applied Physics Letters*, 35(10), p.776.
- IEC, 2008. Photovoltaic Devices—Part 3: Measurement Principles for Terrestrial Photovoltaic (Pv) Solar Devices With Reference Spectral Irradiance Data. In *Int. Stand., IEC 60904–3, 2nd ed.*
- Ilic, O., Jablan, M., Joannopoulos, J.D., Celanovic, I. & Soljačić, M., 2012. Overcoming the black body limit in plasmonic and graphene near-field thermophotovoltaic systems. *Optics Express*, 20(S3), pp.A366–A384.
- International Energy Agency, 2014. *2014 Key World Energy statistic*,
- IPCC, 2014. *Climate Change 2014 Synthesis report. Contributions of working groups I, II and III to the fifth assessment report of the intergovernmental panel on climate change*,
- Ishihara, T., 1994. Optical properties of PbI₂-based perovskite structures. *Journal of Luminescence*, 60-61, pp.269–274.
- Jäger-waldau, A., 2014. *PV Status Report 2014*,
- Jakob, M. & Hilaire, J., 2015. Climate science: Unburnable fossil-fuel reserves. *Nature*, 517(7533), pp.150–152.
- Jancovici, J., 2015. How much of a slave master am I? Available at: http://www.manicore.com/anglais/documentation_a/slaves.html [Accessed August 4, 2015].
- Johnston, S.W. & Ahrenkiel, R.K., 1999. Measurement of the temperature-dependent recombination lifetimes in photovoltaic materials. In *AIP Conference Proceedings*. AIP, pp. 505–510.

- Katz, E. a., Faiman, D., Tuladhar, S.M., Kroon, J.M., Wienk, M.M., Fromherz, T., Padinger, F., Brabec, C.J., et al., 2001. Temperature dependence for the photovoltaic device parameters of polymer-fullerene solar cells under operating conditions. *Journal of Applied Physics*, 90(10), pp.5343–5350.
- Kawajiri, K., Oozeki, T. & Genchi, Y., 2011. Effect of temperature on PV potential in the world. *Environmental science & technology*, 45(20), pp.9030–9035.
- Kerr, M.J., Cuevas, A. & Campbell, P., 2003. Limiting efficiency of crystalline silicon solar cells due to Coulomb-enhanced Auger recombination. *Progress in Photovoltaics: Research and Applications*, 11(2), pp.97–104.
- King, D., 1997. Temperature coefficients for PV modules and arrays: measurement methods, difficulties, and results. In *26th IEEE Photovoltaic Specialists Conference*.
- Kittel, C., 1996. *Introduction to Solid State Physics, 7th Edition*, John Wiley & Sons, Inc.
- Klaassen, D., 1992a. A unified mobility model for device simulation—I. Model equations and concentration dependence. *Solid-State Electronics*, 35(7), pp.953–959.
- Klaassen, D., 1992b. A unified mobility model for device simulation—II. temperature dependence of carrier mobility and lifetime. *Solid-State Electronics*, 35(7), pp.961–967.
- Kosten, E.D.E., Atwater, J.H.J., Parsons, J., Polman, A. & Atwater, H.A., 2013. Highly efficient GaAs solar cells by limiting light emission angle. *Light: Science & Applications*, 2(1), pp.1–6.
- Krauter, S., 2004. Increased electrical yield via water flow over the front of photovoltaic panels. *Solar Energy Materials and Solar Cells*, 82(1-2), pp.131–137.
- Krauter, S. & Hanitsch, R., 1996. Actual optical and thermal performance of PV-modules. *Solar Energy Materials and Solar Cells*, 41-42, pp.557–574.
- Krauter, S., Hanitsch, R. & Moreira, L., 1996. New optical and thermal enhanced PV-modules performing 12% better under true module rating conditions. *25th IEEE Photovoltaic Specialists Conference*, (JUNE).
- Kurtz, S., Whitfield, K., Tamizhmani, G., Koehl, M., Miller, D., Joyce, J., Wohlgemuth, J., Bosco, N., et al., 2011. Evaluation of high-temperature exposure of photovoltaic modules. *Progress in Photovoltaics: Research and Applications*, (March), pp.954–965.
- Kurtz, S., Wohlgemuth, J., Hacke, P., Bosco, N., Kempe, M., Smith, R. & Packard, C.E., 2011. The Challenge to Move from “One Size Fits All” to PV Modules the Customer Needs. In *26th European Photovoltaic Solar Energy Conference and Exhibition*. pp. 3064–3068.
- Landis, G., 1994. Review of solar cell temperature coefficients for space. In *Proceedings*

- of the 13th Space Photovoltaic Research and Technology Conference. pp. 385–399.
- Landis, G.A., Jenkins, P., Scheimant, D. & Ryne, R., 2004. Extended Temperature Solar Cell Technology Development. In *2nd International Energy Conversion Engineering Conference*. pp. 1–7.
- Landsberg, P.T. & Badescu, V., 2000. Carnot factor in solar cell efficiencies. *Journal of Physics D: Applied Physics*, 33(22), pp.3004–3008.
- Laroche, M., Carminati, R. & Greffet, J.J., 2006. Near-field thermophotovoltaic energy conversion. *Journal of Applied Physics*, 100(6).
- Lee, B., Liu, J.Z., Sun, B., Shen, C.Y. & Dai, G.C., 2008. Thermally conductive and electrically insulating EVA composite encapsulant for solar photovoltaic (PV) cell. *eXPRESS Polymer Letters*, 2(5), pp.357–363.
- Lenert, A., Bierman, D.M., Nam, Y., Chan, W.R., Celanović, I., Soljačić, M. & Wang, E.N., 2014. A nanophotonic solar thermophotovoltaic device. *Nature Nanotechnology*, (January), pp.1–5.
- Loferski, J.J., 1956. Theoretical Considerations Governing the Choice of the Optimum Semiconductor for Photovoltaic Solar Energy Conversion. *Journal of Applied Physics*, 27(7), pp.777–784.
- Luque, A. & Martí, A., 1997. Increasing the Efficiency of Ideal Solar Cells by Photon Induced Transitions at Intermediate Levels. *Physical Review Letters*, 78(26), pp.5014–5017.
- Luque, A., Martí, A. & Stanley, C., 2012. Understanding intermediate-band solar cells. *Nature Photonics*, 6(3), pp.146–152.
- Makrides, G., Zinsser, B., Norton, M. & Georghiou, G., 2012. Performance of Photovoltaics Under Actual Operating Conditions. In D. V. Fthenakis, ed. *Third Generation Photovoltaics*. InTech, pp. 201–232.
- Makrides, G., Zinsser, B., Phinikarides, A., Schubert, M. & Georghiou, G.E., 2012. Temperature and thermal annealing effects on different photovoltaic technologies. *Renewable Energy*, 43, pp.407–417.
- Markvart, T., 2008. Solar cell as a heat engine: energy-entropy analysis of photovoltaic conversion. *Physica Status Solidi (a)*, 205(12), pp.2752–2756.
- Martí, A. & Araújo, G.L., 1996. Limiting efficiencies for photovoltaic energy conversion in multigap systems. *Solar Energy Materials and Solar Cells*, 43(2), pp.203–222.
- Menard, E., Meitl, M. & Burroughs, S., 2012. Indirect temperature measurement of CPV solar cells using wavelength shift of the sub-cells luminescence emission peaks. In *27th European Photovoltaic Solar Energy Conference and Exhibition*. pp. 189–193.
- Messina, R. & Ben-Abdallah, P., 2013. Graphene-based photovoltaic cells for near-field

- thermal energy conversion. *Scientific reports*, 3, pp.1–5.
- Micheli, L., Sarmah, N., Luo, X., Reddy, K. & Mallick, T., 2012. Infrared reflecting coverglasses for multijunction cells in a terrestrial high-concentrating photovoltaic system. In *27th European Photovoltaic Solar Energy Conference and Exhibition*. pp. 266–270.
- Mishima, T., Taguchi, M., Sakata, H. & Maruyama, E., 2011. Development status of high-efficiency HIT solar cells. *Solar Energy Materials and Solar Cells*, 95(1), pp.18–21.
- Moser, D., Pichler, M. & Nikolaeva-Dimitrova, M., 2013. Filtering Procedures for Reliable Outdoor Temperature Coefficients in Different Photovoltaic Technologies. *Journal of Solar Energy Engineering*, 136(May 2014), pp.1–10.
- Mulet, J.-P., Joulain, K., Carminati, R. & Greffet, J.-J., 2002. Enhanced radiative heat transfer at nanometric distances. *Microscale Thermophysical Engineering*, 6(3), pp.209–222.
- Murphy, J., McGuire, R. & Bothe, K., 2014. Minority carrier lifetime in silicon photovoltaics: The effect of oxygen precipitation. *Solar Energy Materials and Solar Cells*, pp.0–10.
- Narayanaswamy, A. & Chen, G., 2003. Surface modes for near field thermophotovoltaics. *Applied Physics Letters*, 82(20), pp.3544–3546.
- Nell, M.M.E. & Barnett, A. a. M., 1987. The spectral p-n junction model for tandem solar-cell design. *IEEE Transactions on Electron Devices*, 34(2), pp.257–266.
- Nozik, A.J., 2008. Multiple exciton generation in semiconductor quantum dots. *Chemical Physics Letters*, 457(1-3), pp.3–11.
- NREL, 2015. NREL record efficiency chart. Available at: <http://www.nrel.gov/ncpv/> [Accessed August 5, 2015].
- Olkhovets, A., Hsu, R.C., Lipovskii, A. & Wise, F., 1998. Size-Dependent Temperature Variation of the Energy Gap in Lead-Salt Quantum Dots. *Physical Review Letters*, 81(16), pp.3539–3542.
- Ono, L.K., Raga, S.R., Wang, S., Kato, Y. & Qi, Y., 2015. Temperature-dependent hysteresis effects in perovskite-based solar cells. *J. Mater. Chem. A*, 3, pp.9074–9080.
- Oth, D.H. & Ross, R.G., 1983. Assessing photovoltaic module degradation and lifetime from long term environmental tests. In *29th Annual Technical Meeting of the Institute of Environmental Sciences*.
- Pacala, S. & Socolow, R., 2004. Stabilization wedges: solving the climate problem for the next 50 years with current technologies. *Science (New York, N.Y.)*, 305(5686), pp.968–972.

- Panasonic, 2015. website. Available at: <http://panasonic.net/ecosolutions/solar/hit/> [Accessed August 1, 2015].
- Park, K., Basu, S., King, W.P. & Zhang, Z.M., 2008. Performance analysis of near-field thermophotovoltaic devices considering absorption distribution. *Journal of Quantitative Spectroscopy and Radiative Transfer*, 109(2), pp.305–316.
- Pipe, K., Ram, R. & Shakouri, a., 2002. Bias-dependent Peltier coefficient and internal cooling in bipolar devices. *Physical Review B*, 66(12), pp.1–11.
- Ponce-Alcántara, S., Connolly, J.P., Sánchez, G., Míguez, J.M., Hoffmann, V. & Ordás, R., 2014. A statistical analysis of the temperature coefficients of industrial silicon solar cells. *Energy Procedia*, 55, pp.578–588.
- Press, W.H., 1976. Theoretical maximum for energy from direct and diffuse sunlight. *Nature*, 264(5588), pp.734–735.
- Rajkanan, K., Singh, R. & Shewchun, J., 1979. Absorption coefficient of silicon for solar cell calculations. *Solid-State Electronics*, 22(9), pp.793–795.
- Raman, A.P., Anoma, M.A., Zhu, L., Rephaeli, E. & Fan, S., 2014. Passive radiative cooling below ambient air temperature under direct sunlight. *Nature*, 515, pp.540–544.
- Rau, U., 2007. Reciprocity relation between photovoltaic quantum efficiency and electroluminescent emission of solar cells. *Physical Review B*, 76(8), pp.1–8.
- Rein, S. & Glunz, S.W., 2003. Electronic properties of the metastable defect in boron-doped Czochralski silicon: Unambiguous determination by advanced lifetime spectroscopy. *Applied Physics Letters*, 82(7), pp.1054–1056.
- Richter, A., Glunz, S.W., Werner, F., Schmidt, J. & Cuevas, A., 2012. Improved quantitative description of Auger recombination in crystalline silicon. *Physical Review B*, 86(16), p.165202.
- Richter, A., Hermle, M. & Glunz, S.W., 2013. Reassessment of the limiting efficiency for crystalline silicon solar cells. *IEEE Journal of Photovoltaics*, 3(4), pp.1184–1191.
- Riedel, I., Parisi, J., Dyakonov, V., Lutsen, L., Vanderzande, D. & Hummelen, J.C.C., 2004. Effect of Temperature and Illumination on the Electrical Characteristics of Polymer–Fullerene Bulk-Heterojunction Solar Cells. *Advanced Functional Materials*, 14(1), pp.38–44.
- Rosa-Clot, M., Rosa-Clot, P., Tina, G.M. & Scandura, P.F., 2010. Submerged photovoltaic solar panel: SP2. *Renewable Energy*, 35(8), pp.1862–1865.
- Ross, R. & Gonzalez, C., 1980. Reference conditions for reporting terrestrial photovoltaic performance. In *AS/ISES Annual Meeting*. pp. 1091–1097.
- Ross, R.T., 1967. Some Thermodynamics of Photochemical Systems. *The Journal of*

- Chemical Physics*, 46(12), p.4590.
- Ross, R. G., J. & Smokler, M.I., 1986. Electricity from photovoltaic solar cells: Flat-Plate Solar Array Project final report. Volume VI: Engineering sciences and reliability.
- Royne, A., Dey, C.J. & Mills, D.R., 2005. Cooling of photovoltaic cells under concentrated illumination: A critical review. *Solar Energy Materials and Solar Cells*, 86(4), pp.451–483.
- Rüdiger, M., Greulich, J., Richter, A. & Hermle, M., 2013. Parameterization of Free Carrier Absorption in Highly Doped Silicon for Solar Cells. *IEEE Transactions on Electron Devices*, 60(7), pp.2156–2163.
- Ruppel, W. & Würfel, P., 1980. Upper limit for the conversion of solar energy. *IEEE Transactions on Electron Devices*, 27(4), pp.877–882.
- Sah, C.T., Yamakawa, K.A. & Lutwack, R., 1982. Effect of thickness on silicon solar cell efficiency. *IEEE Transactions on Electron Devices*, 29(5), pp.903–908.
- Schenk, A., 1992. A model for the field and temperature dependence of Shockley-Read-Hall lifetimes in silicon. *Solid-State Electronics*, 35(1), pp.1585–1596.
- Schenk, A., 1998. Finite-temperature full random-phase approximation model of band gap narrowing for silicon device simulation. *Journal of Applied Physics*, 84(7), p.3684.
- Schropp, R., 2008. Oxygenated protocrystalline silicon thin films for wide bandgap solar cells with temperature-insensitive cell performance. In *23th European Photovoltaic Solar Energy Conference*. pp. 2109–2112.
- Schropp, R.E.I., Schüttauf, J.W. & van der Werf, K., 2010. Oxygenated Protocrystalline Silicon Thin Films for Wide Bandgap Solar Cells. *MRS Proceedings*, 1245(September), pp.2109–2112.
- Seif, J.P., Krishnamani, G., Ballif, C. & Wolf, S. De, 2015. Amorphous / crystalline silicon interface passivation : ambient-temperature dependence and implications for solar cell performance. *IEEE Journal of Photovoltaics*, 5(3), pp.718–724.
- Shockley, W., 1948. The Theory of p-n Junctions in Semiconductors and p-n Junction Transistors. *Bell System Technical Journal*, pp.435–489.
- Shockley, W. & Queisser, H.J., 1961. Detailed Balance Limit of Efficiency of p-n Junction Solar Cells. *Journal of Applied Physics*, 32(3), pp.510–519.
- Siefer, G., Abbott, P., Baur, C., Schlegl, T. & Bett, A., 2005. Determination of the temperature coefficients of various III–V solar cells. In *20th European Photovoltaic Solar Energy Conference*. Barcelona, Spain, pp. 495–498.
- Siefer, G. & Bett, A.W., 2012. Analysis of temperature coefficients for III-V multi-junction concentrator cells. *Progress in Photovoltaics: Research and Applications*, 22(5), pp.515–524.

- Silverman, T.J., Deceglie, M.G., Marion, B., Cowley, S., Kayes, B. & Kurtz, S., 2013. Outdoor performance of a thin-film gallium-arsenide photovoltaic module. *39th IEEE Photovoltaic Specialists Conference*, pp.0103–0108.
- Silverman, T.J., Jahn, U., Friesen, G. & ..., 2014. *Characterisation of Performance of Thin-film Photovoltaic Technologies (from Report IEA-PVPS T13-02:2014)*,
- Simovski, C., Maslovski, S., Nefedov, I. & Tretyakov, S., 2013. Optimization of radiative heat transfer in hyperbolic metamaterials for thermophotovoltaic applications. *Optics express*, 21(12), pp.14988–15013.
- Singh, P. & Ravindra, N.M., 2012. Temperature dependence of solar cell performance— an analysis. *Solar Energy Materials and Solar Cells*, 101, pp.36–45.
- Singh, P., Singh, S., Lal, M. & Husain, M., 2008. Temperature dependence of I–V characteristics and performance parameters of silicon solar cell. *Solar Energy Materials and Solar Cells*, 92(12), pp.1611–1616.
- Skoplaki, E. & Palyvos, J.A., 2009a. On the temperature dependence of photovoltaic module electrical performance: A review of efficiency/power correlations. *Solar Energy*, 83(5), pp.614–624.
- Skoplaki, E. & Palyvos, J.A., 2009b. Operating temperature of photovoltaic modules: A survey of pertinent correlations. *Renewable Energy*, 34(1), pp.23–29.
- Sproul, A.B. & Green, M.A., 1993. Intrinsic carrier concentration and minority-carrier mobility of silicon from 77 to 300 K. *Journal of Applied Physics*, 73(3), pp.1214–1225.
- Strevel, N., Trippel, L., Gloeckler, M. & Solar, F., 2012. First Solar : greater energy yields in high-temperature conditions Performance characterization and superior energy yield of First Solar PV power plants in high-temperature conditions. *Photovoltaics International*, (August), pp.1–6.
- Sun, C.H., Jiang, P. & Jiang, B., 2008. Broadband moth-eye antireflection coatings on silicon. *Applied Physics Letters*, 92(6), pp.1–3.
- Svetovoy, V.B. & Palasantzas, G., 2014. Graphene-on-silicon near-field thermophotovoltaic cell. , pp.1–6.
- Swanson, R.M., 1979. A proposed thermophotovoltaic solar energy conversion system. *Proceedings of the IEEE*, 67(3), pp.446–447.
- Sze, S. & Ng, K., 1981. *Physics of semiconductor devices*, New York: Wiley.
- Taguchi, M., Maruyama, E. & Tanaka, M., 2008. Temperature dependence of amorphous/crystalline silicon heterojunction solar cells. *Japanese Journal of Applied Physics*, 47(2 PART 1), pp.814–818.
- Tanay, F., Dubois, S., Enjalbert, N. & Veirman, J., 2011. Low temperature-coefficient for

- solar cells processed from solar-grade silicon purified by metallurgical route. , (March), pp.966–972.
- Tayyib, M., Odden, J.O. & Saetre, T.O., 2014a. Influence of Spectral Composition on the Temperature Coefficients of Solar Cells from Elkem Solar. , (4898), pp.2630–2634.
- Tayyib, M., Odden, J.O. & Saetre, T.O., 2014b. Irradiance Dependent Temperature Coefficients for MC Solar Cells from Elkem Solar Grade Silicon in Comparison with Reference Polysilicon. *Energy Procedia*, 55(1876), pp.602–607.
- Tayyib, M., Odden, J.O. & Saetre, T.O., 2013. UV-induced Degradation Study of Multicrystalline Silicon Solar Cells Made from Different Silicon Materials. *Energy Procedia*, 38, pp.626–635.
- Thurston, C.W., 2012. From land to water. *PV magazine*, (April).
- Tiedje, T., Yablonovitch, E., Cody, G.D. & Brooks, B.G., 1984. Limiting efficiency of silicon solar cells. *IEEE Transactions on Electron Devices*, 31(5), pp.711–716.
- Trupke, T., Green, M.A., Würfel, P., Altermatt, P.P., Wang, A., Zhao, J. & Corkish, R., 2003. Temperature dependence of the radiative recombination coefficient of intrinsic crystalline silicon. *Journal of Applied Physics*, 94(8), pp.4930–4937.
- UNFCCC, 2010. Milestones on the road to 2012: The Cancun Agreements. Available at: http://unfccc.int/key_steps/cancun_agreements/items/6132.php [Accessed August 10, 2015].
- Vaillon, R., Robin, L., Muresan, C. & Ménézo, C., 2006. Modeling of coupled spectral radiation, thermal and carrier transport in a silicon photovoltaic cell. *International Journal of Heat and Mass Transfer*, 49(23-24), pp.4454–4468.
- Varshni, Y.P., 1967. Temperature dependence of the energy gap in semiconductors. *Physica*, 34(1), pp.149–154.
- Virtuani, A., Pavanello, D. & Friesen, G., 2010. Overview of temperature coefficients of different thin film photovoltaic technologies. In *25th European Photovoltaic Solar Energy Conference*.
- Vurgaftman, I., Meyer, J.R. & Ram-Mohan, L.R., 2001. Band parameters for III-V compound semiconductors and their alloys. *Journal of Applied Physics*, 89(11 I), pp.5815–5875.
- WBGU, 2003. *Climate Protection Strategies for the 21st Century. Kyoto and Beyond*,
- Whale, M.D. & Cravalho, E.G., 2002. Modeling and performance of microscale thermophotovoltaic energy conversion devices. *IEEE Transactions on Energy Conversion*, 17(1), pp.130–142.
- Whitaker, C.M., Townsend, T.U., Wenger, H.J., Iliceto, a., Chimento, G. & Paletta, F., 1991. Effects of irradiance and other factors on PV temperature coefficients. *The*

- Conference Record of the Twenty-Second IEEE Photovoltaic Specialists Conference - 1991*, pp.608–613.
- Whitlock, C., Brown, D. & Chandler, W., 2006. *NASA surface meteorology and solar energy: methodology (release 3)*,
- Witmer, L., 2010. *Quantification of the passive cooling of photovoltaics using a green roof*.
- Wolf, A., Biro, D., Nekarda, J., Stumpp, S., Kimmerle, A., Mack, S. & Preu, R., 2010. Comprehensive analytical model for locally contacted rear surface passivated solar cells. *Journal of Applied Physics*, 108(12), p.124510.
- Wolf, S. De, Descoeurdes, A., Holman, Z.C. & Ballif, C., 2012. High-efficiency Silicon Heterojunction Solar Cells: A Review. *Green*, 2, pp.7–24.
- Wu, K., Bera, A., Ma, C., Du, Y., Yang, Y., Li, L. & Wu, T., 2014. Temperature-dependent excitonic photoluminescence of hybrid organometal halide perovskite films. *Phys. Chem. Chem. Phys.*, 16(41), pp.22476–22481.
- Wu, S. & Xiong, C., 2014. Passive cooling technology for photovoltaic panels for domestic houses. *International Journal of Low-Carbon Technologies*, 9(2), pp.118–126.
- Würfel, P., 2009. *Physics of Solar Cells: From Basic Principles to Advanced Concepts*,
- Würfel, P., 1982. The chemical potential of radiation. *Journal of Physics C: Solid State Physics*, 15(18), pp.3967–3985.
- Wysocki, J.J. & Rappaport, P., 1960. Effect of temperature on photovoltaic solar energy conversion. *Journal of Applied Physics*, 31(3), pp.571–578.
- Xiao, C., Yu, X., Yang, D. & Que, D., 2014. Impact of solar irradiance intensity and temperature on the performance of compensated crystalline silicon solar cells. *Solar Energy Materials and Solar Cells*, 128, pp.427–434.
- Xu, P., Chen, S., Xiang, H.-J., Gong, X.-G. & Wei, S.-H., 2014. Influence of Defects and Synthesis Conditions on the Photovoltaic Performance of Perovskite Semiconductor CsSnI₃. *Chemistry of Materials*, 26, pp.6068–6072.
- Yablonovitch, E., 2012. The Opto-Electronic Physics Which Just Broke the Efficiency Record in Solar Cells. In *International School of Solid State Physics 56th course "Materials for Renewable Energy."* Erice, Italy.
- Yoon, S. & Garboushian, V., 1994. Reduced temperature dependence of high-concentration photovoltaic solar cell open-circuit voltage (Voc) at high concentration levels. In *1st World Conference on Photovoltaic Energy Conversion - WCPEC (A Joint Conference of PVSC, PVSEC and PSEC)*. IEEE, pp. 1500–1504.
- Yu, C., Chen, Z., J. Wang, J., Pfenninger, W., Vockic, N., Kenney, J.T. & Shum, K., 2011.

- Temperature dependence of the band gap of perovskite semiconductor compound CsSnI₃. *Journal of Applied Physics*, 110(6), p.063526.
- Zdanowicz, T., 2003. Effect of air mass factor on the performance of different type of pv modules. , pp.2019–2022.
- Zeghbrouck, B. Van, 2011. *Principles of semiconductor devices*,
- Zhang, C., Zhang, J., Hao, Y., Lin, Z. & Zhu, C., 2011. A simple and efficient solar cell parameter extraction method from a single current-voltage curve. *Journal of Applied Physics*, 110(6), pp.1–7.
- Zhao, J. & Green, M.A., 1991. Optimized antireflection coatings for high efficiency silicon solar cells. *IEEE transactions on Electron Devices*, 38(8), pp.1925–1934.
- Zhao, J., Wang, A., Robinson, S.J. & Green, M.A., 1994. Reduced temperature coefficients for recent high performance silicon solar cells. *Progress in Photovoltaics: Research and Applications*, 2(3), pp.221–225.
- Zhu, L., Raman, A., Wang, K.X., Anoma, M.A. & Fan, S., 2014. Radiative cooling of solar cells. *Optica*, 1(1), pp.24–26.
- Zimmermann, C.G., Nömayr, C., Kolb, M. & Caon, A., 2011. A solar cell design for the Bepi Colombo high intensity - High temperature mission. *37th IEEE Photovoltaic Specialists Conference*, pp.3713–3718.

Curriculum Vitae (oct. 2015)

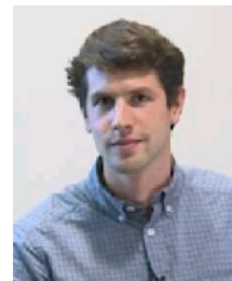
Olivier DUPRE

Permanent address: Jouquetti - 05400 Furmeyer - France






Date of birth and nationality: January 7th, 1989 - French


Email address: dupre.pv@gmail.com

Phone number: +33(0)7 52 67 68 78



Ph.D. Physics of Photovoltaics

Education	
Oct. 2015 	Ph.D. degree in Engineering Physics from INSA Lyon (National Institute of Applied Sciences, http://www.insa-lyon.fr/en).
2011	Energy & Environment Engineering degree from INSA Lyon .
2011	Research Master (M.Sc.) degree from the doctoral school Mechanics, Energy, Civil engineering and Acoustics (MEGA), specialization in Energy and Heat Transfer (in parallel with the last year at INSA Lyon).
2009-2010 	Academic exchange year at NTNU (Norwegian University of Science and Technology, http://www.ntnu.edu) in Trondheim, Norway (teaching language: English).
2006-2011	INSA de Lyon . 2 years of intensive education in mathematics, physics and engineering sciences followed by 3 years of education focused on energy and environment.
Languages	English: fluent, excellent written and oral - TOEIC: 990/990 - 22 months spent in English-speaking countries (Australia, Canada, England, Ireland, and Norway). Scientific writing experience. French: native speaker. German: basic working knowledge.
Professional experience	
Oct. 2012 - Oct. 2015 	Ph.D. thesis at the Centre for Energy and Thermal Sciences of Lyon (CETHIL) (Villeurbanne - France): "Physics of the thermal behavior of photovoltaic devices". Original optimizations of PV devices taking into account their operating conditions. <i>Supervisors: Dr. Rodolphe VAILLON (rodolphe.vaillon@insa-lyon.fr) Prof. Martin A. GREEN (m.green@unsw.edu.au)</i>
Jan. - June 2014 (6 months)  	Invited stay at the Australian Centre for Advanced Photovoltaics (ACAP) and School of Photovoltaic and Renewable Energy Engineering (SPREE) at the University of New South Wales (UNSW) (Sydney - Australia): investigation of the physics of temperature coefficients of solar cells. <i>Local supervisor: Prof. Martin A. GREEN</i>

<p>2012 (8 months)</p> 	<p>Research Engineer at the Centre for Energy and Thermal Sciences of Lyon (CETHIL) (Villeurbanne - France). In-depth analysis of the thermal impacts on the performances of crystalline silicon solar cells. Supported by the National Chair for Research and Teaching Électricité de France (EDF) group – INSA Lyon “Habitats and Energy Innovations” (6 months) and CNRS (2 months).</p>
<p>2011 (6 months)</p>	<p>Research Master at the Centre for Energy and Thermal Sciences of Lyon (CETHIL): study of the electrical and thermal behaviors of thin film solar cells: concepts, theory and modeling (dissertation written in English). <i>Supervisor: Dr. Rodolphe VAILLON</i></p>
<p>Past research activities</p>	
<p>PhD thesis summary</p>	<p>My Ph.D. thesis addressed some thermal issues for solar photovoltaics (PV). Indeed, it is known that the performances of PV cells drop when their temperature increases. My thesis aimed at improving the understanding of the physics of the so-called temperature coefficients (TCs) and that of the heat generation mechanisms in PV devices in order to suggest optimizations that take into account the thermal behavior of PV cells (which is deeply interconnected with their optical and electrical behaviors). This original kind of optimization which obviously depends on the operating conditions fit in the current trend of the PV industry towards products designed for specific locations/conditions.</p>
<p>Publications</p>	
<p>4 Journal Publications</p>	<ul style="list-style-type: none"> • O. Dupré, R. Vaillon, M.A. Green, "Experimental assessment of temperature coefficient theories for silicon solar cells", <i>IEEE Journal of Photovoltaics</i> (42th PVSC special issue), 2015 [accepted] • M.P. Bernardi, O. Dupré, E. Blandre, P-O. Chapuis, R. Vaillon, and M. Francoeur, "Impacts of propagating, frustrated and surface modes on radiative, electrical and thermal losses in nanoscale-gap thermophotovoltaic power generators", <i>Scientific Reports</i>, 5, 11626, 2015 (http://dx.doi.org/10.1038/srep11626) • O. Dupré, R. Vaillon, M.A. Green, "Physics of the temperature coefficients of solar cells", <i>Journal of Solar Energy Materials & Solar Cells</i>, 140, 92-100, 2015 (http://dx.doi.org/10.1016/j.solmat.2015.03.025) • O. Dupré, R. Vaillon, "Optimizations of photovoltaic cells including the minimization of internal heat sources", <i>Journal of Renewable and Sustainable Energy</i>, 6(1), 011201, 2014 (http://dx.doi.org/10.1063/1.4828367)
<p>2 Conference Proceedings</p>	<ul style="list-style-type: none"> • O. Dupré, R. Vaillon, M.A. Green, "Temperature sensitivity of solar cell efficiency: Theory and implications", European PV Solar Energy Conference and Exhibition (EU PVSEC), Hamburg, Germany, Sept. 14-18, 2015 [Abst. + Post.]

- O. Dupré, R. Vaillon, M.A. Green, "Experimental assessment of temperature coefficient theories for silicon solar cells", 42nd IEEE Photovoltaic Specialists Conference (PVSC-42), New Orleans, LA, USA, June 14-19, 2015 [Oral, Best Student Presentation Award Finalist]

**14 Oral and
Poster
Presentations**

- M.P. Bernardi, O. Dupré, E. Blandre, P.O. Chapuis, R. Vaillon, M. Francoeur, "Surface polariton mediated near-field radiation thermophotovoltaic device: radiative, electrical and thermal behaviors", NEXTGEN, Menorca, Spain, April 20-24, 2015 [Abst. + Post.: E.B.]
- O. Dupré, R. Vaillon, M.A. Green, "Temperature coefficients of solar cells: theory and experiment", French American Doctoral Exchange Seminar (FADEX), INES, Bourget du Lac, France, March 22-24, 2015 [Post.]
- O. Dupré, R. Vaillon, M.A. Green, "Physics of the thermal behavior of photovoltaic cells", Invited lecture at a seminar of the School of Photovoltaic and Renewable Energy Engineering (SPREE) at the University of New South Wales (UNSW), Sydney, Australia, June 5, 2014 [Oral]
<http://www2.pv.unsw.edu.au/videos/Olivier-Dupre-5June2014/seminar.php>
- M. Bernardi, O. Dupré, R. Vaillon, P-O. Chapuis, M. Francoeur, "Performance analysis of a nanoscale gap thermophotovoltaic device via a coupled near-field radiation, charge and heat transport model", The 4th ASME Micro/Nanoscale Heat & Mass Transfer International Conference (MNHMT-13), Hong Kong, China, Dec. 11-14, 2013 [Abst. + Oral: P-O.C.]
- M. Bernardi, O. Dupré, R. Vaillon, M. Francoeur, "Performance analysis of a nanoscale gap thermophotovoltaic device via a coupled near-field radiation, charge and heat transport model", ASME 2013 International Mechanical Engineering Congress & Exposition, San Diego, USA, Nov. 15-21, 2013 [Oral: M.B.]
- O. Dupré, R. Vaillon, M. Francoeur, P-O. Chapuis, M.P. Mengüç, "Thermal issues in the design of PV devices: focus on nanoscale-gap thermophotovoltaic cells", 7th International Symposium on Radiative Transfer, RAD-13, Kuşadası, Turkey, June 2-8, 2013 [Abst. + Post. : R.V.]
- O. Dupré, R. Vaillon, M. Francoeur, P-O. Chapuis, M.P. Mengüç, "Thermal issues in the design of PV devices: focus on nanoscale-gap thermophotovoltaic cells", Nanotechnology for Next Generation High Efficiency Photovoltaics Spring International School, Cargèse, France, April 1-6, 2013 [Post.]
- O. Dupré, R. Vaillon, M. Francoeur, P-O. Chapuis, M.P. Mengüç, "Thermal issues in solar and near-field thermo-photovoltaics", 2013 ELyT Lab workshop, Zao To-o-gatta, Japan, Feb. 17-20, 2013 [Abst. + Oral]
- O. Dupré, R. Vaillon, M. Amara, "Investigation of the thermal behavior of c-Si solar cells", Journées Nationales du PhotoVoltaïque, Chantilly, Dec. 11-14, 2012 [Post.]

- O. Dupré, R. Vaillon, M. Amara, "Investigation of the thermal behavior of c-Si cells", Entretiens Jacques Cartier, Lyon, France, Nov. 19-20, 2012 [Post.]
- O. Dupré, R. Vaillon, "Thermal behavior of silicon PV and nano-TPV cells", Journée de la SFT (French Radiation Transfer Network), Odeillo, France, Oct. 10-11, 2012 [Oral]
- O. Dupré, R. Vaillon, M. Amara, "Investigation of the thermal behavior of c-Si solar cells", Workshop *Optique et Energie* of the Pôle Optique Rhône-Alpes, Le Bourget du Lac, France, Oct. 2, 2012 [Post.]
- O. Dupré, R. Vaillon, M. Amara, "Investigation of the thermal behavior of c-Si solar cells", International School of Solid State Physics 56th, Course: *Materials for Renewable Energy*, Erice, Italy, July 18– 28, 2012 [Post.]
- R. Couderc, O. Dupré, M. Amara, R. Vaillon, M. Lemiti, "Thermal and electrical behavior of silicon interdigitated back contact solar cell for CPV applications", PhotoVoltaic Technical Conference – Thin Film & Advanced Silicon Solutions, Aix en Provence, France, May 22-24, 2012 [Post.]

FOLIO ADMINISTRATIFTHÈSE SOUTENUE DEVANT L'INSTITUT NATIONAL
DES SCIENCES APPLIQUÉES DE LYON

NOM : Dupré
(avec précision du nom de jeune fille, le cas échéant)

DATE de SOUTENANCE : 16 Octobre 2015

Prénoms : Olivier , Denis

TITRE : Physics of the thermal behavior of photovoltaic devices
(Physique du comportement thermique des systèmes photovoltaïques)

NATURE : Doctorat

Numéro d'ordre : 2015ISALOO89

Ecole doctorale : MEGA (Mécanique, Energétique, Génie Civil, Acoustique)

Spécialité : Energétique

RESUME :

Cette thèse porte sur l'étude du comportement thermique des systèmes photovoltaïques (PV). La première partie de la thèse rassemble et étend l'état de l'art sur la dépendance en température des rendements de conversion PV. L'analyse détaille l'ensemble des phénomènes physiques mis en jeu afin d'améliorer la compréhension des coefficients de température des différentes technologies de cellules PV. La seconde partie de la thèse recense les travaux de recherches effectués pour mitiger l'impact négatif de la température sur les performances des systèmes PV et propose une approche originale qui consiste à prendre en compte les conditions de fonctionnement du système dans le processus d'optimisation de ses caractéristiques. Afin de réaliser de telles optimisations, un modèle thermique complet et général pour les systèmes de conversion photovoltaïque est développé. Enfin, des applications à des systèmes photovoltaïque et thermophotovoltaïque démontrent la pertinence de l'approche proposée.

MOTS-CLÉS :

Photovoltaïque, Température, Optimisation, Physique, Thermique, Energétique

Laboratoire (s) de recherche :

Centre d'Energétique et de Thermique de Lyon (CETHIL)

Directeur de thèse:

R. Vaillon

Président de jury :

D. Lincot

Composition du jury :

D. Lincot	Directeur de Recherche CNRS (IRDEP, France)	Rapporteur
A. Marti Vega	Professeur (IES, UPM, Espagne)	Rapporteur
S. Dubois	Docteur (CEA - INES, France)	
N. Wyrsh	Docteur, collaborateur scientifique (PV-LAB, EPFL, Suisse)	
M.A. Green	Professeur (ACAP, SPREE, UNSW, Australie)	
R. Vaillon	Directeur de Recherche CNRS (CETHIL, France)	Directeur de Thèse